UNIVERSIDAD NACIONAL AUTÓNOMA DE MÉXICO
PROGRAMA DE POSGRADO EN CIENCIAS DE LA TIERRA

Significado tectónico de rocas del Paleozoico Superior–Mesozoico Inferior y eventos tectono-termales en el sureste del Complejo Acatlán, sur de México

---

Tectonic significance of latest Paleozoic–Early Mesozoic rocks and tectonothermal events in the southeastern Acatlán Complex, southern Mexico

presenta
Maria Helbig

TESIS

sometida en cumplimiento parcial de los requisitos para obtener el grado de
Doctor en Ciencias de la Tierra

ASESORES
J. Duncan Keppie
J. Brendan Murphy
Luigi A. Solari (tutor oficial)

COMITÉ TUTORIAL
Dr. Luigi A. Solari
Dr. J. Duncan Keppie
Dr. Dante Morán Zenteno
Dr. J. Brendan Murphy

Juriquilla, mayo, 2013

COMITÉ DE ADMISIÓN

Dra. Elizabeth Solleiro Rebolledo
Dr. Fernando Ortega Gutiérrez
Dr. Dante J. Morán Zenteno
Dr. Mariano Elías Herrera

COMITÉ PREDOCTORAL

Dr. Luigi A. Solari
Dr. Peter Schaaf
Dr. Susana Alicia Alaniz Alvarez
Dr. Arturo Gómez Tuena
Dr. Luca Ferrari

COMITÉ DE EXAMEN DE GRADO

Dr. J. Duncan Keppie (presidente)
Dr. Michelangelo Martini (vocal)
Dr. Luigi A. Solari (secretario)
Dr. Timothy Lawton (suplente)
Dr. Bodo Weber (suplente)

Universidad Nacional Autónoma de México
Centro de Geociencias, Campus Juriquilla
Blvd Juriquilla 3001 Juriquilla, Querétaro,
C.P. 76230, MÉXICO
mhelbig@geociencias.unam.mx

A mi familia.

RESUMEN

El Complejo triásico–jurásico Ayú en el Sur de México, está constituido por el Litodema Chazumba, la Migmatita Magdalena, rocas intrusivas de San Miguel y los cuerpos máficos y ultramáficos de Tepejillo y Tultitlán, los cuales previamente fueron considerados como parte del Complejo paleozoico Acatlán. El área de estudio se encuentra en un horst y está delimitada por rocas contemporáneas, sedimentarias, continentales, fluviales, no metamórficas y parcialmente deformadas. El Litodema Chazumba esta constituido por una secuencia siliciclástica de probable naturaleza turbidítica, polideformada y metamorfizada en condiciones de facies de anfibolita e intercalada con boudines de orto-anfibolitas. En el sur del área, la secuencia metasedimentaria está afectada por fusión parcial con una edad de ca. 171 Ma, un proceso que formó la Migmatita Magdalena. La migmatización fue acompañada por intrusiones de diques granodioríticos, dioríticos, y graníticos así como cuerpos pegmatiticos de 171–168 Ma, que por lo demás están caracterizados por agrupaciones de circones heredados de edades de ca. 260–290, 320–360, 420–480, 880–990, y 1080–1250 Ma las cuales también caracterizan el Litodema Chazumba. El análisis de zircones detriticos por geocronología por U–Pb en siete muestras arrojó edades más jóvenes en 192, 198, 214, 250, 266, y 291 Ma, todas ellas en conjunto sugieren un límite superior para el depósito en el Triasico Tardío–Jurásico Medio.

La geoquímica de roca total de las orto-anfibolitas con una edad de ca. 170–200 Ma indica una composición en el rango desde basaltos alcalinos y basaltos transicionales hasta tholeiitas tipo N-MORB. Los patrones de elementos de las Tierras Raras (REE) de los basaltos alcalinos (Grupo I) se caracterizan por pendientes fuertemente negativas, mientras los basaltos transicionales (Grupo II) muestran un moderado enriquecimiento de las Tierras Raras ligeras (LREE) sobre las pesadas (HREE). Los basaltos subalcalinos (Grupo III) exhiben un leve enriquecimiento de LREEs y los basaltos subalcalinos del Grupo IV tienen patrones de REEs relativamente planos con un leve empobrecimiento de LREEs. Los diagramas de multiples elementos trazas de anfibolitas de Grupos III–IV revelan anomalías negativas muy definidas de Nb y Ta.

Los valores iniciales de ϵ_{Nd}(t = 190 Ma) de los orto-anfibolitas van desde +9.01 a –2.16. Los basaltos alcalinos tienen valores iniciales de ϵ_{Nd} negativos, sugiriendo procedencia de una fuente más vieja del manto subcontinental con edades modelo T_{DM} de 877 y 791 Ma. Las anfibolitas de Grupos II–IV tienen valores iniciales de ϵ_{Nd} positivos que van desde +2.31 a +9.01, indicando una transición de una fuente de manto más viejo a una más juvenil, lo que es típico de un escenario trasarco. La gequímica de las rocas metasedimentarias sugiere una procedencia de una fuente de rocas ácidas pertenecientes a un arco magmático. Los patrones de REEs normalizados a condrita están caracterizados por enriquecimiento de LREEs, HREEs planos y anomalías negativas de Eu. Las composiciones isotopicas de Sm-Nd indican que la mayoría de las muestras derivaron del basamento cratónico y

grafican encima del Complejo Oaxaqueño con valores ϵ_{Nd} (t = 195 Ma) desde –5.53 a –7.65. Las muestras con valores más altos de ϵ_{Nd} (–1.42 and +1.06) sugieren como una influencia adicional de una componente más juvenil.

La geocronología U–Pb, geoquímica, y estudios isotopicos de Sm–Nd de las anfibolitas y rocas metasedimentarias del Litodema Chazumba son consistentes con sedimentación turbidítica en un ambiente tipo trasarco a lo largo de un margen pasivo rifteado, cerca de un arco contemporáneo. Por lo tanto, se infiere una correlación del Litodema Chazumba con varios conjuntos máficos en el oeste de México y el abanico Potosí que se formaban a lo largo del margen rifteado occidental de Pangea. Es probable que el aplastamiento de la zona de subducción resultase en erosión por subducción durante el Jurásico Temprano–Medio y calbamiento del Litodema Chazumba a profundidades equivalente a condiciones metamórficas de facies de anfibolita. El aumento de inclinación de la placa en subducción y el rifting diacrónico del Golfo de México contribuyó a la extensión tectónica de la porción continental de México y facilitó la exhumación tectónica del Litodema Chazumba por fallamento normal en la falla reactivada de Providencia después del Jurásico Medio–Tardío. En general, la documentación de un conjunto de trascarco en el Complejo Ayú requiere de una sedimentación cercana a un océano en subducción, favoreciendo así el model de reconstrucción Pangea-A.

ABSTRACT

The Triassic–Jurassic Ayú Complex in southern Mexico, formerly inferred to be part of the Paleozoic Acatlán Complex, consists of the Chazumba Lithodeme, the Magdalena Migmatite, the San Miguel intrusive rocks and the mafic to ultramafic Tepejillo and Tultitlán lenses. The study area crops out in a horst and is fault-bounded by contemporaneous, unmetamorphosed and un- to mildly deformed continental fluvial sedimentary rocks. The Chazumba Lithodeme comprises a polydeformed, amphibolite facies metamorphosed siliciclastic, turbiditic sequence that is intercalated with boudinaged ortho-amphibolites. In the south, the metasedimentary sequence is affected by a ca. 171 Ma partial melting which formed the Magdalena Migmatite. Migmatisation was accompanied by 171–168 Ma intrusions of granodioritic, dioritic, and granitic dikes and sheets as well as pegmatite bodies, which are characterised by inherited zircon populations of ca. 260–290, 320–360, 420–480, 880–990, and 1080–1250 Ma that are also found in the Chazumba Lithodeme. U–Pb detrital zircon dating of seven metasedimentary samples from the migmatized and unmigmatized Chazumba Lithodeme yielded youngest detrital zircons and clusters of 192, 198, 214, 250, 266, and 291 Ma, and are interpreted to reflect the Late Triassic–Middle Jurassic deposition of the turbiditic rocks of the Chazumba Lithodeme.

Whole-rock geochemistry of the ca. 170–200 Ma ortho-amphibolites suggests a composition ranging from alkalic and transitional basalts to normalised mid-ocean ridge basalt (N-MORB) tholeiites. Rare earth element (REE) patterns of alkaline basalts (Group I) are characterized by steep negative slopes, whereas transitional basalts (Group II) show

moderate light REE (LREE) enrichment. Subalkalic Group III displays slight LREE enrichment and Group IV has relatively flat REE patterns with slight depletion in LREEs. Multiple trace element plots of Group III–IV amphibolites reveal strongly negative Nb–Ta anomalies.

Initial Nd values (t = 190 Ma) of the amphibolites range from +9.01 to –2.16. Alkalic basalts have negative Nd values, suggesting derivation from an older subcontinental mantle source (T_{DM} = 877 and 791 Ma). Group II–IV amphibolites have positive ϵ_{Nd} values ranging from +2.31 to +9.01, indicating a transition from an older to a relatively juvenile mantle source that is typical of a back-arc setting. The geochemistry of the metasedimentary rocks suggests derivation from an acid-arc source. Chondrite-normalized REE patterns are characterized by LREE enrichment, flat HREE, and negative Eu anomalies. Sm–Nd systematics indicate that most samples were derived from cratonic basement and plot within the Oaxacan Complex envelope with ϵ_{Nd} values (t = 195 Ma) ranging from –5.53 to –7.65. We interpret two samples with higher ϵ_{Nd} values (–1.42 and +1.06) to reflect the additional influence of a more juvenile component.

LA-ICP-MS geochronology, bulk-geochemistry and Sm–Nd systematics of the amphibolites and metasedimentary rocks of the Chazumba Lithodeme are consistent with turbidite sedimentation in a back-arc environment along a rifted passive margin, close to a contemporaneous magmatic arc. Therefore, the Chazumba Lithodeme is inferred to be correlative with various western Mexican Triassic–Jurassic mafic suites and the Potosí fan that formed along the western rifted margin of Pangea. It is probable that flattening of the subduction zone led to subduction erosion during the Early–Middle Jurassic and underthrusting of the Chazumba Lithodeme to depths equivalent to amphibolite facies metamorphism. Steepening of the subducting slab and diachronous rifting within the Gulf of Mexico contributed to extensional tectonics recorded on the Mexican mainland and facilitated the tectonic exhumation of the Chazumba Lithodeme by normal faulting along the reactivated Providencia shear zone in the post Middle–Late Jurassic. More generally, the documentation of arc-back arc assemblages in the Ayu Complex requires deposition adjacent to a subducting ocean, and thus supports a Pangea-A reconstruction.

AGRADECIMIENTOS

Me gustaría agradecer en primer lugar a mis supervisores J. Duncan Keppie, J. Brendan Murphy, y Luigi A. Solari por su compromiso, motivación, asistencia en el campo o en el laboratorio. Duncan, eres verdaderamente una inspiración como geólogo, pensador y ser humano, me enseñaste a tener siempre una vista fresca y franca de ver las cosas y trabajar estratégicamente. Brendan, gracias por tantos años de estímulo, mejorar mis habilidades de escritura y trabajar de manera eficiente. Luigi, gracias por tu crítica constructiva para con mis manuscritos, el asesoramiento metodológico y técnico, las horas de asistencia de laboratorio, el ayuda en traducir la tesis y por mantener la cabeza fría durante cuestiones burocráticas. Estoy obligado a muchas personas involucradas en mi investigación, en primer lugar, a Moritz Kirsch, que fue mi compañero constante e indispensable en el campo, y siempre contribuyó discusiones instructivas. A Mario, Carlos, Gonzalo, Fabián, Damian, Jaroslav Dostal, Cecilio Quesada para conversaciones inspirativas durante varias salidas al campo. Doy las gracias a Consuelo Macías Romo, Alexander Iriondo, Aldo Izaguirre, Carlos, Uwe Martens, Mónica Enríquez, Harim Arvizu, y Ofelia Pérez Arvizu de cuya experiencia en el laboratorio me beneficié mucho durante la preparación de las muestras. Además, me gustaría dar las gracias a Dante Morán Zenteno, Fernando Ortega Gutiérrez, Arturo Gómez Tuena, Roberto S. Molina Garza, Keppie Fraser y Martiny Barbara para discusiones estimulantes. Agradezco mucho los consejos y las sugerencias de mi comité predoctoral, entre otros, Peter Schaaf, Susana Alaniz y Luca Ferrari. Le debo mi sincero agradecimiento a Marta Pereda Miranda, asistente académica del Posgrado en Ciencias de la Tierra, y al abogado Lic. Ana Paola González Cruz, cuya asistencia burocrática extraordinaria me fue de inestimable valor. Esta tesis no habría sido posible sin las becas otorgadas del Consejo Nacional de Ciencia y Tecnología (CONACYT), la Dirección General de Estudios de Posgrado (DGEP) de la UNAM, y el Programa de Posgrado en Ciencias de la Tierra (PPCT), UNAM. De la misma manera, me gustaría dar las gracias a la Universidad Nacional Autónoma de México, que proporciona un ambiente liberal y de espíritu libre para sus estudiantes. Doy las gracias a la gente de las comunidades de Sta. María Ayú, San Miguel Ixitlán, Ixtapan, Tepejillo y Cosoltepec para permitir el acceso a su tierra y por siempre ser amable y tolerante. No encuentro palabras para expresar mi gratitud a mi familia Martina, Johannes, Christoph, Erika, Rudi, Claudi, Isa, Gudrun, Hubert ya la familia de Moritz, Bettina, Micha, FM, Heike, Steffi, Brigitta, y Ruth que todos me apoyaron con mucho cariño durante todos estos años lejos de casa. Mis recuerdos más cálidos de México están compartidos con todos mis amigos en los viajes que hicimos, María de la O, Oscar, Estela, Domingo, Lariza, Dani, Lina, Ramón, Gianluca, Teo, Rosana, Jon, Pierre, Philippe, Gianluca, Clara, Laura, Laurence, Jacobo, Mauricio, Hugo y muchos más. La escena cultural de Querétaro no sería lo mismo sin el Quinto Patio, con todos sus habitantes, especialmente sus gatos. Doy las gracias a mi

querida amiga Bjarnheiður, por sus largas cartas, correos electrónicos y postales de alegría y cariño. A Helena, Andreas, Bert, Kai, Martin, Gundel, Vieli, y toda la banda para mantener la buena vibra de nuestra amistad durante tanto tiempo separados. Doy las gracias a la gente de El Muro: Steph, Marciano, Charlie, Rueda, Wilbert, Nan, y muchos más. Florian, mi querido amigo, me ayudaste tanto con las preguntas en GMT y LaTeX. También me gustaría dar las gracias a Konstanze por su aliento, espíritu, y consejo. Siempre estaré en deuda con mi amor, amigo y compañero, Moritz—¡gracias por esa aventura mexicana, por cuidarme siempre, compartir tanto los días alegres como los difíciles, tu sinceridad, optimismo, y música!

ÍNDICE GENERAL

ÍNDICE DE TABLAS

1

INTRODUCCIÓN

Esta tesis se enfoca en rocas mesozoicas tanto metasedimentarias como ígneas , polideformadas del *Complejo Ayú* en el sur de y al esclarecimiento de su significado tectónico para el desarrollo de la margen occidental de Pangea. El "Complejo Ayú" se introduce como nuevo complejo según el *North American Stratigraphic Code*[*] . Las unidades de rocas del Complejo Ayú fueron asignadas anteriormente al Complejo Acatlán del Paleozoico: los datos anteriormente publicados (Ortega-Gutiérrez, 1975, 1978; Yáñez *et al.*, 1991; Keppie *et al.*, 2004a; Talavera-Mendoza *et al.*, 2005; Keppie *et al.*, 2006b) eran insuficientes para determinar la edad y el ambiente tectónico de estas rocas. Esta tesis incluye un muestreo más completo de los protolitos sedimentarios para fechamiento de circones detríticos e ígneos y de las rocas máficas para estudios isotópicos de Sm-Nd. Además, se realiza un análisis geoquímico de estas rocas para las que no existían datos anteriormente. Los datos geocronológicos, geoquímicos e isotópicos que se presentan en esta tesis, ofrecen una base de datos más amplia para la comprensión del origen de estas rocas, y los procesos tectónicos a lo largo del margen de Pangea para el Mesozoico temprano. Esta tesis es un trabajo cumulativo que consiste de tres publicaciones que conforman los tres capítulos principales (capítulo 2, 3,4).

1.1 MARCO GEOLÓGICO

1.1.1 *General*

La columna estratigráfica para Mesoamérica se caracteriza por el basmento grenvilliano (ca. 1 Ga) del Complejo Oaxaqueño, que subyace ca. 10000 km^2 del sur de México (Fig. 1; Solari *et al.*, 2003, y sus references). Otros afloramientos menores de misma edad se encuentran en el centro y norte de México, y junto con el Complejo Oaxaqueño se conocen como el terreno Oaxaquia (Ortega-Gutiérrez y Ruiz, 1995). Afloramientos localizados en el bloque Maya (Weber y Köhler, 1999; Schaaf *et al.*, 2002; Weber *et al.*, 2005, 2010, 2012), el bloque Chortís (Torres de León *et al.*, 2012) y Andes colombianos (Keppie *et al.*, 2001; Li *et al.*, 2008; Cardona *et al.*, 2010; Ramos, 2010; Ibanez-Mejia *et al.*, 2011, Fig. 1) también podrían haber sido parte del mismo basamento antes de ser desplazados lateralmente después del Mesozoico temprano.

En el sur de México, el Complejo Oaxaqueño está yuxtapuesto contra el Complejo Acatlán a lo largo de la falla de Caltepec (ca. 276 Ma) con direccion norte-sur y me-

[*] NACSN (2005) http://ngmdb.usgs.gov/Info/NACSN/Code2/code2.html

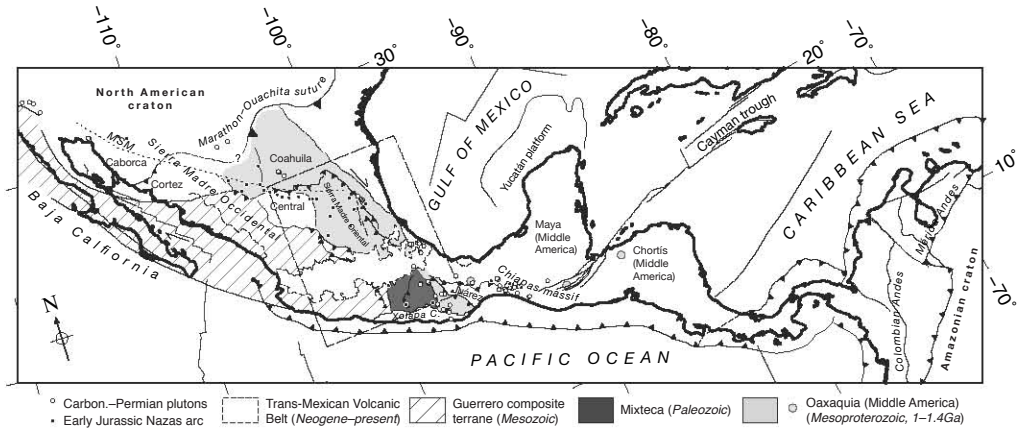

Figura 1.: *Mapa tectónico de Mesoamérica y del norte de Sudamérica con terrenos y provincias principales. Basamento: distribución posible del Terreno Oaxaquia (gris claro) y Terreno Mixteca (gris oscuro) (modificado de Ortega-Gutiérrez y Ruiz, 1995; Keppie et al., 2003; Keppie, 2004; Centeno-García, 2005). Afloramientos de plutones carboniferos–pérmicos modificados de (Kirsch et al., 2012b, y sus referencias), afloramientos del arco jurásico volcánico continental de Nazas de Bartolini et al. (2003); Godínez-Urban et al. (2011). MSM—Mojave-Sonora megashear. El Terreno Compuesto mesozoico de Guerrero (rayado) consiste de los terrenos Tahué, Zihuatanejo, Guanajuato, Arcelia, y Teloloapan (modificados de Keppie, 2004; Centeno-García, 2008). Faja Volcánica Transmexicana modificada de Ferrari (2004).*

canismo transpresional derecho (Elías-Herrera y Ortega-Gutiérrez, 2002; Elías-Herrera *et al.*, 2005). Ambos complejos están traslapados por capas rojas de la formación Matzitzi de edad pérmica inferior (Weber, 1997) o pérmica-triásica medio (Elías-Herrera *et al.*, 2011) lo que sugiere que los complejos Oaxaqueño y Acatlán formaban un compuesto al menos desde el Pérmico–Triásico. Unidades correlacionadas del Complejo Acatlán al norte de la Faja Volcánica Transmexicana se infieren además del mélange ofiolítico paleozoico en el Esquisto Granjeno (Sierra Madre Oriental) y del Gneis de Novillo de una edad de ca. 1 Ga los cuales están yuxtapuestos por cizallamiento transpresional, derecho con dirección NNW (Cameron *et al.*, 2004; Dowe *et al.*, 2005; Nance *et al.*, 2007).

El Complejo Acatlán forma el basamento del terreno Mixteca (Fig. 1) y está compuesto por un conjunto de protolitos sedimentarios e ígneos de bajo grado de metamorfismo y un conjunto de alta presión que se infieren como un residuo de uno o varios océanos paleozoicos (Ortega-Gutiérrez *et al.*, 1999; Talavera-Mendoza *et al.*, 2005; Nance *et al.*, 2006; Keppie *et al.*, 2008b). El cierre de estos océanos y la amalgamación de Pangea son contemporáneos con la intrusión de plutones devónicos–pérmicos en el sur de EE.UU., México y los Andes del norte sugiere un origen un origen del magmatismo durante este periodo de convergencia (Torres *et al.*, 1999; Dickinson y Lawton, 2001; Kirsch *et al.*, 2012b).

El primer mapa del Complejo Acatlán fue realizado por Fernando Ortega-Gutiérrez (Ortega-Gutiérrez, 1975, 1978) que dividó el Complejo Acatlán en el (i) paraautóctono

Grupo Inferior de Petlalcingo (Cámbrico-Ordovícico), (ii) alóctono Grupo superior de Piaxtla, y (iii) la Formación Tecomate y el plutón de Totoltepec (Devónico–Pérmico temprano) (Ortega-Gutiérrez *et al.*, 1999). Sin embargo, esta división se basó en pocos datos geocronológicos. Desde entonces, diversos autores han complementado la base de datos geocronológicos principalmente por medio de análisis por U-Pb y Ar-Ar (Yáñez *et al.*, 1991; Elías-Herrera y Ortega-Gutiérrez, 2002; Keppie *et al.*, 2004a; Sánchez-Zavala *et al.*, 2004; Keppie *et al.*, 2004b; Talavera-Mendoza *et al.*, 2005; Murphy *et al.*, 2006; Vega-Granillo *et al.*, 2007; Miller *et al.*, 2007; Ramos-Arias *et al.*, 2008; Morales-Gámez y Keppie, 2008; Keppie *et al.*, 2008a; Grodzicki *et al.*, 2008; Hinojosa-Prieto *et al.*, 2008; Vega-Granillo *et al.*, 2009; Morales-Gámez *et al.*, 2009; Ortega-Obregón *et al.*, 2009; Keppie *et al.*, 2010; Ramos-Arias y Keppie, 2011; Ramos-Arias *et al.*, 2011; Kirsch *et al.*, 2012b; Keppie *et al.*, 2012c; Kirsch *et al.*, 2012a) y la tectonoestratigrafía tradicional ha sido considerablemente revisada (Talavera-Mendoza *et al.*, 2005; Nance *et al.*, 2006; Keppie *et al.*, 2008b).

La continuación del Complejo Acatlán hacia el norte está cubierta discordantemente por las rocas volcánicas y volcanoclásticas de la Faja Volcánica Transmexicana (Ferrari *et al.*, 1999; Gómez-Tuena *et al.*, 2007). Hacia el oeste, el Complejo Acatlán cabalga calizas cretácicas de la plataforma Guerrero-Morelos a lo largo de la falla de Papalutla (Cretácico Superior–Paleoceno; Ej., Cerca *et al.*, 2007; Ramos-Arias y Keppie, 2011). Xenolitos en diques adakíticos paleocéni cos tempranos que intrusionan las calizas cretácicas contienen circones de ca. 1 Ga (Levresse *et al.*, 2007) lo que sugiere la continuación del basamento Oaxaqueño hacia el oeste por debajo del Complejo Acatlán y la plataforma Guerrero-Morelos. Al sur del Complejo Acatlán, rocas plutónicas y metamórficas de alto grado relacionadas a subducción de edades mesozoicas–cenozoicas del Complejo Xolapa (Schaaf *et al.*, 1995; Ortega-Gutiérrez y Elías-Herrera, 2003; Keppie, 2004; Solari *et al.*, 2007; Pérez-Gutiérrez *et al.*, 2009) fueron cabalgadas y desplazadas a lo largo de la Falla La Venta-Chacalapa con movimiento lateral izquierdo durante el Eoceno–Oligoceno (Ratschbacher *et al.*, 1991; Riller *et al.*, 1992; Tolson, 2005; Solari *et al.*, 2007; Ratschbacher *et al.*, 2009; Keppie *et al.*, 2012a).

1.1.2 *Área de estudio*

El área de estudio se localiza en la frontera entre los estados de Puebla y Oaxaca, entre las ciudades de Acaltán de Osorio, Tehuacán y Huajuapan de León. Las rocas estudiadas incluyen la Formación Chazumba y Migmatita Magdalena que fueron asignadas originalmente al Grupo Petlalcingo de edad inferida del Paleozoico Temprano, y fueron interpretadas como los niveles estratigráficos inferiores del Complejo Acatlán (Ortega-Gutiérrez *et al.*, 1999). Las unidades afloran en un horst delimitado por capas rojas y rocas sedimentarias fluviales, no metamórficas, no deformadas o parcialmente deformadas del Trásico–Jurásico (Morán-Zenteno *et al.*, 1993; Silva-Romo y Mendoza-Rosales,

2000; Silva-Romo *et al*., 2011), y calizas del Cretácico (Morán-Zenteno *et al*., 1993), y está cubiertas discordantemente por rocas volcánicas cenozoicas.

El área está subyacida por una secuencia siliciclástica turbidítica polideformada de alto a medio grado de metamorfismo que consiste en pelitas micáceas, intercaladas con metapsamitas, metagrauvacas y anfibolitas (antes conocida como Formación Chazumba). En el sur, los protolitos metasedimentarios están migmatizados, y denominados como Migmatita Magdalena. La Migmatita Magdalena consiste en gneis, metapelitas y metapsamitas, calsilicatitas, y anfibolitas que son litológicamente semejantes a la Formación Chazumba no migmatizada al norte. Debido a la deformación intensa de la Formación Chazumba y la Migmatita Magdalena, y a la ausencia de estructuras sedimentarias primarias, no es posible determinar la cima ni la base de la estratigrafía. Por lo tanto, Keppie *et al.* (2006b) sugirió cambiar el estatus de la Formación Chazumba y el protolito de la Migmatita Magdalena a un Litodema (es decir, Litodema Chazumba y Magdalena).

Ambas unidades están intrusionadas por diques y cuerpos irregulares de composición diorítica, granodiorítica, granítica, pegmatítica, y leucogranítica los cuales Yáñez *et al.* (1991) llamó rocas intrusivas de San Miguel. Las rocas intrusivas San Miguel fueron fechados por Yáñez *et al.* (1991) y arrojaron una edad de Sm-Nd en granate–roca total de 172 ± 1 Ma, y una edad de Rb-Sr de moscovita–roca total de 175 ± 3 Ma que indican un evento tectonotermal en el Jurásico Medio. Estas edades son similares a una edad U–Pb obtenida por TIMS de un circón redondeado, euhedral, prismático de una leucosoma de la Migmatita Magdalena que arrojó una edad de 171 ± 1 Ma (Keppie *et al*., 2004a), sugiriendo que la fusión parcial del Litodema Magdalena fue contemporánea con la intrusión de las rocas intrusivas de San Miguel. Además, esas edades también representan la edad máxima de deposición de los protolitos metasedimentarios de Jurásico Medio.

Los circones detritícos analizados por U-Pb de un esquisto biotita-moscovita (-granate) en el Litodema Chazumba dieron una edad del circón concordante más joven de 249 ± 20 Ma y un grupo de seis circones con una edad promedio de 300 ± 8 Ma (Talavera-Mendoza *et al*., 2005). En un análisis posterior de una metapsamita del Litodema Chazumba, un solo circón arrojó una edad del Triásico Medio de 239 ± 4 Ma inferida como edad máxima de deposición (Keppie *et al*., 2006b). Edades tempranas similares se obtuvieron para el protolito de la Migmatita Magdalena: Keppie *et al.* (2006b)reportan una edad concordante de un circón sencillo de 304 ± 4 Ma, mientras que los datos de Talavera-Mendoza *et al.* (2005) reportan una edad de un circón sencillo de 244 ± 26 Ma.

En la parte central del Litodema Chazumba, varios cuerpos lenticulares de composición máfico–ultramáfico se encuentran estructuralmente por encima del Litodema Chazumba (Keppie *et al*., 2004a). La lente Tepejillo consiste de cuatro cuerpos ultramáficos de grano grueso (principalmente dunita) y gabroicos que están cortados por diques de diabasa. El contacto entre las rocas metasedimentarias del Litodema Chazumba y la lente Tepejillo está identificado como una capa cablagante plegada (Keppie *et al*., 2004a), sin embargo, no existen datos geocronológicos de este evento de cabalgamiento. El cuerpo de Tultitán consiste de anfibolita masiva y un núcleo de norita metamorfizada. Una análisis concor-

dante por U-Pb LA-ICP-MS de una punta prismática de un circón euhedral de una metanorita arrojó una edad de 174 ± 1 Ma, que se interpreta como la edad de la intrusión para ambas lentes (Keppie *et al.*, 2004a). Los datos geoquímicos de las lentes Tepejillo y Tultitlán se interpretan como cumulatos que intrusionaron la corteza continental inferior (Keppie *et al.*, 2004a).

El contacto norte del Litodema Chazumba está definido por la falla de Providencia con un buzamiento hacia el NE. En el bloque colgante al norte de esa falla afloran las rocas de la Formación Devónico-Carbonífero de Cosoltepec (Talavera-Mendoza *et al.*, 2005), la Formación Tecomate de edad Pérmico y del plutón de Totoltepec de edad Carbonífero–Pérmico (Malone *et al.*, 2002; Keppie *et al.*, 2004a; Kirsch *et al.*, 2012b). El área de la falla de Providencia se caracteriza por un cizallamiento intenso de las rocas metasedimentarias. Las rocas cizalladas dan un buzamiento hacia el NE, lineaciónes de los minerales con dirección NNE–SSW y estructuras S–C indican un transporte tectónico hacia el SSW. Los fechamientos por $^{40}Ar/^{39}Ar$ de moscovita de rocas adentro de la falla de Providencia arrojó una edad 224 Ma, respectivamente, lo que sugiere que las rocas del Complejo Acatlán pasaran la isoterma de ca. 350°C (Keppie *et al.*, 2004a). El contacto entre el bloque colgante y el Litodema Chazumba se caracteriza por la abundancia de anfibolitas, parecido a la localidad típica de la Formación Cosoltepec donde anfibolitas masivas marcan su límite.

1.2 MOTIVACIÓN Y OBJECTIVOS

1.2.1 *Edades de deposito*

Estudios previos de circones detríticos indican que la Formación Chazumba y el protolito de la Migmatita Magdalena fueron depositados en el Pérmico Inferior (Talavera-Mendoza *et al.*, 2005) o entre el Pérmico-Triásico y el Jurásico Medio (Keppie *et al.*, 2006b). Por lo tanto, el tiempo de formación del Litodema Chazumba, la Migmatita Magdalena, las rocas intrusivas de San Miguel y los lentes Tepejillo y Tultitlán traslapa la ruptura de Pangea y así despierta dudas en la inclusión de estas unidades en el Complejo Acatlán. Además, la Formación Chazumba y el protolito de la Migmatita Magdalena se consideraron como dos diferentes sucesiones sedimentarias debido a la ausencia de anfibolitas en la Formación Chazumba (Ortega-Gutiérrez, 1975, 1978; Ortega-Gutiérrez *et al.*, 1999). Sin embargo, los dos estudios anteriores de circones detríticos indican similares edades de depósito (Keppie *et al.*, 2004a, 2006b; Talavera-Mendoza *et al.*, 2005) y sugieren que sus protolitos sedimentarios podrían ser parte de la misma unidad. La primera parte de la tesis (capítulo 2) tiene como objetivo determinar un tiempo más preciso para la sedimentación de las rocas meteasedimentarias, y evalúa las fuentes potenciales sedimentarias usando geocronología U-Pb en circones detríticos e ígneas por LA-ICP-MS. Las edades que se presentan en el capítulo 2 indican que estas rocas son considerablemente más jóvenes que las que definen el Complejo Acatlán. Por lo tanto, el Litodema Chazumba, la Migmatita Magdalena, las rocas intrusivas de San Miguel, y los lentes

máficos–ultramáficos de Tepejillo y Tultilán están asignados a un complejo nuevo y estarán referidos como Complejo Ayú.

1.2.2 *Ambiente tectónico*

Basado en características litológicas, los protolitos sedimentarios de la Formación Chazumba y Migmatita Magdalena fueron interpretados como depósitos de trinchera y antearco de un margen convergente (Ortega-Gutiérrez *et al.*, 1999), o como parte de un prisma acrecional (Ramírez-Espinosa, 2001) o de una cuña clástica (Keppie *et al.*, 2006b). La segunda parte de la tesis (capítulo 3) intenta identificar el ambiente tectónico mediante el uso de geoquímica. Aunque, la geoquímica de rocas clásticas se ha utilizado tradicionalmente para establecer el ambiente tectónico en cuencas sedimentarias (Ej., Bhatia, 1983; Taylor y McLennan, 1985; Bhatia y Crook, 1986; Roser y Korsch, 1988), el éxito muy variable de diagramas de discriminación de rocas clásticas sugiere que una firma geoquímica de una roca sedimentaria es una función compleja dependiente del tipo de la fuente de roca, el grado de meteoraziación, clasificación, reciclaje, diagénesis, metamorfismo, etc. (Armstrong-Altrin y Verma, 2005, y sus referencias). Por lo tanto, la interpretación geoquímica se combina aquí con geocronología U–Pb y estudios isotópicos de Sm-Nd para ganar más información de la fuente de esas rocas sedimentarias. Además la geoquímica de las rocas sedimentarias se complementa con la geoquímica y estudios isotópicos de Sm-Nd de las anfibolitas que afloran como boudins y estructuras *pinch-and-swell* intercaladas con las rocas metasedimetarias del Litodema Chazumba y la Migmatita Magdalena. Sin embargo, la gran parte de las inferencias acerca de la petrogénesis de las rocas se basan en las abundancias de los elementos de alto potencial ionico (HFSEs) y REEs que se consideran relativamente inmóviles durante los procesos secundarios, por lo que preservan las características originales geoquímicas de las rocas estudiadas (Winchester y Floyd, 1977; Taylor y McLennan, 1985).

1.2.3 *Origen alóctono del Complejo Ayú?*

La yuxtaposición del Complejo Ayú Triásico–Jurásico Medio de medio–alto grado contra secuencias sedimentarias contemporáneas, continentales, fluviales, no metamorfoseadas, y parcialmente deformadas aún no está entendido. Es probable que las rocas del Complejo Ayú sean alóctonas y emplazadas tectónicamente en la roca encajonante.

Rocas litológicamente similares contemporáneas subyacen en el Terreno Compuesto Guerrero y el Terreno Central (Centeno-García, 2005, 2008) y pueden estar correlacionadas con el Complejo Ayú. El Terreno Compuesto Guerrero ocupa la mayor parte del occidente de México. Entre el Terreno Compuesto Guerrero y la continuación del norte de Oaxaquia, la Mesa Central forma el Terreno Central. Las rocas más antiguas en el Terreno Central consisten en sucesión siliciclástica, marina, deformada de edad Triásico Tardío (Díaz-Salgado *et al.*, 2003; Anderson *et al.*, 2005; Centeno-García, 2005, 2008) que

se infiere como parte del sistema de Abanico submarino Potosí (Centeno-García y Silva-Romo, 1997; Silva-Romo *et al.*, 2000; Centeno-García, 2005; Barboza-Gudiño *et al.*, 2008, 2010). Las partes distales del Abanico Potosí están inferidas sobreyacer rocas de la corteza oceánica del Complejo Arteaga sugiriendo deposición a lo largo de un margen pasivo rifteado (Centeno-García, 2008; Martini *et al.*, 2009). El rifting en el Triásico/Pérmico está documentado en el Gneis Francisco (Complejo Sonobari en el Terreno Tahué, Keppie *et al.*, 2006a) y en el Complejo Juchatengo (Grajales-Nishimura *et al.*, 1999), respectivamente, y sugiere extensión de la corteza que se expandó a todo lo largo del margen occidental de Oaxaquia. Posteriormente, las rocas del Abanico Potosí fueron deformadas durante la subducción de litósfera oceánica durante el Jurásico Inferior y estuvieron incorporadas en un complejo de acreción relacionado a subducción (Centeno-García, 2008). Sincrónicamente, la intrusión de granitos peraluminosos sintectónicos registran la colisión del Terreno Compuesto Guerrero con los terrenos Mixteca y Oaxaquia que resultó en una deformación intensa de las rocas triásicas volcanogénicas del Esquisto Tejupilco (Elías-Herrera *et al.*, 2000, 2003).

El capítulo 3 examina la hipótesis que las rocas triásicas del Terreno Compuesto Guerrero y del Terreno Central estén correlacionadas con los protolitos siliclásticos y las anfibolitas del Complejo Ayú utilizando geoquímica de elementos mayores y traza así como estudios isotópicos de Sm-Nd para determinar su evolución petrogenética y ambiente tectónico, seguido por una comparación con el Abanico autóctono Potosí y las implicaciones para la paleogeografía de Mesoamérica en el Mesozoico Temprano.

1.2.4 *Paleogeografía*

Aunque hay un consenso general de una configuración de Pangea-A al tiempo de su desintergración (Ej., Domeier *et al.*, 2012), todavía queda controversa la paleogeografía de Mesoamerica dentro de esa configuración (Weber *et al.*, 2007; Vega-Granillo *et al.*, 2009; Keppie y Keppie, 2012). Resolver esta controversia es importante para proporcionar una base para la comprensión de la geodinámica de la amalgación y ruptura de Pangea. Muchos autores (Elías-Herrera y Ortega-Gutiérrez, 2002; Keppie, 2004; Centeno-García, 2005; Weber *et al.*, 2007; Keppie *et al.*, 2008b, 2010; Keppie y Keppie, 2012) localizan los terrenos Mixteca y Oaxaquia a lo largo del margen occidental de Pangea-A central, entre Laurentia y Amazonia, flanqueados al oeste por la zona de subducción del paleo-Pacífico y al este por rifts asociados con la apertura del Golfo de México. En cambio, Talavera-Mendoza *et al.* (2005) y Vega-Granillo *et al.* (2007 y 2009) proponen una posición de los Terrenos Oaxaquia y Mixteca dentro del orógeno Ouachita entre el terreno Maya y Laurentia. En ambas reconstrucciones, el margen Triásico occidental de Pangea está ocupado por la Mesa Central (Terreno Central). Además, el bloque Chortís ha sido reconstruido como fuera del suroeste de México (*"Pacific model"*: Ej., Ross y Scotese, 1988, Dickinson y Lawton, 2001, Rogers *et al.*, 2007, Silva-Romo, 2008, Pindell *et al.*, 2012) o por el lado occidental del Golfo de México (*"Pirate Model"*: Keppie y Keppie, 2012).

El capítulo 4 es una guía de una excursión geológica del Proyecto Internacional de Correlación Geológica Programa 597 International Geological Correlation Program Project 597 (*Amalgamation and breakup of Pangæa*) y se llevó a cabo durante la 108ª reunión anual de la GSA Cordilleran Section en Querétaro, México (28–31 marzo, 2012). La guía examina la actividad de la zona de subducción a lo largo de la periferia de Mesoamérica de approx. 300-200 Ma y sugiere proximidad de esas rocas al paleo-Pacífico, y favorece una posición paleogeográfica Pangea-A.

1.3 METODOLOGÍA

1.3.1 *Geocronología U–Pb por LA-ICP-MS*

Doce muestras (Tabla 1) fueron coleccionadas para fechamiento por U-Pb en circones ablación por ablación láser y espectrometría de masas con fuente de plasma de acoplamiento inductivo (LA-ICP-MS) en el Laboratorio de Estudios Isotópicos (LEI)*, Centro de Geociencias, UNAM, México.

5–10 kg de cada muestra fueron trituradas, lavadas y tamizadas a fracciones de 250-177, 177-149, y 149-125 m. Los minerales pesados fueron concentrados por separación por forma con utilizando la mesa Wilfley. Minerales no magnéticos fueron separados con un separador magnético isodinámico Frantz. Otros minerales no magnéticos (cuarzo, feldespato, y apatita) se separaron por separación por densidad en una columna de líquido pesado de yoduro de metileno. Para cada muestra, los circones (aprox. 120-150 zircones para muestras detríticas, 60-70 zircones para muestras ígneas) fueron escogidos a mano del concentrado bajo un microscopio binocular sin ninguna selección preferente con respecto a las características ópticas y físicas. Los circones fueron montados en resina epóxica y luego pulidos. Los zircones fueron visualizados bajo catodoluminiscencia, utilizando un luminoscopio ELM 3R, para ayudar a la interpretación (zonificación interna, selección de spot).

Los análisis isotópicos se realizaron con un sistema de ablación láser Resolution LPX220 ArF Excimer acoplado a un cuadrupolo Thermo Xii series ICP-MS (Solari *et al*., 2010). Un haz de 34 m fue utilizado para todos los análisis de los granos. Durante el análisis de circón las señales se midieron para los siguientes isótopos: ^{206}Pb, ^{207}Pb, ^{208}Pb, ^{232}Th, ^{238}U. ^{204}Pb para la corrección de Pb común no se mide porque su muy baja abundancia en circón está encubierto por ^{204}Hg, presente en el gas portador He. Para individuar la eventual presencia de inclusiones en el zircón; se pueden también emplear las intensidades de P, Ti, Y, Nb, y REEs como indicadores de fosfato o silicato o inclusiones como indicadores petrogenéticos (Ej., Hoskin y Ireland, 2000, Hoskin y Schaltegger, 2003). El fraccionamiento instrumental, así como el que está inducido durante la ablación (down-hole fractionation) se realizan usando mediciones repetidas de un circón de referencia (estándar Plešovice; Sláma *et al*., 2008). La rutina del muestreo analítico incluye un vidrio estándar (NIST 610), cinco circones estándar, cinco circones desconocidos, seguido por uno circón estándar cada 5 desconocidos, terminado con dos circones estándar. Los análisis de vidrio estándar NIST se utilizan para recalcular las concentraciones de elementos traza del circón analizado. Los análisis adquiridos en función del tiempo se reducen off-line utilizando un software casero escrito en R (Tanner y Solari, 2009, Solari y Tanner, 2011).

La concordia, así como los cálculos de error de las edades se obtienen utilizando el plug-in Isoplot v. 3.70 para Excel (Ludwig, 2008). Distribuciones de probabilidad de den-

* http://www.geociencias.unam.mx/~solari/index_files/LEI/Quienes_somos.html

sidad e histogramas están graficadas utilizando AgeDisplay (Sircombe, 2004). Las incertidumbres observadas (1σ desviación estándar relativa) de las proporciones de $^{206}Pb/^{238}U$, $^{207}Pb/^{206}Pb$ y $^{208}Pb/^{232}Th$ del circón estándar Plešovice (0,6, 0,9 y 1,1 %, respectivamente) se sumaron cuadráticamente con el error estándar de las relaciones isotópicas medidas en los circones desconocidos, lo cual considera la heterogeneidad de los circones estándar naturales. El Pb común se evaluó por el coeficiente $^{207}Pb/^{206}Pb$, por graficar todos los análisis como diagramas Tera-Wasserburg (Tera y Wasserburg, 1972). La corrección de Pb común se realiza con el método algebraico de Andersen (2002). En las figuras, tablas y resultados, las edades $^{206}Pb/^{238}U$ están reportadas para circones más jovenes que 1.0 Ga, y las edades $^{207}Pb/^{206}Pb$ para los granos más viejos. Las edades $^{207}Pb/^{206}Pb$ tienen un error mayor debido a la propagación cuadrática del error de $^{207}Pb/^{235}U$, además de sufrir de la imprecisión en la medición de ^{207}Pb por medio del cuadrupolo. Las edades $^{207}Pb/^{206}Pb$ se consideran entonces como edades mínimas. Los datos de U-Pb se citan con errores 2σ. Como criterio estadístico de rechazo para todos los análisis, una discordancia normal de 10 % e inversa de 5 % fue elegida. Ninguno de circones fuera de ese rango se incluyen en las discusiones (Harris *et al.*, 2004, Dickinson y Gehrels, 2008, Gehrels, 2011). Por lo tanto, Los análisis cuya discordancia es mayor al 90 % se utilizan para la edad de cristalización de una roca ígnea. La edad máxima de sedimentación de las rocas metasedimentarias se considera robusta si pertenece a un grupo de tres o más circones cuyos elipses de error se traslapan (Gehrels *et al.*, 2006). Sin embargo, en algunas muestras, un número estadísticamente grande de circones concordantes no fue obtenido. Por otro lado, Jeffries *et al.* (2003) considera un solo análisis de circón concordante cuando las proporciones de $^{206}Pb/^{238}U$, $^{207}Pb/^{238}U$, y $^{206}Pb/^{207}Pb$ arrojaron la misma edad dentro incertidumbres pequeñas.

1.3.2 *Analísis geoquímicos por XRF y ICP-MS*

Veinticuatro muestras de anfibolitas y treinta y ocho muestras metasedimentarias se analizaron por fluorescencia de rayos X para abundancias en roca total de elementos mayores y traza (V, Cr, Co, Ni, Cu, Zn, Ga, Rb, Sr, Y, Zr, Nb, Ba, Pb, Th, U), en el *Regional Geochemical Centre at Saint Mary's University*, Nova Scotia. La precisión y exactitud está generalmente dentro de 5 % para la mayoría de los elementos mayores, y dentro de 5–10 % para elementos menores y traza. Los detalles de los procedimientos analíticos están descritos en Dostal *et al.* (1986 y 1994). De estas muestras, 12 y 23 anfibolitas y rocas metasedimentarias, respectivamente, fueron seleccionados para análisis de elementos traza (Y, Zr, Nb, Ba, Hf, Ta, Th) y tierras raras (REE) por espectrometría de masas con fuente de plasma de acoplamiento inductivo (ICP-MS) en *Memorial University, Newfoundland* (según los métodos descritos en Jenner *et al.*, 1990). La precisión exactitud de estos datos están mejores que 10 %; el procedimiento analítico está descrito en detalle en Longerich *et al.* (1990).

1.3.3 *Estudios isotópicos de Sm-Nd*

Diez muestras de anfibolita y siete de rocas metasedimentarias de la selección para ICP-MS fueron elegidas para estudios isotópicos de Sm-Nd los cuales se realizaron is isotópicos se realizaron en *Atlantic Universities Regional Isotopic Facility (AURIF), Memorial University, Newfoundland*. Las concentraciones de Sm y Nd, así como las composiciones isotópicas y las proporciones se midieron por espectrometría de masas con fuente de ionización térmica con dilución isotópica (ID-TIMS) después de la separación química de Nd y Sm por cromatografía de intercambio iónico (véase Kerr *et al*., 1995). El fraccionamiento instrumental de masa de isótopos de Nd se corrige relativo a ^{144}Nd = 0.7219 (O'Nions *et al*., 1977) utilizando la ley de fraccionamiento Raleigh. La precisión externa se evaluó por análisis repetidos del estándar JNDI-1 (Tanaka *et al*., 2000). La diferencia entre el valor certificado (^{143}Nd/^{144}Nd = 0.512115) y el promedio (0.512101 ± 0.000008 [n = 45]) se suma con el valor medido para ^{143}Nd/^{144}Nd después de la corrección realizada añadiendo un trazador isotópico. Los errores indicados en la Tabla 23 representan los errores estándar de las mediciones individuales de ^{143}Nd/^{144}Nd a un nivel de confianza del 95 %. Los valores ϵ_{Nd} se calcularon en relación a ^{143}Nd/^{144}Nd = 0.512638 para CHUR (Goldstein *et al*., 1984). Para los valores iniciales, se usaron ^{147}Sm/^{144}Nd = 0.1967 (Jacobsen y Wasserburg, 1980) y λ^{147}Sm = 6.54 x 10-12 yr^{-1} (Steiger y Jäger, 1977). Las edades model T_{DM} se calcularon de dos maneras: $T_{DM}(1)$ corresponde al modelo de manto empobrecido de DePaolo (1981b y 1988), y $T_{DM}(2)$ asume una evolución linear del manto empobrecido entre un valor de +10 (hoy) y 0 a 4.5 Ga (Goldstein *et al*., 1984). Los valores de $T_{DM}(1)$ están citados en el texto.

2

GEOCRONOLOGÍA U–PB DE LOS PROTOLITOS METASEDIMENTARIOS E ÍGNEAS DEL COMPLEJO AYÚ

Helbig, M., Keppie, J.D., Murphy, J.B., y Solari, L.A. U–Pb geochronological constraints on the Triassic–Jurassic Ayú Complex, southern Mexico: Derivation from the western margin of Pangea-A. *Gondwana Research* **22**(3–4):910–927 (2012)

CONTRIBUCIONES DE COAUTORES:

- **Maria Helbig:** Concepto y plan del proyecto, trabajo de campo y laboratorio incluso mapeo, muestreo, separación de circones, catodoluminiscencia y análisis de U–Pb por LA-ICP-MS en circones, interpretación de datos, borrador de un modelo tectónico, redacción del artículo
- **J. Duncan Keppie:** Concepto y plan del proyecto, supervisión/asistencia para el trabajo del campo, participación en interpretar los datos y desarrollar un modelo, revisión del artículo, financiamiento
- **J. Brendan Murphy:** supervisión, asistencia durante el trabajo del campo, revisión del artículo, financiamiento
- **Luigi A. Solari:** Asistencia en procesar y interpreter los dates, revisión del artículo, encargado del laboratorio LA-ICP-MS, financiamiento

Nota: *La etiqueta en el dibujo encima del diagrama de Tera-Wasserburg de muestra MH-81 en Figura 5, p. 916 en Helbig et al. (2012) debe leer MH-81, no MH-49.*

Gondwana Research 22 (2012) 910–927

Contents lists available at SciVerse ScienceDirect

Gondwana Research

journal homepage: www.elsevier.com/locate/gr

U–Pb geochronological constraints on the Triassic–Jurassic Ayú Complex, southern Mexico: Derivation from the western margin of Pangea-A

Maria Helbig [a,*], J. Duncan Keppie [b], J. Brendan Murphy [c], Luigi A. Solari [a]

[a] Universidad Nacional Autónoma de México, Centro de Geociencias, Campus Juriquilla, Juriquilla, Querétaro 76230, Mexico
[b] Universidad Nacional Autónoma de México, Instituto de Geología, Ciudad Universitaria, Del. Coyoacán, Mexico City 04510, Mexico
[c] Department of Earth Sciences, St. Francis Xavier University, Antigonish, Nova Scotia, Canada B2G 2W5

ARTICLE INFO

Article history:
Received 25 November 2011
Received in revised form 25 February 2012
Accepted 1 March 2012
Available online 27 March 2012

Handling Editor: R.D. Nance

Keywords:
Mexico
Pangea breakup
Triassic–Jurassic
Ayú Complex
Acatlán Complex
Zircon geochronology
Tectonics

ABSTRACT

We present LA-ICP-MS (laser ablation inductively coupled plasma mass spectrometry) U–Pb detrital and igneous zircon data of poly-deformed metamorphic and igneous rocks of the Ayú area, southern Mexico. These rocks were previously inferred to be part of the Late Paleozoic Acatlán Complex, but new age data indicate that they formed in the Mesozoic and should be placed in the newly designated Ayú Complex. The Ayú Complex comprises polydeformed metasedimentary rocks (Chazumba Lithodeme) of a turbidite-like protolith that are intercalated with boudinaged ortho-amphibolites with transitional arc- to MORB tholeiitic geochemistry. In the south, the metasedimentary sequence is affected by a ca. 171 Ma partial melting which formed the Magdalena Migmatite. Migmatization was accompanied by 171–168 Ma intrusions of granodioritic, dioritic, and granitic dikes and sheets as well as pegmatite bodies, which are characterized by inherited zircon populations of ca. 260–290, 320–360, 420–480, 880–990, and 1080–1250 Ma that are also found in the Chazumba Lithodeme. U–Pb (detrital zircon) dating of seven metasedimentary samples from the migmatized and unmigmatized Chazumba Lithodeme yielded youngest detrital zircons and clusters of 192, 198, 214, 250, 266, and 291 Ma, and are interpreted to reflect the Late Triassic–Middle Jurassic deposition of turbiditic rocks. The transitional arc–tholeiitic geochemistry of the Chazumba amphibolites is consistent with turbidite sedimentation in a back-arc environment along a rifted passive margin, close to a contemporaneous magmatic arc. Inferred flattening of the subduction zone led to subduction erosion during the Early–Middle Jurassic and underthrusting of the Chazumba Lithodeme to depths equivalent to amphibolite facies metamorphism. Steepening of the subducting slab and diachronous rifting within the Gulf of Mexico contributed to extensional tectonics recorded on the Mexican mainland and facilitated the tectonic exhumation of the Chazumba Lithodeme by normal faulting along the reactivated Providencia shear zone during the Middle–Late Jurassic. More generally, the documentation of arc-back arc assemblages in the Ayú Complex requires deposition adjacent to a subducting ocean, and thus supports a Pangea-A reconstruction that was synchronous with the breakup of Pangea.

1. Introduction

Tectonic mechanisms responsible for the amalgamation and dispersal of the last supercontinent Pangea are still highly debated (Murphy and Nance, 2008; Murphy et al., 2009; Roberts, 2012). The configuration of Pangea during the Late Paleozoic–Early Mesozoic is controversial with the Pangea-A and Pangea-B configurations being the main contenders (Domeier et al., 2012). Pangea-A is essentially the Wegenerian fit (Bullard et al., 1965; Smith and Hallam, 1970) and implies that Pangea's configuration did not change significantly between amalgamation and breakup. However, paleomagnetic data from Permian–Triassic rocks resulted in a significant cratonic overlap between Gondwana and North America if a Pangea-A reconstruction is used. This led to a modification of the Pangea-A reconstruction, in which parts of Middle America were moved westwards relative to Laurentia (Van der Voo and French, 1974). Another proposed solution is a Pangea-B configuration in which Africa is located south of central Europe and South America. This model requires ca. 3500 km dextral megashear with respect to North America to accommodate the transition from Pangea-B to Pangea-A between amalgamation and breakup (Irving, 1977).

In Mexico, paleogeographic reconstructions based on paleomagnetic data have been used to propose: (i) a Permian–Triassic Pangea-A reconstruction where southern Mexico lies approximately in its present location relative to North America (Fang et al., 1989; Alva-Valdivia et al., 2001), and (ii) a Pangea-B reconstruction placing southern Mexico off eastern North America during the Jurassic (Böhnel, 1999; Fig. 1a). There are also Middle American variants of the Pangea-A model with southern Mexico placed either on the western margin of Pangea

* Corresponding author.
E-mail address: maria.helbig@gmail.com (M. Helbig).

1342-937X/$ – see front matter
doi:10.1016/j.gr.2012.03.004

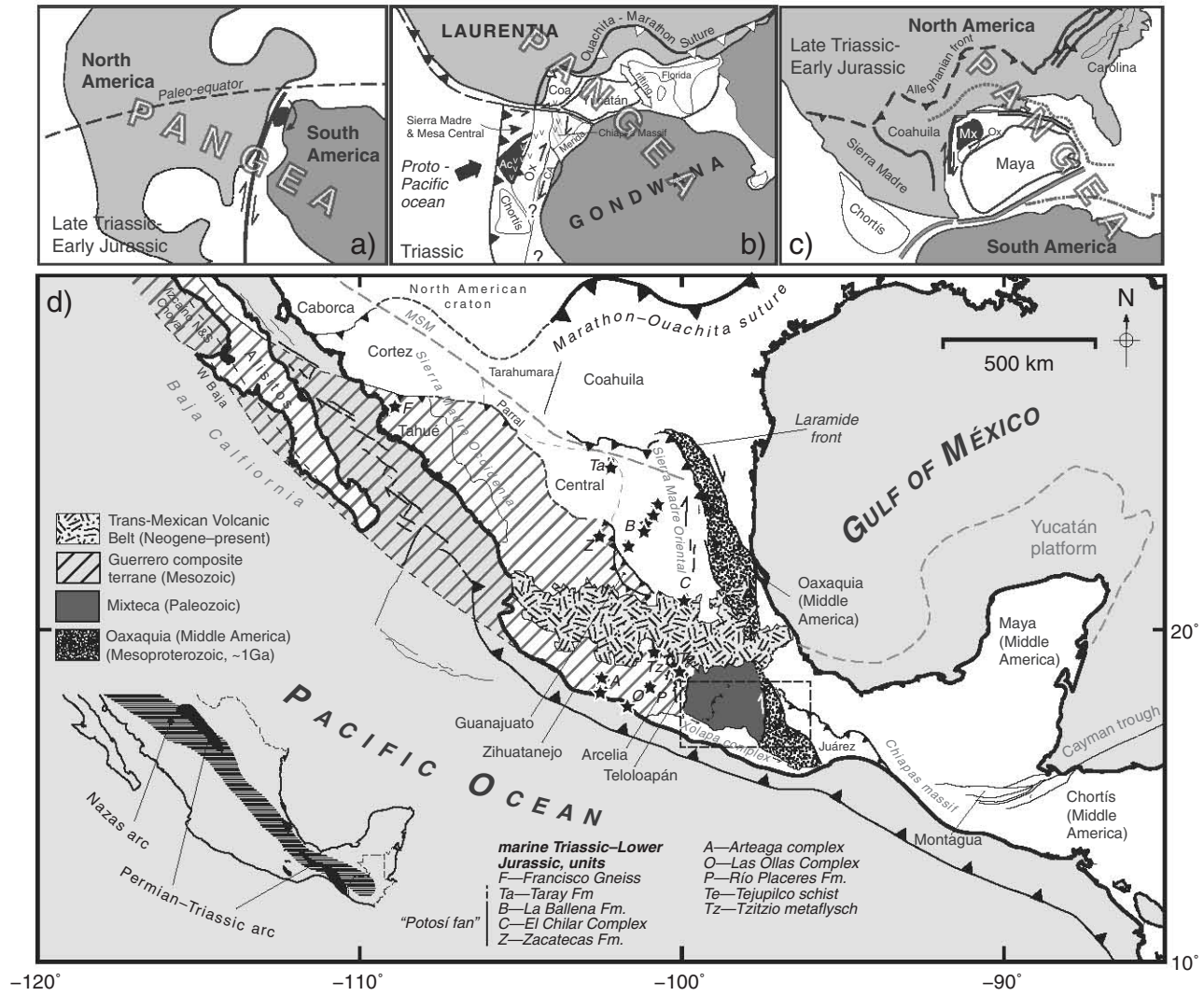

Fig. 1. a–c) Early Mesozoic reconstructions for southern Mexico: a) based on paleomagnetic data, Böhnel (1999) infers the Mixteca terrane (black) to be located off eastern Canada along a dextral megashear zone (Pangea-B). b) the Acatlán Complex (Ac) and Oaxaquia (Ox) are placed on the western margin of Pangea (Pangea-A), V — position of the Permian–Triassic East Mexico arc, Coa — Coahuila, CA — Colombian Andes (after Elías-Herrera and Ortega-Gutiérrez, 2002; Keppie, 2004; Centeno-García, 2005; Weber et al., 2007); c) Vega-Granillo et al. (2009a) place the Mixteca (Mx) and Oaxaquia (Ox) terranes within Pangea, between the Maya block and southern North America (Pangea-A). d) Main tectono-stratigraphic terranes and geologic provinces of Mexico. Basement rocks: Oaxaquia (stippled) and Mixteca terrane (dark grey) after Keppie (2004); Dowe et al. (2005). The Mesozoic Guerrero composite terrane (striped area) comprises the Tahué, Guanajuato, Arcelia, and Teloloapán terranes (after Keppie, 2004; Centeno-García, 2008). Trans-Mexican Volcanic belt from Ferrari (2004). Small inset map shows the distribution of rocks of the Permian–Triassic East Mexico magmatic arc (in black; after Torres et al., 1999) and the Triassic–Middle Jurassic Nazas arc (striped area; after Bartolini et al., 2003; Godínez-Urban et al., 2011). Stars indicate locations of Triassic–Lower Jurassic deep marine facies in central and southwestern Mexico. Box in main map shows location of map in Fig. 2.

(e.g. Keppie, 2004; Keppie et al., 2008b, 2010; Fig. 1b) or within Pangea between the Maya terrane and southern North America (Talavera-Mendoza et al., 2005; Vega-Granillo et al., 2007, 2009a; Fig. 1c).

In the Paleozoic, the Mexican mainland was comprised of the ca. 1–1.4 Ga Middle America terrane and the fringing Paleozoic Mixteca terrane that resided along the northern margin of Amazonia which collided with the North American craton during the Late Paleozoic (Fig. 1; Campa-Uranga and Coney, 1983; Dickinson and Lawton, 2001; Elías-Herrera and Ortega-Gutiérrez, 2002; Keppie, 2004; Poole et al., 2005). The marginal position of these terranes along the western periphery of Pangea in the Late Paleozoic was inferred from the presence of a Permian–Triassic granitoid belt straddling southwestern North America, western Mexico and the Northern Andes related to subduction of Paleo-Pacific oceanic lithosphere (Torres et al., 1999). After a brief hiatus this arc was re-established as the Triassic–Middle Jurassic Nazas arc, which extended from Sonora and Baja California through the Mixteca and Oaxaquia terranes to Chiapas and Guatemala (Bartolini et al., 2003; Barboza-Gudiño et al., 2008; Centeno-García, 2008; González-León et al., 2009; Venegas-Rodríguez, 2009; Godínez-Urban et al., 2011; Rubio-Cisneros and Lawton, 2011; Fig. 1). These events were contemporaneous with the opening of the Gulf of Mexico (Marzoli et al., 1999), i.e. the breakup of Pangea, which progressed from Triassic intracontinental rifting to drifting in the Middle Jurassic.

In this context, the rocks of the eastern Mixteca terrane of southern Mexico are critical because reconnaissance studies have yielded preliminary ages that possibly span the breakup of Pangea (Talavera-Mendoza et al., 2005; Keppie et al., 2006b; Nance et al. 2006a). In detail, however, the age of these rocks are poorly constrained and their tectonic significance has been variously interpreted:

1. The rocks were assigned to the Acatlán Complex and interpreted as part of a Cambrian–Ordovician accretionary complex (trench–forearc complex, Petlalcingo Group; Ortega-Gutiérrez, 1975; Ortega-Gutiérrez et al., 1999) or a Lower Paleozoic continental rise prism (Ramírez-Espinosa, 2001) that developed prior to the amalgamation of Pangea.

2. Talavera-Mendoza et al. (2005) inferred an Upper Pennsylvanian–Lower Permian age for these rocks based on detrital zircon ages and inferred deposition in an oceanic basin that developed from an intracontinental pull-apart basin (Vega-Granillo et al., 2009a), prior to the break-up of Pangea.
3. Reconnaissance geochronological studies (Keppie et al., 2006b) constrained the depositional ages of these rocks between 303 and 171 Ma (uppermost Permian–Lower Jurassic) based on U–Pb ages of detrital zircons and crosscutting dikes, and inferred deposition in a clastic wedge coeval with Permian–Triassic thrusting along the western margin of Pangea.

The reconnaissance geochronological data raise the possibility that the metasedimentary rocks in this region may be younger than initially considered, but require a more comprehensive study in order to properly define their significance relative to the amalgamation and breakup of Pangea.

In this paper, we present LA-ICP-MS (laser ablation inductively coupled plasma mass spectrometry) U–Pb detrital and igneous zircon data from polydeformed metamorphic and igneous rocks of the former Chazumba Formation and Magdalena Migmatite (Ortega-Gutiérrez et al., 1999), which were previously inferred to be part of the Late Paleozoic Acatlán Complex. This study aims to determine a more precise time for deposition, evaluate the age of different sediment sources for the protolith rocks of the study area, and assess the tectonic significance of these rocks in the light of these new data.

2. Geological setting

South-central Mexico is partly underlain by the Mixteca terrane consisting of the Paleozoic Acatlán Complex (Ortega-Gutiérrez, 1975; Keppie et al., 2008b, 2012; Figs. 1 and 2). The Acatlán Complex comprises mainly a Neoproterozoic–Ordovician clastic sequence intruded by ca. 480–440 Ma bimodal, rift-related igneous rocks, and Late Devonian–Permian shallow marine units characterized by meta-psammites, metapelites, and tholeiitic mafic volcanic rocks (Keppie et al., 2008b). Despite the large amount of recently published geochemical and geochronological data for rocks of the Acatlán Complex (e.g. Talavera-Mendoza et al., 2005; Keppie et al., 2006b; Murphy et al., 2006; Keppie and Dostal, 2007; Middleton et al., 2007; Miller et al., 2007; Grodzicki et al., 2008; Hinojosa-Prieto et al., 2008; Morales-Gámez and Keppie, 2008; Ramos-Arias et al., 2008; Dostal and Keppie, 2009; Galaz Escanilla et al., 2009; Morales-Gámez et al., 2009a, 2009b; Ortega-Obregón et al., 2009; Vega-Granillo et al., 2009a, 2009b; Ortega-Obregón et al., 2010), the interpretation of its geological development throughout the Paleozoic remain controversial (Talavera-Mendoza et al., 2005; Nance et al., 2006b; Keppie et al., 2008b; Vega-Granillo et al., 2009a). Although these authors disagree on the paleogeographic location (and hence the relationship of these rocks to the amalgamation of Pangea), they generally agree that the Late Paleozoic history of the Acatlán Complex records subduction-related arc magmatism dominated by the Permian Totoltepec pluton and the broadly synchronous deposition of clastic rocks of the Tecomate Formation in the eastern Acatlán Complex.

To the east, the Acatlán Complex is tectonically juxtaposed against the ca. 1–1.4 Ga Oaxacan Complex (Oaxaquia) along the 276 Ma dextral transpressional Caltepec Fault zone (Figs. 1 and 2; Elías-Herrera and Ortega-Gutiérrez, 2002). The northern continuation of the Acatlán Complex is obscured by Neogene–Present volcanic and volcaniclastic rocks of Trans-Mexican Volcanic Belt (e.g. Ferrari et al., 1999; Gómez-Tuena et al., 2007). To the south, Mesozoic–Cenozoic continental arc magmatism formed mid-crustal, plutonic and high-grade metamorphic rocks in the Xolapa Complex (Schaaf et al., 1995; Ortega-Gutiérrez and

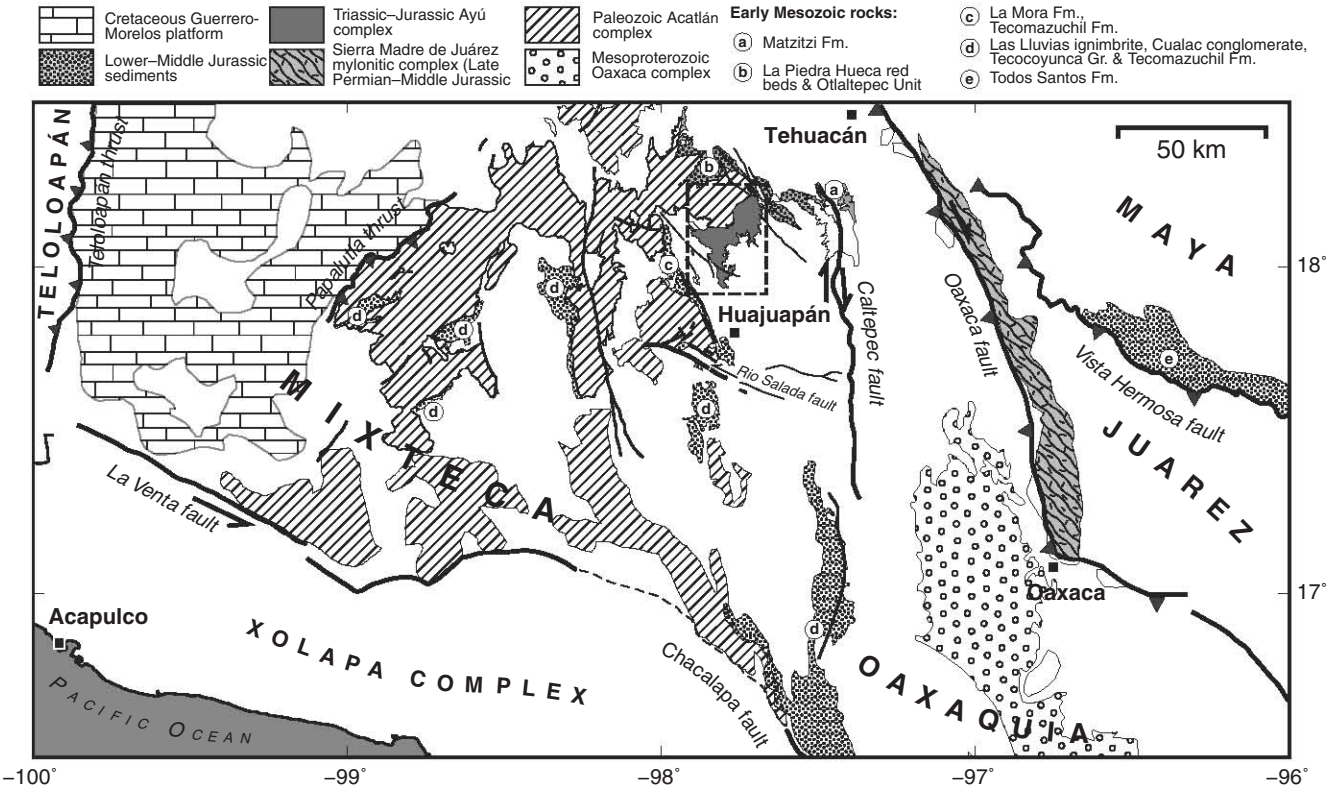

Fig. 2. Pre-Cenozoic map of Southern Mexico. The Oaxacan Complex forms the basement of Oaxaquia (circles) against which the Acatlán Complex (striped) is tectonically juxtaposed along the Permian dextral transpressional Caltepec Fault. Dark grey areas are rocks of the Early Mesozoic Ayú Complex. Stippled areas are unmetamorphosed Lower–Middle Jurassic sedimentary rocks. Letters refer to unit names given in the legend above. Major faults are labeled. Terrane names in capital letters. Box indicates location of study area (Fig. 4).

Elías-Herrera, 2003; Keppie, 2004; Solari et al., 2007; Pérez-Gutiérrez et al., 2009). These rocks were displaced sinistrally along the La Venta–Chacalapa Fault during Eocene–Oligocene time (Ratschbacher et al., 1991; Riller et al., 1992; Tolson, 2005; Solari et al., 2007; Ratschbacher et al., 2009). The Acatlán and Oaxacan complexes are unconformably overlain by unmetamorphosed continental redbeds, siliciclastic fluvial deposits and shallow marine shelf sediments of Upper Permian to Middle Jurassic age (Fig. 2; Caballero-Miranda et al., 1990; Morán-Zenteno et al., 1993; Silva-Romo and Mendoza-Rosales, 2000; Centeno-García et al., 2009; Elías-Herrera et al., 2011; Rubio-Cisneros and Lawton, 2011; Silva-Romo et al., 2011), which mark the Early Mesozoic continental margin of southern Mexico. To the west, the Acatlán Complex is thrust over Cretaceous limestones of the Guerrero–Morelos platform along the Upper Cretaceous–Paleocene Papalutla Fault (Cerca et al., 2007; Ramos-Arias and Keppie, 2011; Fig. 2). Xenoliths in Tertiary adakitic dikes that intrude the Cretaceous limestones contain Proterozoic and Permian–Triassic zircons suggesting that the Guerrero–Morelos platform is underlain by rocks of these ages (Levresse et al., 2007). To the west of the Guerrero–Morelos platform lies the Mesozoic Guerrero composite terrane (Fig. 2), which extends over most of western Mexico and comprises various subterranes (Tahué, Guanajuato, Zihuatanejo, Arcelia, and Teloloapán terranes; Centeno-García, 2008). The Guerrero composite terrane is characterized by submarine and sparse, subaerial volcanic and sedimentary successions of Upper Jurassic (Tithonian) to middle Upper Cretaceous (Cenomanian) age and has a complex evolution involving several episodes of accretion and rifting, and eventual collision with Oaxaquia (Centeno-García, 2008). Between the Guerrero composite terrane and the northern continuation of Oaxaquia (Fig. 1), the Mesa Central plateau forms the so-called "Central terrane", the oldest rocks of which are made up of deformed Late Triassic deep-marine siliciclastic successions and are interpreted as turbidites deposited in a subduction-related accretionary complex (Taray Formation: Díaz-Salgado et al., 2003; Anderson et al., 2005; Centeno-García, 2005). These turbidites formed part of a submarine fan system (Ballena Formation: Centeno-García and Silva-Romo, 1997; Silva-Romo et al., 2000; Barboza-Gudiño et al., 2008, 2010), called the Potosí fan (Centeno-García, 2005), that was fed by an extensive river system (Alamar Formation: Barboza-Gudiño et al., 2010) and deposited along the western margin of Oaxaquia (Centeno-García, 2005, 2008). Distal parts of the Potosí fan are inferred to overlie oceanic crust and have been designated the Zihuatanejo terrane (Centeno-García, 2008; Martini and Ferrari, 2009). All of these rocks were deformed during east-vergent subduction of the Paleo-Pacific during the Early Jurassic, forming a wide accretionary prism of deformed turbidites and intercalated blocks of chert, limestone and pillow basalts (Zacatecas Formation, El Chilar Complex, Arteaga Complex, and Las Ollas Complex: Burckhardt and Scalia, 1906; Centeno-García and Silva-Romo, 1997; Talavera-Mendoza et al., 2007; Centeno-García, 2008; Dávila-Alcocer et al., 2009; Ortega-Flores et al., 2012). Synchronously, the ca. 187 Ma syntectonic intrusion of peraluminous granites records the collision of the Guerrero composite terrane with the Mixteca/Oaxaquia terranes that resulted in intense deformation of the Tejupilco volcanogenic rocks (Elías-Herrera et al., 2000, 2003). In the Late Cretaceous, the Central terrane was thrust beneath the Zihuatanejo terrane, which in turn was thrust over the Guanajuato terrane, which were together thrust over the continental margin (Centeno-García, 2008). South of the Trans-Mexican Volcanic Belt, the Zihuatanejo terrane was separated from the continental margin by intra-/back-arc rifting during the Cretaceous (Centeno-García, 2008; Martini and Ferrari, 2009).

2.1. Study area

The studied rocks crop out west of the Caltepec Fault zone and south of the eastern Acatlán Complex in a horst bounded by Upper Triassic–Jurassic redbeds (La Mora Fm., Tecomazúchil Fm., Piedra Hueca and Otlaltepec Unit: Morán-Zenteno et al., 1993; Silva-Romo and Mendoza-Rosales, 2000; Silva-Romo et al., 2011; Fig. 2), Cretaceous limestones (Morán-Zenteno et al., 1993), and by unconformably overlying Cenozoic volcanic rocks (Fig. 4). The area is underlain by a poly-deformed and metamorphosed flysch- or turbiditic siliciclastic sequence consisting of micaceous pelites interlayered with metapsammites, metagreywackes, and amphibolites (Chazumba Formation: Ortega-Gutiérrez, 1978; Chazumba Lithodeme: Keppie et al., 2006b). Similar metasedimentary rocks in the southern study area (Magdalena Lithodeme: Keppie et al., 2006b) underwent partial melting at 171 ± 1 Ma (Magdalena Migmatite; U–Pb concordant zircon age: Keppie et al., 2004) accompanied by the intrusion of dioritic, granodioritic, granitic, pegmatitic as well as leucogranitic sheets and dikes of the same age (San Miguel intrusives: Yáñez et al., 1991; Ortega-Gutiérrez et al., 1999; Keppie et al., 2004; Fig. 4). The protoliths of the Magdalena Migmatite include gneisses, metapelites and metapsammites, calc-silicate rocks, and amphibolites that are similar in composition to the unmigmatized northern metasedimentary sequence. Two previous U–Pb LA-ICP-MS detrital zircon studies from both the northern metasedimentary protolith and the protolith of the Magdalena Migmatite, once considered different units (Ortega-Gutiérrez et al., 1999), suggest similar depositional ages (Keppie et al., 2004, 2006b; Talavera-Mendoza et al., 2005). A biotite–muscovite(–garnet) schist in the Chazumba Lithodeme yields a youngest single zircon age of 249 ± 20 Ma (Talavera-Mendoza et al., 2005) and a robust youngest zircon-cluster of six grains with a mean age of 300 ± 8 Ma. In a subsequent analysis of a metapsammite from the Chazumba Lithodeme, a single zircon yields a Middle Triassic age of 239 ± 4 Ma inferred to provide the maximum depositional age for the unit (Keppie et al., 2006b). Similar young ages are reported for the protolith of the Magdalena Migmatite. Keppie et al. (2006b) report a youngest single zircon age of 304 ± 4 Ma, whereas the data of Talavera-Mendoza et al. (2005) yield a youngest detrital zircon of 244 ± 26 Ma. However, most of these depositional ages are derived from a single zircon and may not be geologically significant. Nonetheless, Keppie et al. (2006b) suggested that the similarity in protolith composition and depositional age of the Chazumba and Magdalena Lithodemes indicate that they share the same protolith.

In the central part of the study area, two mafic–ultramafic tectonic lenses lie structurally above the metasedimentary rocks of the Chazumba Lithodeme (Keppie et al., 2004) (Fig. 4). The Tepejillo lens consists of four bodies that are composed of coarse crystalline ultramafic (mainly dunite) to gabbroic rocks and are cut by diabase dikes. Geochemically, they are interpreted as parts of cumulate bodies intruded into the lower continental crust (Keppie et al., 2004). The contact between the metasedimentary rocks and the Tepejillo lens has been mapped as a folded thrust. The Tultitán lens consists of massive amphibolite and a core of metamorphosed norite. One concordant U–Pb LA-ICP-MS analysis of a prismatic tip of a euhedral zircon from a metanorite yields an age of 174 ± 1 Ma, which is interpreted as age of intrusion for both lenses (Keppie et al., 2004).

At its northern margin, the metasedimentary rocks of the Chazumba Lithodeme is truncated by a NE-dipping shear zone, here named the Providencia shear zone (Fig. 4). The Devonian–Carboniferous Cosoltepec Formation (Talavera-Mendoza et al., 2005), the Permian Tecomate Formation and the Carboniferous–Permian Totoltepec pluton are exposed in the hanging wall of this shear zone (Malone et al., 2002; Keppie et al., 2004; Kirsch et al., 2010; Fig. 3). Rocks in the vicinity of this shear zone are intensely shared and contain a dominant N- to NNE-dipping foliation with N-trending mineral lineations and s–c fabrics in the Tecomate Formation that indicate top-to-the-south tectonic transport (Malone et al., 2002). $^{40}Ar/^{39}Ar$ dating of amphibole and muscovite from rocks within the Providencia shear zone yield ages of 214 Ma and 224 Ma, respectively, suggesting that the rocks of the Acatlán Complex cooled through ca. 540 °C and 350 °C at about that time (Keppie et al., 2004). The contact to the Chazumba Lithodeme is marked by the occurrence of amphibolites that is also

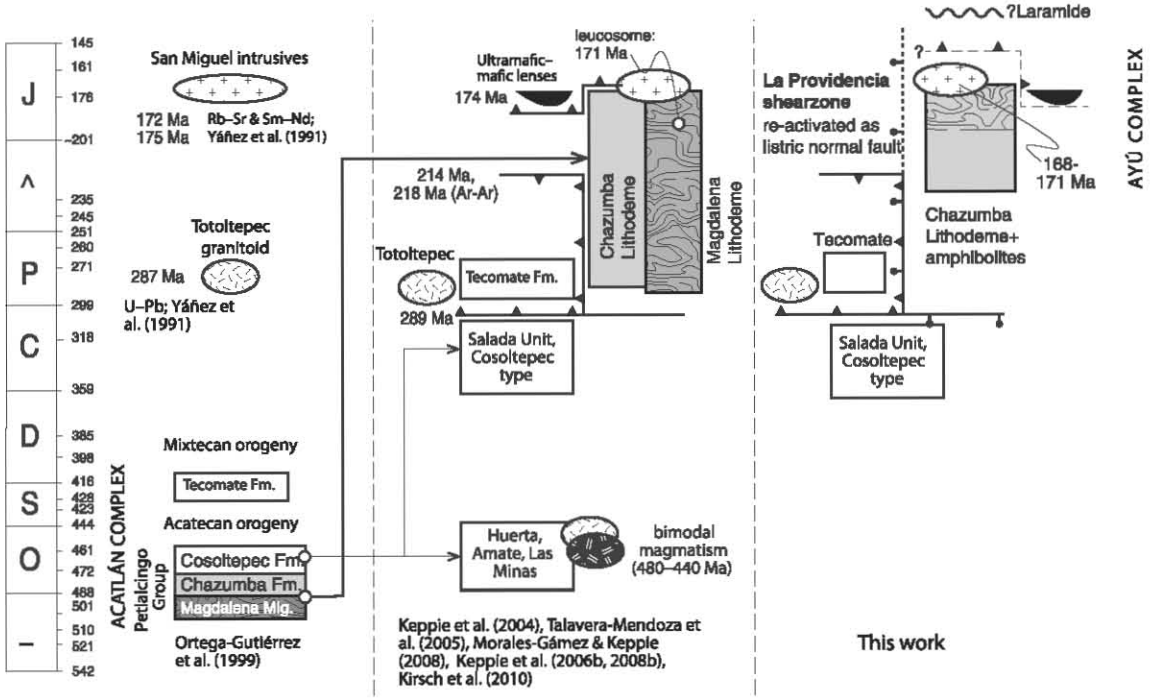

Fig. 3. Comparison of different stratigraphies by several authors (Ortega-Gutiérrez et al., 1999; Keppie et al., 2004; Talavera-Mendoza et al., 2005; Keppie et al., 2006b, 2008b; Morales-Gámez and Keppie, 2008; Kirsch et al., 2010) for the eastern units in the Acatlán Complex. This work proposes the exclusion of the Chazumba Lithodeme (including the Magdalena Migmatite), the ultramafic Tepejillo and Tultitlán lenses (black), the ortho-amphibolites, and the San Miguel intrusives from the Acatlán Complex and their placement into a new complex — the Early Mesozoic Ayú Complex. Abbreviations: Є = Cambrian, O = Ordovician, S = Silurian, D = Devonian, C = Carboniferous, P = Permian, TR = Triassic, J = Jurassic.

typical for the Cosoltepec area where massive amphibolites mark the southern limit of the Cosoltepec Formation (location shown in Fig. 4; amphibolites are not drawn in map, but are sketched in the cross-section below).

3. Methodology

Twelve samples (see Table DR-1) were collected for U–Pb zircon dating by laser ablation inductively coupled plasma mass spectrometry (LA-ICP-MS) at the Laboratorio de Estudios Isotópicos (LEI), Centro de Geociencias, UNAM, Mexico. 6–10 kg of each rock sample were crushed, washed and sieved to 250–177 μm, 177–149 μm, and 149–125 μm fractions. Heavy minerals were concentrated using the Wilfley table. Non-magnetic minerals were separated by employing a Frantz isodynamic magnetic separator. By exploiting differences in mineral densities, other non-magnetic minerals (quartz, feldspars, and apatite) were separated in a column of methylene iodide heavy liquid. For each sample, zircons (120–150 for detrital zircons, 70 for igneous zircons) were handpicked from the concentrate under a binocular microscope; no selection was made regarding optical and physical characteristics. Zircons were embedded in epoxy casting resin and polished. To assist interpretation (internal zoning, spot selection), the zircons were imaged under cathodoluminescence using an ELM 3R luminoscope. The isotope analyses were performed with a Resolution M050 ArF Excimer laser ablation system coupled to a Thermo Xii series quadrupole ICP-MS (Solari et al., 2010a). The concordia and age-error calculations were obtained using Isoplot v. 3.70 (Ludwig, 2008). The probability density distribution and histogram plots were produced using AgeDisplay (Sircombe, 2004). Common Pb was evaluated using the $^{207}Pb/^{206}Pb$ ratio, graphing all the analyses on Tera–Wasserburg plots (Tera and Wasserburg, 1972). In the figures, tables and results, $^{206}Pb/^{238}U$ ages are used for zircons younger than 1.0 Ga, whereas older grains are quoted using their $^{207}Pb/^{206}Pb$ ages. The latter ages become increasingly imprecise below 1.0 Ga due to small amounts of ^{207}Pb. The $^{207}Pb/^{206}Pb$ ages are also considered to be minimum ages due to the effect of possible Pb loss (Dickinson and Gehrels, 2009). 2σ errors are quoted for the U–Pb data. As a statistical rejection criterion for all analyses, 10% normal and 5% reverse discordancy was chosen (Harris et al., 2004; Dickinson and Gehrels, 2008; Gehrels, 2011) and none of these zircons are included in the discussions below. Hence, zircon analyses with >90% concordance are used to date the time of intrusion in igneous rocks or the maximum age of deposition in metasedimentary rocks. The latter is considered robust if it belongs to a cluster of three or more zircons with similar ages (Gehrels et al., 2006). In some samples, however, a statistically large number of concordant grains was not attainable. On the other hand, Jeffries et al. (2003) regarded as concordant a single, high-precision zircon analysis with $^{206}Pb/^{238}U$, $^{207}Pb/^{238}U$, and $^{207}Pb/^{206}Pb$ ratios that yielded the same age within small uncertainties.

4. Results

In total, 764 analyses of zircon grains in twelve samples were performed, of which 119 analyses were discarded based upon their discordance (>10% and < −5%). All data, including sampling locations and field relationships, can be found in the data repository (Supplementary Table 1). All reported errors described in the text are 2σ. Tera–Wasserburg plots are illustrated in Figs. 5–7, and relative probability distributions for detrital zircons are shown in Fig. 8.

4.1. Intrusive rocks

A granitic dike, sample MH-81 (Fig. 5), which intrudes metasedimentary rocks 20 m away from the collected metasedimentary samples TEP-474-3 and TEP-474-4, exhibits populations with age ranges of 281–336, 720–774, 873–994, and 1078–1253 Ma that are similar to

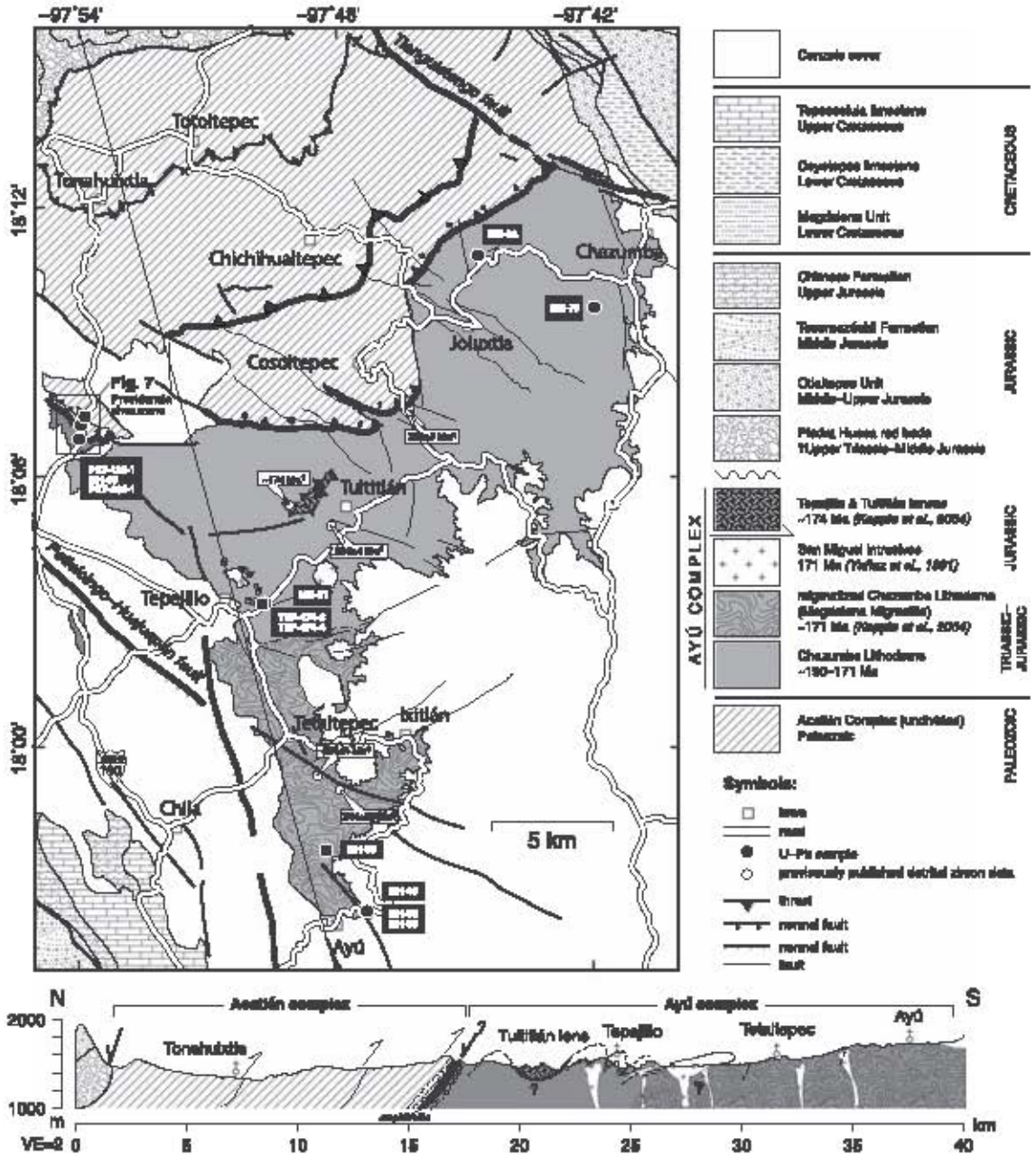

Fig. 4. Geological map of the Ayú Complex and Permian–Triassic arc assemblages of the Acatlán Complex to the north. The Ayú Complex crops out in a fault block. Unmetamorphosed sediments of Lower–Middle Jurassic age are in tectonic contact with the Acatlán Complex in the north, contacts with Ayú Complex are covered by Cenozoic rocks. Black dots indicate sampling locations for U–Pb LA-ICP-MS analyses (bold — robust mean age, others — single grain age); white dots are detrital and igneous zircon samples of previous studies: [1)]Keppie et al., 2004, [2)]Talavera-Mendoza et al., 2005, [3)]Keppie et al., 2006b. A simplified N–S cross-section with a vertical exaggeration of 2 is drawn below. Box locates detailed map of the Providencia shear zone (Fig. 7).

age ranges obtained from the host rock (Fig. 5). One concordant analysis yields 244 ± 4 Ma (Fig. 5). The youngest zircons (168 ± 2, 180 ± 4, 192 ± 4 Ma; Middle–Early Jurassic) do not form a cluster but instead are distributed along the concordia line with a ca. 12 Ma interval. The oldest of these zircons (192 ± 4 Ma) displays a similar age to those that occur in the metasedimentary sample (PET-484-1) located about 100 m south of the Providencia shear zone (compare Figs. 8 and 5).

A granitic dike (MH-49) that crosscuts sample MH-50 (Fig. 5) is characterized by a Middle Mississippian age population (322–342 Ma; Fig. 5). Further notable populations include 263–283 Ma (Middle–Early Permian), 209–242 Ma (Late Triassic), and 171–186 Ma (Middle–Early Jurassic). The youngest, slightly discordant, zircon is not part of a cluster and has an age of 171 ± 4 Ma (Middle Jurassic; Fig. 5). Notably, this sample only contains one Neoproterozoic zircon and lacks any major Precambrian zircon populations.

A leucogranitic dike, sample MH-59, yielded 36 zircon analyses with age populations in the ranges 160–174, 287–364, 416–484, and 1113–1180 Ma (Fig. 5). The three youngest zircons yield ages of 160 ± 2, 163 ± 2 Ma, and 170 ± 2 Ma, respectively (Middle Jurassic; Fig. 5).

4.2. Unmigmatized Chazumba Lithodeme

Sample TEP-474-3, a micaceous metapsammite, and adjacent sample TEP-474-4, a micaceous metapelite, yielded 93 and 94 analyses meeting the aforementioned concordance criteria, respectively

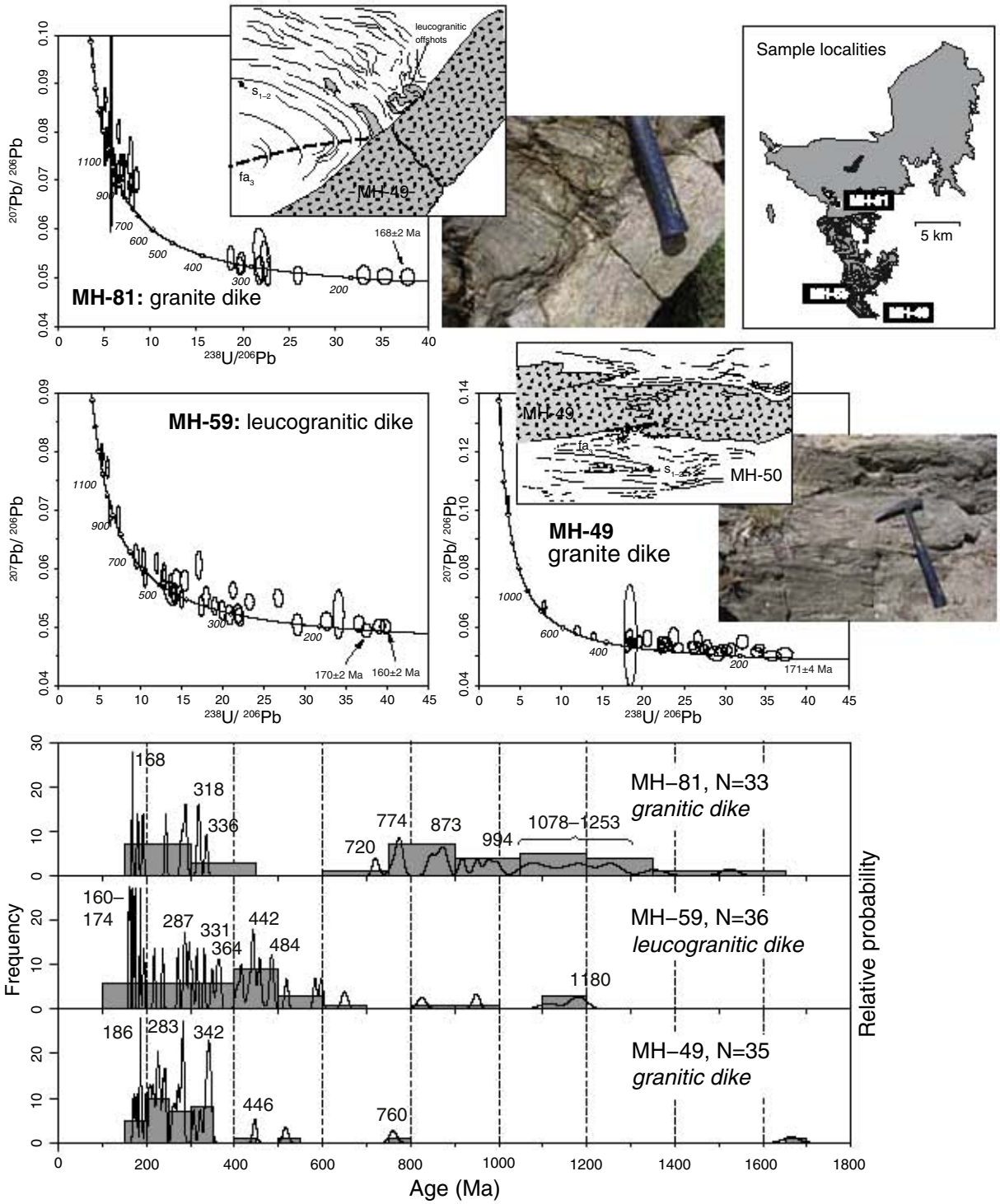

Fig. 5. Top: Tera–Wasserburg concordia plots for U–Pb isotopic data of analyzed igneous zircons. Sample MH-81 (granite dike) was collected from beneath the thrust contact of the Tepejillo lens and crosscuts the metasedimentary samples TEP-474-3 and TEP-474-4 (see images to left for field relationships). Samples MH-49 (granite dike cutting metapelitic sample MH-50, see images to left for field relationships) and MH-59 (leucogranitic dike) were collected in the southern, migmatized metasedimentary rocks (Magdalena Migmatite). See index map for sample localities. Bottom: histogram and relative probability plots of igneous zircon analyses that match 90 to 105% concordance criteria. Note abundant inherited zircons.

(Fig. 6). The samples were taken at the same field location to test the sensitivity of our results to varying grain size. The age spectra are of both samples are characterized by detrital zircon clusters of Neoproterozoic to Mesoproterozoic ages as well as Early Permian ages (Fig. 8). The metapsammite sample has detrital zircon populations with age ranges of 255–281, 559–690, and 977–1140 Ma. The latter population contains two major peaks at 977 and 998 Ma. The youngest detrital grain yields an age of 255 ± 4 Ma (Late Permian). A cluster of the next three youngest concordant zircons has a mean age of 269 ± 2 Ma (Middle Permian). A further population of four grains yields a mean age of 281 ± 2 Ma (Early Permian). The micaceous metapelite is characterized by zircon clusters with age ranges of 269–292, 685–895,

and 924–1332 Ma (with a single peak at 1003 Ma). The youngest zircons (Early–Middle Permian) are slightly discordant (259 ± 4, 261 ± 6, and 268 ± 4 Ma) yielding a mean age of 263 ± 13 Ma (Middle–Late Permian), which is (within error) the same age as TEP-474-3. The second youngest cluster of three zircons (287 ± 4, 292 ± 2, and 297 ± 4 Ma) yields a mean age of 292 ± 9 Ma (Early Permian), which is (within error) similar to the cluster in sample TEP-474-3.

In the eastern Chazumba Lithodeme, a metapsammite (MH-28) yielded 73 analyses (Fig. 6). The largest detrital zircon population has an age range of 902–1303 Ma with the maximum at 1149 Ma (Fig. 8). Smaller groups give age ranges of 262–369 and 590–703 Ma. The youngest grains yield slightly discordant ages of 250 ± 6 Ma (Permian–Triassic boundary) and 262 ± 4 Ma (Middle Permian). A cluster consisting of two grains (290 ± 6 and 296 ± 4 Ma) yields a mean age of 294 ± 3 Ma. Sample MH-73, a micaceous schist (psammitic), yielded 87 analyses (Fig. 6). The ages define populations similar to those of sample MH-28 (Fig. 8). The major group of detrital zircons exhibits ages ranging from 918 to 1443 Ma with the peak at 1150 Ma (Fig. 8). The younger population ranges from 287 to 323 Ma. The youngest detrital zircon yields an age of 257 ± 4 Ma (Late Permian; Fig. 6). A cluster of the three next youngest grains yields a mean age of 291 ± 15 Ma (Early Permian).

4.3. Migmatized Chazumba Lithodeme

Sample MH-50, a micaceous metapelite (paleosome), yielded 61 interpretable analyses (Fig. 6). There are no dominant detrital zircon age populations (Fig. 8). Notable populations occur at 225–239 Ma

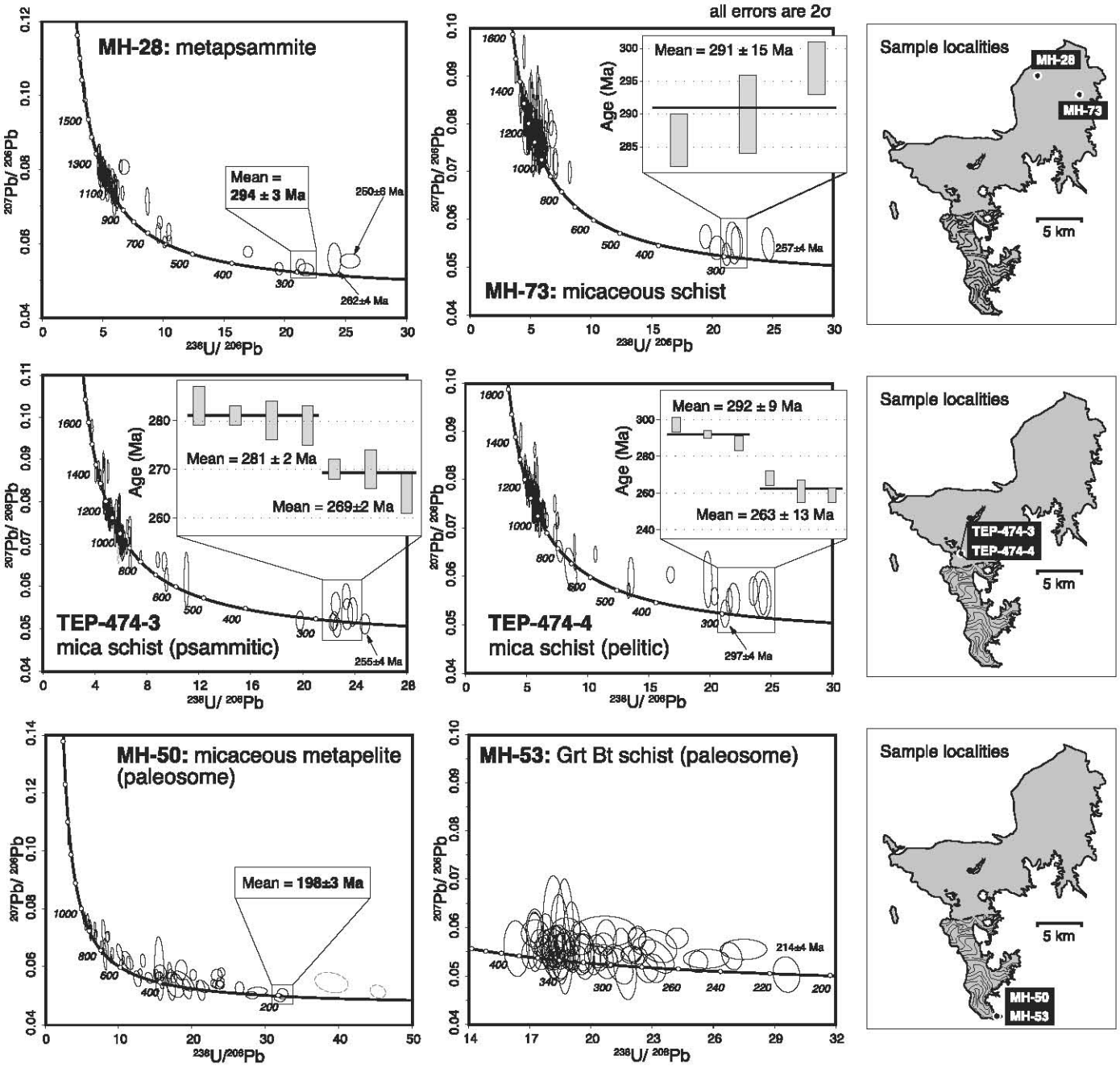

Fig. 6. Tera–Wasserburg concordia plots for U–Pb isotopic data of analyzed detrital zircons (from N to S: MH-28, MH-73, TEP-474-3, TEP-474-4, MH-50 and MH-53). Mineral abbreviations are after Whitney and Evans (2009). See index maps for sample localities.

(Late Triassic), 265–297 Ma (Late Permian), 359–406 Ma (Devonian), 442–597 Ma (Cambrian–Ordovician) and 680–1063 Ma (Neo-Mesoproterozoic). The youngest reliable age (i.e. fulfilling the criteria of Jeffries et al., 2003) is represented by the two youngest concordant zircons with low errors (196 ± 4 and 199 ± 4 Ma) with a mean age of 198 ± 3 Ma (Early Jurassic).

Sample MH-53, a paleosome consisting of garnet–biotite schist, yielded 70 useful analyses out of a total of 96 (Fig. 6). Ages range from 214 to 383 Ma, with a significant cluster of Carboniferous ages (320–370 Ma) and a peak at ca. 345 Ma (Mississippian) (Fig. 8). The youngest concordant zircon has an age of 214 ± 4 Ma (Late Triassic).

4.4. Providencia shear zone

Rocks (PET-480-1, MH-96) from within the Providencia shear zone (Fig. 7) are affected by strong deformation. The amount of zircons found in each sample was relatively small. The northernmost sample, PET-480-1, is a mylonitic phyllite and yielded 19 concordant analyses (out of 32 analyses). The obtained ages lie with the ranges 440–467, 535–565, 612–682, and 780–952 Ma (Fig. 8). The youngest, slightly discordant detrital zircon has an age of 314 ± 4 Ma (Pennsylvanian), which is followed by two grains (329 ± 8 and 339 ± 8 Ma) with a mean age of 334 ± 6 Ma (Mississippian, Fig. 7).

Sample MH-96, a graphite- and feldspar-bearing mylonitic metasedimentary rock from the footwall rock of the Providencia shear zone, yielded 24 representative analyses out of 28. The major detrital zircon population ranges from 1126 to 1236 Ma (Mesoproterozoic, Fig. 8), with minor peaks at 823 and 888 Ma. One grain yields the only early Paleozoic age (487 ± 6 Ma; Early Ordovician). The two youngest zircons yield ages of 281 ± 4 Ma and 295 ± 8 Ma (Early Permian; Fig. 7).

The micaceous metapsammite sample (PET-484-1) was taken 100 m south of the shear zone and yielded only 17 useful analyses. Relatively narrow age spectra ranging from 194 to 339 Ma were obtained with populations of 317–339, 276–280, and 234–244 Ma (Fig. 8). The two youngest grains (190 ± 4 and 193 ± 4 Ma) have a mean age of 192 ± 3 Ma (Early Jurassic, Fig. 7).

5. Interpretation

5.1. Intrusive ages

All of the dated crosscutting granitic dikes have ages between ca. 160 and 171 Ma, which are broadly similar to the Sm–Nd and Rb–Sr

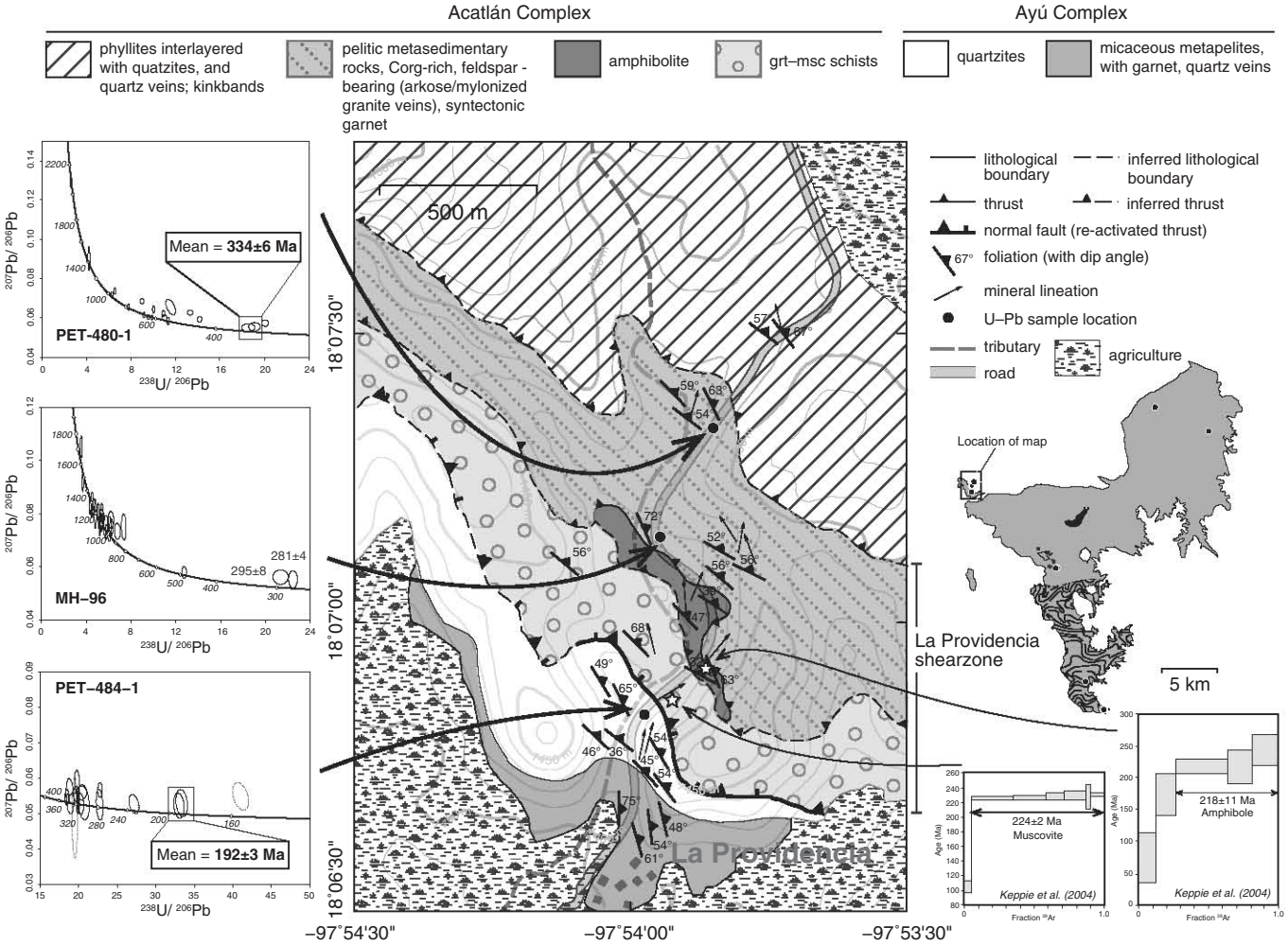

Fig. 7. Detailed map of the Providencia shear zone showing contact relationships between the northern Tecomate Formation, Cosoltepec Formation and the southern Chazumba Lithodeme. Rocks within the shear zone are strongly mylonitized and comprise packages of phyllites, pelitic metasedimentary rocks, amphibolites and garnet-bearing micaceous schists. South of the shear zone, rocks comprise massive quartzites and micaceous metapelites. U–Pb sample localities for three metasedimentary rocks (PET-480-1, MH-96, and PET-484-1) are indicated with black dots and Tera–Wasserburg plots are shown to the left. $^{40}Ar/^{39}Ar$ ages to the right are by Keppie et al. (2004).

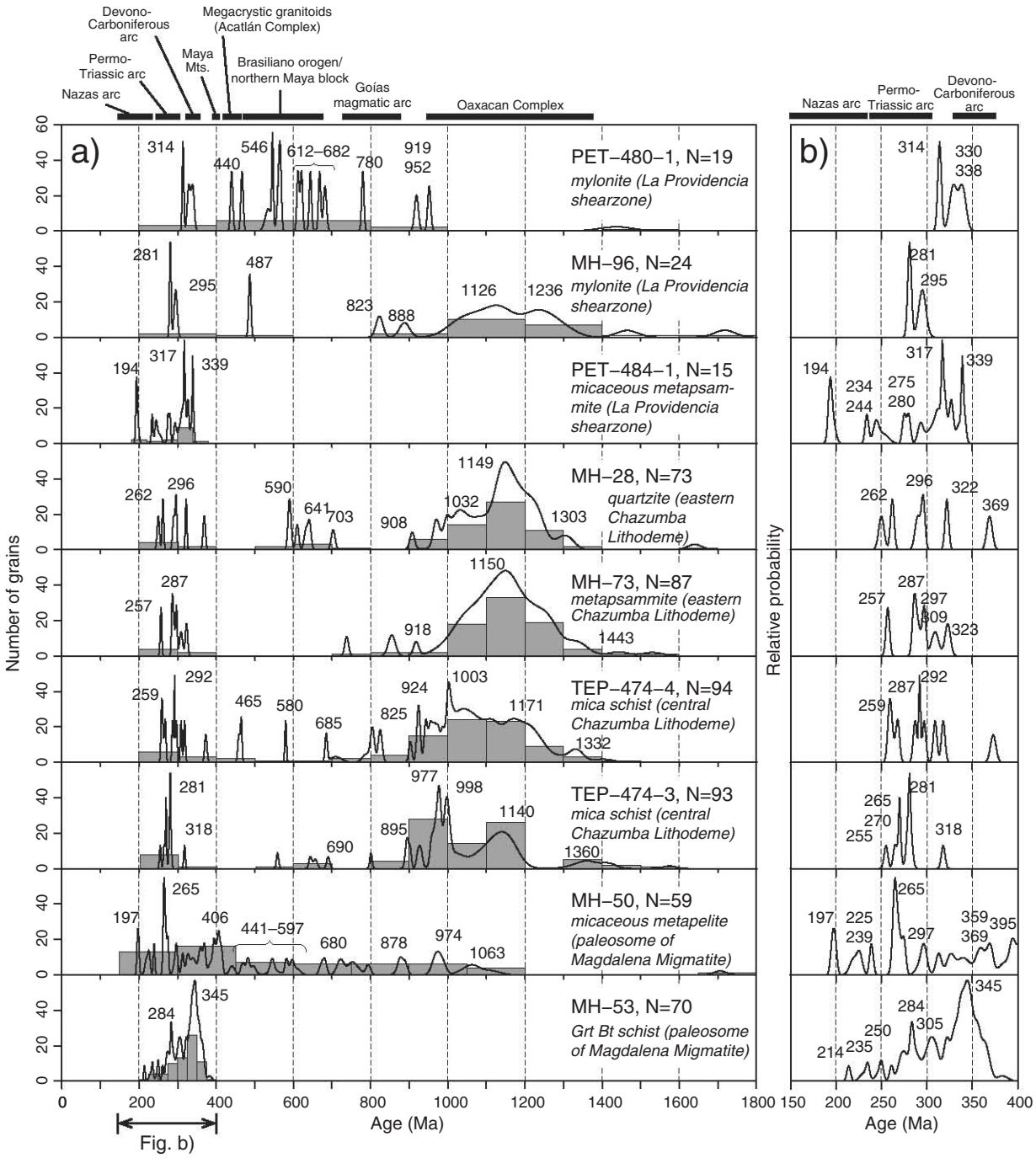

Fig. 8. Histogram and relative probability plots of zircon analyses that yielded 90 to 105% concordance for all metasedimentary rocks. a) Plot for the age range of 0–1800 Ma, b) plot for a detailed subset of 150–400 Ma. Black bars illustrate possible zircon provenances.

whole rock garnet and biotite ages (172 ± 1 Ma and 175 ± 3, respectively; Yáñez et al., 1991) as well as the 161 ± 2 Ma $^{40}Ar/^{39}Ar$ muscovite cooling age (Keppie et al., 2004). The U–Pb data are also similar to the age of migmatization as dated in a leucosome in the southern part of the area (171 ± 1 Ma — single grain thermal ionization mass spectrometry age; Keppie et al., 2004), suggesting that the genesis of granitic dikes and the migmatites may be related. The rest of the dated zircons in the igneous rocks are interpreted as inherited xenocrysts as they are also found in the metasedimentary host rocks (compare histograms in Figs. 5 and 8). These xenocrysts were either incorporated during magma intrusion of the adjacent wall rock, or were transported from a deeper crustal level where the melt was generated (e.g. Miller et al., 2003). Collectively, these data suggest that the granites were generated in, and intruded, the same basement rock between 171 Ma and 160 Ma (Middle Jurassic).

5.2. Depositional age constraints

U–Pb detrital zircon geochronology has shown that the metasedimentary succession of the Chazumba Lithodeme is very heterogeneous and that even dense sampling cannot provide a uniform youngest depositional age. A minimum depositional age for the protolith of

the Magdalena Migmatite and the non-migmatitic part of the Chazumba Lithodeme is constrained by the 168–170 Ma granitic dikes cutting both lithologies, limiting the minimum depositional age to the Bajocian (Middle Jurassic). Although the intrusive bodies do not yield significant clusters representing a crystallization age, zircons of these ages occur in all the dated igneous rocks and mutually confirm each other. The ca. 168–170 Ma crystallization age is also supported by earlier Sm–Nd (garnet/whole rock) and Rb–Sr (muscovite/whole rock) isotopic studies by Yáñez et al. (1991), which yielded ages of 172 Ma and 175 Ma, respectively.

The detrital data presented in this study yield only a few zircon analyses (N = 14) of Triassic and Lower Jurassic age in each detrital zircon sample for the Chazumba Lithodeme. The geological significance of these data becomes apparent when combining the youngest zircons into a single plot (Fig. 9a and b). Samples MH-50 and PET-484-1 each have a pair of two overlapping zircon analyses at 198 Ma, and 192 Ma, respectively. Further, various analyses yield Early–Middle Triassic zircons. The REE patterns of these youngest zircons have smooth, undisturbed LREE (light rare earth elements) and indicate that they did not crystallize during high-grade metamorphism, suffer crystal damage, or hydrothermal alteration (e.g. Hoskin and Schaltegger, 2003; Fig. 9c).

The maximum limit for the time of deposition of the Magdalena Migmatite protolith is provided by two samples (MH-53 and MH-50): 214 ± 4 Ma (Norian; Upper Triassic) and 198 ± 3 Ma (Hettangian; Early Jurassic), respectively. These ages are significantly younger than the previously documented youngest zircons for the protolith (Talavera-Mendoza et al., 2005; Keppie et al., 2006b). The youngest detrital zircons from the various samples of the non-migmatic part of the Chazumba Lithodeme have yielded 192 ± 3 Ma (PET-484-1), 263 ± 13 and 269 ± 2 Ma (beneath the Tepejillo ultramafic lens; TEP-474-4, TEP-474-3), and 250 ± 6 Ma and 257 ± 4 Ma (eastern Chazumba Lithodeme; MH-28, MH-73). The youngest zircons in samples MH-50 and PET-484-1 of Early Jurassic age (198 ± 3 Ma and 192 ± 3 Ma) constrain both the protolith of the Magdalena Migmatite and the unmigmatized Chazumba Lithodeme to a maximum depositional age of Early Jurassic suggesting that the clastic protolith should be regarded as the same unit, namely the Chazumba Lithodeme. Regarding the spatial distribution, the geochronological data indicate that deposition of the metasedimentary rocks in the western parts of the Chazumba Lithodeme commenced penecontemporaneously in the Lower Jurassic. The depositional ages in the central and eastern part of the Chazumba Lithodeme are older (Permian–Triassic) and may represent either a different stratigraphic level in the sedimentary column of the Chazumba Lithodeme or different local provenances. But due to the polydeformation of the metasedimentary rocks, the possibility that some deposition may have started in the Triassic cannot be precluded.

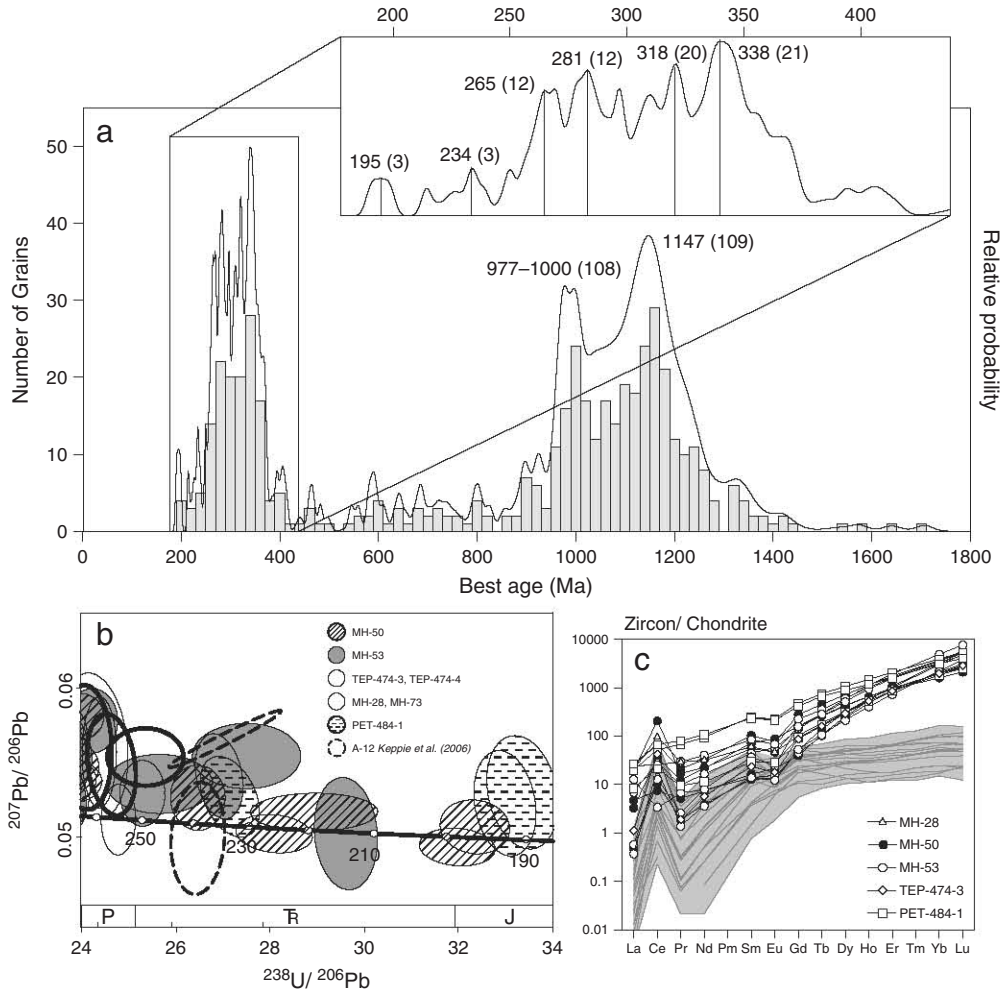

Fig. 9. a) Histogram and relative probability diagram for all detrital zircons samples of the Chazumba Lithodeme (MH-28, MH-50, MH-53, MH-73, TEP-474-3, TEP-474-4, and PET-484-1). b) Tera–Wasserburg concordia plot combining the youngest detrital zircons of the Chazumba Lithodeme; 14 grains yielded Early Mesozoic ages. Data include analyses from this work and Keppie et al. (2006b). c) Chondrite-normalized REE patterns for the plotted Triassic–Jurassic zircons in b).

The youngest zircons in the Providencia shear zone yield Lower Permian–Carboniferous ages (281 ± 4 Ma, 295 ± 8 Ma, and 334 ± 6 Ma) and are similar to those in the Totoltepec granitoid and the Tecomate Formation of the Acatlán Complex (Kirsch et al., 2010) suggesting that the zircons were derived from these units.

Taken together, the geochronological data indicate that the Chazumba Lithodeme, the ortho-amphibolites, the minor intrusives and migmatites, and the ultramafic to mafic tectonic lenses (Tepejillo and Tultitlán lenses) are of Early Mesozoic age and, hence, differ in age from the Paleozoic Acatlán Complex and do not record the same tectonic history. As a consequence, the Mesozoic rocks are assigned to a new complex, namely the "Ayú Complex", named after the town Santa María Ayú near the southern boundary of the study area.

5.3. Provenance

Based on multiple sampling of the same unit, it is apparent that the Chazumba Lithodeme is a very complex and heterogeneous metasedimentary succession and comprises metamorphosed strata of both very confined and mixed provenance. Many of the age populations documented in the metamorphosed clastic rocks of the Chazumba Lithodeme can be found in relatively local sources. The Early Jurassic to Middle Triassic detrital zircons in these rocks may have been derived from the igneous rocks of the Nazas arc (Fig. 8), which was active from the Middle Triassic to Middle Jurassic (Bartolini et al., 2003). Early Triassic and Carboniferous–Permian zircons may have been derived from the Eastern Mexico magmatic arc (for summary see Kirsch et al., in press). In particular, Middle–Late Permian zircons (250–265 Ma) may be derived from the ca. 255 Ma Etla granite or correlatives in the northern Oaxcan complex (Ortega-Obregón et al., 2012). The ca. 270 Ma detrital zircon ages are similar to crystallization ages of the Cozahuico granite located in the Caltepec Fault zone (Elías-Herrera and Ortega-Gutiérrez, 2002) and coeval plutons located in the northern Oaxacan Complex (La Carbonera stock: Solari et al., 2001; Ortega-Obregón et al., 2012). Pennsylvanian to Early Permian detrital zircons (310–280 Ma) correspond to the crystallization ages of the Totoltepec pluton (Keppie et al., 2004; Kirsch et al., 2010; Fig. 8). However, they could also have been transported from correlative sites in the Eastern Mexico Permian–Triassic arc.

Ostensibly, eclogitic rocks from the high-pressure Piaxtla Suite of the Acatlán Complex, which were probably exposed by the Late Carboniferous (Middleton et al., 2007), could be a source of the Carboniferous zircons. However, these zircons are characterized by pronounced enrichment in LREE relative to the HREE (heavy rare earth elements), a trait typical of zircons with an igneous origin (Hoskin and Schaltegger, 2003; Fig. 10a). Furthermore, the zircons have a pronounced positive Ce anomaly and a negative Eu anomaly that can be explained as a function of oxygen fugacity and by plagioclase fractionation (see Hoskin et al., 2000; Hoskin and Schaltegger, 2003). In contrast, high-grade metamorphic zircons are characterized by a general depletion in LREE, flat HREE patterns and the absence of a Eu anomaly (e.g. Rubatto, 2002; Bröcker et al., 2010; Fig. 10a). The Th/U ratio in zircons is extremely sensitive to protolith composition and/or the local chemical environment of formation (Harley et al., 2007) and so is considered an unreliable signature to discriminate metamorphic from igneous zircons (compare to Hoskin and Ireland, 2000; Rubatto, 2002; Hoskin and Schaltegger, 2003), but can be used to distinguish provenances. The very low Th/U ratios (0.001–0.01) of Carboniferous zircons dated in an eclogite and in a leucosome of the high-pressure Piaxtla Suite (Asís Lithodeme: Middleton et al., 2007) compared with the relatively high Th/U ratios (ca. 0.12–0.95) of the Ayú Complex clastic rocks support the conclusion that the eclogites are not viable sources for the dated samples (MH-53, PET-484-1) of the Chazumba Lithodeme (Fig. 10b). However, there are examples of Carboniferous igneous rocks including the Aserradero rhyolite in the Sierra Madre terrane (334 ± 39 Ma; Stewart et al., 1999), the La Pezuña rhyolite in the Coahuila terrane (331 ± 4 Ma; López, 1997), the Altos Cuchumatanes in the Maya Block (ca. 312–317 Ma, Solari et al., 2010b; Fig. 10b), the Totoltepec pluton in the Acatlán Complex (306 ± 2 Ma; Kirsch et al., 2010; Fig. 10b), and the Cuananá plutonic complex in the southern Caltepec Fault zone (ca. 307 Ma; Vega-Carrillo et al., 1998; Elías-Herrera et al., 2005) or their correlatives, that could have provided the Mississippian detrital zircons. Correlative Carboniferous metasedimentary units, such as the Cosoltepec Formation (Talavera-Mendoza et al., 2005), the Tecomate Formation (Kirsch et al., 2010), the Salada unit (Keppie et al., 2008a), the Zumpango unit (Ortega-Obregón et al., 2009; Ramos-Arias and Keppie, 2011) and the Coatlaco unit (Grodzicki et al., 2008), each contain a few Mississippian zircons with relatively high Th/U ratios (ca. 0.05–2.0). It is thus probable that these units contain detritus derived from the same sources (Keppie et al., 2008b). On the other hand, Keppie et al. (2008b, 2010) proposed that Devonian–Lower Carboniferous zircons of the metasedimentary rocks in the Acatlán complex were derived from a magmatic arc on the western margin of Pangea that was partially removed by subduction erosion.

Devonian zircons are relatively rare, but form a major population in sample MH-50 (Fig. 8) with a peak at 406 Ma. A possible source could be the Maya Mountains (Yucatán Peninsula) where 404–420 Ma ages

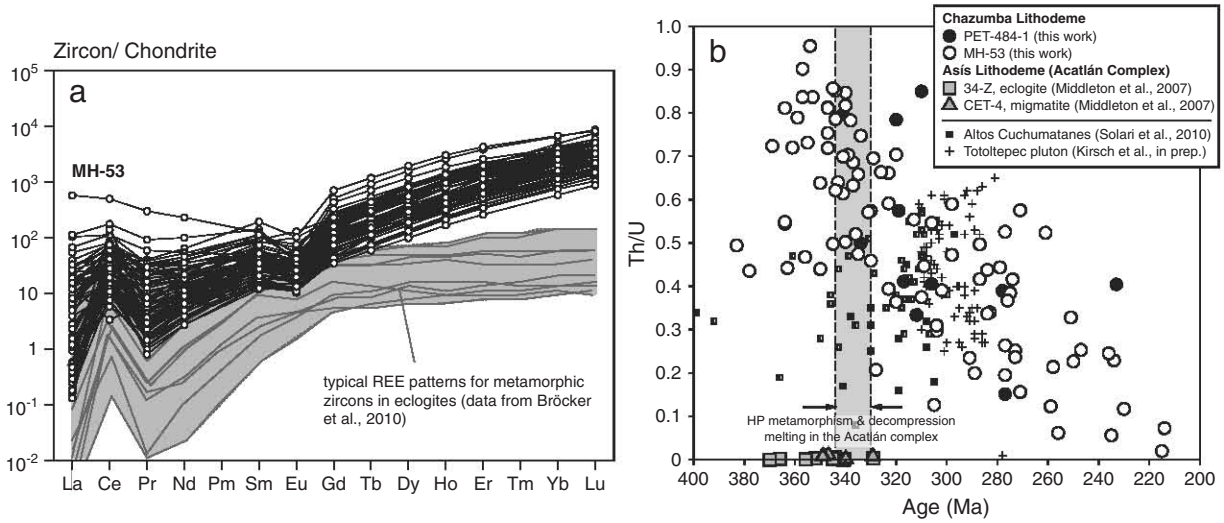

Fig. 10. a) Chondrite-normalized REE plot (Sun and McDonough, 1989) for all zircons of sample MH-53. These show steep REE patterns typical for zircons of igneous origin (compare REE patterns for metamorphic zircons from eclogites by Bröcker et al. (2010); - gray shaded area). b) Th/U ratios vs. age (Ma) for detrital zircons of samples MH-53 and PET-484-1 compared to two samples of the Asís Lithodeme (Piaxtla Suite, Middleton et al., 2007) and other possible magmatic sources (Altos Cuchumatanes, Solari et al., 2010b; Totoltepec pluton, Kirsch et al., 2010).

are reported from plutons dated with U–Pb thermal ionization mass spectrometry by Steiner and Walker (1996). Further, Martens et al. (2010) report a 406 + 7/− 6 Ma rhyolite from the volcaniclastic Bladen Formation.

Ordovician to earliest Silurian zircon populations are most likely derived from a suite of megacrystic granitoid rocks, which are part of a rift-related bimodal intrusive suite within the Acatlán Complex (Middleton et al., 2007; Miller et al., 2007; Vega-Granillo et al., 2007; Hinojosa-Prieto et al., 2008; Keppie et al., 2008a; Fig. 8). A small population of 500–700 Ma zircons probably corresponds to the Pan-African Brasiliano orogenic cycle (Pimentel and Fuck, 1992; Pimentel et al., 1997) or recycled detritus from the Yucatán block (Keppie et al., 2011, 2012; Fig. 8). Another group with 750–900 Ma ages may have been derived from the Goiás magmatic arc within the Brasiliano orogen (Pimentel et al., 2000; Fig. 8).

The provenance for the predominant population of Mesoproterozoic zircons (990–1400 Ma) that occurs in almost all samples (except for PET-484-1 and MH-53) may be found in the rocks of the adjacent Oaxacan Complex (Keppie et al., 2003; Solari et al., 2003; Fig. 8) or may be recycled from various Paleozoic rocks within the Acatlán Complex. The relative probability distributions for the metasedimentary rocks of the Chazumba Lithodeme exhibit two patterns: (1) populations that show a main peak at ca. 990–1000 Ma, a subordinate population with ages ranging from 1000 to 1300 Ma and a minor peak at ca. 1140–1170, and (2) populations that show distributions with a major peak at 1150 Ma (Fig. 8). The different provenance patterns may be the effect of different drainage systems that changed over time. However, the Proterozoic detritus may have been subjected to several cycles of re-reworking and re-deposition, and thus may not represent proximal provenances.

One paleosome sample (MH-53) shows very similar zircon age populations to those in the metapsammite (PET-484-1) sampled south of the Providencia shear zone, suggesting these rocks had a similar provenance. The lack of pre-Devonian detritus in these two samples, which only yield grains of ca. 200–400 Ma, suggests a change in provenance from east to west.

6. Tectonic implications

6.1. Environment of deposition

Determination of the depositional environment for the protoliths of the Chazumba Lithodeme is complicated by superimposed polyphase deformation and amphibolite facies metamorphism. Moreover, the Ayú Complex is in tectonic contact with unmetamorphosed continental redbeds of Lower–Middle Jurassic age in the north and with shallow-marine sediments of similar age in the southwest (Figs. 2 and 4). Nonetheless, the abundance of micaceous pelites intercalated with quartzites suggests the protoliths were either part of a continental rise prism or a clastic wedge (Keppie et al., 2006b). Major and trace element geochemistry of the boudinaged ortho-amphibolites that are interlayered with the Chazumba Lithodeme shows that the amphibolites are of igneous origin and represent transitional arc- to MORB-tholeiites that intruded in a back-arc setting (Helbig et al., 2010). In the Tahué terrane, amphibolites of the bimodal Norian Francisco gneiss are interpreted to be within-plate, continental rift tholeiites (Keppie et al., 2006a; Fig. 1), similar to the amphibolites in the Chazumba Lithodeme. The boudinaged Chazumba amphibolites contain in-situ or in-source leucosomes suggesting they underwent partial melting (e.g. Sawyer, 2008). These relationships suggest that the amphibolites were emplaced either during or after deposition of the Chazumba Lithodeme, but before metamorphism of the Chazumba Lithodeme protoliths.

Potential correlative Triassic to Lower Jurassic clastic strata may occur in the Potosí fan (Central terrane, in the Sierra Madre, and in the Zihuatanejo terrane; see e.g. Centeno-García, 2005, 2008), comprised of quartz-rich turbidites, partly with dismembered blocks of chert, limestone and pillow basalts (Taray Formation, La Ballena Formation, El Chilar Complex, and Zacatecas Formation; Figs. 1 and 11). The Potosí fan was fed by an extensive river system (Alamar Formation, Barboza-Gudiño et al., 2010) with Mesoproterozoic, Neoproterozoic and Permian–Triassic provenances, zircons from which are present in both the Potosí fan turbidites and the Chazumba Lithodeme (Fig. 11). Slabs of pillow basalt that can be found in the distal parts of the Potosí fan in the Zihuatanejo terrane are of primitive oceanic affinity (Arteaga Complex and Las Ollas Complex: Centeno-García and Silva-Romo, 1997) and are inferred to be part of a marginal (Centeno-García, 2005, 2008; Martini and Ferrari, 2009), or back-arc basin (Elías-Herrera et al., 2000). To the east of these rocks, the Late to Early Triassic Río Placeres Fm. (Pantoja-Alor and Gómez-Caballero, 2003; Fig. 11) and the Tzitzio metaflysch crop out in the Huetamo area (Zihuatanejo terrane), where the latter yielded youngest zircons at ca. 250 Ma (Talavera-Mendoza et al., 2007; Martini and Ferrari, 2009; Fig. 11). These coeval strata in the Potosí fan (Central and Zihuatanejo terranes) have similar detrital zircon populations to those of the Chazumba Lithodeme suggesting a similar provenance (Fig. 11). However, the Potosí fan and correlative units exhibit only minor abundances of Mesoproterozoic zircons. The lack of ca. 1.4 Ga ages may indicate that (1) the Proterozoic detritus (or older detritus in general), having been affected by several cycles of re-reworking and re-deposition, is not a reliable indicator of provenance, or that (2) the scarcity of U–Pb detrital zircon data from the Central terrane and Guerrero composite terrane hinders evaluation of this region as a potential source.

Collectively, our results indicate that (i) the Chazumba Lithodeme probably formed in the same tectonic setting as the Potosí turbiditic fan, and (ii) the intrusion or deposition of transitional arc- to MORB-tholeiites formed during rifting along the margin of the Mexican mainland. If so, the Chazumba Lithodeme is a southern correlative unit of the turbidites deposited on the inboard side of a back-arc basin that was situated along the western margin of northern Oaxaquia and the Mixteca terranes (Fig. 12a). In the southern Guerrero composite terrane, the Central terrane rift–passive continental margin rocks are absent and a Cretaceous arc complex separates the Zihuatanejo terrane from the continental margin (Centeno-García, 2008). The absence of the Central terrane here suggests that the Chazumba Lithodeme is probably a vestige of the portion of the Central terrane that was removed from the continental margin by underthrusting beneath the Pangean margin (Fig. 12c–d).

Late Triassic magmatic zircons in the Chazumba Lithodeme are likely to have been derived from a magmatic arc. Evidence for the existence of such an arc may be the Triassic–Early Jurassic metasedimentary volcanogenic assemblage of the Tejupilco schist in the Teloloapán terrane (Figs. 1 and 11; Elías-Herrera et al., 2000, 2003), which is of calc-alkaline affinity and represents an evolved arc that developed on a thinned or rifted continental margin (Elías-Herrera et al., 2000, 2003; Martini and Ferrari, 2009; Figs. 11 and 12c). Elías-Herrera et al. (2000, 2003) propose the presence of an east-facing arc with the Late Triassic Arteaga Complex as its back-arc basin, whereas Martini and Ferrari (2009) favor a west-facing arc. The polarity of the subduction zone remains a matter of debate (e.g. Centeno-García, 2008) and the data presented here cannot resolve this problem.

6.2. Tectonic emplacement

It is envisaged that the Ayú Complex was thrust beneath the continental margin of Oaxaquia/Mixteca resulting in polydeformation and migmatization, and was then tectonically emplaced into the Acatlán Complex and the overlying strata (Fig. 12b–e). The timing of this process is constrained by geochronological data: (i) underthrusting post-dates the youngest detrital zircons in the Chazumba Lithodeme (ca. 195–234 Ma; this paper; Fig. 9a); (ii) polyphase deformation is probably related to telescoping of the back-arc basin; (iii) peak metamorphism and migmatization occurred during deformation at 171 ±

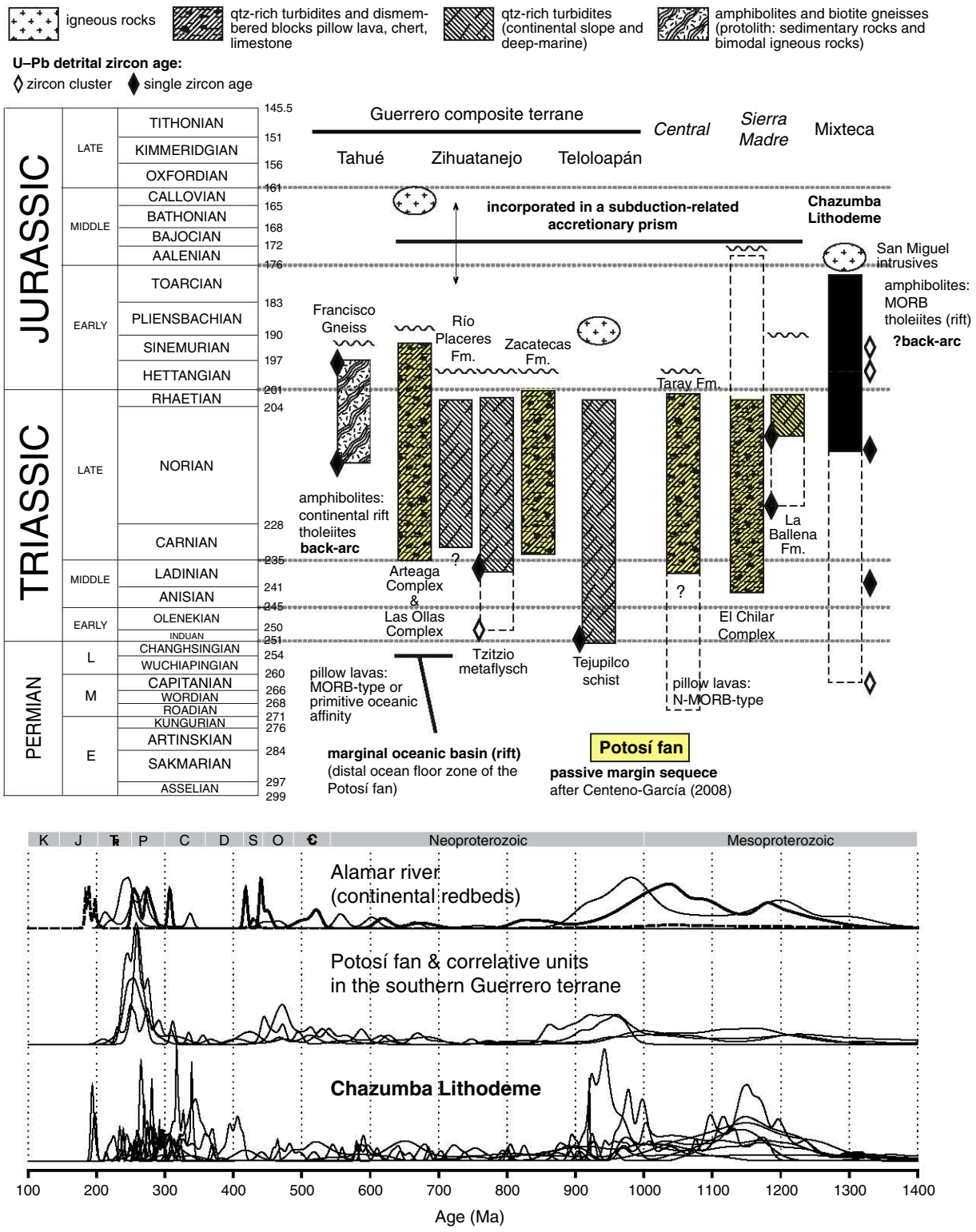

Fig. 11. Top: Stratigraphic columns of Triassic–Lower Jurassic strata for the Guerrero composite terrane, the Central terrane and the margin of Pangea (Sierra Madre, Mixteca/Oaxaquia). Geochronological constraints for Francisco gneiss: Keppie et al., 2006a; Arteaga Complex: Campa-Uranga et al., 1982; Las Ollas Complex: Centeno-García et al., 2003; Talavera-Mendoza et al., 2007; Río Placeres Formation: Pantoja-Alor and Gómez-Caballero, 2003; Tzitzio metaflysch: Talavera-Mendoza et al., 2007; Martini and Ferrari, 2009; Zacatecas Formation: Burckhardt and Scalia, 1906; Bartolini et al., 2002; Tejupilco schist: Elías-Herrera et al., 2000, 2003; Martini and Ferrari, 2009; Taray Formation: Díaz-Salgado et al., 2003; Anderson et al., 2005; El Chilar Complex: Dávila-Alcocer et al., 2009; Ortega-Flores et al., 2012; La Ballena Formation: Centeno-García and Silva-Romo, 1997; Silva-Romo et al., 2000. Time scale is after Walker and Geissman (2009). Bottom: Relative probabilities for zircon populations of the Chazumba Lithodeme (this work, Talavera-Mendoza et al., 2005, Keppie et al., 2006b) compared to provenances of the Potosí fan (La Ballena Fm.: Venegas-Rodríguez, 2009; Barboza-Gudiño et al., 2010; Tzitzio metaflysch: Talavera-Mendoza et al., 2007; Martini and Ferrari, 2009; Tejupilco schist: Martini and Ferrari, 2009). Zircon populations from continental redbeds of the lower Huizachal group (Alamar Formation: Barboza-Gudiño et al., 2010; Rubio-Cisneros and Lawton, 2011).

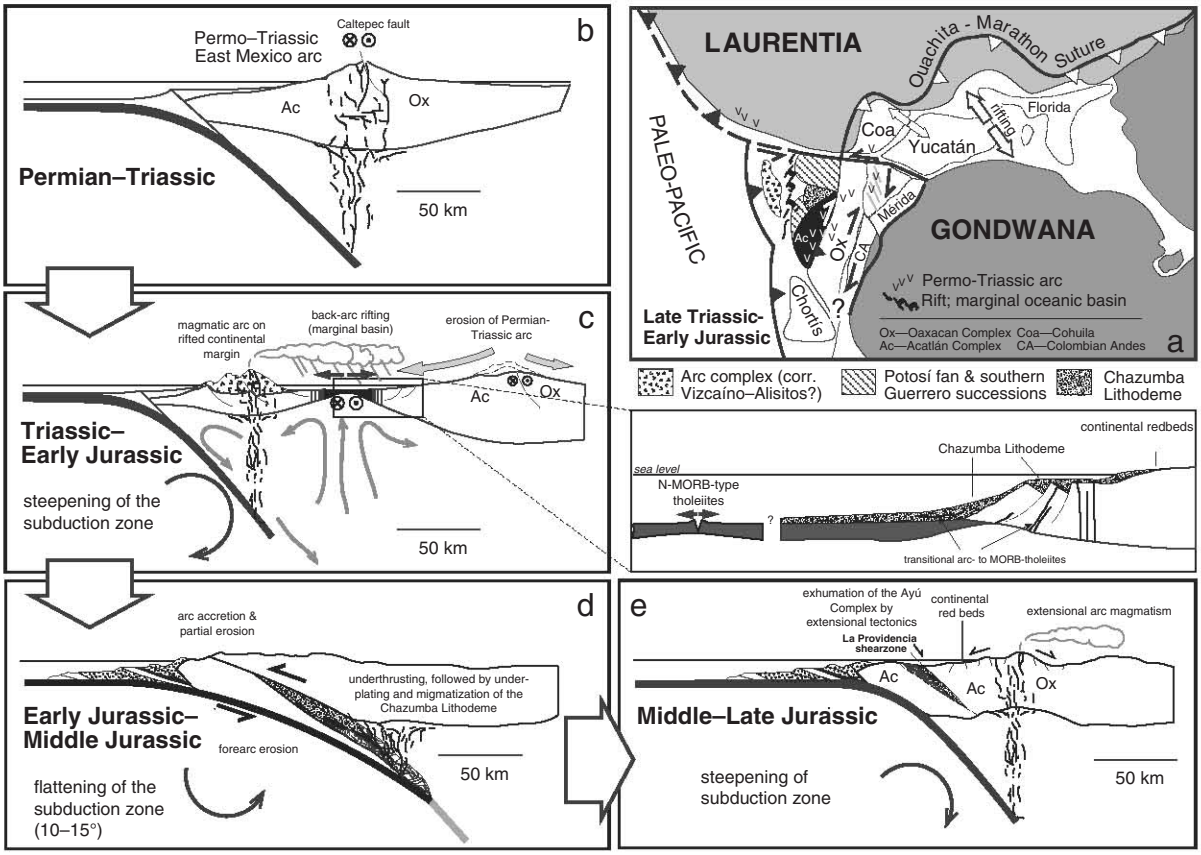

Fig. 12. a) Paleogeographic reconstruction of the western Pangean margin for Triassic and Early Jurassic time (modified after Pindell, 1985; Elías-Herrera and Ortega-Gutiérrez, 2002; Weber et al., 2007; Centeno-García, 2008. b–e) Tectonic evolution of the Ayú Complex: b) Permian–Triassic East Mexico arc as high-relief compressional continental arc forms on the Oaxacan and Acatlán Complexes; c) re-steepening of the subduction zone causes extension in the overriding plate, arc magmatism on stretched continental crust and eventually back-arc basin formation, deposition of the Triassic–Late Jurassic turbiditic successions and intrusion of rift-related tholeiites in the form of dikes or lava flows (see box for details); d) flattening of the subduction zone in the Early–Middle Jurassic causes collision of the magmatic arc, with subduction erosion taking down a large forearc piece (including the Chazumba Lithodeme), followed by underplating and partial melting (Magdalena Migmatite); e) uplift and exhumation of the Ayú Complex by extension in the overriding plate as subduction zone re-steepens.

1 Ma at temperatures of ≥700 °C and depths of ca. 19 km (Keppie et al., 2004); (iv) uplift and erosion through ca. 350 °C took place by 161 ± 2 Ma and 154 ± 6 Ma in the Tepejillo area and through ca. 280 °C by 150 ± 2 Ma in the Ayú area ($^{40}Ar/^{39}Ar$ muscovite and biotite cooling ages; Keppie et al., 2004) implying a cooling rate of 20–35 °C/Ma; and (v) extrapolation of this cooling rate suggests that the Ayú Complex would not have reached the surface until ca. 152–147 Ma (latest Jurassic/earliest Cretaceous). This exhumation history could explain why detritus from the Ayú Complex has not been reported in the adjacent low-grade Triassic and Jurassic rocks.

The boundary between the Ayú and Acatlán complexes is a major shear zone (Providencia shear zone, Fig. 7) that was previously mapped as a thrust based on s–c fabrics in the hanging wall (Malone et al., 2002). However, $^{40}Ar/^{39}Ar$ dating indicates that these fabrics are Late Triassic (Keppie et al., 2004; Fig. 7), and thus developed contemporaneously with the deposition of the Chazumba Lithodeme. We infer that this Triassic shear zone was reactivated during or after the Middle Jurassic as a listric normal fault (c.f. Wheeler et al., 2003) and formed the upper boundary of the Chazumba Lithodeme during its exhumation (Figs. 4 and 7).

To the northeast, the Ayú Complex is further bounded by the Tianguistengo normal fault, which cuts the Middle Jurassic Piedra Hueca Unit. The Petlalcingo–Huajuapán Fault (Fig. 4) is probably Late Jurassic, and was reactivated during the Cenozoic (Martiny et al., 2012). Regionally, Middle Permian–Jurassic deformation is characterized by top-to-north extensional shearing in Paleozoic outliers deposited on the Oaxacan Complex (Centeno-García and Keppie, 1999) and left-lateral displacement along the 180 Ma E–W/NW–SE trending Salado River Fault involving ductile deformation and medium-grade metamorphism (Martiny et al., 2012; Fig. 2).

Early Jurassic underthrusting of the Chazumba Lithodeme followed by Middle Jurassic peak metamorphism was synchronous with the deformation of the Potosí fan (Centeno-García, 2008) and correlative southern sedimentary units (Talavera-Mendoza et al., 2007; Martini and Ferrari, 2009), and the syntectonic intrusion of Middle Jurassic plutons along the eastern margin of the Guerrero composite terrane (Elías-Herrera et al., 2000, 2003). Exhumation of the Chazumba Lithodeme took place at the same time as Late Jurassic extension in the Guerrero composite terrane (Centeno-García, 2008). Numeric modeling shows that shallowing and steepening of the Benioff zone can lead to cyclic contraction (subduction erosion) and extension in the overriding plate, respectively (sensu von Huene and Scholl, 1991; Collins, 2002; Keppie et al., 2009; Fig. 12). Underthrusting of the inboard margin of the back-arc basin could have been along a synthetic thrust parallel to the Benioff zone (Fig. 12d). Preservation of along-strike parts of the inboard passive margin suggests that underthrusting may have been bounded by transform faults that limit the lateral extent of the eroded margin. The Middle–Late Jurassic exhumation of the Ayú Complex under extension was synchronous with extension in the Nazas arc along the Pangean margin (Bartolini et al., 2003), which may reflect the steepening of the Paleo-Pacific subduction zone. Thus, the origin of the back-arc basin origin and underthrusting, polyphase deformation

and metamorphism of the Ayú Complex are all consistent with the development of the complex on the margin of Pangea-A and support previous conclusions that the Nazas arc formed along the western margin of Pangea-A. These data are incompatible with a Pangea-B configuration (Böhnel, 1999) or with a location of the Acatlán and Ayú complexes in the future Gulf of Mexico ca. 1500 km from the western margin of Pangea-A (Vega-Granillo et al., 2007).

Supplementary data to this article can be found online at doi:10.1016/j.gr.2012.03.004.

Acknowledgments

We would like to thank the two anonymous reviewers' constructive comments on the first draft of the paper. We acknowledge the Consejo Nacional de Ciencia y Tecnología (CONACyT; Project CB-2005-1/24894), Programa de Apoyo a Proyectos de Investigación (PAPIIT: IN100108-3) and N.S.E.R.C. (Canada). Carlos Ortega-Obregón y Ofelia Pérez-Arvizu provided technical assistance in the Laboratorio de Estudios Isotópicos, Centro de Geociencias. This is a contribution to IGCP Project 597.

References

Alva-Valdivia, L.M., Goguitchaichvili, A., Grajales-Nishimura, J.M., de Dios-González, A.L.F., Urrutia-Fucugauchi, J., Rosales, C., Morales, J., 2001. Further constraints for Permo–Carboniferous magnetostratigraphy: case study of the sedimentary sequence from San Salvador–Patlanoaya (Mexico). Comptes Rendus Geoscience 334, 811–817.

Anderson, T.H., Jones, N.W., McKee, J.W., 2005. The Taray Formation: Jurassic (?) mélange in northern Mexico — tectonic implications. Geological Society of America Special Paper 393, 427–455.

Barboza-Gudiño, J.R., Orozco-Esquivel, M.T., Gómez-Anguiano, M., Zavala-Monsiváis, A., 2008. The Early Mesozoic volcanic arc of western North America in northeastern Mexico. Journal of South American Earth Sciences 25, 49–63.

Barboza-Gudiño, J.R., Zavala-Monsiváis, A., Venegas-Rodríguez, G., Barajas-Nigoche, L.D., 2010. Late Triassic stratigraphy and facies from northeastern Mexico: tectonic setting and provenance. Geosphere 6, 621–640.

Bartolini, C., Lang, H., Cantú-Chapa, A., Barboza-Gudiño, R., 2002. The Triassic Zacatecas Formation in Central Mexico: paleotectonic, paleogeographic, and paleobiogeographic implications. In: Bartolini, C., Buffler, R.T., Cantú-Chapa, A. (Eds.), The Western Gulf of Mexico Basin: tectonics, sedimentary basins, and petroleum systems: AAPG Memoir, 75, pp. 295–315.

Bartolini, C., Lang, H., Spell, T., 2003. Geochronology, geochemistry and tectonic setting of the Mesozoic Nazas arc in north-central Mexico, and its continuation to northern South America. In: Bartolini, C., Buffler, C., Blickwede, J. (Eds.), The Circum-Gulf of Mexico and the Caribbean: hydrocarbon habitats, basin formation, and plate tectonics: AAPG Memoir, 79, pp. 427–461.

Böhnel, H.N., 1999. Paleomagnetic study of Jurassic and Cretaceous rocks from the Mixteca terrane (Mexico). Journal of South American Earth Sciences 12, 545–556.

Bröcker, M., Klemd, R., Kooijman, E., Berndt, J., Larionov, A., 2010. Zircon geochronology and trace element characteristics of eclogites and granulites from the Orlica–Śnieżnik complex, Bohemian Massif. Geological Magazine 147, 339–362.

Bullard, E., Everett, J.E., Smith, A.G., 1965. The fit of the continents around the Atlantic. Philosophical Transactions of the Royal Society A: Mathematical, Physical and Engineering Sciences 258, 41–51.

Burckhardt, C., Scalia, S., 1906. Géologie des environs de Zacatecas. 10th International Geological Congress, Mexico City 16, 26.

Caballero-Miranda, C., Morán-Zenteno, D.J., Urrutia-Fucugauchi, J., Silva-Romo, G., Böhnel, H.N., Churado-Chichay, Z., Cabral-Cano, E., 1990. Paleogeography of the northern portion of the Mixteco terrain, southern Mexico, during the Middle Jurassic. Journal of South American Earth Sciences 3, 195–211.

Campa-Uranga, M.F., Coney, P.J., 1983. Tectono-stratigraphic terranes and mineral resource distributions in Mexico. Canadian Journal of Earth Sciences 20, 1040–1051.

Campa-Uranga, M.F., Ramirez, J., Bloome, C., 1982. La secuencia volcánico-sedimentaria etamorfizada del Triásico (Ladiniano–Cárnico) de la región de Tumbiscatio, Michoacán. Convención Geológica Nacional Abstracts, 6a. Sociedad Geológica Mexicana, p. 48.

Centeno-García, E., 2005. Review of Upper Paleozoic and Lower Mesozoic stratigraphy and depositional environments of central and west Mexico: Constraints on terrane analysis and paleogeography. In: Anderson, T.H., Nourse, J.A., McKee, J.W., Steiner, M.B. (Eds.), The Mojave–Sonora megashear hypothesis: development, assessment, and alternatives: Geological Society of America Special Paper, 393, pp. 233–258.

Centeno-García, E., 2008. The Guerrero Composite Terrane of western Mexico: collision and subsequent rifting in a supra-subduction zone. In: Draut, A., Clift, P.D., Scholl, D. (Eds.), Formation and applications of the sedimentary record in arc collision zones: Geological Society of America Special Paper, 436, pp. 279–308.

Centeno-García, E., Keppie, J.D., 1999. Latest Paleozoic early Mesozoic structures in the central Oaxaca Terrane of southern Mexico: deformation near a triple junction. Tectonophysics 301, 231–242.

Centeno-García, E., Silva-Romo, G., 1997. Petrogenesis and tectonic evolution of central Mexico during Triassic–Jurassic time. Revista Mexicana de Ciencias Geológicas 14, 244–260.

Centeno-García, E., Corona-Chávez, P., Talavera-Mendoza, O., Iriondo, A., 2003. Geology and tectonic evolution of the Western Guerrero Terrane — a transect from Puerto Vallarta to Zihuatanejo, Mexico. Geologic Transects Across Cordilleran Mexico, Guidebook for the Field Trips of the 99th Geological Society of America Cordilleran Section Annual Meeting. Geological Society of America, Puerto Vallarta, Jalisco, pp. 201–228.

Centeno-García, E., Mendoza-Rosales, C.C., Silva-Romo, G., 2009. Sedimentology and significance of the volcanism of the Matzitzi Formation (upper Paleozoic), Lus Reyes Metzontla–San Luis Atolotitlán region, Puebla State. Revista Mexicana de Ciencias Geológicas 26, 18–36.

Cerca, M., Ferrari, L., López-Martínez, M., Martiny, B.M., Iriondo, A., 2007. Late Cretaceous shortening and early Tertiary shearing in the central Sierra Madre del Sur, southern Mexico: insights into the evolution of the Caribbean–North American plate interaction. Tectonics 26, TC3007.

Collins, W., 2002. Hot orogens, tectonic switching, and creation of continental crust. Geology 30, 535–538.

Dávila-Alcocer, V.M., Centeno-García, E., Valencia, V.A., Fitz-Díaz, E., 2009. Una nueva interpretación de la estratigrafía de la Región de Tolimán, Estado de Querétaro. Boletín de la Sociedad Geológica Mexicana 61, 1–7.

Díaz-Salgado, C., Centeno-García, E., Gehrels, G.E., 2003. Stratigraphy, depositional environments, and tectonic significance of the Taray Formation, Northern Zacatecas State, Mexico. Geological Society of America Abstracts with Programs 35, 71.

Dickinson, W.R., Gehrels, G.E., 2008. Sediment delivery to the Cordilleran foreland basin: insights from U–Pb ages of detrital zircons in Upper Jurassic and Cretaceous strata of the Colorado Plateau. American Journal of Science 308, 1041–1082.

Dickinson, W.R., Gehrels, G.E., 2009. Use of U–Pb ages of detrital zircons to infer maximum depositional ages of strata: a test against a Colorado Plateau Mesozoic database. Earth and Planetary Science Letters 288, 115–125.

Dickinson, W.R., Lawton, T.F., 2001. Carboniferous to Cretaceous assembly and fragmentation of Mexico. Geological Society of America Bulletin 113, 1142–1160.

Domeier, M., Van der Voo, R., Torsvik, T.H., 2012. Paleomagnetism and Pangea: the road to reconciliation. Tectonophysics 514–517, 14–43.

Dostal, J., Keppie, J.D., 2009. Geochemistry of low-grade clastic rocks in the Acatlán Complex of southern Mexico: evidence for local provenance in felsic-intermediate igneous rocks. Sedimentary Geology 222, 241–253.

Dowe, D.S., Nance, R.D., Keppie, J.D., Cameron, K.L., Ortega-Rivera, A., Ortega-Gutiérrez, F., Lee, J.W.K., 2005. Deformational history of the Granjeno Schist, Ciudad Victoria, Mexico: constraints on the closure of the Rheic Ocean? International Geology Review 47, 920–937.

Elías-Herrera, M., Ortega-Gutiérrez, F., 2002. Caltepec Fault zone: an Early Permian dextral transpressional boundary between the Proterozoic Oaxacan and Paleozoic Acatlán complexes, southern Mexico, and regional tectonic implications. Tectonics 21, 1–18.

Elías-Herrera, M., Sánchez-Zavala, J.L., Macías-Romo, C., 2000. Geologic and geochronologic data from the Guerrero terrane in the Tejupilco area, southern Mexico: new constraints on its tectonic interpretation. Journal of South American Earth Sciences 13, 355–375.

Elías-Herrera, M., Ortega-Gutiérrez, F., Sánchez-Zavala, J.L., Macías-Romo, C., 2003. The real Guerrero terrane, southern Mexico: new insights from recent studies. Geological Society of America Abstracts with Programs 35.

Elías-Herrera, M., Ortega-Gutiérrez, F., Sánchez-Zavala, J.L., Macías-Romo, C., Ortega-Rivera, A., Iriondo, A., 2005. La falla de Caltepec: raíces expuestas de una frontera tectónica de larga vida entre dos terrenos continentales del sur de México. Grandes Fronteras Tectónicas de México: Boletín de la Sociedad Geológica Mexicana, Volumen Conmemorativo del Centenario 57, 83–109.

Elías-Herrera, M., Ortega-Gutiérrez, F., Macías-Romo, C., Sánchez-Zavala, J.L., Solari, L.A., 2011. Colisión oblicua del Cisuraliano–Guadalopiano entre bloques continentales en el sur de México: Evidencias estratigráfico-estructurales y geocronológicas. Simposio en Honor del Dr. Zoltan de Cserna, México, D.F. , pp. 159–164.

Fang, W., Van der Voo, R., Molina Garza, R.S., Morán-Zenteno, D.J., Urrutia-Fucugauchi, J., 1989. Paleomagnetism of the Acatlán terrane, southern Mexico: evidence for terrane rotation. Earth and Planetary Science Letters 94, 131–142.

Ferrari, L., 2004. Slab detachment control on mafic volcanic pulse and mantle heterogeneity in central Mexico. Geology 32, 77–80.

Ferrari, L., López-Martínez, M., Aguirre-Díaz, G., Carrasco-Núñez, G., 1999. Space–time patterns of Cenozoic arc volcanism in central Mexico: from the Sierra Madre Occidental to the Mexican Volcanic Belt. Geology 27, 303–306.

Galaz Escanilla, G., Keppie, J.D., Solari, L.A., 2009. Complejo Acatlán en el área de Tehuitzingo, Estado de Puebla, sur de México: evidencias de su evolución tectónica. GEOS 29, 48–49.

Gehrels, G.E., 2011. Detrital zircon U–Pb geochronology: current methods and new opportunities. In: Busby, C., Azor-Pérez, A. (Eds.), Tectonics of Sedimentary Basins: Recent Advances. John Wiley & Sons, Ltd., pp. 45–62.

Gehrels, G.E., Valencia, V.A., Pullen, A., 2006. Detrital zircon geochronology by laser-ablation multicollector ICPMS at the Arizona Laserchron Center. In: Olszewski, T. (Ed.), Geochronology: Emerging Opportunities, Paleontological Society Short Course, October 21, 2006, Philadelphia, PA: Paleontological Society Papers, pp. 67–76.

Godínez-Urban, A., Lawton, T.F., Molina Garza, R.S., Iriondo, A., Weber, B., López-Martínez, M., 2011. Jurassic volcanic and sedimentary rocks of the La Silla and Todos Santos Formations, Chiapas: record of Nazas arc magmatism and rift-basin formation prior to opening of the Gulf of Mexico. Geosphere 7, 121–144.

Gómez-Tuena, A., Langmuir, C.H., Goldstein, S.L., Straub, S.M., Ortega-Gutiérrez, F., 2007. Geochemical evidence for slab melting in the Trans-Mexican Volcanic Belt. Journal of Petrology 48, 537–562.

González-León, C.M., Valencia, V.A., Lawton, T.F., Jeffrey, M.A., Gehrels, G.E., William, J.L., Montijo-Contreras, O., Fernández, M.A., 2009. The lower Mesozoic record of detrital zircon U–Pb geochronology of Sonora, México, and its paleogeographic implications. Revista Mexicana de Ciencias Geológicas 26, 301–314.

Grodzicki, K.R., Nance, R.D., Keppie, J.D., Dostal, J., 2008. Structural, geochemical and geochronological analysis of metasedimentary and metavolcanic rocks of the Coatlaco area, Acatlán Complex, southern Mexico. Tectonophysics 461, 311–323.

Harley, S.L., Kelly, N.M., Möller, A., 2007. Zircon behaviour and the thermal histories of mountain chains. Elements 3, 25–30.

Harris, A.C., Allen, C.M., Bryan, S.E., Campbell, I.H., Holcombe, R.J., Palin, J.M., 2004. ELA–ICP-MS U? Pb zircon geochronology of regional volcanism hosting the Bajo de la Alumbrera Cu? Au deposit: implications for porphyry-related mineralization. Mineralium Deposita 39, 46–67.

Helbig, M., Keppie, J.D., Murphy, J.B., Solari, L.A., 2010. Jurassic amphibolites of the Eastern Acatlán Complex (Southern Mexico) related to both back-arc rifting and the opening of the Gulf of Mexico? Geological Society of America Abstracts with Programs 42, 679.

Hinojosa-Prieto, H.R., Nance, R.D., Keppie, J.D., Dostal, J., Ortega-Rivera, A., Lee, J.W.K., 2008. Ordovician and Late Paleozoic–Early Mesozoic tectonothermal history of the La Noria area, northern Acatlán Complex, southern Mexico: record of convergence in the Rheic and paleo-Pacific oceans. Tectonophysics 461, 324–342.

Hoskin, P.W.O., Ireland, T., 2000. Rare earth element chemistry of zircon and its use as a provenance indicator. Geology 28, 627–630.

Hoskin, P.W.O., Schaltegger, U., 2003. The composition of zircon and igneous and metamorphic petrogenesis. Reviews in Mineralogy and Geochemistry 53, 27–62.

Hoskin, P.W.O., Kinny, P.D., Kinny, P.D., Wyborn, D., Chappell, B.W., 2000. Identifying accessory mineral saturation in granitoid magmas: an integrated approach. Journal of Petrology 41, 1365–1396.

Irving, E., 1977. Drift of the major continental blocks since the Devonian. Nature 270, 304–309.

Jeffries, T.E., Fernández-Suárez, J., Corfu, F., Gutiérrez-Alonso, G., 2003. Advances in U–Pb geochronology using a frequency quintupled Nd:YAG based laser ablation system (lambda = 213 nm) and quadrupole based ICP-MS. Journal of Analytical Atomic Spectrometry 18, 847–855.

Keppie, J.D., 2004. Terranes of Mexico revisited: a 1.3 billion year odyssey. International Geology Review 46, 765–794.

Keppie, J.D., Dostal, J., 2007. Ordovician–Devonian oceanic basalts in the Cosoltepec Formation, Acatlán Complex, southern México: vestiges of the Rheic Ocean? The evolution of the Rheic Ocean: from Avalonian–Cadomian active margin to Alleghenian–Variscan collision: Geological Society of America Special Paper, 423, pp. 477–487.

Keppie, J.D., Dostal, J., Cameron, K.L., Solari, L.A., Ortega-Gutiérrez, F., López, R., 2003. Geochronology and geochemistry of Grenvillian igneous suites in the northern Oaxacan Complex, southern Mexico: tectonic implications. Precambrian Research 12, 365–389.

Keppie, J.D., Nance, R.D., Dostal, J., Ortega-Rivera, A., Miller, B.V., Fox, D., Powell, J., Mumma, S., Lee, J.W.K., 2004. Mid-Jurassic tectonothermal event superposed on a Paleozoic geological record in the Acatlán Complex of Southern Mexico: hotspot activity during the breakup of Pangea. Gondwana Research 7, 239–260.

Keppie, J.D., Dostal, J., Miller, B.V., Ortega-Rivera, A., Roldán-Quintana, J., Lee, J.W.K., 2006a. Geochronology and geochemistry of the Francisco gneiss: Triassic continental rift tholeiites on the Mexican margin of Pangea metamorphosed and exhumed in a Tertiary core complex. International Geology Review 48, 1–16.

Keppie, J.D., Nance, R.D., Fernández-Suárez, J., Storey, C.D., Jeffries, T.E., Murphy, J.B., 2006b. Detrital zircon data from the Eastern Mixteca Terrane, Southern Mexico: evidence for an Ordovician–Mississippian continental rise and a Permo–Triassic clastic wedge adjacent to Oaxaquia. International Geology Review 48, 97–111.

Keppie, J.D., Dostal, J., Miller, B.V., Ramos-Arias, M.A., Morales-Gámez, M., Nance, R.D., Murphy, J.B., Ortega-Rivera, A., Lee, J.W.K., Housh, T., Cooper, P., 2008a. Ordovician–earliest Silurian rift tholeiites in the Acatlán Complex, southern Mexico: evidence of rifting on the southern margin of the Rheic Ocean. Tectonophysics 461, 130–156.

Keppie, J.D., Dostal, J., Murphy, J.B., Nance, R.D., 2008b. Synthesis and tectonic interpretation of the westernmost Paleozoic Variscan orogen in southern Mexico: from rifted Rheic margin to active Pacific margin. Tectonophysics 461, 277–290.

Keppie, D.F., Currie, C.A., Warren, C., 2009. Subduction erosion modes: comparing finite element numerical models with the geological record. Earth and Planetary Science Letters 287, 241–254.

Keppie, J.D., Nance, R.D., Ramos-Arias, M.A., Lee, J.W.K., Dostal, J., Ortega-Rivera, A., Murphy, J.B., 2010. Late Paleozoic subduction and exhumation of Cambro–Ordovician passive margin and arc rocks in the northern Acatlán Complex, southern Mexico: geochronological constraints. Tectonophysics 495, 213–229.

Keppie, J.D., Dostal, J., Norman, M., Urrutia-Fucugauchi, J., Grajales-Nishimura, J.M., 2011. Study of melt and a clast of 546 Ma magmatic arc rocks in the 65 Ma Chicxulub bolide breccia, northern Maya block, Mexico: western limit of Ediacaran arc peripheral to northern Gondwana. International Geology Review 53, 1180–1193.

Keppie, J.D., Nance, R.D., Dostal, J., Lee, J.K.W., Ortega-Rivera, A., 2012. Constraints on the subduction erosion/extrusion cycle in the Paleozoic Acatlán Complex of southern Mexico: geochemistry and geochronology of the type Pixtla Suite. Gondwana Research 4, 1050–1065. http://dx.doi.org/10.1016/j.gr.2011.07.020.

Kirsch, M., Keppie, J.D., Murphy, J.B., Solari, L.A., 2010. Arc-related, Permo–Carboniferous plutonism in a synchronous pull-apart basin along the western margin of Pangea in southern Mexico. Geological Society of America Abstracts with Programs 42, 678.

Kirsch, M., Keppie, J.D., Murphy, J.B., Solari, L.A., in press. Permian–Carboniferous arc magmatism and basin evolution along the western margin of Pangea: geochemical and geochronological evidence from the eastern Acatlán Complex, southern Mexico. Geological Society of America Bulletin.

Levresse, G., Tritlla, J., Deloule, E., Pinto-Linares, P., 2007. Is there a Grenvillian basement in the Guerrero–Morelos platform of Mexico? Geologica Acta 5, 167–175.

López, R., 1997. The pre-Jurassic geotectonic evolution of the Coahuila terrane, northwestern Mexico: Grenville basement, a late Paleozoic arc, Triassic plutonism, and the events south of the Ouachita suture. Ph.D. thesis. University of California. Santa Cruz, CA.

Ludwig, K., 2008. User's Manual for Isoplot 3.70. volume 4 of *A Geochronological Toolkit for Microsoft Excel*. Berkeley Geochronology Center Special Publication.

Malone, J., Nance, R.D., Keppie, J.D., Dostal, J., 2002. Deformational history of part of the Acatlán Complex: Late Ordovician–Early Silurian and Early Permian orogenesis in southern Mexico. Journal of South American Earth Sciences 15, 511–524.

Martens, U., Weber, B., Valencia, V.A., 2010. U/Pb geochronology of Devonian and older Paleozoic beds in the southeastern Maya block, Central America: its affinity with peri-Gondwanan terranes. Geological Society of America Bulletin 122, 815–829.

Martini, M., Ferrari, L., 2009. Cretaceous–Eocene magmatism and Laramide deformation in southwestern Mexico: no role for terrane accretion. In: Kay, S., Ramos, V.A., Dickinson, W.R. (Eds.), Backbone of the Americas: shallow subduction, plateau uplift, and ridge and terrane collision: Geological Society of America Memoir, 204, pp. 151–182.

Martiny, B.M., Morán-Zenteno, D.J., Tolson, G., Silva-Romo, G., López-Martínez, M., 2012. The Salado River Fault: reactivation of an Early Jurassic fault in a transfer zone during Laramide deformation in southern Mexico. International Geology Review 2, 144–164.

Marzoli, A., Renne, P.R., Piccirillo, E.M., Ernesto, M., Bellieni, G., De Min, A., 1999. Extensive 200-million-year-old continental flood basalts of the Central Atlantic Magmatic Province. Science 284, 616–618.

Middleton, M., Keppie, J.D., Murphy, J.B., 2007. PTt constraints on exhumation following subduction in the Rheic Ocean from eclogitic rocks in the Acatlán Complex of southern México. The evolution of the Rheic Ocean: From Avalonian–Cadomian active margin to Alleghenian–Variscan collision: Geological Society of America Special Paper, 423, pp. 489–509.

Miller, C.F., Meschter Mc Dowell, S., Mapes, R.W., 2003. Hot or cold granites? Implications of zircon saturation temperatures and preservation of inheritance. Geology 31, 529–532.

Miller, B.V., Dostal, J., Keppie, J.D., 2007. Ordovician calc-alkaline granitoids in the Acatlán Complex, southern México: geochemical and geochronologic data and implications for the tectonics of the Gondwanan margin of the Rheic Ocean. In: Linnemann, U., Nance, R.D., Kraft, P., Zulauf, G. (Eds.), The evolution of the Rheic Ocean: From Avalonian–Cadomian active margin to Alleghenian–Variscan collision: Geological Society of America Special Paper, 423, pp. 465–475.

Morales-Gámez, M., Keppie, J.D., 2008. Ordovician–Silurian rift-passive margin on the Mexican margin of the Rheic Ocean overlain by Carboniferous–Permian periarc rocks: evidence from the eastern Acatlán Complex, southern Mexico. Tectonophysics 461, 291–310.

Morales-Gámez, M., Keppie, J.D., Dostal, J., 2009a. Carboniferous tholeiitic dikes in the Salada unit, Acatlán Complex, southern Mexico: a record of extension on the western margin of Pangea. Revista Mexicana de Ciencias Geológicas 133–142.

Morales-Gámez, M., Keppie, J.D., Lee, J.W.K., Ortega-Rivera, A., 2009b. Palaeozoic structures in the Xayacatlán area, Acatlán Complex, southern Mexico: transtensional rift- and subduction-related deformation along the margin of Oaxaquia. International Geology Review 51, 279–303.

Morán-Zenteno, D.J., Caballero-Miranda, C., Silva-Romo, G., Ortega-Guerrero, B., González-Torres, E., 1993. Jurassic–Cretaceous paleogeographic evolution of the northern Mixteca terrane, southern Mexico. Geofísica Internacional 32, 453–473.

Murphy, J.B., Nance, R.D., 2008. The Pangea conundrum. Geology 36, 703–706.

Murphy, J.B., Keppie, J.D., Nance, R.D., Miller, B.V., Dostal, J., Middleton, M., Fernández-Suárez, J., Jeffries, T.E., Storey, C.D., 2006. Geochemistry and U–Pb protolith ages of eclogitic rocks of the Asis Lithodeme, Piaxtla Suite, Acatlán Complex, southern Mexico: tectonothermal activity along the southern margin of the Rheic Ocean. Journal of the Geological Society of London 163, 683–695.

Murphy, J.B., Nance, R.D., Cawood, P.A., 2009. Contrasting modes of supercontinent formation and the conundrum of Pangea. Gondwana Research 15, 408–420.

Nance, R.D., Miller, B.V., Keppie, J.D., Murphy, J.B., Dostal, J., 2006a. The Acatlán Complex, southern Mexico: record of Pangea assembly to breakup. Geology 34, 857–860.

Nance, R.D., Miller, B.V., Keppie, J.D., Murphy, J.B., Dostal, J., 2006b. Comment on "U–Pb geochronology of the Acatlán Complex and implications for the Paleozoic paleogeography and tectonic evolution of southern Mexico" by O. Talavera-Mendoza, J. Ruiz, G.E. Gehrels, D.M. Meza-Figueroa, R. Vega-Granillo and M.F. Campa-Uranga [Earth Planet. Sci. Lett. 235 (2005) 682–699]. Earth and Planetary Science Letters, 245, pp. 471–475.

Ortega-Flores, B., Solari, L.A., Ortega-Obregón, C., 2012. Detrital zircon U–Pb geochronology of the Toliman sequences, central Mexico: possible provenance sources. Geological Society of America Cordilleran Section — 108th Annual Meeting (29–31 March 2012).

Ortega-Gutiérrez, F., 1975. The Pre-Mesozoic geology of the Acatlán area, south Mexico. Ph.D. thesis. University of Leeds. Leeds.

Ortega-Gutiérrez, F., 1978. Estratigrafía del Complejo Acatlán en la Mixteca Baja, Estados de Puebla y Oaxaca. Universidad Nacional Autónoma de México, Instituto de Geología Revista 2, 112–131.

Ortega-Gutiérrez, F., Elías-Herrera, M., 2003. Wholesale melting of the southern Mixteco terrane and origin of the Xolapa Complex. Geological Society of America Abstracts with Programs 35.

Ortega-Gutiérrez, F., Elías-Herrera, M., Reyes-Salas, M., Macías-Romo, C., López, R., 1999. Late Ordovician–Early Silurian continental collisional orogeny in southern Mexico and its bearing on Gondwana–Laurentia connections. Geology 27, 719–722.

Ortega-Obregón, C., Keppie, J.D., Murphy, J.B., Lee, J.W.K., Ortega-Rivera, A., 2009. Geology and geochronology of Paleozoic rocks in western Acatlán Complex, southern Mexico: evidence for contiguity across an extruded high-pressure belt and constraints on Paleozoic reconstructions. Geological Society of America Bulletin 121, 1678–1694.

Ortega-Obregón, C., Murphy, J.B., Keppie, J.D., 2010. Geochemistry and Sm–Nd isotopic systematics of Ediacaran–Ordovician, sedimentary and bimodal igneous rocks in the western Acatlán Complex, southern Mexico: evidence for rifting on the southern margin of the Rheic Ocean. Lithos 114, 155–167.

Ortega-Obregón, C., Solari, L.A., Ortega-Gutiérrez, F., Elías-Herrera, M., 2012. Arc-related intrusions in the Oaxacan Complex: evidence for Early to Late Permian Pacific plate subduction beneath the west central margin of Gondwana. Geological Society Cordilleran Section — 108th Annual Meeting (29–31 March 2012).

Pantoja-Alor, J., Gómez-Caballero, J., 2003. Geologic features and biostratigraphy of the Cretaceous of southwestern México (Guerrero Terrane). In: Alcayde, M., Gómez-Caballero, J. (Eds.), Geologic Transects across Cordilleran Mexico, Guidebook for the Field Trips of the 99th Geological Society of America Cordilleran Section Annual Meeting, Puerto Vallarta, Jalisco, Mexico, 4–7 April 2003. : Special Publication, 1. Universidad Nacional Autónoma de México, Instituto de Geología, pp. 229–260.

Pérez-Gutiérrez, R., Solari, L.A., Gómez-Tuena, A., Martens, U., 2009. Mesozoic geologic evolution of the Xolapa migmatitic complex north of Acapulco, southern Mexico: implications for paleogeographic reconstructions. Revista Mexicana de Ciencias Geológicas 26, 201–221.

Pimentel, M.M., Fuck, R.A., 1992. Neoproterozoic crustal accretion in central Brazil. Geology 20, 375–379.

Pimentel, M.M., Whitehouse, M.J., Viana, M.d.G., Fuck, R.A., Nuno, M., 1997. The Mara Rosa Arch in the Tocantins Province: further evidence for Neoproterozoic crustal accretion in Central Brazil. Precambrian Research 81, 299–310.

Pimentel, M.M., Fuck, R.A., Jost, H., Ferreira Filho, C., de Araujo, S., 2000. The basement of the Brasilia fold belt and the Goias magmatic arc. In: Cordani, U., Thomas Filho, A., Campos, D. (Eds.), Tectonic Evolution of South America. 31st International Geological Congress, Rio de Janeiro, Brasil, pp. 195–230.

Pindell, J.L., 1985. Alleghenian reconstruction and subsequent evolution of the Gulf of Mexico, Bahamas, and Proto-Caribbean. Tectonics 4, 1–39.

Poole, F.G., Perry Jr., W.J., Madrid, R.J., Amaya-Martínez, R., 2005. Tectonic synthesis of the Ouachita–Marathon–Sonora orogenic margin of southern Laurentia: stratigraphic and structural implications for timing of deformational events and plate-tectonic model. The Mojave–Sonora megashear hypothesis: development, assessment, and alternatives: Geological of Society of America Special Paper, 393, pp. 543–596.

Ramírez-Espinosa, J., 2001. Tectono-magmatic evolution of the Paleozoic Acatlán Complex in southern Mexico, and its correlation with the Appalachian system. Ph.D. thesis. University of Arizona. Tucson.

Ramos-Arias, M.A., Keppie, J.D., 2011. U–Pb Neoproterozoic–Ordovician protolith age constraints for high- to medium-pressure rocks thrust over low-grade metamorphic rocks in the Ixcamilpa area, Acatlán Complex, southern Mexico. Canadian Journal of Earth Sciences 48, 45–61.

Ramos-Arias, M.A., Keppie, J.D., Ortega-Rivera, A., Lee, J.W.K., 2008. Extensional Late Paleozoic deformation on the western margin of Pangea, Patlanoaya area, Acatlán Complex, southern Mexico. Tectonophysics 448, 60–76.

Ratschbacher, L., Riller, U., Meschede, M., Herrmann, U., Frisch, W., 1991. 2nd look at suspect terranes in southern Mexico. Geology 19, 1233–1236.

Ratschbacher, L., Franz, L., Min, M., Bachmann, R., Martens, U., Stanek, K.P., Stübner, K., Nelson, B.K., Herrmann, U., Weber, B., López-Martínez, M., Jonckheere, R., Sperner, B., Tichomirowa, M., McWilliams, M.O., Gordon, M., Meschede, M., Bock, P., 2009. The North American–Caribbean Plate boundary in Mexico–Guatemala–Honduras. Geological Society, London, Special Publications 328, 219–293.

Riller, U., Ratschbacher, L., Frisch, W., 1992. Left-lateral transtension along the Tierra Colorada deformation zone, northern margin of the Xolapa magmatic arc of southern Mexico. Journal of South American Earth Sciences 5, 237–249.

Roberts, N.M.W., 2012. Increased loss of continental crust during supercontinent amalgamation. Gondwana Research 21, 994–1000.

Rubatto, D., 2002. Zircon trace element geochemistry: partitioning with garnet and the link between U–Pb ages and metamorphism. Chemical Geology 184, 123–138.

Rubio-Cisneros, I.I., Lawton, T.F., 2011. Detrital zircon U–Pb ages of sandstones in continental red beds at Valle de Huizachal, Tamaulipas, NE Mexico: record of Early–Middle Jurassic arc volcanism and transition to crustal extension. Geosphere 7, 159–170.

Sawyer, E.W., 2008. Atlas of Migmatites. The Canadian Mineralogist Special Publication, vol. 9. Ottawa.

Schaaf, P., Morán-Zenteno, D.J., Hernández Bernal, M., Solís-Pichardo, G., Tolson, G., Kohler, H., 1995. Paleogene continental margin truncation in southwestern Mexico: geochronological evidence. Tectonics 14, 1339–1350.

Silva-Romo, G., Mendoza-Rosales, C.C., 2000. La unidad Piedra Hueca secuencia clástica paleozoica (sur de Puebla). GEOS, 2a Reunión Nacional de Ciencias de la Tierra, Unión Geofísica Mexicana, Resúmenes y Programa, p. 325.

Silva-Romo, G., Arellano-Gil, J., Mendoza-Rosales, C.C., Nieto-Obregón, J., 2000. A submarine fan in the Mesa Central, Mexico. Journal of South American Earth Sciences 13, 429–442.

Silva-Romo, G., Mendoza-Rosales, C.C., Campos-Madrigal, E., Centeno-García, E., 2011. Formación La Mora, unidad estratigráfica nueva del Triásico en el Terreno Mixteca (noroeste de Huajuapán de León, Oax., México): Sedimentología Y su significado. Simposio en Honor del Dr. Zoltan de Cserna, México, D.F. , pp. 114–115.

Sircombe, K.N., 2004. AgeDisplay: an EXCEL workbook to evaluate and display univariate geochronological data using binned frequency histograms and probability density distributions. Computers and Geosciences 30, 21–31.

Smith, A.G., Hallam, A., 1970. The fit of the southern continents. Nature 225, 139–144.

Solari, L.A., Dostal, J., Ortega-Gutiérrez, F., Keppie, J.D., 2001. The 275 Ma arc-related La Carbonera stock in the northern Oaxacan Complex of southern Mexico: U–Pb geochronology and geochemistry. Revista Mexicana de Ciencias Geológicas 18, 149–161.

Solari, L.A., Keppie, J.D., Ortega-Gutiérrez, F., Cameron, K.L., López, R., Hames, W., 2003. 990 and 1100 Ma Grenvillian tectonothermal events in the northern Oaxacan Complex, southern Mexico: roots of an orogen. Tectonophysics 365, 257–282.

Solari, L.A., de León, R.T., Pineda, G.H., Solé, J., Solís-Pichardo, G., Hernandez-Treviño, T., 2007. Tectonic significance of Cretaceous–Tertiary magmatic and structural evolution of the northern margin of the Xolapa Complex, Tierra Colorada area, southern Mexico. Geological Society of America Bulletin 119, 1265–1279.

Solari, L.A., Gómez-Tuena, A., Bernal, J., Pérez-Arvizu, O., Tanner, M., 2010a. U–Pb zircon geochronology with an integrated LA–ICPMS microanalytical workstation: achievements in precision and accuracy. Geostandards and Geoanalytical Research 34, 5–18.

Solari, L.A., Ortega-Gutiérrez, F., Elías-Herrera, M., Gómez-Tuena, A., Schaaf, P., 2010b. Refining the age of magmatism in the Altos Cuchumatanes, western Guatemala, by LA–ICPMS, and tectonic implications. International Geology Review 52, 977–998.

Steiner, M.B., Walker, J.D., 1996. Late Silurian plutons in Yucatan. Journal of Geophysical Research 101, 17727–17735.

Stewart, J.H., Blodgett, R.B., Boucot, A.J., Carter, J.L., López, R., 1999. Exotic Paleozoic strata of Gondwanan provenance near Ciudad Victoria, Tamaulipas, México. Laurentia–Gondwana Connections before Pangea: Geological Society of America Special Paper, 336, pp. 1–26. Boulder, CO.

Sun, S.S., McDonough, W., 1989. Chemical and isotopic systematics of oceanic basalts: implications for mantle composition and processes. In: Saunders, A., Norry, M. (Eds.), Magmatism in the Ocean Basins: Geological Society Special Publication, 42, pp. 313–345.

Talavera-Mendoza, O., Ruiz, J., Gehrels, G.E., Meza-Figueroa, D., Vega-Granillo, R., Campa-Uranga, M.F., 2005. U–Pb geochronology of the Acatlán Complex and implications for the Paleozoic paleogeography and tectonic evolution of southern Mexico. Earth and Planetary Science Letters 235, 682–699.

Talavera-Mendoza, O., Ruiz, J., Gehrels, G.E., Valencia, V.A., Centeno-García, E., 2007. Detrital zircon U/Pb geochronology of southern Guerrero and western Mixteca arc successions (southern Mexico): new insights for the tectonic evolution of southwestern North America during the late Mesozoic. Geological Society of America Bulletin 119, 1052–1065.

Tera, F., Wasserburg, G., 1972. U–Th–Pb systematics in three Apollo 14 basalts and the problem of initial Pb in lunar rocks. Earth and Planetary Science Letters 14, 281–304.

Tolson, G., 2005. La falla Chacalapa en el sur de Oaxaca. Boletín de la Sociedad Geológica Mexicana 57, 111–122.

Torres, R., Ruiz, J., Patchett, P.J., 1999. Permo–Triassic continental arc in eastern Mexico: tectonic implications for reconstructions of southern North America. Geological Society of America Special Paper 340, 191–196.

Van der Voo, R., French, R., 1974. Apparent polar wandering for the Atlantic-bordering continents: Late Carboniferous to Eocene. Earth-Science Reviews 10, 99–119.

Vega-Carrillo, J.d.J., Elías-Herrera, M., Ortega-Gutiérrez, F., 1998. Complejo plutónico de Cuanana: Basamento prejurásico en el borde meridional del terreno Mixteco e interpretación litotectónica. Reunión Nacional de Ciencias de la Tierra, Soc. Geol. Mex, p. 145.

Vega-Granillo, R., Talavera-Mendoza, O., Meza-Figueroa, D., Ruiz, J., Gehrels, G.E., López-Martínez, M., 2007. Pressure–temperature–time evolution of Paleozoic high-pressure rocks of the Acatlán Complex (southern Mexico): implications for the evolution of the Iapetus and Rheic Oceans. Geological Society of America Bulletin 119, 1249–1264.

Vega-Granillo, R., Meza-Figueroa, D., Ruiz, J., Talavera-Mendoza, O., López-Martínez, M., 2009a. Structural and tectonic evolution of the Acatlán Complex, southern Mexico: its role in the collisional history of Laurentia and Gondwana. Tectonics 28, 1–25.

Vega-Granillo, R., Talavera-Mendoza, O., Meza-Figueroa, D., Ruiz, J., López-Martínez, M., Gehrels, G.E., 2009b. Pressure–temperature–time evolution of high-pressure rocks of the Acatlán Complex (southern Mexico): implications for the evolution of the Iapetus and Rheic Oceans: reply. Geological Society of America Bulletin 121, 1460–1464.

Venegas-Rodríguez, G., 2009. Geocronología de circones detríticos en capas del Jurásico Inferior de las áreas de la Sierra de Catorce y El Alamito en el estado de San Luis Potosí. Revista Mexicana de Ciencias Geológicas 26, 466–481.

von Huene, R., Scholl, D., 1991. Observations at convergent margins concerning sediment subduction, subduction erosion, and the growth of continental crust. Reviews of Geophysics 29, 279–316.

Walker, J., Geissman, J.W., 2009. 2009 geologic time scale. Atlantic 19 22967-22967.

Weber, B., Iriondo, A., Premo, W.R., Hecht, L., Schaaf, P., 2007. New insights into the history and origin of the southern Maya block, SE Mexico: U–Pb-SHRIMP zircon geochronology from metamorphic rocks of the Chiapas massif. International Journal of Earth Sciences 96, 253–269.

Wheeler, J., Butler, R., Freeman, S., Inger, S., Pickles, C., 2003. Kinematic reworking and exhumation within the convergent Alpine Orogen. Tectonophysics 365, 77–102.

Whitney, D.L., Evans, B., 2009. Abbreviations for names of rock-forming minerals. American Mineralogist 95, 185–187.

Yáñez, P., Patchett, P.J., Ortega-Gutiérrez, F., Gehrels, G.E., 1991. Isotopic studies of the Acatlán Complex, southern Mexico: implications for Paleozoic North American tectonics. Geological Society of America Bulletin 103, 817–828.

3

GEOQUÍMICA Y ESTUDIOS ISOTÓPICOS DE SM–ND DE LOS PROTOLITOS METASEDIMENTARIOS Y MÁFICOS

Helbig, M., Keppie, J.D., Murphy, J.B., y Solari, L.A. Exotic rifted passive margin of a back-arc basin off western Pangea: geochemical evidence from the Early Mesozoic Ayú Complex, southern Mexico. *International Geology Review* (2013)

CONTRIBUCIONES DE COAUTORES:

- **Maria Helbig:** Concepto y plan del proyecto, trabajo de campo y laboratorio incluso mapeo, y muestreo, interpretación de datos, borrador de un modelo, redacción del artículo
- **J. Duncan Keppie:** Concepto y plan del proyecto, supervisión/asistencia para el trabajo del campo, desarrollar un modelo, revisión del borrador del artículo
- **J. Brendan Murphy:** Asistencia en el campo (muestreo), participación en interpretar los datos, revisión del artículo, financiamiento
- **Luigi A. Solari:** revisión del artículo

International Geology Review
i*First*, 2012, 1–19

Exotic rifted passive margin of a back-arc basin off western Pangea: geochemical evidence from the Early Mesozoic Ayú Complex, southern Mexico

Maria Helbig[a]*, J. Duncan Keppie[b], J. Brendan Murphy[c] and Luigi A. Solari[a]

[a]*Centro de Geociencias, Universidad Nacional Autónoma de México, Querétaro, Mexico;* [b]*Departamento de Geología Regional, Instituto de Geología, Universidad Nacional Autónoma de México, México D.F., Mexico;* [c]*Department of Earth Sciences, St. Francis Xavier University, Antigonish, Nova Scotia B2G 2W5, Canada*

(*Accepted 2 November 2012*)

Recent detrital zircon studies of metamorphosed and polydeformed rocks of the early Mesozoic Ayú Complex in southern Mexico suggest an allochthonous origin along the western Pangean margin. Bulk-rock geochemistry of the ca. 170–200 Ma ortho-amphibolites suggests a composition ranging from alkalic and transitional basalts to normalized mid-ocean ridge basalt (N-MORB) tholeiites. Rare earth element (REE) patterns of alkaline basalts (Group I) are characterized by steep negative slopes, whereas transitional basalts (Group II) show moderate light REE (LREE) enrichment. Subalkalic Group III displays slight LREE enrichment and Group IV has relatively flat REE patterns with slight depletion in LREEs. Multiple trace element plots of Group III–IV amphibolites reveal strongly negative Nb–Ta anomalies caused by subduction zone contamination. Initial ε_{Nd} values ($t = 190$ Ma) of the amphibolites range from +9.01 to –2.16. Alkalic basalts have negative ε_{Nd} values, suggesting derivation from an older subcontinental mantle source ($T_{DM} = 877$ and 791 Ma). Group II–IV amphibolites have positive ε_{Nd} values ranging from +2.31 to +9.01, indicating a transition from an older to a relatively juvenile mantle source that is typical of a back-arc setting. The geochemistry of the metasedimentary rocks suggests derivation from an acid-arc source. Chondrite-normalized REE patterns are characterized by enriched LREEs, flat HREE, and negative Eu anomalies. Sm–Nd systematics indicate that most samples were derived from cratonic basement and plot within the Oaxacan Complex envelope with ε_{Nd} values ($t = 195$ Ma) ranging from –5.53 to –7.65. We interpret two samples with higher ε_{Nd} values (–1.42 and +1.06) to reflect the additional influence of a more juvenile component. The amphibolites and metasedimentary rocks of the Ayú Complex document back-arc activity and are inferred to be correlative with various western Mexican Triassic–Jurassic mafic suites and the Potosí fan that formed along the western rifted margin of Pangea.

Keywords: Triassic; southern Mexico; amphibolites; back-arc basin; Pangea break-up

1. Introduction

Although there is a general consensus of a Pangea-A configuration at the time of supercontinent break-up (e.g. see Domeier *et al.* 2012), there is still considerable controversy about the Middle American palaeogeography within that configuration (Weber *et al.* 2007; Vega-Granillo *et al.* 2009; Keppie and Keppie 2012). Resolving this controversy is important to provide a basis for understanding the geodynamics of the amalgamation and break-up of Pangea. During the Triassic, many authors (Elías-Herrera and Ortega-Gutiérrez 2002; Keppie 2004; Centeno-García 2005; Weber *et al.* 2007; Keppie *et al.* 2008, 2010; Keppie and Keppie 2012) locate the Mixteca and Oaxaquia terranes of southern Mexico along the western margin of central Pangea-A, between Laurentia and Amazonia, flanked to the west by the palaeo-Pacific subduction zone and to the east by rifts associated with the opening of the Gulf of Mexico (Marzoli *et al.* 1999; Figure 1A). In contrast, Talavera-Mendoza *et al.* (2005) and Vega-Granillo *et al.* (2007, 2009) proposed that the Oaxaquia and Mixteca terranes lay within the Ouachitan orogen between the Maya terrane and Laurentia (Figure 1B). In both reconstructions, during the Triassic, the western margin of Pangea was occupied by the Mesa Central (Central terrane), which is interpreted to be the Triassic basement of the Guerrero composite terrane (Centeno-García 2008; Figure 2A). Furthermore, the Chortís block has been reconstructed as either off southwestern Mexico (Pacific model: e.g. Ross and Scotese 1988; Dickinson and Lawton 2001; Rogers *et al.* 2007; Silva-Romo 2008; Pindell *et al.* 2012; Figure 1C) or along the western side of the Gulf of Mexico (Keppie and Keppie 2012; Figure 1D).

Recently published geochronological data bearing on Mexican palaeogeograhy led Helbig *et al.* (2012) to suggest that the Early Mesozoic Ayú Complex of southern Mexico is an exotic slice of the western Pangean continental margin

*Corresponding author. Email: maria.helbig@gmail.com

ISSN 0020-6814 print/ISSN 1938-2839 online

http://dx.doi.org/10.1080/00206814.2012.751171
http://www.tandfonline.com

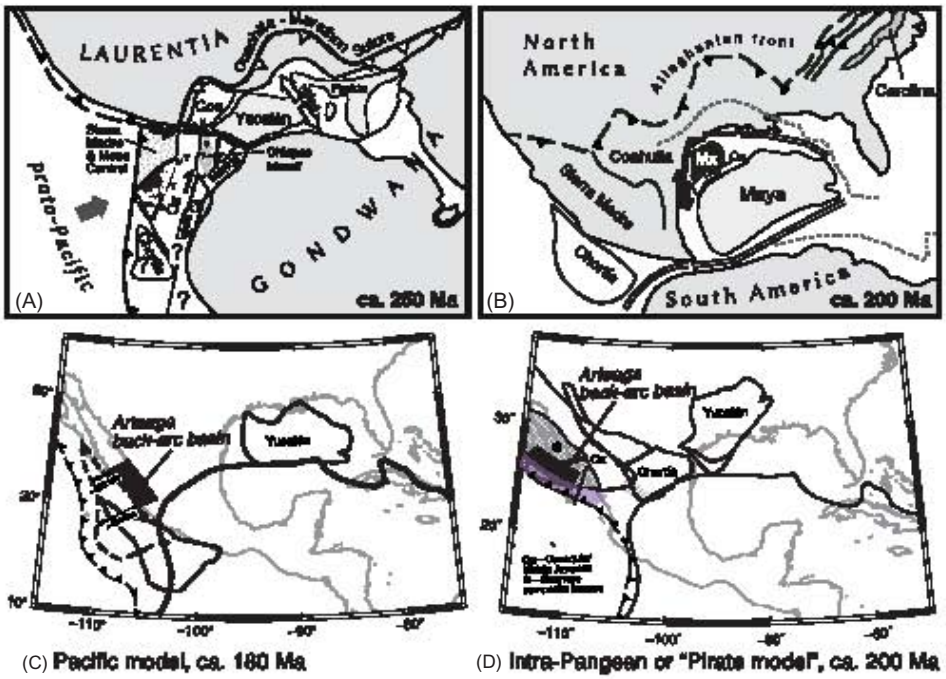

Figure 1. (A)–(B) Early Mesozoic Pangea-A reconstructions for the Middle American terranes: (A) the Acatlán Complex (Ac) and Oaxaquia (Ox) are placed on the western margin of Pangea, V – position of the Permian–Triassic arc, Coa – Coahuila, and CA – Colombian Andes (after Elías-Herrera and Ortega-Gutiérrez 2002; Keppie 2004; Centeno-García 2005; Weber *et al.* 2007); (B) Vega-Granillo *et al.* (2009) places the Mixteca (Mx) and Oaxaquia (Ox) terranes within the Ouachitan collisional zone, between the Maya block and southern North America. (C)–(D) Relevant reconstructions for the palaeogeography of the western margin of Middle America: (C) Pacific model representative for all model variants that place the Chortís block off southern Mexico (Wilson 1966; Pindell and Dewey 1982; Pindell 1985; Ross and Scotese 1988; Dickinson and Lawton 2001; Pindell *et al.* 2006; Rogers *et al.* 2007; Silva-Romo 2008; Pindell *et al.* 2012). Chortís block outline after Ross and Scotese (1988), dashed outline avoids overlap with South America and implies a more northern position. (D) Intra-Pangean or 'Pirate' model suggested by Keppie and Keppie (2012). Both reconstructions modified after Keppie and Keppie (2012). Purple shaded area: possible Late Triassic arc position.

that was tectonically emplaced into the Palaeozoic Acatlán Complex during the initial stages of Pangea break-up. Detrital zircon data of metamorphosed siliciclastic rocks (Chazumba Lithodeme) constrain deposition within ca. 200 and 170 Ma (Figures 2B and 3; Helbig *et al.* 2012) and suggest that the protoliths may be correlative with the extensive Triassic/Early Jurassic turbiditic Potosí fan in the Central terrane (Figure 2B) that was deposited into the Arteaga basin that lay along the western margin of continental Mexico (Centeno-García *et al.* 1993; Centeno-García and Silva-Romo 1997; Silva-Romo *et al.* 2000; Centeno-García 2005, 2008). In addition to a voluminous turbidite succession, the Chazumba Lithodeme is characterized by boudinaged amphibolites, which are potentially correlative with the mafic rocks of the Arteaga basin. However, there are no geochemical data for the metasedimentary and amphibolitic rocks of the Chazumba Lithodeme, which would test this correlation. A critical test of this hypothesis is the geochemistry of the mafic and metasedimentary rocks of the Ayú Complex that will allow comparison with autochthonous Pangean marginal rocks and the determination of their tectonic setting.

In this article, we present major and trace element geochemistry as well as Sm–Nd isotopic data for the amphibolitic and metasedimentary rocks of the Chazumba Lithodeme in order to describe their petrogenetic evolution and tectonic setting. This is followed by a critical assessment of the comparison between the Chazumba Lithodeme and the autochthonous Potosí fan and its implications for the palaeogeography of Middle America in the early Mesozoic.

2. Geologic setting

South-central Mexico is partly underlain by the Palaeozoic Acatlán Complex, which forms the Mixteca terrane (Figure 2B; Ortega-Gutiérrez 1975, 1978; Keppie *et al.* 2008; and references therein). To the east, the Acatlán Complex is tectonically juxtaposed against the ca. 1–1.4 Ga Oaxacan Complex along the 276 Ma dextral transcurrent Caltepec fault zone (Figure 2B; Elías-Herrera and Ortega-Gutiérrez 2002). Both the Acatlán and Oaxacan complexes are unconformably overlain by upper Permian to Middle Jurassic unmetamorphosed continental redbeds,

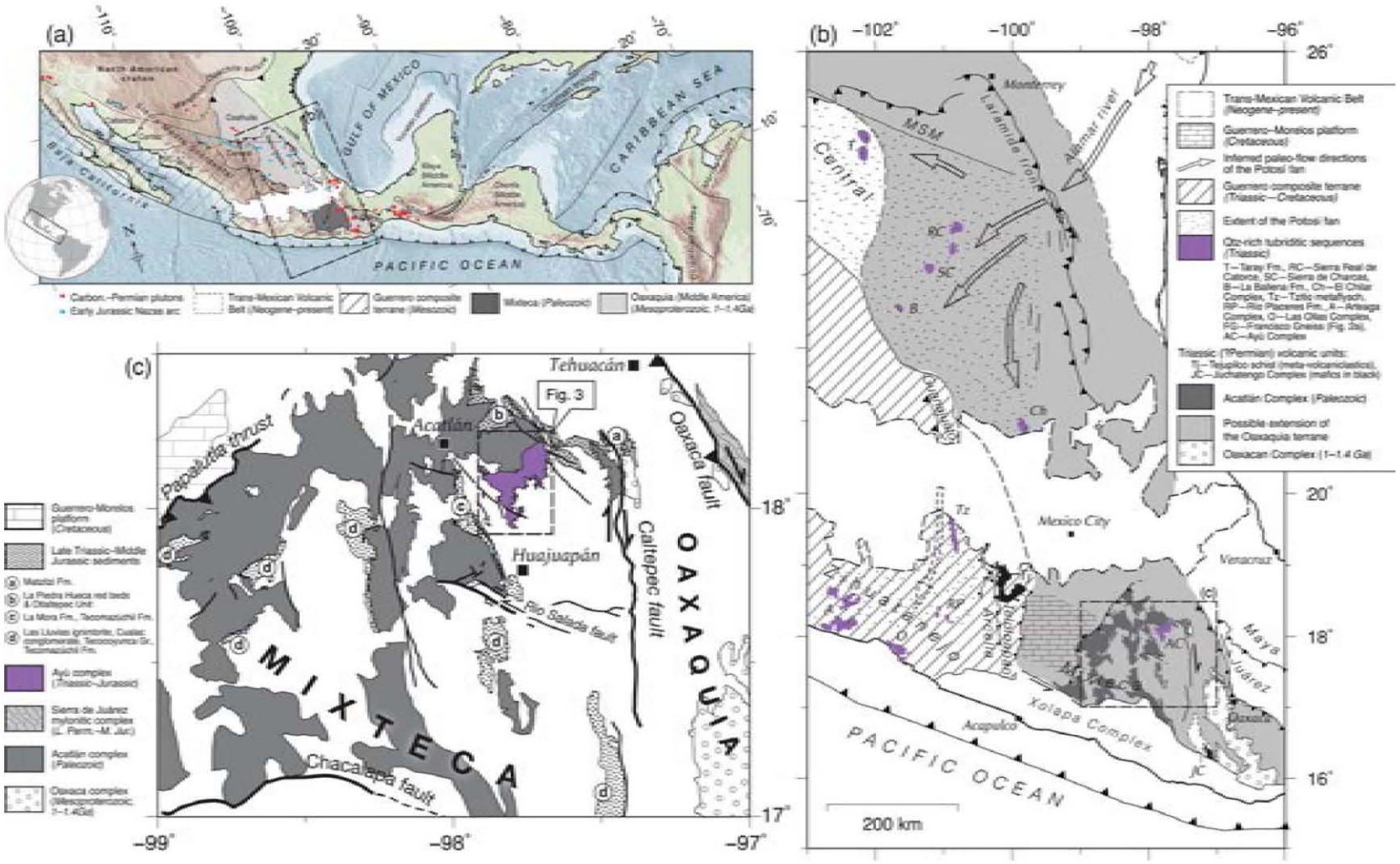

Figure 2. (A) Main tectono-stratigraphic terranes and geologic provinces of Middle America. Basement rocks: Oaxaquia (light grey) and Mixteca terrane (dark grey) after Keppie (2004); Dowe *et al.* (2005). MSM – Mojave-Sonora megashear. The Mesozoic Guerrero composite terrane (striped area) comprises the Tahué, the Zihuatanejo, the Guanajuato, the Arcelia, and the Teloloapán terranes (after Keppie 2004; Centeno-García 2008). Trans-Mexican Volcanic belt (from Ferrari 2004). (B) Geological map of central southern Mexico. Purple areas inidicate locations of Triassic–Lower Jurassic deep marine facies in central and southwestern Mexico. (C) Pre-Cenozoic units of southern-central Mexico: Oaxacan Complex (circles) is juxtaposed against the Acatlán Complex (dark grey) along the Permian dextral transpressional Caltepec Fault. Purple area represents rocks of the Early Mesozoic Ayú Complex (see also Figure 3). Stippled areas are unmetamorphosed Lower–Middle Jurassic continental sedimentary rocks. Letters refer to unit names given in the respective legend.

siliciclastic fluvial deposits, and shallow marine shelf strata, which characterize the Early Mesozoic continental margin of southern Mexico (Caballero-Miranda *et al.* 1990; Morán-Zenteno *et al.* 1993; Silva-Romo and Mendoza-Rosales 2000; Centeno-García *et al.* 2009; Elías-Herrera *et al.* 2011; Rubio-Cisneros and Lawton 2011; Silva-Romo *et al.* 2011).

To the west, the Acatlán Complex is thrust over Cretaceous limestones of the Guerrero-Morelos platform along the Upper Cretaceous–Palaeocene Papalutla fault (Figure 2B; Cerca *et al.* 2007; Ramos-Arias and Keppie 2011). To the west of the Guerrero-Morelos platform lies the Mesozoic Guerrero composite terrane (Figures 2A and 2B), which occupies most of western Mexico and consists of various subterranes (Tahué, Guanajuato, Zihuatanejo, Arcelia, and Teloloapan terranes; Centeno-García, 2008). The Guerrero composite terrane is characterized by submarine and sparse, subaerial volcanic and sedimentary successions of Upper Jurassic (Tithonian) to middle Upper Cretaceous (Cenomanian) age, which are interpreted as parts of a volcanic arc complex involved in several episodes of accretion and rifting, and eventual collision with Oaxaquia (Centeno-García 2008; Martini *et al.* 2011). Between the Guerrero composite terrane and the northern continuation of Oaxaquia (Figures 2A and 2B), the Mesa Central plateau forms the Central terrane. The oldest rocks in the Central terrane are made up of a deformed Late Triassic deep-marine siliciclastic succession (Taray Formation: Díaz-Salgado *et al.* 2003; Anderson *et al.* 2005; Centeno-García 2005, 2008). These turbidites formed parts of a submarine fan system (Ballena Formation: Centeno-García and Silva-Romo 1997; Silva-Romo *et al.* 2000; Centeno-García 2005; Barboza-Gudiño *et al.* 2008, 2010), called the Potosí fan, that was fed by an extensive river system (Alamar Formation: Barboza-Gudiño *et al.* 2010; Figure 2B). Distal parts of the Potosí fan are inferred to overlie oceanic crust of the Arteaga Complex, suggesting deposition along a rifted passive margin (Centeno-García 2008; Martini *et al.* 2009). Rifting in the Late Permian–Triassic has further been documented in the Tahué terrane (Francisco Gneiss, Sonobari Complex; Keppie *et al.* 2006a) and in the Juchatengo Complex (Grajales-Nishimura *et al.* 1999, Figures 2A and 2B) and suggests widespread crustal extension along the western margin of Oaxaquia. Rocks of the Potosí fan were subsequently deformed during inferred east-vergent subduction of palaeo-Pacific oceanic lithosphere in the Early Jurassic and incorporated into a subduction-related accretionary complex (Centeno-García 2008). Synchronously, the ca. 187 Ma syntectonic intrusions of peraluminous granites record the collision of the Guerrero composite terrane with the Mixteca/Oaxaquia terranes and resulted in intense deformation of the Triassic Tejupilco volcanogenic rocks (Elías-Herrera *et al.* 2000, 2003).

2.1. Ayú Complex

The Ayú Complex comprises Triassic–Jurassic polydeformed metasedimentary and igneous rocks (Figure 3; Helbig *et al.* 2012) that crop out west of the Caltepec fault zone and south of the eastern Acatlán Complex in a horst bounded by Upper Triassic–Jurassic redbeds, Cretaceous limestones (Morán-Zenteno *et al.* 1993; Silva-Romo and Mendoza-Rosales 2000; Silva-Romo *et al.* 2011), and unconformably overlying Cenozoic volcanic rocks (Figure 2C). All units of the Ayú Complex and their field relationships are described in detail in Helbig *et al.* (2012) and are summarized here.

The Ayú Complex includes the Triassic/Early Jurassic Chazumba Lithodeme, a voluminous poly-deformed and metamorphosed turbiditic siliciclastic sequence consisting of micaceous pelites, intercalated with massive metapsammites, metagreywackes, and amphibolites (Ortega-Gutiérrez 1978; Keppie *et al.* 2006b). The metasedimentary rocks are mainly composed of garnet–biotite(–muscovite) schists and gneisses. Amphibolites consist of calcic hornblende, plagioclase, quartz, biotite, garnet, and epidote and occur as intercalated boudins or pinch-and-swell structures.

In the southern part of the Ayú Complex, the metasedimentary rocks and amphibolites underwent partial melting at 171 ± 1 Ma (Magdalena Migmatite; U–Pb concordant zircon age: Keppie *et al.* 2004), an event that was accompanied by coeval intrusions of dioritic, granodioritic, granitic, pegmatitic, as well as leucogranitic sheets and dikes (San Miguel intrusives: Yáñez *et al.* 1991; Ortega-Gutiérrez *et al.* 1999; Keppie *et al.* 2004; Helbig *et al.* 2012). Combined with the maximum age of deposition for the metasedimentary rocks (Helbig *et al.* 2012), the age of the amphibolites is inferred to be ca. 195–170 Ma.

At its northern margin, the metasedimentary rocks of the Chazumba Lithodeme are truncated by the NE-dipping Providencia shear zone (Figure 3). The Devonian–Carboniferous Cosoltepec Formation (Talavera-Mendoza *et al.* 2005), the Permian Tecomate Formation, and the Carboniferous–Permian Totoltepec pluton are exposed in the hanging wall of this shear zone (Malone *et al.* 2002; Keppie *et al.* 2004; Kirsch *et al.* 2012a).

3. Methodology

Twenty-four amphibolite samples and thirty-eight metasedimentary rocks were collected and analysed by X-ray fluorescence for major and certain trace elements (V, Cr, Co, Ni, Cu, Zn, Ga, Rb, Sr, Y, Zr, Nb, Ba, Pb, Th, U) at the Regional Geochemical Centre, St. Mary's University, Canada (analytical methods described after Dostal *et al.* 1994). From these samples, 12 amphibolites and 23 metasedimentary rocks were selected for additional trace element (Y, Zr, Nb, Ba, Hf, Ta, Th) and rare earth element (REE) analyses by ICP-MS at Memorial University,

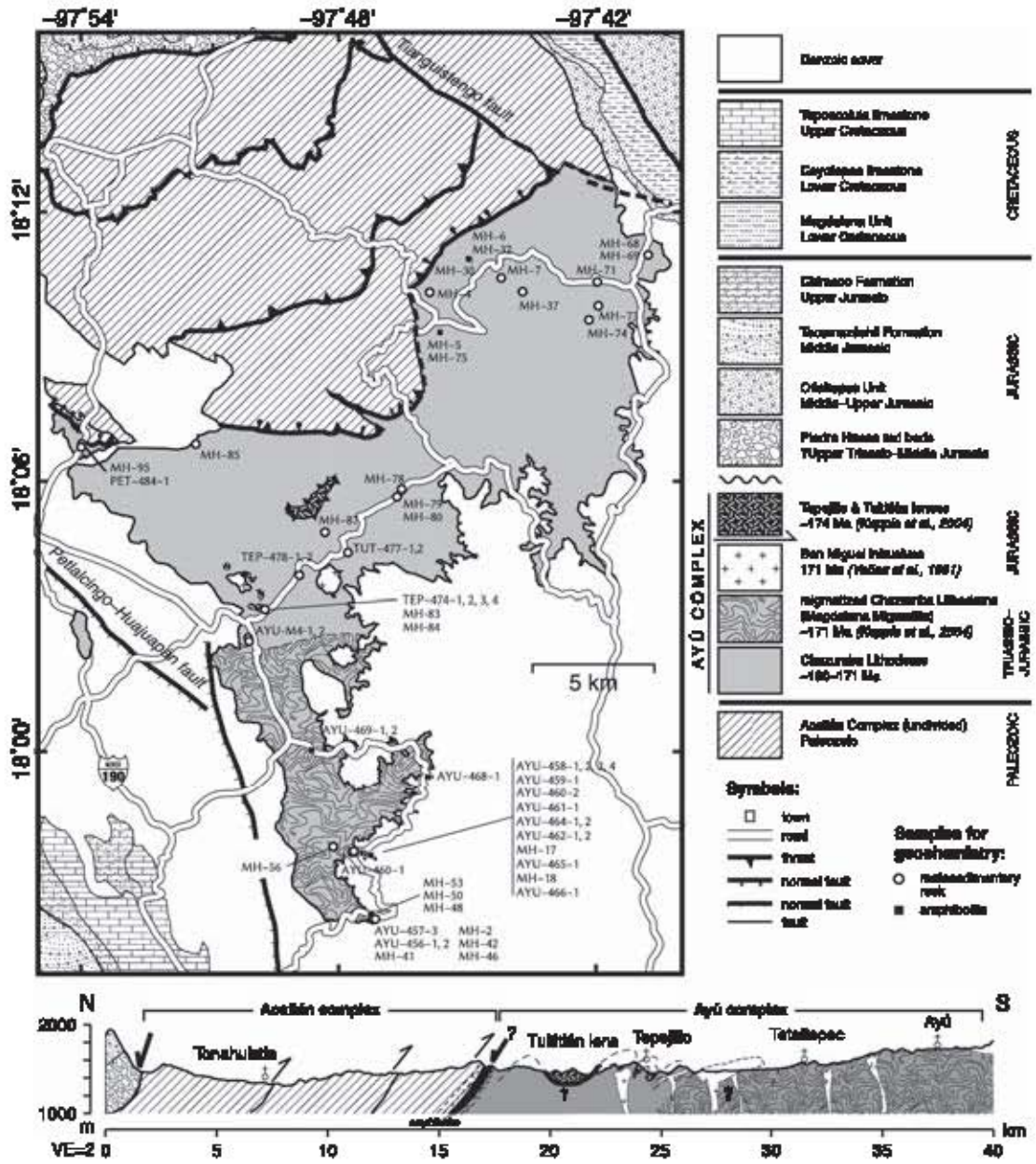

Figure 3. Geological map of the Ayú Complex and Permian–Triassic arc assemblages of the Acatlán Complex to the north. Sampling locations for major and trace element geochemistry as well as Sm–Nd isotopic analyses are plotted as filled squares (amphibolites), filled circles (pelites), and empty circles (psammites). A simplified N–S cross-section with a vertical scale of 2 is drawn below.

Newfoundland (according to methods described in Jenner *et al.* 1990). Ten amphibolite and seven metasedimentary samples, respectively, were then chosen for Sm–Nd isotopic analyses carried out at Atlantic Universities Regional Isotopic Facility (AURIF), Memorial University, Newfoundland, Canada (Kerr *et al.* 1995). Details of the analytical methods are given in the online supplementary document, DR-1. Sampling locations are listed in Table DR-2. The XRF and ICP-MS analyses and the Sm–Nd isotopic data are presented in Tables DR-3, DR-4, and DR-5, respectively (online supplementary files DR-1, DR-2, DR-3, DR-4, and DR-5 can be found at http://dx.doi.org/10.1080/00206814.2012.751171).

4. Results

The geochemical data show that the rocks have been affected by varying degrees of secondary alteration such as low- to high-grade metamorphism and weathering. This alteration primarily influenced the alkali and alkaline earth element concentrations and is reflected by the loss on ignition (LOI). The LOI ranges between 0.50 and 2.69 for all

amphibolites (Table DR-2) and between 0.59 and 5.18 for the metasedimentary rocks (Table DR-3). Most inferences about the petrogenesis of the rocks will be based on the abundances of high-field strength elements (HFSEs) and REEs that are considered relatively immobile during secondary processes, and should therefore preserve the original geochemical characteristics of the studied rocks (Winchester and Floyd 1977; Taylor and McLennan 1985).

4.1. Amphibolites

The amphibolitic rocks have SiO_2 contents ranging between 44.7 and 56.2 wt% (LOI-free) and display relatively wide ranges of TiO_2 (1.1–3.8 wt%), FeO_t (11.2–15.8 wt%), MgO (4.7–11.1 wt%), P_2O_5 (0.1–0.7 wt%), V (199–418 ppm), Cr (16–1632 ppm), Ni (11–503 ppm), Y (18–34 ppm), and Zr (75–449 ppm) (Table DR-2). The Zr/TiO_2 vs. Ni diagram indicates that the amphibolites have an igneous protolith (Figure 4A). The low Nb/Y (0.083–0.395) ratios of most of the amphibolites are typical of subalkaline basalts (Figure 4B), although the high Nb/Y ratios (Nb/Y = 2.1–2.2) of two samples (AYU-462-1 and AYU-462-2) are characteristic of alkalic basalt suites, and six samples straddle the boundary between the subalkaline and the alkaline fields (MH-48, AYU-458-1, AYU-458-2, AYU-459-1, AYU-468-1, and AYU-460-2; Nb/Y = 0.7–0.8). The subalkalic rocks display a strong positive correlation between TiO_2 and FeO_t/MgO ($r = 0.25$) and is indicative of enrichment of these elements during fractionation, which is consistent with tholeiitic trends, whereas the transitional to alkalic basalts plot above the typical trend (Figure 4C).

The chondrite-normalized REE patterns display a wide variation characterized by either (1) enrichment of light REEs (LREEs) with steep negative slopes or (2) relatively flat patterns (Figure 5A) and are subdivided into four groups. Two alkalic amphibolite samples (AYU-462-1 and AYU-462-2; Group I) are characterized by steep negative slopes with $(La/Yb)_N = 16.0–17.4$ and $(La/Sm)_N = 3.7–4.0$ and $La_N = 247–275$ and $Yb_N = 15–16$ times chondrite and high $\Sigma REE = 111.4–120.2$ppm. Three transitional samples (MH-48, AYU-458-2, AYU-460-2; Group II) show moderate LREE enrichment with slopes characterized by $(La/Yb)_N = 3.9–5.2$, $(La/Sm)_N = 1.8–2.7$ (Figure 5A), and $\Sigma REE = 43.7–49.9$ ppm. One transitional sample (AYU-460-2) has a flat HREE pattern ($Gd/Yb_N = 1.1$). Subalkalic samples MH-30, MH-32, AYU-464-1, and AYU-466-1 (Group III, Figure 5A) display slight LREE enrichment with $(La/Yb)_N = 1.5–3.4$, $(La/Sm)_N = 1.0–1.5$, and $\Sigma REE = 23.3–32.3$ ppm. MH-17, MH-18, MH-75, and AYU-469-2 (Group IV, Figure 5A) have REE patterns that are relatively flat with slight depletion in LREEs with $(La/Yb)_N = 0.8–1.2$ and $(La/Sm)_N = 0.8–0.9$ and have low $\Sigma REE = 16.2–18.6$ ppm. The LREE enrichment in Groups I and II are consistent with melting of a garnet lherzolite mantle source, which together with the within-plate alkalic signature supports the existence of thick continental lithosphere. In contrast, the flat REE profiles of Groups III and IV are typical of melting of a relatively shallow spinel lherzolite mantle.

Normalized mid-ocean ridge basalt (N-MORB)-normalized trace element abundances of the amphibolites also show a wide variation from smooth negative trends to very jagged patterns (Figure 5B). Group I amphibolites display smooth negative trends with enrichment of the large ion lithophile elements (LILEs) over the HFSEs (Figure 5B). Group I samples are characterized by a negative Sr and a positive Ti anomaly. Abundances of Y, Yb, and Lu are similar to N-MORB. Group II is characterized by elevated LILEs and positive U and Pb anomalies. A positive Ti anomaly is present in two samples (MH-48 and AYU-458-2), whereas AYU-460-2 shows a negative Ti anomaly and has a flat section through Dy, Y, Yb, and Lu that are similar to N-MORB (Figure 5B).

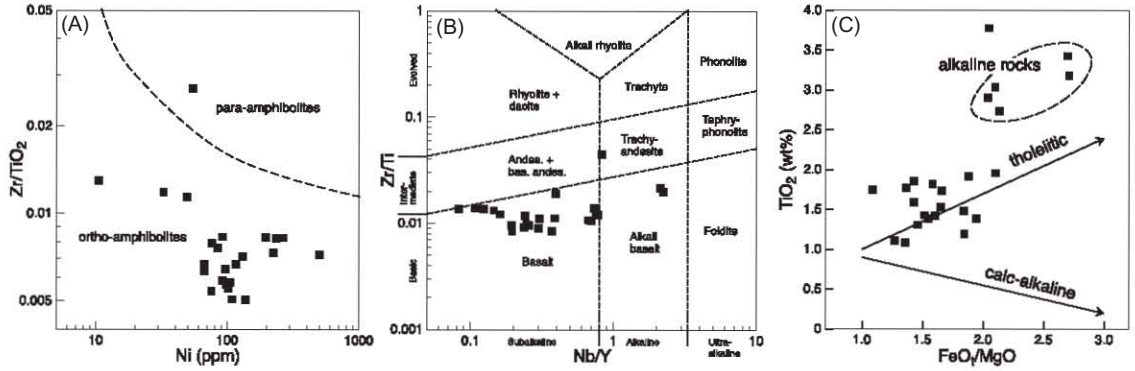

Figure 4. Plots for amphibolites: (A) Zr/TiO_2 vs. Ni diagram after Winchester and Max (1982), classification diagrams for igneous rocks after Winchester and Floyd (1977) (B) and Pearce (1996) (C), and (D) TiO_2 vs. FeO_t/MgO diagram distinguishing calc-alkaline and tholeiitic trends after Miyashiro (1974).

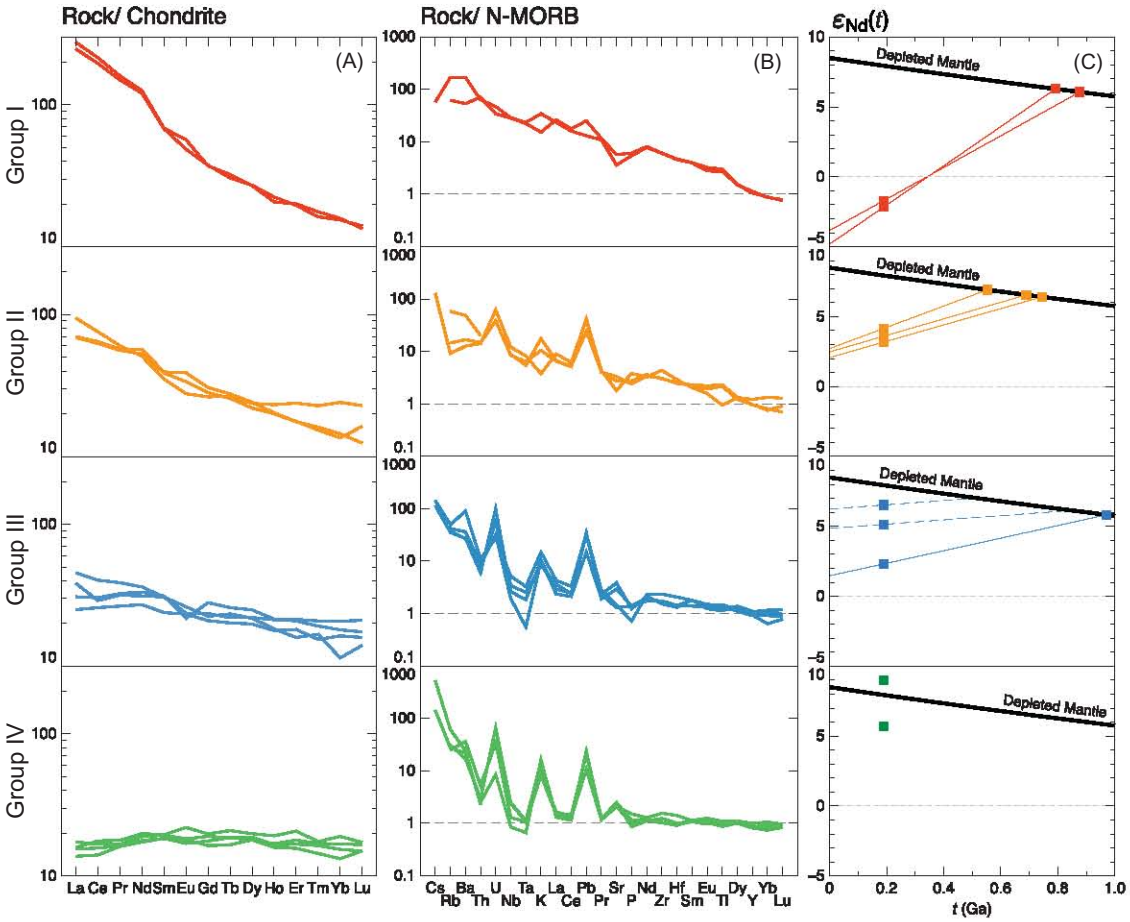

Figure 5. (A) Chondrite- and (B) N-MORB-normalized REE and trace element patterns for the amphibolitic rocks (normalizing values after Sun and McDonough 1989). Amphibolites are grouped into four different suites, I (red), II (orange), III (blue), and IV (green). (C) $\varepsilon_{Nd}(t)$ vs. time for each amphibolite group, initial ε_{Nd} for $t = 190$ Ma, evolution curves in bold lines for $^{147}Sm/^{144}Nd < 0.165$ (Stern, 2002), dashed lines for $^{147}Sm/^{144}Nd \approx 0.185$, Group IV amphibolites with $^{147}Sm/^{144}Nd >> 0.165$ yielded no significant Sm/Nd evolution curves. Depleted mantle curve from DePaolo (1988).

Group III shows well-defined zig-zag patterns that are distinguished by negative anomalies of Th, Nb, Ta, La, and Ce. Abundances of Nd, Zr, Hf, the middle REEs, and the HREEs have slight negative trends similar to N-MORB (Figure 5B). Amphibolites of Group IV are characterized by a negative Th anomaly and deep Nb–Ta and La–Ce troughs and abundances of most HFSEs being similar to N-MORB (Figure 5B).

HFS elemental plots (e.g. Figure 6) generally distinguish the amphibolites as either within-plate basalts (WPBs) or plate-margin basalts. Groups I and II and samples (similar to Group II) AYU-458-1, AYU-459-1, and AYU-468-1 are characterized by relatively high Zr/Y, Ti, and Ti/Y ratios, which is a characteristic of WPBs (Figures 6A–6D; Pearce 1996). Group III and IV amphibolites with relatively low Zr/Y, Ti/Y, and Nb/Y ratios, in combination with the strong positive correlation between TiO_2 and FeO_t/MgO (Figure 4C), suggests that these amphibolites are predominantly sub-alkaline tholeiites of either MOR or volcanic arc affinity (Figures 6A–6D). However, the high Ti–Cr abundances are indicative of an ocean-floor setting (Pearce 1975).

Cr–Y abundances of Group I plot within the overlapping volcanic arc basalt (VAB) and WPB fields (Figure 7A). The high Y and low Cr contents suggest that the mantle source for these rocks underwent minor partial melting followed by major fractionation of mafic phases. Group II amphibolites have also relatively low Cr contents and plot within the range of Group I and III–IV amphibolites. Group III–IV amphibolites are typical of either MORB or WPBs (Figure 7A). Using Cr as a fractionation index, the subvertical trend of Group III–IV amphibolites is consistent with the partitioning of Cr into early crystallizing mafic phases, such as olivine, Cr-spinel, and pyroxene. The relatively high Y abundances for all amphibolite Groups indicate a low degree of partial melting with respect to mantle compositions (Wood 1979; Figure 7A). In the V–Ti diagram, the amphibolites of

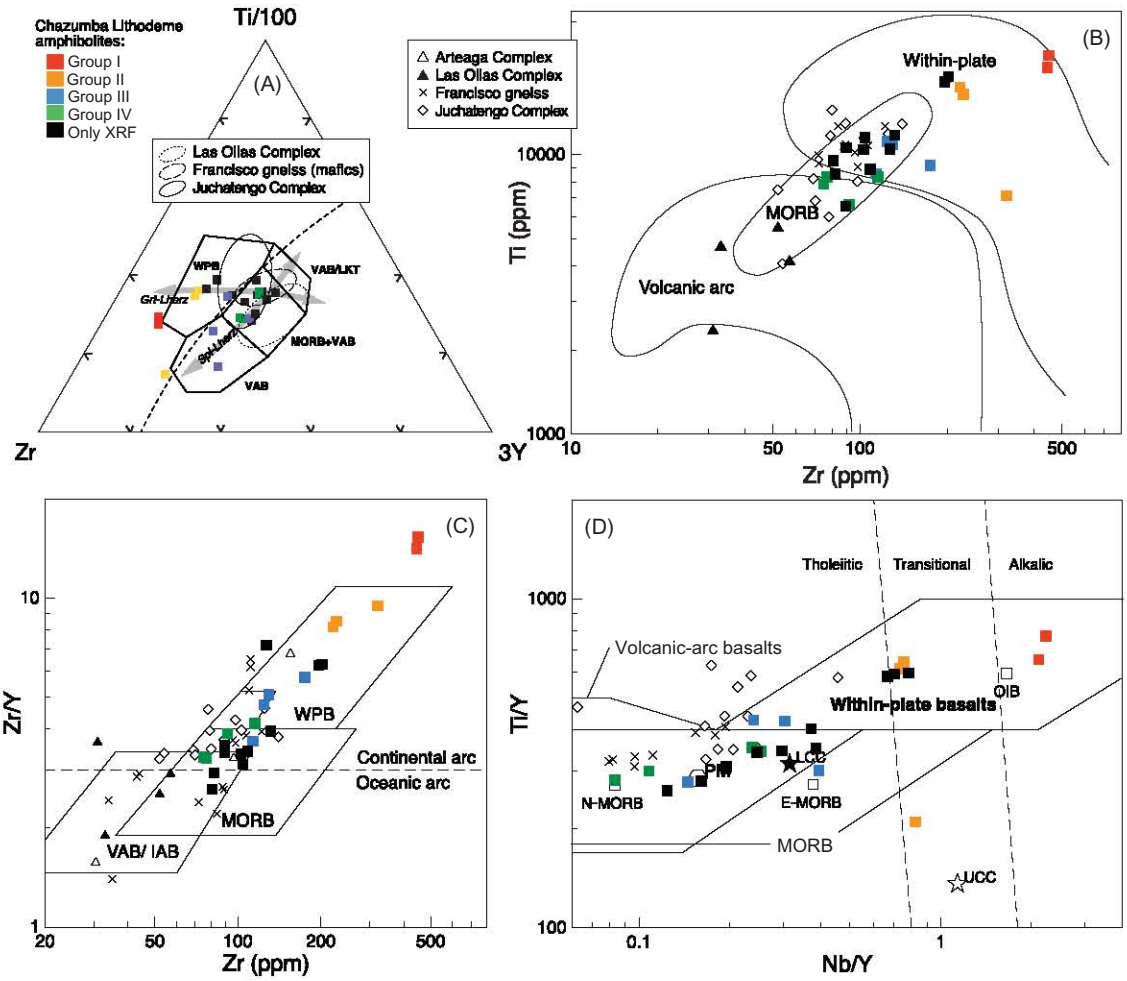

Figure 6. Trace element plots of amphibolites. Where data available, fields (A) or symbols (B, C, D) of Triassic mafic rocks from western and southern Mexico are plotted for comparison: Arteaga Complex (Centeno-García 1994; Centeno-García and Silva-Romo 1997), Las Ollas Complex (Talavera-Mendoza 2000), Francisco gneiss mafic rocks (Keppie *et al.* 2006a), and Juchatengo basalts (Grajales-Nishimura *et al.* 1999). (A) triangular Ti–Zr–Y plot after Pearce and Cann (1973) with dividing line (dashed) between within-plate basalts (WPB) and other magma suites (VAB – volcanic arc basalt, MORB – mid-ocean ridge basalt, LKT – low potassium tholeiites/calc-alkalic basalts), grey arrows depict fractionation trends of the shallow (Spl-lherzolite) and deeper (Grt-lherzolite) mantle; (B) Ti vs. Zr diagram after Pearce *et al.* (1981); (C) Zr/Y vs. Zr after Pearce and Norry (1979) and Pearce (1983) with dividing line at Zr/Y = 3 for oceanic and continental arc basalts, abbreviations see (A); (D) Ti/Y vs. Nb/Y after Pearce (1982), compositions of primitive mantle (PM), normal mid-ocean ridge basalt (N-MORB), enriched MORB (E-MORB), and ocean-island basalt (OIB) after Sun and McDonough (1989), and upper continental crust (UCC) and lower continental crust (LCC) after Taylor and McLennan (1985).

Group I and II have Ti/V ratios between 43 and 75, values typical of alkali basalts (Figure 7B). Group III and IV samples have Ti/V ratios between 20 and 50 and plot in the MORB and back-arc basalt field.

Variable contamination by either subduction zone or crustal components can be identified by the Ce/Yb vs. Ta/Yb and Th/Yb vs. Ta/Yb plots diagrams (Figures 7C and 7D; Pearce 1982, 1996). The amphibolites plot above the typical mantle array in these diagrams, suggesting varying degrees of crustal or subduction zone contamination. On the Th/Yb vs. Ta/Yb and Ce/Yb vs. Ta/Yb plots (Figures 7C and 7D), all amphibolites plot slightly above the mantle array, suggesting that the magmas were primarily derived from the mantle, with samples MH-30 (III), MH-75 (IV), and AYU-469-2 (IV) showing evidence of significant contamination by either a crustal or a subduction zone component. Group IV amphibolites have a depleted mantle signature with Ta/Yb, Th/Yb, and Ce/Yb smaller than primitive mantle compositions (Figures 7C and 7D). With the exception of sample MH-30, Group III amphibolites show enriched mantle compositions plotting between primitive mantle and enriched MORB (E-MORB) compositions. The transitional and alkalic rocks (I, II) are strongly enriched in Ta/Yb and plot between lower

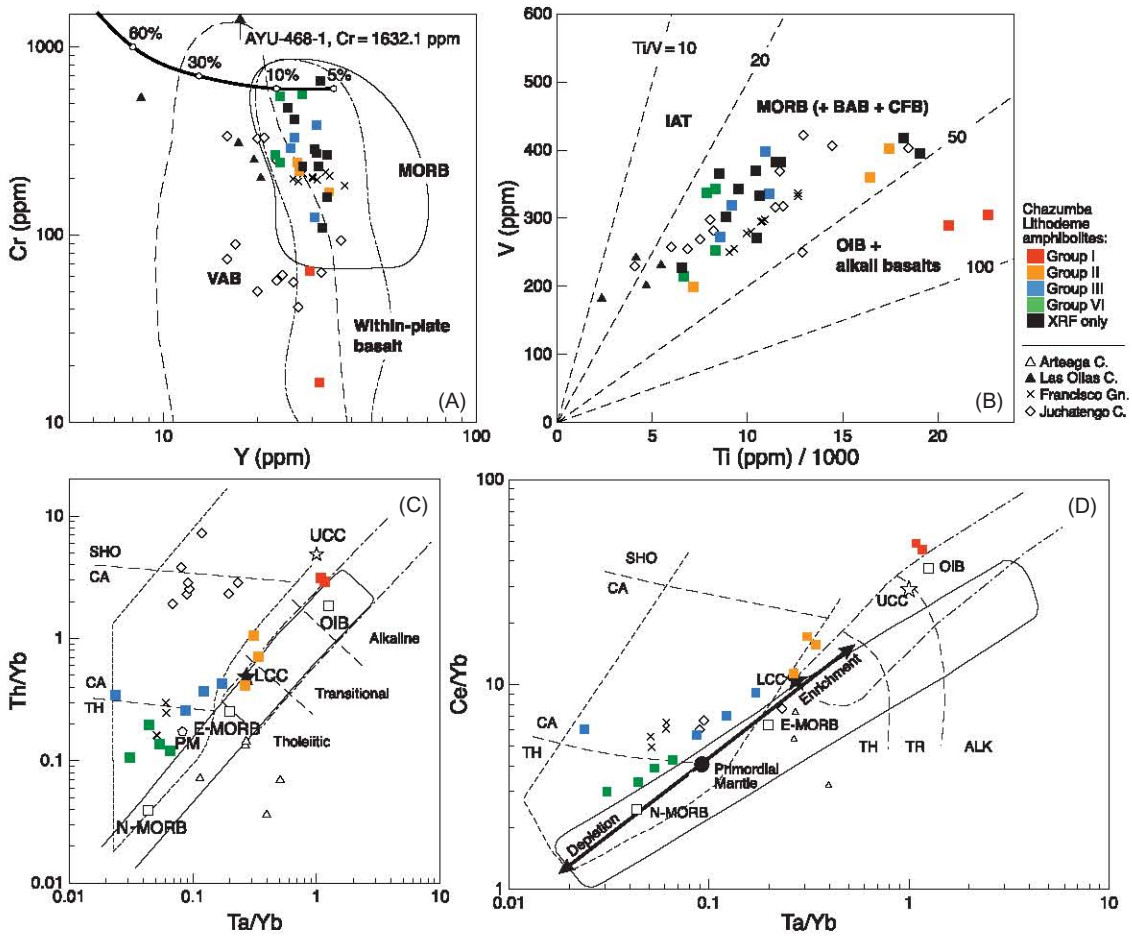

Figure 7. (A) Cr–Y plot after Pearce (1982) with partial melting trends for primordial mantle composition $Ol_{0.6}Opx_{0.2}Cpx_{0.1}Pl_{0.1}$, VAB – volcanic arc basalts, MORB – mid-ocean ridge basalts. (B) V–Ti after Shervais (1982), IAT – island arc tholeiites, BAB – back-arc basin, CFB – continental flood basalts. (C) Th/Yb vs. Ta/Yb after Pearce (1982); Pearce (1996); (D) Ce/Yb vs. Ta/Yb after Pearce (1982), TH – tholeiitic, CA – calc-alkaline, SHO – shoshonitic, TR – transitional, ALK – alkaline. Triassic mafic rocks from western and southern Mexico are plotted for comparison: Arteaga Complex (Centeno-García 1994; Centeno-García and Silva-Romo 1997), Las Ollas Complex (Talavera-Mendoza 2000), Francisco gneiss mafic rocks (Keppie *et al.* 2006a), and Juchatengo basalts (Grajales-Nishimura *et al.* 1999).

continental crust, upper continental crust (UCC), and ocean-island basalt (OIB) compositions.

The Sm–Nd signature of the amphibolites varies widely with initial ε_{Nd} values between –2.16 and +9.01 (t = 190 Ma), in which, within each amphibolite group, the ε_{Nd} values show a systematic increase from Group I to Group IV amphibolites (Figure 5C). Group I amphibolites are the less radiogenic samples with initial ε_{Nd} values of –2.16 and –1.70 with T_{DM} model ages of 877 and 791 million years (Figure 5C). Group II have ε_{Nd} values of +3.17 to +4.15 and model ages of 553 to 744 million years. Group III has ε_{Nd} values of +2.31 to +6.53, and yielded one reliable T_{DM} model age (i.e. $^{147}Sm/^{144}Nd <$ 0.165; Stern 2002) of 970 million years. Group IV amphibolites are the most radiogenic samples with ε_{Nd} values of +5.68 to +9.01, with sample MH-75 plotting above the depleted mantle curve (Figure 5C).

4.2. *Metasedimentary rocks*

Thirty-eight metasedimentary samples collected for geochemistry show a large variation in chemical composition with SiO_2 ranging from 54.3 to 94.7 wt% and Al_2O_3 from 2.3 to 22.7 wt%. Using the classification scheme of Herron (1997), the metasedimentary rocks span the range of Fe-sandstones, sublithic arenites, and quartz arenites. SiO_2 displays negative correlations with Al_2O_3 ($r = -0.98$), FeO_t ($r = -0.92$), MgO ($r = -0.41$), and K_2O ($r = -0.66$), reflecting the varying proportions of clay and quartz of the protoliths. Chondrite-normalized REE patterns of the Chazumba Lithodeme show moderate enrichment of LREEs over HREEs with La/Yb_N ranging between 4.1 and 8.4, flat HREE patterns of Gd/Yb_N between 0.8 and 1.5 and negative Eu anomalies with Eu/Eu^* between 0.6 and 1.1 (Figure 8, Table DR-3). These characteristics suggest

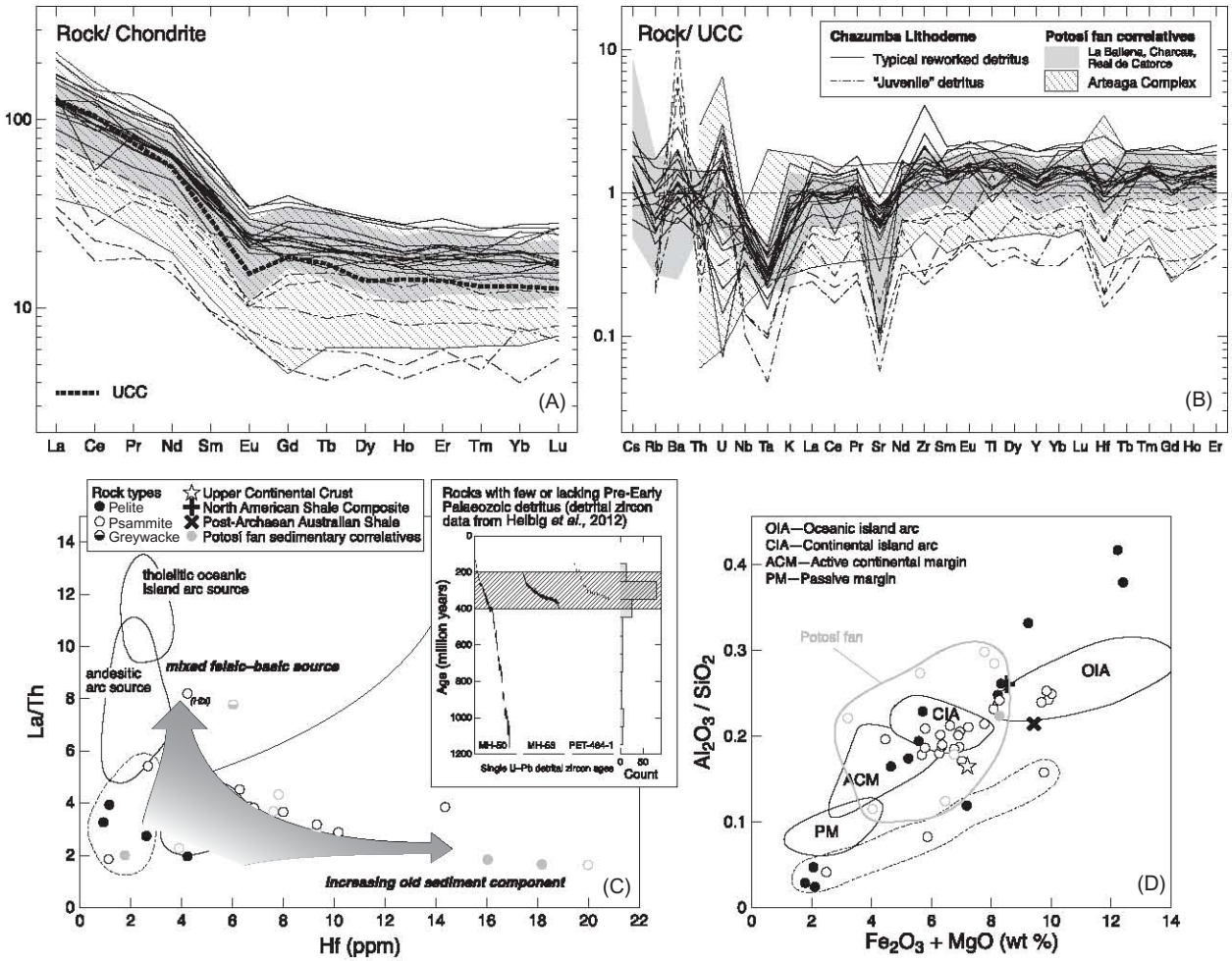

Figure 8. (A) Chondrite-normalized REEs of the metasedimentary rocks of the Chazumba Lithodeme, normalizing values after Sun and McDonough (1989), upper continental crust (UCC) from Taylor and McLennan (1995) plotted for comparison. (B) UCC-normalized trace element diagram (normalizing values after Taylor and McLennan 1995). Key for (A) same as in (B). (C) La/Th vs. Hf variation diagram after Floyd and Leveridge (1987), dash-dotted area includes metasedimentary samples of the Chazumba Lithodeme of low Hf concentrations and of few or no Pre-Early Palaeozoic detritus (U–Pb detrital zircon data from Helbig *et al.* 2012); (D) Al_2O_3/SiO_2 vs. Fe_2O_3 + MgO after Bhatia (1983), same key as in (C). Potosí fan correlatives: La Ballena Formation, Sierra de Charcas, Real de Catorce and Arteaga Complex (Varales and Jaltomate formations) from Centeno-García *et al.* (1993); Centeno-García (1994); Barboza-Gudiño *et al.* (2010).

that the source of the metasedimentary rocks probably comprised felsic to intermediate rocks. Four samples (MH-37, MH-41, MH-85, and MH-95) lack a Eu anomaly. Samples MH-85, MH-95, PET-484-1, MH-50, and MH-53 are characterized by very low REE abundances with respect to the rest of the samples (Figure 8A; dash-dotted lines).

UCC-normalized trace element patterns are characterized by Ba, U, and Zr enrichment and strong depletion in Sr and HFSEs (Th, Nb, Ta, Hf) (Figure 8B). The negative Nb–Ta anomaly may reflect depletion of these elements in the source rock and/or the erosion of a source derived from arc magmas (McCulloch and Gamble 1991; Saunders *et al.* 1991). Negative Sr anomalies may reflect plagioclase weathering. Samples MH-85, MH-95, PET-484-1, MH-50, and MH-53 are characterized by strong trace element depletion possibly due to the dilution effects associated with high silica content (SiO_2 = 80–94 wt.%; Figure 8B; dash-dotted lines).

The range of Al_2O_3/TiO_2 (14.3–30.5 wt%), Cr/Th (2.9–20.4 ppm), Th/Co (0.3–1.3 ppm), Cr/V (0.3–0.8 ppm), and V/Ni (1.9–10.4 ppm) ratios and low MgO, Fe2O3, Cr, Ni, and Co abundances suggests that the majority of samples are derived from felsic sources (Taylor and McLennan 1985; Feng and Kerrich 1990; Cullers 1994; Girty *et al.* 1996). A felsic rock source is further indicated by the La/Th vs. Hf diagram displaying widely varying Hf values with relatively minor variation

in La/Th, a wide range of young and old sediment sources (Figure 8C; Floyd and Leveridge 1987). Most metasedimentary rocks have La/Th and Hf values typical of acid-arc sources (Hf = 3–7 ppm; Floyd and Leveridge 1987). Samples MH-85, MH-95, PET-484-1, MH-50, and MH-53 are characterized by relatively low Hf (1–3 ppm) values.

A continental island arc and active continental margin setting is indicated by Al_2O_3/SiO_2 values ranging from 0.03 to 0.52, and Fe_2O_3 + MgO values ranging between 1.8 and 12.4 wt% (Figure 8D; Bhatia 1983). Some samples, mostly from either the Providencia shear-zone or the southern Magdalena Migmatite have relatively low Al_2O_3/SiO_2 (approximately 0.03–0.05 and approximately 0.1), a characteristic that is consistent with the geochemistry of passive margin-type sediments (Bhatia 1983; Figure 8D).

Sm–Nd isotopic compositions are highly variable. Most samples are characterized by initial ε_{Nd} values between –7.65 and –5.53 (t = 195 Ma) with T_{DM} model ages of 1308–1444 million years. Two samples (MH-50 and MH-53) are more radiogenic with ε_{Nd} values of –1.42 and +1.06 with T_{DM} model ages of 949 and 776 million years, respectively (Table DR-4).

5. Discussion

5.1. Protoliths

5.1.1. Amphibolites

Our results indicate that the amphibolite protoliths of the Chazumba Lithodeme comprise a suite ranging from continental within-plate alkalic and transitional basalts (Groups I and II) to N-MORB tholeiites with a superimposed arc signature (Groups III and IV) that is typical of a back-arc setting. The steep REE patterns of Groups I and II (Figure 5A) indicate melt generation in a garnet lherzolite mantle, and their flat N-MORB-normalized trace element patterns suggest a within-plate origin (Figure 5B). In contrast, the rather flat REE patterns of the N-MORB tholeiites (Groups III and IV) are typical of partial melting of the shallow (spinel-lherzolite) mantle and indicative of thinner continental lithosphere typical of MORB melts. Furthermore, Group III and IV amphibolites are characterized by depletion in Nb and Ta indicative of either arc activity or crustal contamination (Figures 5A and 5B).

The geochemical patterns correspond with the Sm–Nd isotopic systematics indicating that the alkalic to transitional basalts (Groups I and II) were derived from an older subcontinental lithospheric mantle (SCLM) that was progressively replaced by a younger mantle, represented by Group III and IV amphibolites. Taken together, the varying trace element, REE and Sm–Nd patterns in the amphibolites indicate magma generation in different mantle sources, an interpretation that is consistent with gradual thinning and the eventual replacement of the older SCLM by younger juvenile mantle, consistent with the progressive development of a back-arc setting.

With the exception of one sample (MH-32), the Sm–Nd systematics of Group III and IV tholeiites (Figure 5C) coupled with the negative Nb–Ta anomalies (Figure 5C) indicate contamination by subduction processes rather than by continental crust. However, one Group III sample (MH-32) shows signs of crustal assimilation as indicated by the ε_{Nd} value (t = 200 Ma) vs. $^{147}Sm/^{144}Nd$ plot (Figure 9), where it plots on a mixing trend consistent with minor host rock assimilation of potential basement rocks (Oaxacan Complex, Chazumba Lithodeme metasedimentary rocks, Potosí fan correlatives; Figure 9). The alkalic and transitional basalts (Groups I and II) together with two amphibolite samples of Yáñez *et al.* (1991) plot on a trend consistent with a higher degree of fractional crystallization in these rocks (Figure 9).

Insights into the composition of the 'old' SCLM source of Group I and II basalts can be obtained by comparing Sm–Nd isotopic data with equivalent data from older (Carboniferous–Permian) mafic rocks of the Acatlán Complex (Yáñez *et al.* 1991; Torres *et al.* 1999; Murphy *et al.* 2006; Kramer 2008; Ortega-Obregón *et al.* 2010a,b; Kirsch *et al.* 2012b). The Carboniferous–Permian mafic rocks are characterized by more negative ε_{Nd} values at t = 200 Ma, and older T_{DM} model ages (ca. 800–1200 million years; Figure 10A) than Group I and II basalts, suggesting that the old SCLM was beginning to be replaced by a more juvenile mantle when Group I and II amphibolites were generated. With continued back-arc rifting, a more juvenile mantle was generated which was the source for Group III and IV basalts. We therefore interpret our Sm–Nd data to be indicative of the progressive replacement of the SCLM by juvenile mantle as back-arc rifting developed.

5.1.2. Metasedimentary rocks

The geochemistry of the metasedimentary rocks indicates that the protoliths of the Chazumba Lithodeme had predominantly felsic sources of different age, which is consistent with detrital zircon studies of Helbig *et al.* (2012). Samples characterized by predominantly inherited, Proterozoic detritus (e.g. MH-30, MH-73, TEP-474-1 to 4) display a geochemistry typical of the Oaxacan Complex basement rocks (Figures 8C and 8D). On the other hand, metasedimentary rocks that lack Proterozoic detritus have a geochemistry generally depleted in trace elements in comparison to the old detritus-bearing metasedimentary rocks (Figures 8A and 8B) and are characterized by low Hf abundances (Figure 8C). The provenance characteristics also conform to Sm–Nd systematics of the metasedimentary protoliths. Typically, most samples plot within the Oaxacan Complex envelope (Figure 10B), whereas samples lacking Proterozoic zircons

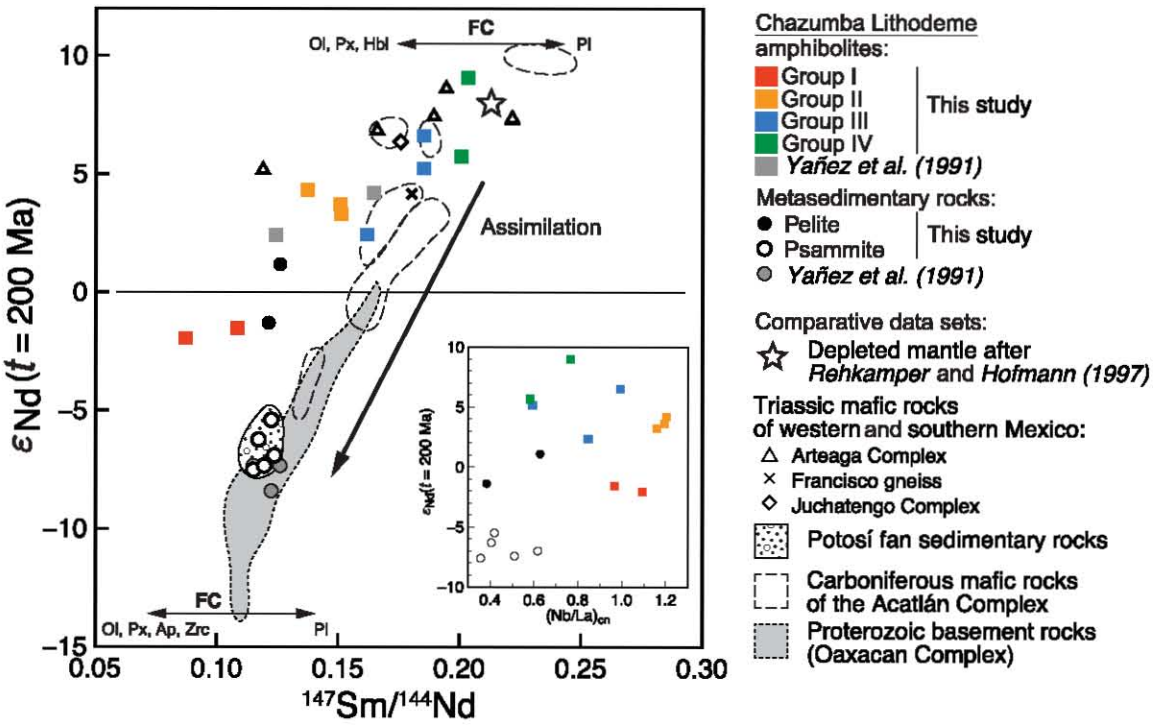

Figure 9. εNd ($t = 200$ Ma) vs. $^{147}Sm/^{144}Nd$ plot comparing several mafic suites and metasedimentary reservoirs: Proterozoic basement rocks (Patchett and Ruiz 1987; Ruiz *et al.* 1988b), Carboniferous–Permian mafic rocks from the Acatlán Complex (Ortega-Obregón *et al.* 2010a,b; Kirsch *et al.* 2012b), Triassic/Early Jurassic mafic rocks of western and southern Mexico (Centeno-García *et al.* 1993; Centeno-García 1994; Grajales-Nishimura *et al.* 1999; Valencia-Moreno *et al.* 2001; Centeno-García *et al.* 2003), potential mixing and fractional crystallization trends are shown with arrows, Depleted mantle compositions after Rehkamper and Hofmann (1997); inset: ε_{Nd} ($t = 200$ Ma) vs. Nb/La_{cn} plot for amphibolite groups and metasedimentary rocks.

have more positive ε_{Nd} values, which suggests that the geochemistry of these rocks represent a local or original signature that is not blurred by recycled older material.

5.2. *Correlative units*

5.2.1. *Mafic rocks*

There are only few data sets of potentially correlative Triassic–Jurassic mafic rocks of Mexico: (1) pillow basalts from the Arteaga Complex (Figure 2B) are interpreted to be part of a marginal ocean basin ('Arteaga basin') that formed in the Triassic at the western margin of continental Mexico (Centeno-García *et al.* 1993; Centeno-García 2008; Martini *et al.* 2010); (2) meta-volcanic rocks of the Las Ollas Complex in the Zihuatanejo terrane (Figure 2B) have been attributed either to an intraoceanic arc (Talavera-Mendoza 2000) or to the Arteaga basin (Centeno-García 2008); (3) mafic rocks of the Francisco Gneiss (Sonobari Complex: Valencia-Moreno *et al.* 2001) in the Tahué terrane (Figure 2A; Keppie *et al.* 2006a; and (4) ?Permian–Triassic basalts of the Juchatengo Complex in the southern Oaxaquia terrane (Figure 2B; Grajales-Nishimura *et al.* 1999). Geochemical analyses on the mafic rocks have been performed by various authors: six samples in the Arteaga Complex (Centeno-García *et al.* 1993; Centeno-García 1994), six samples in the Las Ollas Complex (Talavera-Mendoza 2000; Talavera-Mendoza and Guerrero-Suastegui 2000), nine samples from the Francisco Gneiss (Keppie *et al.* 2006a), and 13 samples from the Juchatengo Complex (Grajales-Nishimura *et al.* 1999). Sm–Nd isotopic systematics were available for the Arteaga Complex (Centeno-García *et al.* 1993), the Tejupilco schist (Elías-Herrera *et al.* 2000), the Francisco Gneiss (Keppie *et al.* 2006a), and the Juchatengo Complex (Grajales-Nishimura *et al.* 1999).

Despite the limited data, some general comparisons can be made. Geochemically, the most similar rocks are the Francisco mafic gneisses. Their geochemistry is typical of within-plate continental tholeiites (Keppie *et al.* 2006a) and show similar trends to the Group III Chazumba amphibolites (Figures 6 and 7A–7D). The Juchatengo basalts are inferred to be of back-arc or within-plate affinity (Grajales-Nishimura *et al.* 1999) and show similar geochemistry as the Group III and IV amphibolites. The Arteaga Complex mafic rocks have primitive N-MORB to E-MORB compositions typical of continental arc magmatism (Figure 11). The Las Ollas Complex mafic rocks show significantly different geochemistry in that they are typical of island arc tholeiites (Figures 6A–6C, 7, 11).

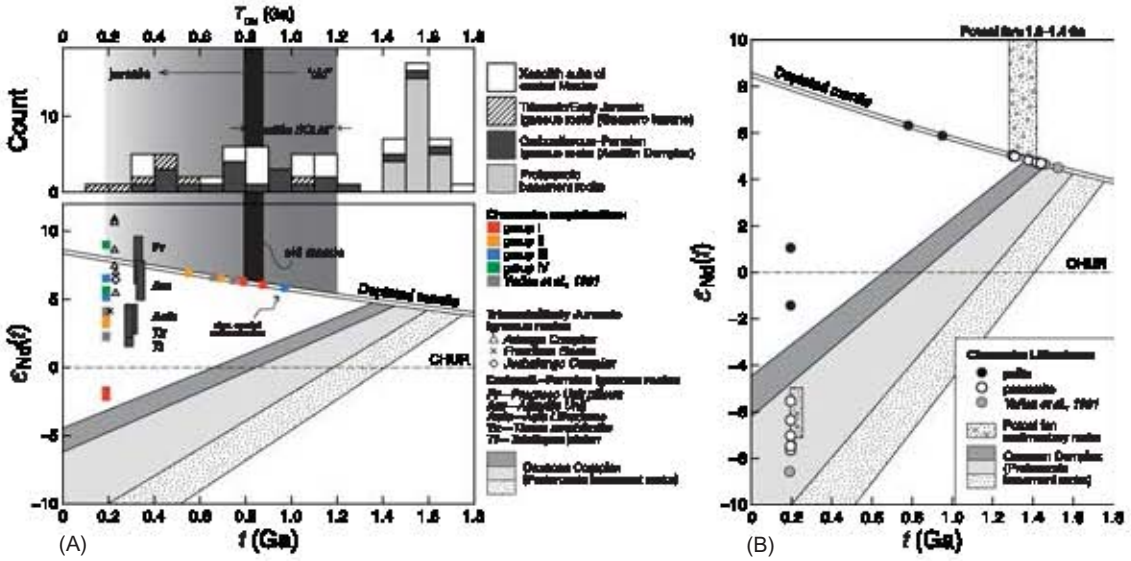

Figure 10. (A) εNd(t) vs. time plot comparing Sm–Nd isotopic data of the amphibolitic rocks in the Chazumba Lithodeme (red, orange, green, blue: this study; grey: Yáñez *et al.* 1991) and various (meta-)igneous rocks of western Mexico. Depleted mantle curve from DePaolo (1988). Hisogram above shows T_{DM} age abundances for different rocks suites: Proterozoic basement rocks (Patchett and Ruiz 1987; Ruiz *et al.* 1988b), arc-related Carboniferous–Permian igneous rocks (Yáñez *et al.* 1991; Torres *et al.* 1999; Murphy *et al.* 2006; Kramer 2008; Ortega-Obregón *et al.* 2010a,b; Kirsch *et al.* 2012b), Triassic/Early Jurassic igneous rocks of western and southern Mexico (Centeno-García *et al.* 1993; Centeno-García 1994; Grajales-Nishimura *et al.* 1999; Valencia-Moreno *et al.* 2001; Centeno-García *et al.* 2003), xenolith suite from central Mexico (Ruiz *et al.* 1988a; Schaaf *et al.* 1994). (B) $\varepsilon_{Nd}(t)$ vs. time plot comparing Sm–Nd isotopic data of the Chazumba Lithodeme metasedimentary rocks (black: this study; grey: Yáñez *et al.* 1991) in comparison to ε_{Nd} values of the Potosí fan correlative rocks: Varales Formation/Arteaga Complex, La Ballena Formation, Placeres Complex (Centeno-García *et al.* 1993; Centeno-García 1994).

Nonetheless, the Chazumba Lithodeme amphibolites may have been part of the Arteaga basin suite that is characterized by arc-parallel as well as across-arc geochemical variations (Figure 12). ε_{Nd} values for these Triassic–Jurassic mafic rocks range from +4.2 to +11.2 (t = 200 Ma) and have generally a more juvenile mantle source than the Chazumba Lithodeme amphibolites (Figure 10A) with T_{DM} model ages ranging between approximately 200 and 500 million years (for $^{147}Sm/^{144}Nd < 0.165$). Only the Francisco gneiss mafic sample has an older T_{DM} model age of 833 million years (recalculated after data by Valencia-Moreno *et al.* 2001), which is similar to Group I and II Chazumba Lithodeme amphibolites and the 'Acatlán SCLM' (Figure 10A). These comparisons suggest that the mafic rocks of the Francisco Gneiss were probably extracted from the same SCLM underlying continental Mexico, whereas the mafic rocks of the Arteaga, Las Ollas, or Juchatengo complexes probably formed closer to the arc or in a later stage of a developing back-arc basin when the 'Acatlán SCLM' had already been replaced (Figure 12). However, more geochronological work on the Juchatengo Complex is needed to constrain this particular rifting event. According to Elías-Herrera *et al.* (2000, 2003), Sm–Nd data of the 187 Ma Tizapa granite and gneiss xenoliths from the eastern Teloloapán terrane suggest that the Triassic Tejupilco schist represents the remains of an arc that formed on Grenvillian basement and therefore advocates continental arc activity and related back-arc rifting processes along the continental edge during the Triassic–Jurassic.

5.2.2. *Metasedimentary rocks*

The metasedimentary rocks of the Potosí fan deposits show similar negative ε_{Nd} as the Chazumba Lithodeme metasedimentary rocks consistent with a predominant sediment source from the Oaxacan Complex or from recycled Oaxacan Complex rocks (Figure 10B). However, as shown in Figure 8C, some metasedimentary samples of the Chazumba Lithodeme have a trend characterized by La/Th and Hf depletion suggesting the influx of relatively young detritus and is consistent with the gradual erosion of an arc system and the progressive incision of the arc's plutonic roots that results in an increased zircon release, the main host phase for Hf (Floyd and Leveridge 1987). This geochemical trait is also consistent with detrital zircon U–Pb geochronological data of these samples (Helbig *et al.* 2012), which reveal no or rare inherited Proterozoic zircons (Figure 8C). The Sm–Nd systematics of two meta-pelitic rocks in the Chazumba Lithodeme (MH-41 and MH-53) that are more radiogenic indicate a younger and/or a local detrital source (Figure 10B).

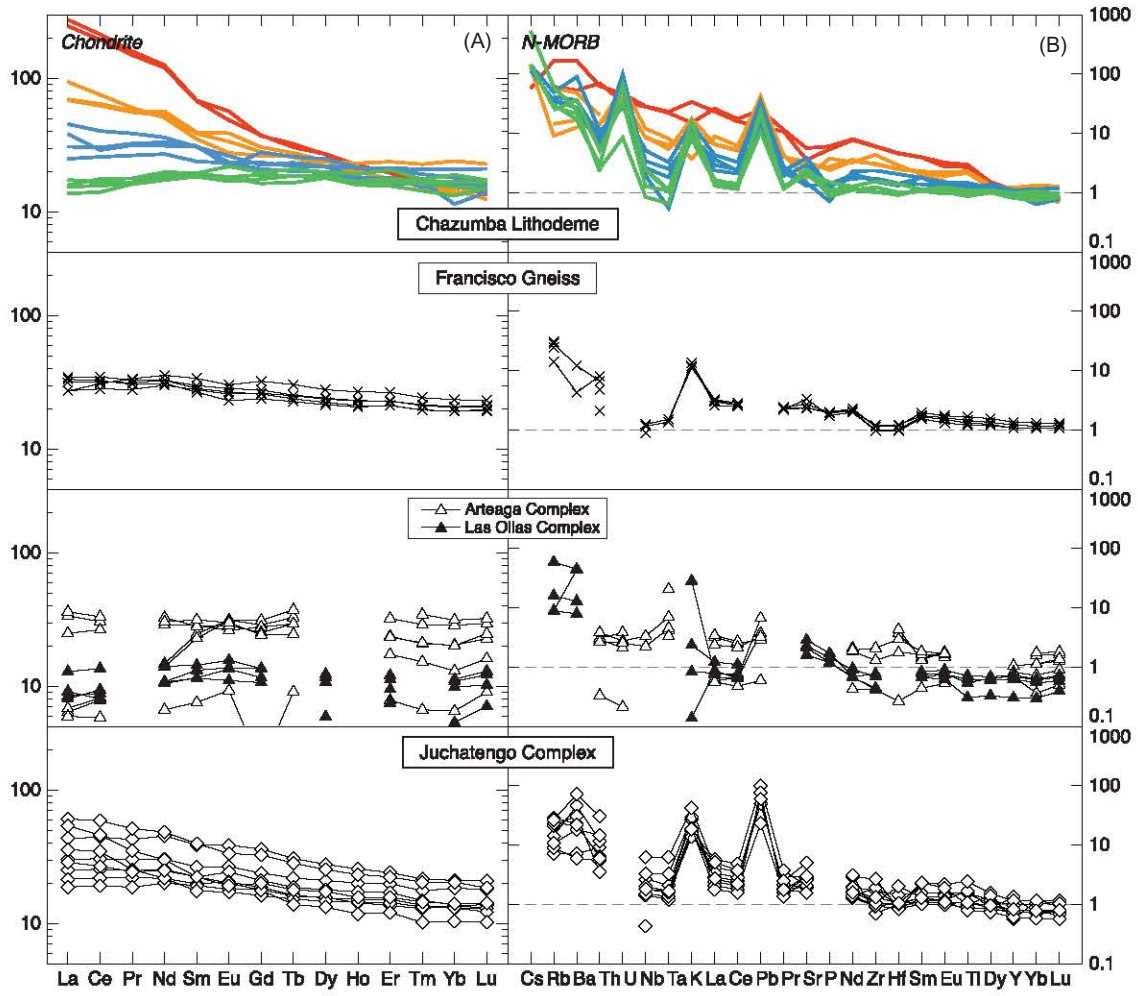

Figure 11. (A) Chondrite-normalized REE patterns and (B) N-MORB-normalized trace element patterns of amphibolite Groups I–IV in comparison to mafic rocks of the Francisco gneiss (Keppie *et al.* 2006a), the Arteaga Complex (Centeno-García *et al.* 1993; Centeno-García 2008), the Las Ollas Complex (Talavera-Mendoza 2000; Talavera-Mendoza and Guerrero-Suastegui 2000) and the Juchatengo Complex (Grajales-Nishimura *et al.* 1999).

On the other hand, the Potosí fan deposits have older T_{DM} model ages and are dominated by Proterozoic detritus. Taken together, we suggest that sedimentary sources likely varied laterally along the Arteaga basin throughout the late Palaeozoic and Mesozoic as major lateral displacements took place between the Middle American terranes (e.g. Alaniz-Álvarez *et al.* 1996; Elías-Herrera and Ortega-Gutiérrez 2002). Such displacements may also have resulted from high-oblique subduction along the arc and caused the Arteaga basin to open as a long and narrow marginal basin oblique to the spreading direction (Figure 12).

5.3. Palaeogeographic implications

Our data suggest that the western margin of Middle America during Late Triassic–Early Jurassic was characterized by subduction relatively close to the continental margin that caused back-arc rifting along this margin. This, in turn, requires the Mixteca terrane to have lain along the margin of Pangea and is not consistent with a proposed Pangea-A variant by Vega-Granillo *et al.* (2009) that places the Mixteca terrane about 1500 km away from the Pangean margin and within the Ouachitan orogen. Furthermore, these data provide insights into the controversies concerning the relative positions of the Middle American terranes in the Jurassic. For example, if the Chortís block, which is about 400 km in width, was located south of southern Mexico at that time (Pacific model: Pindell *et al.* 2012 and references therein), Jurassic magmatic arc activity should occur within that block. Torres de León *et al.* (2012) recently dated orthogneisses in the Motagua fault zone at ca. 170 Ma. However, the tectonic setting of this magmatic event and the temporal–spatial relationships between this event and the coeval Jurassic Nazas arc (Figure 2A) have not been established yet. In this reconstruction, the distance between the Jurassic Nazas arc and the trench would have been about

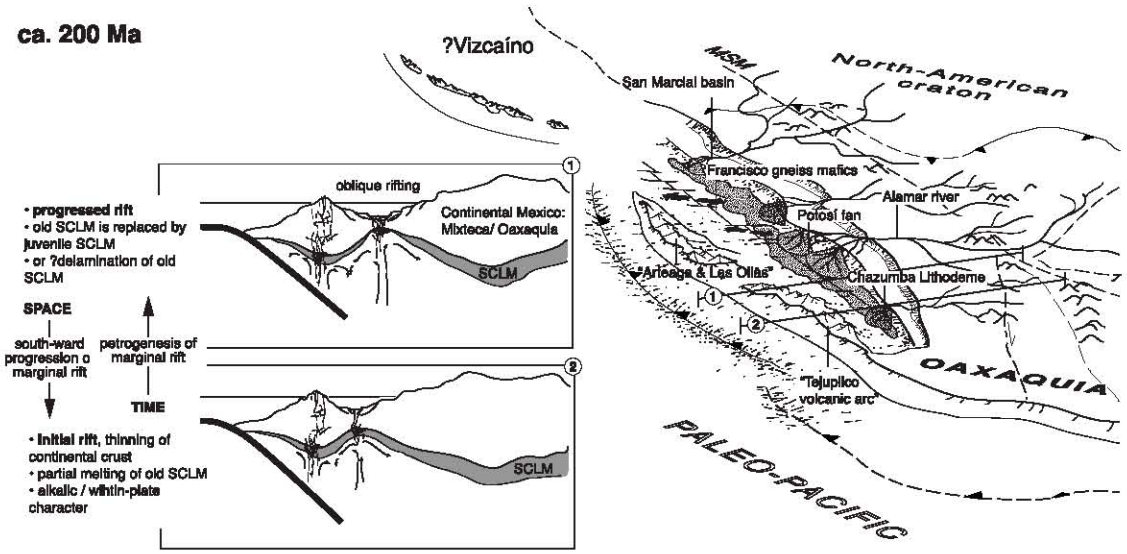

Figure 12. Palaeogeographic reconstruction and petrogenetic model of the western Pangean margin for Triassic and Early Jurassic time (modified after Elías-Herrera and Ortega-Gutiérrez 2002; Weber *et al.* 2007; Centeno-García 2008).

700 km, implying that the dip of the Benioff zone would have been 8°, which is too small to produce arc magmatism (e.g. Ramos *et al.* 2002). However, if the dip of the Benioff zone changed from flat to steep at 600 km from the trench, the Nazas arc magmatism could be generated.

An alternative reconstruction (Keppie and Keppie 2012) suggests that the Chortís block resided in the future Gulf of Mexico during the Jurassic (Figure 1D). In this reconstruction, the Nazas arc occurs along the Pangean continental margin in Mexico about 200 km from the trench: translating to a Benioff zone dip of 30°, which is consistent with an intra-Pangean location for the Chortís block. Thus, our data from the Ayú Complex cannot distinguish between these two palaeogeographic locations for the Chortís block. Resolution of these competing reconstructions requires focused studies on the evolution of these terranes in the Jurassic.

6. Conclusions

The Upper Triassic–Lower Jurassic Chazumba Lithodeme of the Ayú Complex in southern Mexico is a turbiditic siliciclastic sequence consisting of predominantly felsic sources and that is inferred to have been deposited in a passive margin or back-arc type setting. Amphibolites within the Chazumba metasedimentary rocks comprise a suite of alkaline to transitional basalts and N-MORB tholeiites with a superimposed arc signature that appear to have formed in a back-arc setting. This bulk-rock geochemistry is consistent with Sm–Nd systematics that document a gradual thinning of the continental lithosphere as old as ca. 800 Ma. The SCLM was progressively replaced by juvenile mantle typical of extensive regimes.

We interpret the Chazumba Lithodeme as a correlative of the Potosí fan that formed part of the western rifted margin of Pangea during Late Triassic/Early Jurassic time. Sedimentary rocks of the Potosí fan are geochemically very similar to the Chazumba Lithodeme metasedimentary units, and both are inferred to have a provenance in the Oaxacan Complex. Geochemistry and Sm–Nd systematics of the Francisco gneiss mafic rocks are the most similar rocks to the Chazumba Lithodeme amphibolites; differences of the other correlative mafic rocks can be explained by lateral and strike-parallel variations in the Arteaga back-arc basin (Centeno-García 2008). Along strike to the south, the Potosi fan is absent, and we infer that it was thrust beneath the Acatlán Complex to be extruded as the Ayú Complex (Helbig *et al.* 2012).

Our documenteation of Early Mesozoic back-arc activity implies a retreating west-facing magmatic arc that stretched along western edge of continental Mexico.

Acknowledgements

We acknowledge the Consejo Nacional de Ciencia y Tecnología (CONACyT; Project CB-2005-1/24894), Programa de Apoyo a Proyectos de Investigación (PAPIIT: IN100108-3), and Natural Sciences and Engineering Research Council of Canada (NSERC Discovery Grant 62239). MH is grateful to Moritz Kirsch for field work assistance and critical discussions. This is a contribution to IGCP Project 597.

References

Alaniz-Álvarez, S.A., Der, H., Van, P., Nieto-Samaniego, A.F., and Ortega-Gutiérrez, F., 1996, Radiometric and kinematic evidence for Middle Jurassic strike-slip faulting in southern Mexico related to the opening of the Gulf of Mexico: Geology, v. 24, no. 5, p. 443–446.

Anderson, T.H., Jones, N.W., and McKee, J.W., 2005, The Taray Formation: Jurassic (?) mélange in northern

Mexico – Tectonic implications: Geological Society of America Special Paper, v. 393, p. 427–455.

Barboza-Gudiño, J.R., Orozco-Esquivel, M.T., Gómez-Anguiano, M., and Zavala-Monsiváis, A., 2008, The Early Mesozoic volcanic arc of western North America in northeastern Mexico: Journal of South American Earth Sciences, v. 25, p. 49–63.

Barboza-Gudio, J.R., Zavala-Monsivis, A., Venegas-Rodrguez, G., and Barajas-Nigoche, L.D., 2010, Late Triassic stratigraphy and facies from northeastern Mexico: Tectonic setting and provenance: Geosphere, v. 6, p. 621–640.

Bhatia, M.R., 1983, Plate Tectonics and geochemical composition of sandstones: The Journal of Geology, v. 91, no. 6, p. 611–627.

Caballero-Miranda, C., Morán-Zenteno, D.J., Urrutia-Fucugauchi, J., Silva-Romo, G., Böhnel, H.N., Churado-Chichay, Z., and Cabral-Cano, E., 1990, Paleogeography of the northern portion of the Mixteco terrain, southern Mexico, during the Middle Jurassic: Journal of South American Earth Sciences, v. 3, no. 4, p. 195–211.

Centeno-García, E., 1994, Tectonic evolution of the Guerrero Terrane: Western Mexico, University of Arizona.

Centeno-García, E., 2005, Review of Upper Paleozoic and Lower Mesozoic stratigraphy and depositional environments of central and west Mexico: Constraints on terrane analysis and paleogeography, *in* Anderson, T.H., Nourse, J.A., McKee, J.W., and Steiner, M.B., eds., The Mojave-Sonora megashear hypothesis: Development, assessment, and alternatives: Geological Society of America Special Paper 393, p. 233–258.

Centeno-García, E., 2008, The Guerrero Composite Terrane of western Mexico: Collision and subsequent rifting in a supra-subduction zone, *in* Draut, A., Clift, P.D., and Scholl, D., eds., Formation and applications of the sedimentary record in arc collision zones: Geological Society of America Special Paper 436, p. 279–308.

Centeno-García, E., Corona-Chávez, P., Talavera-Mendoza, O., and Iriondo, A., 2003, Geology and Tectonic evolution of the Western Guerrero Terrane – A transect from Puerto Vallarta to Zihuatanejo, Mexico, in Geologic Transects Across Cordilleran Mexico, Guidebook for the field trips of the 99th Geological Society of America Cordilleran Section Annual Meeting, Geological Society of America, Puerto Vallarta, Jalisco, p. 201–228.

Centeno-García, E., Mendoza-Rosales, C.C., and Silva-Romo, G., 2009, Sedimentology and significance of the volcanism of the Matzitzi Formation (upper Paleozoic), Lus Reyes Metzontla-San Luis Atolotitlán region, Puebla State: Revista Mexicana de Ciencias Geológicas, v. 26, no. 1, p. 18–36.

Centeno-García, E., Ruiz, J., Coney, P.J., Patchett, P.J., and Ortega-Gutiérrez, F., 1993, Guerrero terrane of Mexico: Its role in the Southern, Cordillera from new geochemical data: Geology, v. 21, p. 419–422. doi: 10.1130/0091-7613(1993)021<0419:GTOMIR>2.3.CO;2.

Centeno-García, E., and Silva-Romo, G., 1997, Petrogenesis and tectonic evolution of central Mexico during Triassic-Jurassic time: Revista Mexicana de Ciencias Geológicas, v. 14, no. 2, p. 244–260.

Cerca, M., Ferrari, L., López-Martínez, M., Martiny, B.M., and Iriondo, A., 2007, Late Cretaceous shortening and early Tertiary shearing in the central Sierra Madre del Sur, southern Mexico: Insights into the evolution of the Caribbean-North American plate interaction: Tectonics, v. 26, no. 3, p. TC3007. doi: 10.1029/2006TC001981.

Cullers, R., 1994, The controls on the major and trace element variation of shales, siltstones, and sandstones of Pennsylvanian–Permian age from uplifted continental blocks in Colorado to platform sediment in Kansas, USA: Geochimica et Cosmochimica Acta, v. 58, no. 22, p. 4955–4972.

DePaolo, D.J., 1988, Neodymium isotope geochemistry: Berlin, Springer, 187 p.

Dickinson, W.R., and Lawton, T.F., 2001, Carboniferous to Cretaceous assembly and fragmentation of Mexico: Geological Society of America Bulletin, v. 113, no. 9, p. 1142–1160.

Domeier, M., Van der Voo, R., and Torsvik, T.H., 2012, Paleomagnetism and Pangea: The road to reconciliation: Tectonophysics, v. 514–517, no. C, p. 14–43. doi: 10.1016/j.tecto.2011.10.021.

Dostal, J., Dupuy, C., and Caby, R., 1994, Geochemistry of the Neoproterozoic Tilemsi belt of Iforas (Mali, Sahara): A crustal section of an oceanic island arc: Precambrian Research, v. 65, p. 55–69.

Dowe, D.S., Nance, R.D., Keppie, J.D., Cameron, K.L., Ortega-Rivera, A., Ortega-Gutiérrez, F., and Lee, J.W.K., 2005, Deformational History of the Granjeno Schist, Ciudad Victoria, Mexico: Constraints on the Closure of the Rheic Ocean?: International Geology Review, v. 47, no. 9, p. 920–937.

Díaz-Salgado, C., Centeno-García, E., and Gehrels, G.E., 2003, Stratigraphy, Depositional Environments, and Tectonic Significance of the Taray Formation, Northern Zacatecas State, Mexico: Geological Society of America Abstracts with Programs, v. 35, no. 4, p. 71.

Elías-Herrera, M., and Ortega-Gutiérrez, F., 2002, Caltepec fault zone: An Early Permian dextral transpressional boundary between the Proterozoic Oaxacan and Paleozoic Acatlán complexes, southern Mexico, and regional tectonic implications: Tectonics, v. 21, no. 3, p. 1–18.

Elías-Herrera M., Ortega-Gutiérrez, F., Macías-Romo, C., Sánchez-Zavala, J.L., and Solari, L.A., 2011, Colisión oblicua del Cisuraliano–Guadalopiano entre bloques continentales en el sur de México: Evidencias estratigráfico-estructurales y geocronológicas, *in* Simposio en Honor del Dr. Zoltan de Cserna (Libro de Resúmenes): México, Universidad Nacional Autónoma de México, p. 159–164.

Elías-Herrera, M., Ortega-Gutiérrez, F., Sánchez-Zavala, J.L., and Macías-Romo, C., 2003, The real Guerrero terrane, southern Mexico: New insights from recent studies: Geological Society of America Abstracts with Programs, v. 35, no. 27–5.

Elías-Herrera, M., Sánchez-Zavala, J.L., and Macías-Romo, C., 2000, Geologic and geochronologic data from the Guerrero terrane in the Tejupilco area, southern Mexico: New constraints on its tectonic interpretation: Journal of South American Earth Sciences, v. 13, no. 4–5, p. 355–375.

Feng, R., and Kerrich, R., 1990, Geochemistry of fine-grained clastic sediments in the Archean Abitibi greenstone belt, Canada: Implications for provenance and tectonic setting: Geochimica et Cosmochimica Acta, v. 54, p. 1061–1081.

Ferrari, L., 2004, Slab detachment control on mafic volcanic pulse and mantle heterogeneity in central Mexico: Geology, v. 32, no. 1, p. 77–80. doi: 10.1130/G19887.1.

Floyd, P., and Leveridge, B., 1987, Tectonic environment of the Devonian Gramscatho basin, south Cornwall: Framework mode and geochemical evidence from turbiditic sandstones: Journal of the Geological Society, London, v. 144, no. 4, p. 531.

Girty, G., Ridge, D., Knaack, C., Johnson, D., and AlRiyami, R., 1996, Provenance and depositional setting of Paleozoic chert and argillite, Sierra Nevada, California: Journal of Sedimentary Research, v. 66, no. 1, p. 107–118.

Grajales-Nishimura, J.M., Centeno-García, E., Keppie, J.D., and Dostal, J., 1999, Geochemistry of Paleozoic basalts from the Juchatengo complex of southern Mexico: Tectonic implications: Journal of South American Earth Sciences, v. 12, no. 6, p. 537–544.

Helbig, M., Keppie, J.D., Murphy, J.B., and Solari, L.A., 2012, U–Pb geochronological constraints on the Triassic–Jurassic Ayú Complex, southern Mexico: Derivation from the western margin of Pangea-A: Gondwana Research, v. 22, no. 3–4, p. 910–927. doi: 10.1016/j.gr.2012.03.004.

Herron, M.M., 1997, Geochemical classification of terrigenous sands and shales from core or log data: Journal of Sedimentary Petrology, v. 58, no. 5, p. 820–829.

Jenner, G., Longerich, H.P., Jackson, S.E., and Fryer, B., 1990, ICP-MS – A powerful tool for high-precision trace-element analysis in Earth sciences: Evidence from analysis of selected U.S.G.S. reference samples: Chemical Geology, v. 83, p. 133–148.

Keppie, D.F., and Keppie, J.D., 2012, An alternative Pangea reconstruction for Middle America with the Chortis Block in the Gulf of Mexico: Tectonic implications: International Geology Review, v. 54, no. 14, p. 1685–1696. doi: 10.1080/00206814.2012.676361.

Keppie, J.D., 2004, Terranes of Mexico revisited: A 1.3 billion year odyssey: International Geology Review, v. 46, no. 9, p. 765–794.

Keppie, J.D., Dostal, J., Miller, B.V., Ortega-Rivera, A., Roldán-Quintana, J., and Lee, J.W.K., 2006, Geochronology and Geochemistry of the Francisco Gneiss: Triassic Continental Rift Tholeiites on the Mexican Margin of Pangea Metamorphosed and Exhumed in a Tertiary Core Complex: International Geology Review, v. 48, no. 1, p. 1–16.

Keppie, J.D., Dostal, J., Murphy, J.B., and Nance, R.D., 2008, Synthesis and tectonic interpretation of the westernmost Paleozoic Variscan orogen in southern Mexico: From rifted Rheic margin to active Pacific margin: Tectonophysics, v. 461, no. 1–4, p. 277–290. doi: 10.1016/j.tecto.2008.01.012.

Keppie, J.D., Nance, R.D., Dostal, J., Ortega-Rivera, A., Miller, B.V., Fox, D., Powell, J., Mumma, S., and Lee, J.W.K., 2004, Mid-Jurassic Tectonothermal Event Superposed on a Paleozoic Geological Record in the Acatlán Complex of Southern Mexico: Hotspot Activity During the Breakup of Pangea: Gondwana Research, v. 7, p. 239–260.

Keppie, J.D., Nance, R.D., Fernández-Suárez, J., Storey, C.D., Jeffries, T.E., and Murphy, J.B., 2006, Detrital Zircon Data from the Eastern Mixteca Terrane, Southern Mexico: Evidence for an Ordovician–Mississippian Continental Rise and a Permo-Triassic Clastic Wedge Adjacent to Oaxaquia: International Geology Review, v. 48, p. 97–111.

Keppie, J.D., Nance, R.D., Ramos-Arias, M.A., Lee, J.W.K., Dostal, J., Ortega-Rivera, A., and Murphy, J.B., 2010, Late Paleozoic subduction and exhumation of Cambro-Ordovician passive margin and arc rocks in the northern Acatlán Complex, southern Mexico: Geochronological constraints: Tectonophysics, v. 495, no. 3–4, p. 213–229.

Kerr, A., Jenner, G.A., and Fryer, B.J., 1995, Sm–Nd isotopic geochemistry of Precambrian to Paleozoic granitoid suites and the deep-crustal structure of the southeast margin of the Newfoundland Appalachians: Canadian Journal of Earth Sciences, v. 32, no. 2, p. 224–245. doi: 10.1139/e95-019.

Kirsch, M., Keppie, J.D., Murphy, J.B., and Lee, J.K.W., 2012a, Arc plutonism in a transtensional regime: The late Palaeozoic Totoltepec pluton, Acatlán Complex, southern Mexico: International Geology Review, iFirst, doi: 10.1080/00206814.2012.693247.

Kirsch, M., Keppie, J.D., Murphy, J.B., and Solari, L.A., 2012b, Permian–Carboniferous arc magmatism and basin evolution along the western margin of Pangea: geochemical and geochronological evidence from the eastern Acatlán Complex, southern Mexico: Geological Society of America Bulletin, v. 124, no. 9/10, p. 1607–1628. doi: 10.1130/B30649.1.

Kramer, B., 2008, Estratigrafía y geoquímica de las rocas magmáticas del Paleógeno en el occidente de Oaxaca y su significado petrogenético y tectónico [Ph.D. thesis]: México, Universidad Nacional Autónoma de México, 160 p.

Malone, J., Nance, R.D., Keppie, J.D., and Dostal, J., 2002, Deformational history of part of the Acatlán Complex: Late Ordovician-Early Silurian and Early Permian orogenesis in southern Mexico: Journal of South American Earth Sciences, v. 15, no. 5, p. 511–524.

Martini, M., Ferrari, L., López-Martínez, M., Cerca-Martínez, M., Valencia, V.A., and Serrano-Durán, L., 2009, Cretaceous–Eocene magmatism and Laramide deformation in southwestern Mexico: No role for terrane accretion, *in* Kay, S., Ramos, V.A., and Dickinson, W.R., eds., Backbone of the Americas: Shallow Subduction, Plateau Uplift, and Ridge and Terrane Collision, Geological Society of America Memoir 204, p. 151–182.

Martini, M., Ferrari, L., López-Martínez, M., and Valencia, V.A., 2010, Stratigraphic redefinition of the Zihuatanejo area, southwestern Mexico: Revista Mexicana de Ciencias Geológicas, v. 27, no. 3, p. 412–430.

Martini, M., Mori, L., Solari, L.A., and Centeno-García, E., 2011, Sandstone Provenance of the Arperos Basin (Sierra de Guanajuato, Central Mexico): Late Jurassic–Early Cretaceous Back-Arc Spreading as the Foundation of the Guerrero Terrane: The Journal of Geology, v. 119, no. 6, p. 597–617. doi: 10.1086/661989.

Marzoli, A., Renne, P.R., Piccirillo, E.M., Ernesto, M., Bellieni, G., and De Min, A., 1999, Extensive 200-million-year-old continental flood basalts of the Central Atlantic Magmatic Province: Science, v. 284, p. 616–618.

McCulloch, M., and Gamble, J.A., 1991, Geochemical and geodynamical constraints on subduction zone magmatism: Earth and Planetary Science Letters, v. 102, p. 358–374.

Miyashiro, A., 1974, Volcanic rock series in island arcs and active continental margins: American Journal of Science, v. 274, p. 321–355.

Morán-Zenteno, D.J., Caballero-Miranda, C., Silva-Romo, G., Ortega-Guerrero, B., and González-Torres, E., 1993, Jurassic-Cretaceous paleogeographic evolution of the northern Mixteca terrane, southern Mexico: Geofísica Internacional, v. 32, no. 3, p. 453–473.

Murphy, J.B., Keppie, J.D., Nance, R.D., Miller, B.V., Dostal, J., Middleton, M., Fernández-Suárez, J., Jeffries, T.E., and Storey, C.D., 2006, Geochemistry and U-Pb protolith ages of eclogitic rocks of the Asis Lithodeme, Piaxtla Suite, Acatlán Complex, southern Mexico: Tectonothermal activity along the southern margin of the Rheic Ocean: Journal of the Geological Society: London, v. 163, p. 683–695.

Ortega-Gutiérrez, F., 1975, The Pre-Mesozoic geology of the Acatlán area, south Mexico [Ph.D. Thesis]: UK, University of Leeds.

Ortega-Gutiérrez, F., 1978, Estratigrafía del Complejo Acatlán en la Mixteca Baja, Estados de Puebla y Oaxaca: Universidad Nacional Autónoma de México, Instituto de Geología Revista, v. 2, no. 2, p. 112–131.

Ortega-Gutiérrez, F., Elías-Herrera, M., Reyes-Salas, M., Macías-Romo, C., and López, R., 1999, Late Ordovician-Early Silurian continental collisional orogeny in southern Mexico and its bearing on Gondwana-Laurentia connections: Geology, v. 27, no. 8, p. 719–722.

Ortega-Obregón, C., Keppie, J.D., and Murphy, J.B., 2010a, Geochemistry of Carboniferous low metamorphic grade sedimentary and tholeiitic igneous rocks in the western Acatlán complex, southern Mexico: Deposition along the active western margin of Pangea: Revista Mexicana de Ciencias Geológicas, v. 27, p. 238–253.

Ortega-Obregón, C., Murphy, J.B., and Keppie, J.D., 2010b, Geochemistry and Sm–Nd isotopic systematics of Ediacaran–Ordovician, sedimentary and bimodal igneous rocks in the western Acatlán Complex, southern Mexico: Evidence for rifting on the southern margin of the Rheic Ocean: Lithos, v. 114, no. 1–2, p. 155–167. doi: 10.1016/j.lithos.2009.08.005.

Patchett, P.J., and Ruiz, J., 1987, Nd isotopic ages of crust formation and metamorphism in the Precambrian of eastern and southern Mexico: Contributions to Mineralogy and Petrology, v. 96, no. 4, p. 523–528.

Pearce, J.A., 1975, Basalt geochemistry used to investigate past tectonic environments on Cyprus: Tectonophysics, v. 25, p. 41–67.

Pearce, J.A., 1982, Trace element characteristics of lavas from destructive plate boundaries, *in* Thorpe, S.R., ed., Orogenic andesites and related rocks: Chichester, England, John Wiley and Sons, p. 525–548.

Pearce, J.A., 1983, Role of the sub-continental lithosphere in magma genesis at active continental margins, *in* Hawkesworth, M., and Norry, C., eds., Continental basalts and mantle xenoliths: Nantwich, Cheshire, Shiva Publications, p. 230–249.

Pearce, J.A., 1996, A user's guide to basalt discrimination diagrams, *in* Wyman, D.A., ed., Trace element geochemistry of volcanic rocks: Applications for Massive Sulphide Exploration: St John's, New Foundland, Geological Association of Canada, Short Course Notes. p. 79–113.

Pearce, J.A., Alabaster, T., Shelton, A., and Searle, M., 1981, The Oman Ophiolite as a Cretaceous Arc-Basin Complex: Evidence and Implications: Philosophical Transactions of The Royal Society of London Series A-Mathematical Physical and Engineering Sciences, v. 300, no. 1454, p. 299–317.

Pearce, J.A., and Cann, J., 1973, Tectonic setting of basic volcanic rocks determined using trace element analyses: Earth and Planetary Science Letters, v. 19, p. 290–300.

Pearce, J.A., and Norry, M., 1979, Petrogenetic implications of Ti, Zr, Y, and Nb variations in volcanic rocks: Contributions to Mineralogy and Petrology, v. 69, no. 1, p. 33–47.

Pindell, J.L., 1985, Alleghenian reconstruction and subsequent evolution of the Gulf of Mexico, Bahamas, and Proto-Caribbean: Tectonics, v. 4, no. 1, p. 1–39.

Pindell, J.L., and Dewey, J.F., 1982, Permo-Triassic reconstruction of western Pangea and the evolution of the Gulf of Mexico/Caribbean region: Tectonics, v. 1, no. 2, p. 179–211.

Pindell, J.L., Kennan, L., Stanek, K.-P., Maresch, W.V., and Draper, G., 2006, Foundations of Gulf of Mexico and Carribean evolution: Eight controversies resolved: Geologica Acta, v. 4, no. 1–2, p. 303–341. doi: 10.1029/2001JB000884.

Pindell, J.L., Maresch, W.V., Martens, U., and Stanek, K., 2012, The Greater Antillean Arc: Early Cretaceous origin and proposed relationship to Central American subduction mélanges: Implications for models of Caribbean evolution: International Geology Review, v. 54, no. 2, p. 131–143. doi: 10.1080/00206814.2010.510008.

Ramos, V.A., Cristallini, E.O., and Pérez, D.J., 2002, The Pangean flat-slab of the Central Andes: Journal of South American Earth Sciences, v. 15, p. 59–78.

Ramos-Arias, M.A., and Keppie, J.D.. 2011, U-Pb Neoproterozoic-Ordovician protolith age constraints for high- to medium-pressure rocks thrust over low-grade metamorphic rocks in the Ixcamilpa area, Acatlán Complex, southern Mexico: Canadian Journal of Earth Sciences, v. 48, no. 1, p. 45–61, doi: 10.1139/E10-082.

Rehkamper, M., and Hofmann, A.W., 1997, Recycled ocean crust and sediment in Indian Ocean MORB: Earth and Planetary Science Letters, v. 147, no. 1–4, p. 93–106. doi: 10.1016/S0012-821X(97)00009-5.

Rogers, R.D., Mann, P., and Emmet, P.A.. 2007, Tectonic terranes of the Chortis block based on integration of regional aeromagnetic and geologic data, *in* Mann, P. ed., Geologic and tectonic development of the Caribbean plate in northern Central America, Geological Society of America Special Paper 428, p. 65–88.

Ross, M.I., and Scotese, C.R., 1988, A hierarchical tectonic model of the Gulf of Mexico and Caribbean region: Tectonophysics, v. 155, p. 139–168.

Rubio-Cisneros, I.I., and Lawton, T.F., 2011, Detrital zircon U-Pb ages of sandstones in continental red beds at Valle de Huizachal, Tamaulipas, NE Mexico: Record of Early-Middle Jurassic arc volcanism and transition to crustal extension: Geosphere, v. 7, no. 1, p. 159–170. doi: 10.1130/GES00567.S1.

Ruiz, J., Patchett, P.J., and Arculus, R.J., 1988a, Nd-Sr isotope composition of lower crustal xenoliths – Evidence for the origin of mid-tertiary felsic volcanics in Mexico: Contributions to Mineralogy and Petrology, v. 99, p. 36–43.

Ruiz, J., Patchett, P.J., and Ortega-Gutiérrez, F., 1988b, Proterozoic and Phanerozoic basement terranes of Mexico from Nd isotopic studies: Geological Society of America Bulletin, v. 100, no. 2, p. 274–281.

Saunders, A.D., Norry, M.J., and Tarney, J., 1991, Fluid influence on the trace element compositions of subduction zone magmas: Philosophical Transactions – Royal Society of London, A, v. 335, no. 1638, p. 377–392.

Schaaf, P., Heinrich, W., and Besch, T., 1994, Composition and Sm-Nd isotopic data of the lower crust beneath San Luis Potosi, central Mexico: Evidence from a granulite-facies xenolith suite: Chemical Geology, v. 118, p. 63–84.

Shervais, J., 1982, Ti-V plots and the petrogenesis of modern and ophiolitic lavas: Earth and Planetary Science Letters, v. 59, no. 1, p. 101–118.

Silva-Romo, G., 2008, The Guayape-Papalutla fault system: A continuous Cretaceous structure from southern Mexico to the Chortis block? Tectonic implications: COMMENT and REPLY: Geology, v. 36, no. 1, p. 75–78, doi: 10.1130/G24032A.1.

Silva-Romo, G., Arellano-Gil, J., Mendoza-Rosales, C.C., and Nieto-Obregón, J., 2000, A submarine fan in the Mesa Central, Mexico: Journal of South American Earth Sciences, v. 13, p. 429–442.

Silva-Romo, G., and Mendoza-Rosales, C.C., 2000, La unidad Piedra Hueca secuencia clástica paleozoica (sur de Puebla), *in* GEOS, 2a Reunión Nacional de Ciencias de la Tierra, Resúmenes y Programa, Puerto Vallarta: Jalisco, Unión Geofísica Mexicana, v. 20, p. 325.

Silva-Romo, G., Mendoza-Rosales, C.C., Campos-Madrigal, E., and Centeno-García, E., 2011, Formación La Mora,

unidad estratigráfica nueva del Triásico en el Terreno Mixteca (noroeste de Huajuapán de León, Oax., México): Sedimentología y su significado, in Simposio en Honor del Dr. Zoltan de Cserna (Libro de Resúmenes): México, Universidad Nacional Autónoma de México, p. 114–115.

Stern, R.J., 2002, Crustal evolution in the East African Orogen: A neodymium isotopic perspective: Journal of African Earth Sciences, v. 34, p. 109–117.

Sun, S.-S., and McDonough, W.. 1989, Chemical and isotopic systematics of oceanic basalts: Implications for mantle composition and processes, *in* Saunders, A. and Norry, M. eds., Magmatism in the Ocean Basins: Geological Society Special Publication 42, p. 313–345.

Talavera-Mendoza, O., 2000, Mélanges in southern Mexico: Geochemistry and metamorphism of Las Ollas complex (Guerrero terrane): Canadian Journal of Earth Sciences, v. 37, p. 1309–1320.

Talavera-Mendoza, O., and Guerrero-Suastegui, M., 2000, Geochemistry and isotopic composition of the Guerrero Terrane (western Mexico): Implications for the tectonomagmatic evolution of southwestern North America during the Late Mesozoic: Journal of South American Earth Sciences, v. 13, p. 297–324.

Talavera-Mendoza, O., Ruiz, J., Gehrels, G.E., Meza-Figueroa, D., Vega-Granillo, R., and Campa-Uranga, M.F., 2005, U-Pb geochronology of the Acatlán Complex and implications for the Paleozoic paleogeography and tectonic evolution of southern Mexico: Earth and Planetary Science Letters, v. 235, p. 682–699.

Taylor, S.R., and McLennan, S.M., 1985, The Continental Crust: its composition and evolution: Oxford, Blackwell.

Taylor, S.R., and McLennan, S.M.. 1995, The geochemical evolution of the continental crust: Reviews of Geophysics, v. 33, no. 2, p. 241–265, doi: 10.1029/95RG00262.

Torres, R., Ruiz, J., and Patchett, P.J., 1999, Permo-Triassic continental arc in eastern Mexico: Tectonic implications for reconstructions of southern North America: Geological Society of America Special Paper, v. 340, p. 191–196.

Torres de León, R., Solari, L.A., Ortega-Gutiérrez, F., and Martens, U., 2012, The Chortis Block–southwestern Mexico connections: U-Pb zircon geochronology constraints: American Journal of Science, v. 312, no. 3, p. 288–313. doi: 10.2475/03.2012.02.

Valencia-Moreno, M., Ruiz, J., Barton, M.D., Patchett, P.J., Zürcher, L., Hodkinson, D.G., and Roldán-Quintana, J., 2001, A chemical and isotopic study of the Laramide granitic belt of northwestern Mexico: Identification of the southern edge of the North American Precambrian basement: Geological Society of America Bulletin, v. 113, no. 11, p. 1409–1422. doi: 10.1130/0016-7606(2001)113<1409:ACAISO>2.0.CO;2.

Vega-Granillo, R., Meza-Figueroa, D., Ruiz, J., Talavera-Mendoza, O., and López-Martínez, M., 2009, Structural and tectonic evolution of the Acatlán Complex, southern Mexico: Its role in the collisional history of Laurentia and Gondwana: Tectonics, v. 28, no. 4, p. 1–25. doi: 10.1029/2007TC002159.

Vega-Granillo, R., Talavera-Mendoza, O., Meza-Figueroa, D., Ruiz, J., Gehrels, G.E., and López-Martínez, M., 2007, Pressure-temperature-time evolution of Paleozoic high-pressure rocks of the Acatlán Complex (southern Mexico): Implications for the evolution of the Iapetus and Rheic Oceans: Geological Society of America Bulletin, v. 119, no. 9/10, p. 1249–1264.

Weber, B., Iriondo, A., Premo, W.R., Hecht, L., and Schaaf, P., 2007, New insights into the history and origin of the southern Maya block, SE Mexico: U-Pb-SHRIMP zircon geochronology from metamorphic rocks of the Chiapas massif: International Journal of Earth Sciences, v. 96, no. 2, p. 253–269. doi: 10.1007/s00531-006-0093-7.

Wilson, T.J., 1966, Are the structures of the Caribbean and Scotia arc regions analogous to ice rafting?: Earth and Planetary Science Letters, v. 1, no. 5, p. 335–338, doi: 10.1016/0012-821X(66)90019-7.

Winchester, J., and Floyd, P., 1977, Geochemical discrimination of different magma series and their differentiation products using immobile elements: Chemical Geology, v. 20, no. 4, p. 325–343.

Winchester, J., and Max, M., 1982, The geochemistry and origins of the Precambrian rocks of the Rosslare Complex, SE Ireland: Journal of the Geological Society: London, v. 139, p. 309–319.

Wood, D.A., 1979, A variably veined suboceanic upper mantle – Genetic significance for mid-ocean ridge basalts from geochemical evidence: Geology, v. 7, p. 499–503.

Yáñez, P., Patchett, P.J., Ortega-Gutiérrez, F., and Gehrels, G.E., 1991, Isotopic studies of the Acatlán Complex, southern Mexico: Implications for Paleozoic North American Tectonics: Geological Society of America Bulletin, v. 103, no. 6, p. 817–828.

4

TECTÓNICA EN LA PERIFERIA DE PANGEA DURANTE SU DESINTEGRACIÓN

Keppie, J.D., Galaz Escanilla, G., Helbig, M., y Kirsch, M. Amalgamation and Breakup of Pangæa: the type example of the supercontinent Cycle. En *International Geological Correlation Program Project #597: Late Paleozoic–Early Mesozoic of the Acatlán and Ayu complexes, southern Mexico: events on the periphery of Pangæa synchronous with amalgamation and breakup*, págs. 1–17. Geological Society of America, Cordilleran Section, 108th Annual Meeting (2012b)

CONTRIBUCIONES DE COAUTORES:

- J. Duncan Keppie: Organización y líder de la excursión, concepto y borrador la guía de la excursión, figuras 1 a 2
- Dr. Gonzalo Galaz-Escanilla: co-líder de la excursión, descripciones para las paradas 3–1 a 3–7; redacción de las figuras 7 a 8
- Maria Helbig: co-líder de la excursión, descripciones para las paradas 1–1 a 1–6; redacción de las figuras 3 a 5;
- Moritz Kirsch: co-líder de la excursión, descripciones para las paradas 2–1 to 2–8; redacción de la figura 6

GSA Cordilleran Section, 108th Annual Meeting
Field Trip 1
31 March–4 April 2012

Amalgamation and Breakup of Pangæa: the type example of the supercontinent Cycle

International Geological Correlation Program Project #597: Late Paleozoic–Early Mesozoic of the Acatlán and Ayu complexes, southern Mexico: events on the periphery of Pangæa synchronous with amalgamation and breakup

J. Duncan Keppie
Gonzalo Galaz-Escanilla
Departamento de Geología Regional, Insituto de Geología, Universidad Nacional Autónoma de México, 04510 Mexico, D.F.
Maria Helbig
Mortiz Kirsch
Centro de Geociencias, Universidad Nacional Autónoma de México, Campus Juriquilla, 76230 Querétaro, QRO, Mexico

INTRODUCTION

There is widespread acceptance that between 300 and 200 million years ago, all of the Earth's continental land masses were assembled into a giant supercontinent, Pangæa, surrounded by a superocean, Panthalassa. However, different configurations have been proposed, e.g., Pangæa A1, A2, B, and C (Fig. 1A). Reconstructions based on Mexican paleomagnetic data have been used to support both A and B models:

(a) PANGEA-A. A Permo-Triassic Pangea-A reconstruction where southern Mexico lies approximately in its present location relative to North America (Fang et al., 1989, Alva-Valdivia et al., 2002);

(b) PANGEA-B. A Pangea-B reconstruction placing southern Mexico off eastern Canada during the Jurassic (Fig. 1B: Böhnel, 1999).

There are also Middle American variants of the Pangea-A reconstruction:

(i) southwestern Mexico is placed either along the western margin of Pangea (Fig. 1C and 1D: Keppie, 2004, Keppie et al., 2008, 2010), or within Pangea between the Maya terrane and southern USA (Fig. 1E: Talavera-Mendoza et al.,2005, Vega-Granillo et al., 2007, 2009);

(ii) the Yucatan block is placed either within Pangea along the southern margin of USA (Fig. 1F: Pindell and Dewey, 1982), or on the western margin of Pangea during the mid-late Permian migrating into the Gulf of Mexico by the Middle Jurassic (Steiner, 2005);

(iii) the Chortis block has generally been placed off southwestern Mexico on the western marin of Pangea (Fig. 1E)(e.g., Pindell and Dewey, 1982), or within the within Pangea along the eastern margin of Mexico (Fig. 1G: Keppie and Keppie, in review).

On this field trip we will examine the evidence for subduction-related tectonics during the Pennsylvanian-Jurassic in the Ayu and Acatlán complexes, which suggests proximity to an ocean that is more consistent with the Pangea-A model (Fig. 2).

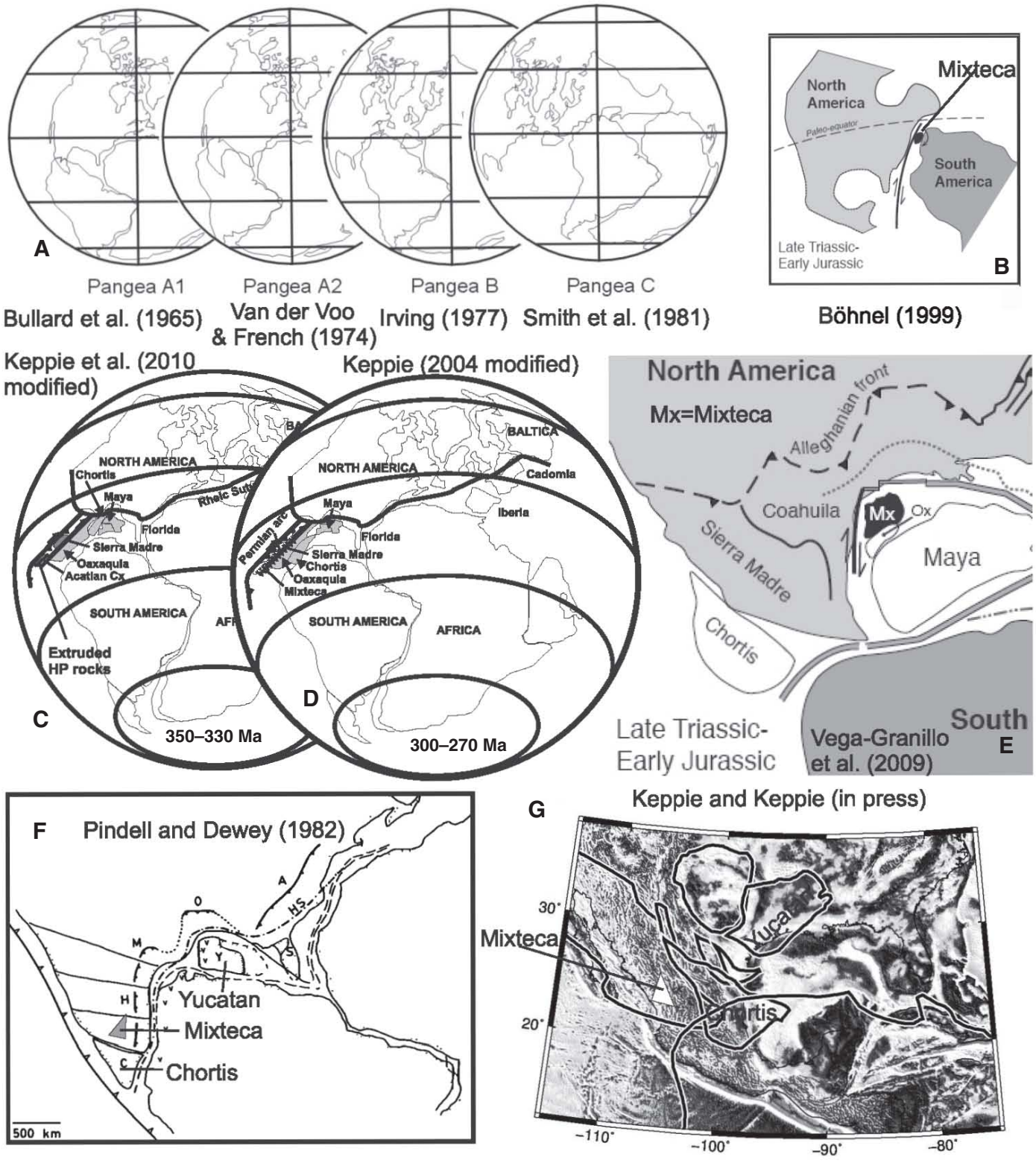

Figure 1. Reconstructions of Pangea by various authors.

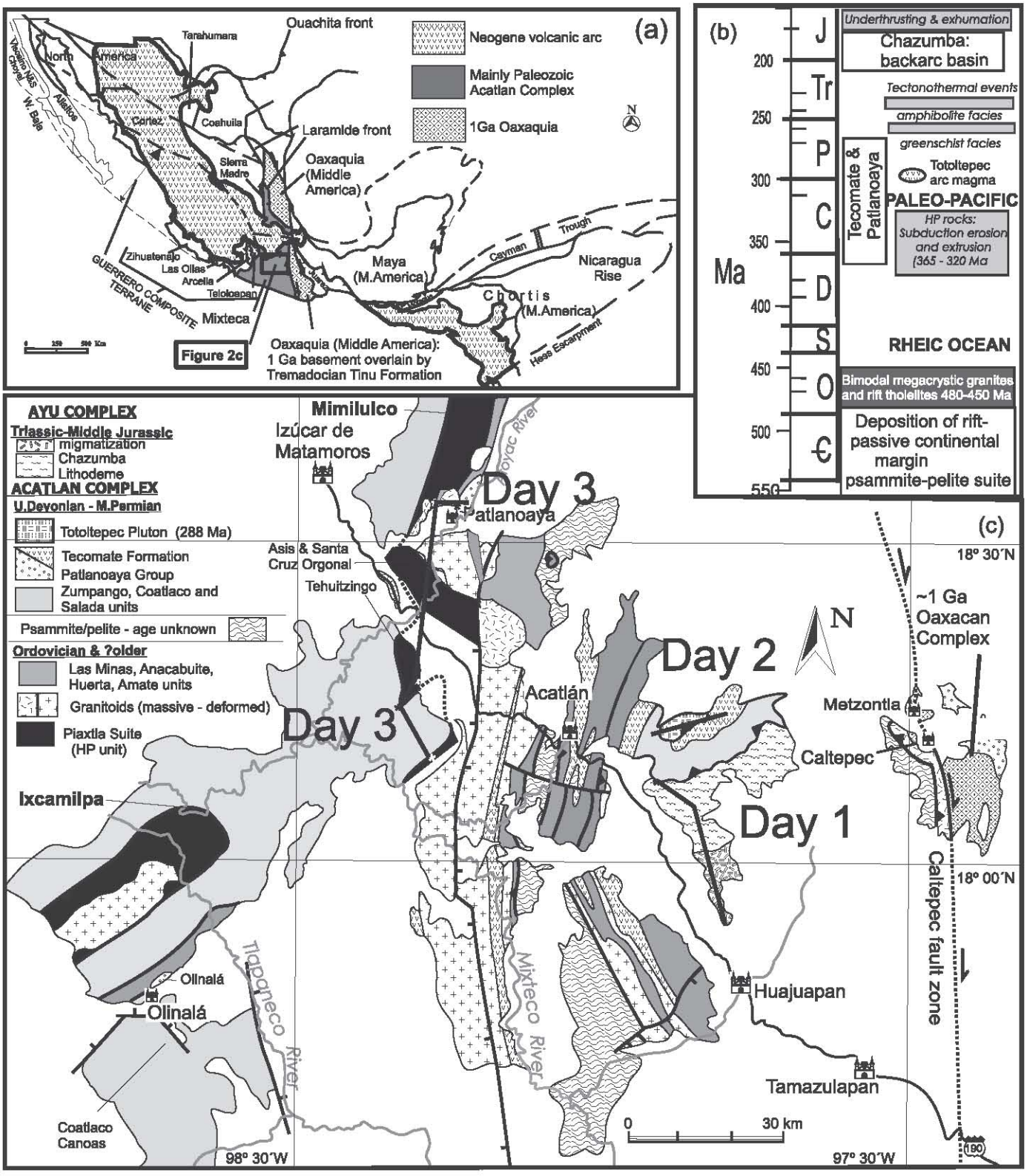

Figure 2. (A) Terranes of Middle America (after Keppie, 2004); (B) Ages od units in the Acatlán Complex; (C) Map of the Acatlán Complex (modified after Keppie et al., 2010) showing the field trip route.

DAY 1

Maria Helbig and J. Duncan Keppie

The Triassic-Jurassic Ayú Complex Southern Mexico: Evidence for Deposition on the Proximal Margin of a Backarc Basin, Underthrusting and Extrusion into the Acatlán Complex during the Breakup of Pangea-A

Helbig, M, Keppie, J.D., Murphy, J.B., and Solari, L.A., in press. U-Pb geochonological constraints on the Triassic–Jurassic Ayú Complex southern Mexico: derivation from the western margin of Pangea: Gondwana Research.

ABSTRACT

Rocks of the newly designated Ayú Complex are located in the eastern Mixteca terrane (southern Mexico), and comprise polyphase-deformed turbiditic rocks (Chazumba Lithodeme) that are intercalated with boudinaged ortho-amphibolites. In the south, the metasedimentary sequence is affected by partial melting and grades into the ~171 Ma Magdalena Migmatite. Migmatitzation was accompanied by 171–168 Ma granitoid minor intrusions and pegmatites with inherited zircon populations of ca. 260–290, 320–360, 420–480, 880–990, and 1080–1250 Ma that are also found in the Chazumba Lithodeme. Detrital U/Pb zircon ages from the migmatized and unmigmatized Chazumba Lithodeme yielded clusters of ca. 297, 266, 250, 214, 198, and 192 Ma, suggesting Upper Triassic—Lower Jurassic deposition. The MORB tholeiitic geochemistry of the amphibolites within the Chazumba Lithodeme indicates a back-arc environment with sedimentation occurring along the inboard rifted passive margin, the Upper Triassic–Lower Jurassic detrital zircons being derived from a contemporaneous, outboard magmatic arc. These characteristics suggest correlation with the lens-shaped Central terrane typified by the Potosi turbiditic fan in the rift-passive margin of Pangea that is absent west of the Mixteca terrane. The presence of this arc requires deposition adjacent to a subducting ocean and thus supports a Pangea-A reconstruction. Early Jurassic flattening of the subduction zone is inferred to have led telescoping of the Triassic–Early Jurassic back arc basin, during which the Chazumba Lithodeme was thrust beneath the Pangean margin where it was metamorphosed under amphibolite facies metamorphic conditions. It is further inferred that Middle-Upper Jurassic steepening of the subducting zone led to tectonic exhumation of the Chazumba Lithodeme by normal faulting along the reactivated Providencia Shear Zone. Deposition, underthrusting and exhumation of the Chazumba Lithodeme are synchronous with the breakup of Pangea and the opening of the Gulf of Mexico.

STOP 1-1 (W97.78834, N17.9387426: Fig. 3)
Location: Road between Sta. María Ayú and Ahuehuetitlán, riverbed of Río La Peña.

Micaceous schists and garnet-biotite gneisses are intercalated with boudinaged amphibolites, that underwent migmatization at ~171 Ma (leucosome dated by Keppie et al., 2004) and formed a mappable unit, called the Magdalena Migmatite. This tectonothermal event was accompanied by syntectonic intrusion of granitic, granodioritic and dioritic dikes and sheets (Yañez et al., 1991). A granite dike that cuts the paleosome yielded only one igneous zircon of 171 ± 4 (Middle Jurassic), whereas the rest of the dated grains are inherited zircons. Two paleosome samples of the Magdalena Migmatite yielded youngest detrital zircons of ~198 Ma (Early Jurassic) and 214 Ma (Late Triassic), respectively. Amphibolites were previously dated by Keppie et al. (2004) and showed $^{40}Ar/^{39}Ar$ cooling ages of 150 ± 2 Ma for biotite and 136 ± 2 for hornblende, suggesting rapid exhumation. Geochemically, amphibolites sampled across the Ayú Complex are MORB-like, rift-related tholeiites (Helbig et al., 2010). The majority of the ortho-amphibolites have jagged NMORB-normalized REE patterns that imply contamination either by a crustal and/or subduction component and suggest a formation in a back-arc basin.

STOP 1-2 (W97.807052°, N17.9987634°: Fig. 3)
Location: short road stop east of Tetaltepec.

Structural relationships in the Magdalena Migmatite: Large scale, close to open, upright to gently inclined parasitic fold (F_4) that folds the leucosome and boudinaged S_3-parallel granite sheets.

STOP 1-3 (W97.830789°, N18.036058°: Fig. 3)
Location: Riverbed, south of San Miguel Ixtápan.

Partially molten, and strongly deformed metasedimentary rocks that are intruded by granodiorites and pegmatites. Xenoliths are probably the metasedimentary host rock and show internal foliation as well as partial melting of the fertile domains. $^{40}Ar/^{39}Ar$ dating of a pegmatite and a granitic sheet yielded 167 ± 2 Ma for muscovite, and 155 ± 5 Ma for biotite (Keppie et al., 2004).

STOP 1-4 (W97.832239°,N18.0421378°: Fig. 3)
Location: Road section, south of San Miguel Ixtapan.

Outcrop exhibits a dike that cuts across the micaceous schists and feeds a granite sheet. The emplacement of the granite sheet is parallel to the main foliation, inflating the surrounding metapelitic host rock. The dike continues its way into the hanging metasedimentary host rock. Where in the contact with the host rock, the dike is overprinted by the same fabric as in the metasedimentary rocks. The rock is affected by later brittle normal block faulting. The fabric-parallel granite sheets show sharp contacts with the metapelites and exhibit minor pinch-and-swell structures and a distinct tectono-magmatic foliation at their margins suggesting stress-related emplacement.

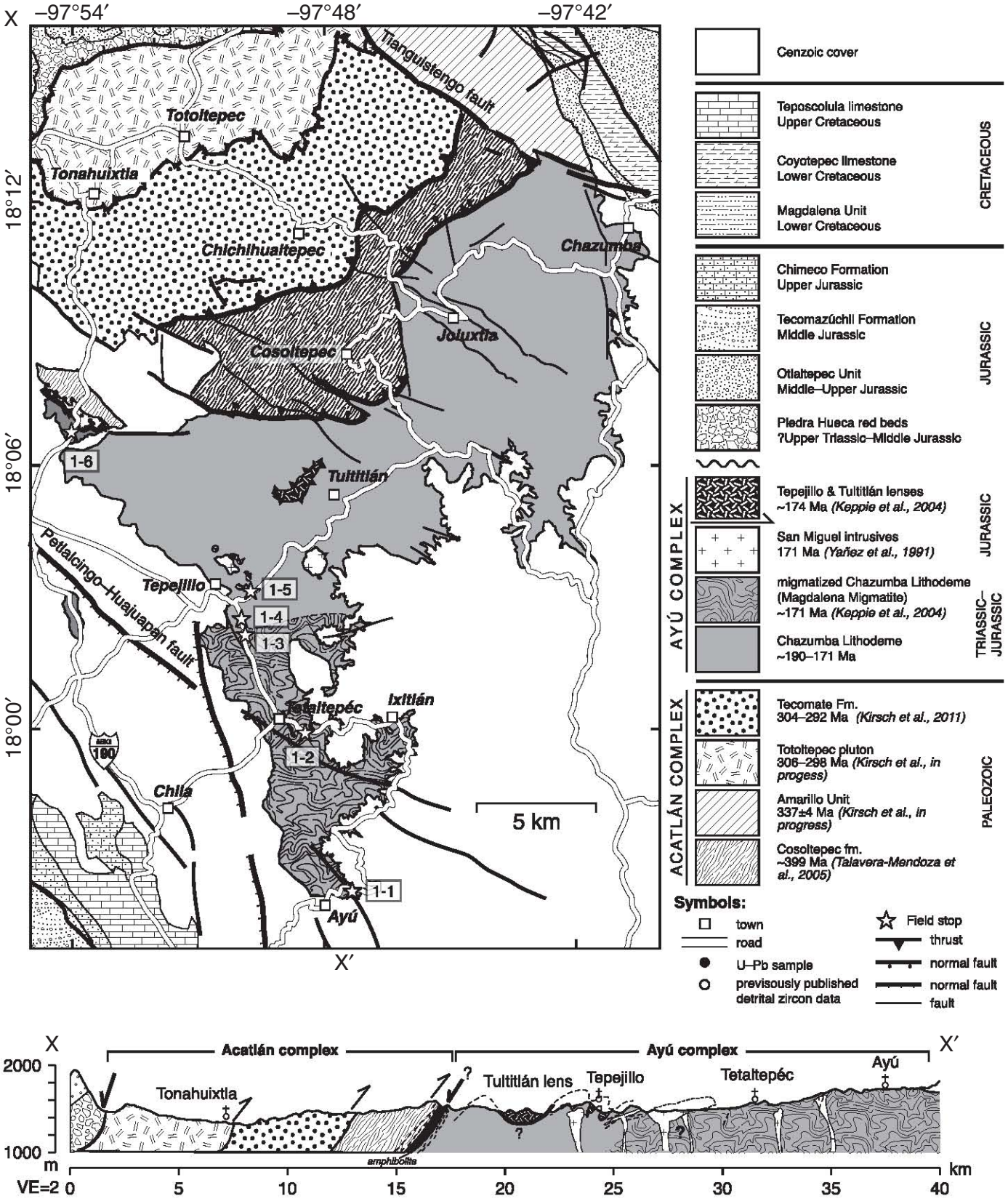

Figure 3. Geological map and section of the Totoltepec-Ayu area, southern Mexico showing field trip stops (modified after Helbig et al., in press).

STOP 1-5 (W97.828639°, N18.0526397°: Fig. 4)
Location: Foothills of the Cerro de La Peña (Cenozoic volcanic plug), north of Tejepillo; San Miguel Ixtapan road exit to Tultitlán.

Micaceous schists intercalated with minor quartzites are intruded by granites, leucogranitic and aplitic dikes. A granite dike cuts a tight, recumbent E-trending F_3 fold in the metasedimentary host rock. Small leucogranite veins that probably originate from the dike are parallel to the folded S_2 fabric. These relationships suggest that the intrusion was syn- to late-tectonic with respect to F_3. The granite is characterized by zircon inheritance and the crystallization age is inferred from the youngest grain with an age of 168 Ma. U-Pb detrital zircon analyses of a psammitic and a pelitic mica schist yielded maximum depositional ages of ~269 Ma and ~263 Ma (Middle Permian), respectively.

In the hanging wall, the mafic-ultramafic Tepejillo lens lies structurally as a nappe above the Chazumba Lithodeme (Keppie et al., 2004) and consists of four bodies that crop out along the foothills of Cenozoic volcanic plug (C. La Peña). The Tepejillo lens comprises coarse crystalline ultramafic (mainly dunite) to gabbroic rocks that are cut by diabase dikes. Geochemically, they are interpreted as part of a cumulatic body intruded into the lower continental crust (Keppie et al., 2004). The contact between the metasedimentary rocks of the Chazumba Lithodeme and the Tepejillo lens has been mapped as a folded thrust (Keppie et al., 2004). The Tultitán lens, 4 km to the northeast of the Tepejillo lens, consists of massive amphibolite and a core of metamorphosed norite. One concordant U-Pb LA-ICP-MS analysis of a prismatic tip of a euhedral zircon from a metanorite yielded an age of 174 ± 1 Ma, which is interpreted as age of intrusion for both lens (Keppie et al., 2004). Biotite from a gabbroic dike of the Tepejillo lens yielded a $^{40}Ar/^{39}Ar$ cooling age of 166 ± 2 Ma, whereas muscovite from a granite dike yielded a $^{40}Ar/^{39}Ar$ age of 161 ± 2 Ma (Keppie et al., 2004), suggesting excess argon in the biotite. Lower power increments of Late Cretaceous to Tertiary age can be observed in almost all $^{40}Ar/^{39}Ar$ analyses, implying that the Ayú Complex was affected by a later deformational event.

STOP 1-6 (W97.899842°, N18.113004°: Fig. 5)
Location: road section near the town La Providencia, on the road between Petlalcingo and Tonhuixtla.

Reactivation of a Triassic S-vergent thrust fault as a listric normal fault in the Middle-Late Jurassic. The Providencia shear zone forms a major structural feature between rocks of the Acatlán Complex (Tecomate Formation and Cosoltepec Formation) and the Ayú Complex and comprises weathered mylonites.

A micaceous metapsammite just south of the shear zone yielded only seventeen concordant analyses. Relatively narrow age spectra ranging from 194 to 339 Ma were obtained with the two youngest grains (190 ± 4, 193 ± 4 Ma) forming a mean of 192 ± 19 Ma (Early Jurassic). To the north of the shear zone, a mylonitic phyllite yielded a youngest detrital zircon age of 314 ± 4 Ma, which lies within the error of the mean of the three youngest grains with an age of 321 ± 30 Ma (Late Mississippian/Early Pennsylvanian). A graphite- and feldspar-bearing mylonitic metasedimentary rock, yielded two youngest detrital zircon ages of 281 ± 4 Ma and 295 ± 8 Ma with a mean age of 284 ± 71 Ma (Early Permian).

The presence of a major shear zone (Providencia Shear Zone) that separates the Acatlán Complex from the Ayú Complex was previously mapped as a thrust based on s-c fabrics in the hanging block (Malone et al., 2002; Keppie et al., 2004). However, $^{40}Ar/^{39}Ar$ cooling ages for amphibole of an amphibolite lens and muscovite from micaceous schists, north of the shearzone yielded cooling ages of ~214 Ma and ~224 Ma, respectively (Keppie et al., 2004). These fabrics are Late Triassic, and thus developed before or during the deposition of the Chazumba Lithodeme. It is envisaged that this Triassic shear zone was reactivated during or after the Middle Jurassic as a listric normal fault and formed the upper boundary of the exhuming Chazumba Lithodeme.

DAY 2
Moritz Kirsch and J. Duncan Keppie

Lower Permo-Carboniferous Arc Magmatism and Sedimentation on the Margin of Pangea-A

Kirsch, M., Keppie, J.D., Murphy, J.B., and Solari, L.A. in press. Permian-Carboniferous arc magmatism and basin evolution along the western margin of Pangea: geochemical and geochronological evidence from the eastern Acatlán Complex, southern Mexico: GSA Bulletin.

ABSTRACT

The Late Paleozoic evolution of Mexico records part of a continental arc that extends along the western margin of Pangea from western USA to the northern Andes. In the Acatlán Complex of southern Mexico, an arc assemblage consisting of a Permo-Carboniferous intrusion (Totoltepec pluton) and Permian sedimentary rocks (Tecomate Formation) offers a rare opportunity to examine events along the periphery of Pangea at the critical stage of final amalgamation.

The Totoltepec pluton ranges in composition from hornblendite and hornblende gabbro through diorite to tonalite, trondhjemite, granodiorite and monzo-granite. U-Pb LA-ICP-MS zircon analyses yield concordant ages of 306 ± 2 Ma in minor marginal mafic to ultramafic rocks and 289 ± 2 Ma for the main, more voluminous mafic to felsic intrusion. Major and trace element geochemistry of the Totoltepec rocks exhibit a tholeiitic to calc-alkaline character, high LILE/HFSE and flat REE patterns, which is typical of arc-related magmas. The precursor gabbroic rocks display εNd(t) values ranging from +1.3 to +3.3 (t = 306 Ma), whereas rocks from the main body of the pluton have εNd(t) values between −0.8 and +2.6 (t = 289 Ma).

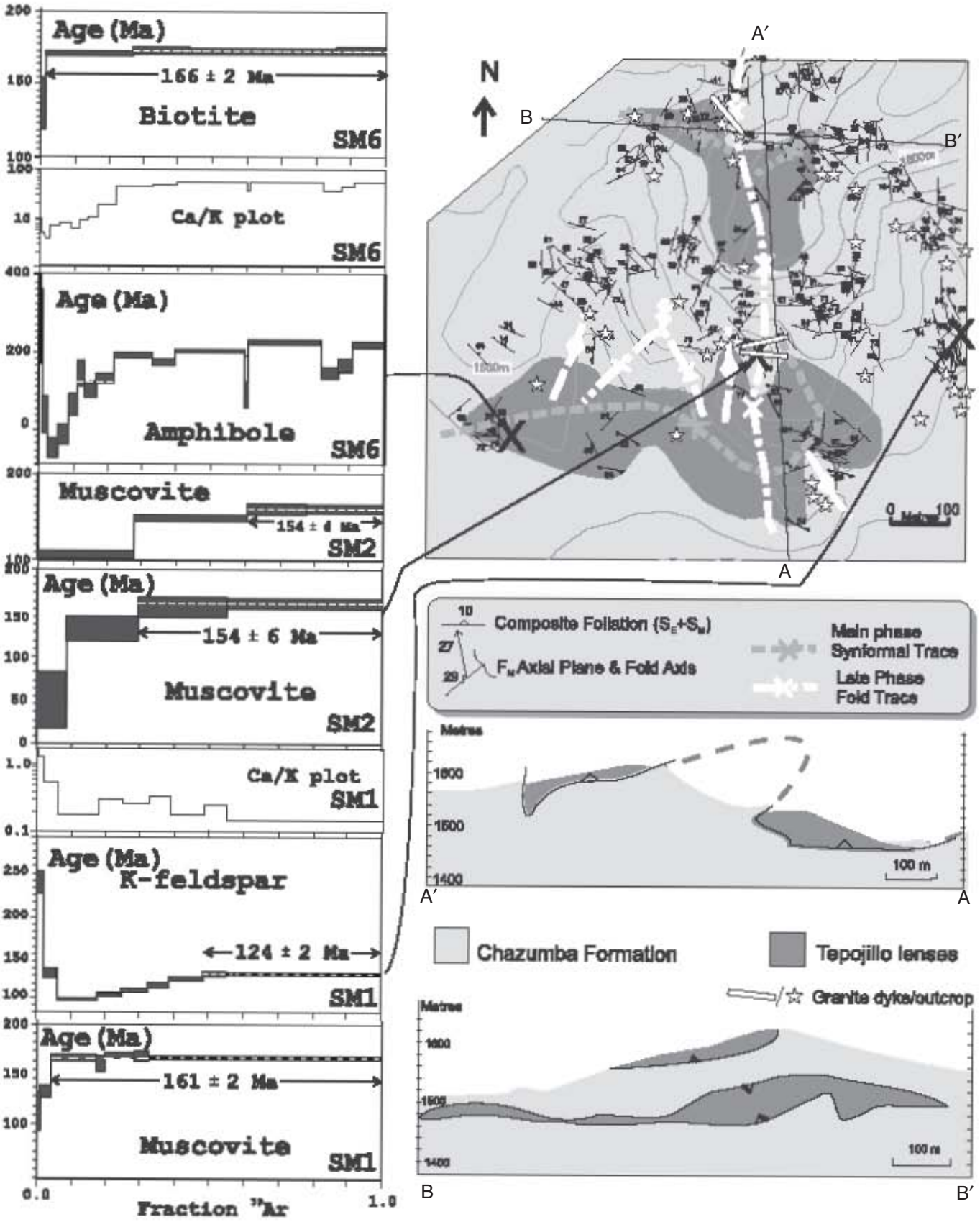

Figure 4. Stop 1-5: geological map, age data, and section of the Tepejillo ultramafic lens (after Keppie et al., 2004).

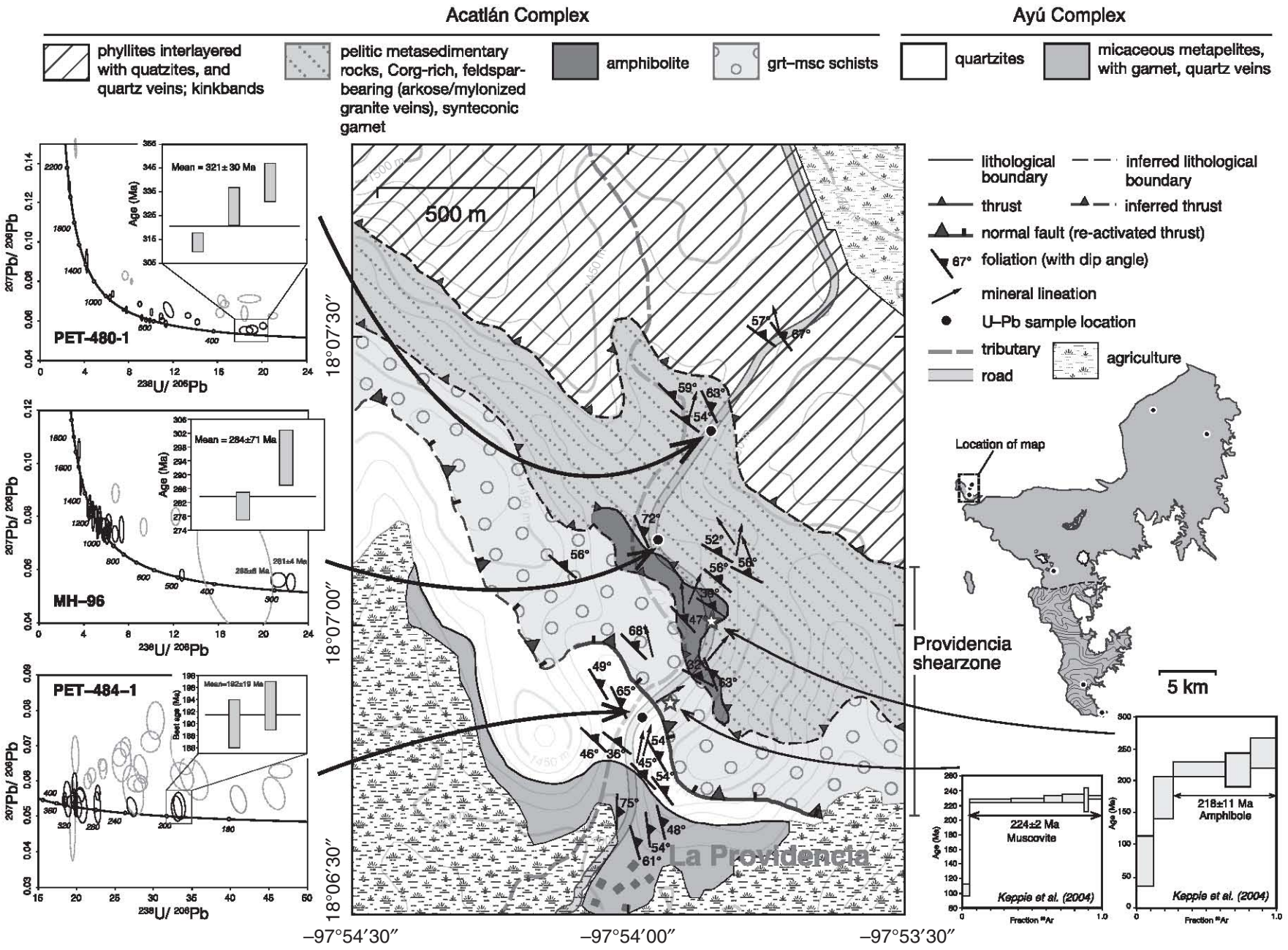

Figure 5. Stop 1-6: geological map and geochronology of the La Providencia shear zone (modified after Helbig et al., in press)

All of the samples are variably affected by wall rock assimilation, mixing and fractionation processes, but are more juvenile compared to contemporaneous arc-related igneous rocks in southern Mexico, suggesting the pluton was emplaced into thinner crust in a less mature part of the arc or along a fault that acted as a conduit for mantle-derived melts.

The Tecomate Formation consists of low-grade, poorly sorted, compositionally immature and largely unweathered metapsammites and metapelites. Several factors indicate derivation from the Permo-Carboniferous arc: (i) an arc-related geochemistry, (ii) εNd(t) values ranging from −5.7 to +0.3 (t = 280 Ma) that overlap those of the Totoltepec pluton, and (iii) detrital zircons with predominantly Permo-Carboniferous ages. The depositional age of the Tecomate Formation is constrained between the youngest detrital zircon population (ca. 280 Ma) and a published Ar/Ar age of 263 ± 3 Ma from the Tecomate Formation in the adjacent area. However, a metapsammite sample from the base of the Tecomate Formation yielded only Proterozoic zircons, indicating that deposition may have initiated earlier. Possible correlative sequences that may have been deposited in a similar peri-arc setting include the latest Pennsylvanian to Middle Permian Tecomate Formation type area, the latest Devonian to Lower Permian Patlanoaya Group, the Early to Middle Permian Tuzancoa Formation, the Middle Permian Los Hornos Formation, and the Olinalá Formation of Middle to Upper Permian age.

Kirsch, M., Keppie, J.D., Murphy, J.B. and Lee, J.K.W., in preparation. Structural history of the arc-related Totoltepec pluton, Acatlán Complex, southern Mexico: Syntectonic emplacement along a mid-crustal transpressional shear zone.

ABSTRACT

The 306–289 Ma tholeiitic to calc-alkaline Totoltepec pluton in the eastern Acatlán Complex, southern Mexico, is part of a Permo-Carboniferous continental magmatic arc along the western margin of Pangea. The pluton is a well-exposed, composite, felsic to ultramafic intrusive suite containing a conspicuous mesoscopic fabric, making it an ideal place to study the relationship between tectonic processes in magmatic arcs and pluton emplacement.

We use an integrated approach combining field observations, structural measurements, analysis of micro-fabrics, as well as Al-in-hornblende thermobarometry and $^{40}Ar/^{39}Ar$ thermochronology to decipher the structural evolution of the Totoltepec pluton. The data suggest that the pluton was emplaced in ~20 km depth and rapidly uplifted to allow it to cool to ~400 °C within 6 ± 2 Ma. The elongate pluton shape, parallel, decreasing temperature fabrics, similar crystallization and deformation ages and the rapid exhumation of the pluton speak for a syntectonic emplacement. A subvertical, fanning foliation and subhorizontal to subvertical lineations as well as the presence of internal, margin-parallel sinistral shear zones suggest emplacement along a transpressional fault. Hornblende-bearing diorites and tonalites within the low to medium-temperature solid-state domain in the southern part of the pluton exhibit a compositional and textural banding that is interpreted to have formed by a combination of steep igneous layering, layer-parallel dike injection and melt-enhanced deformation.

Although we were unable to document any regional-scale structures that may have controlled its intrusion, the timing and emplacement mechanism of the Totoltepec pluton is similar to that reported for syn-tectonic Late Carboniferous to Early Permian plutons along the Caltepec Fault zone that separates the Mixteca terrane from the Oaxacan Complex. Strike-slip tectonism along this fault may be associated with oblique subduction of the paleo-Pacific beneath the western margin of Pangea.

STOP 2-1. (W97.88385°, N18.214033°: Fig. 6)

Transpressional shear zone within the Totoltepec pluton near Santo Domingo Tonahuixtla. Here, strongly banded and foliated hornblende-bearing diorite and tonalite is intruded by felsic and mafic dikes at low angles to the WSW-striking planar fabric. Hornblende fish and asymmetrically boudinaged dikes consistently display sinistral kinematics. The crystallization age of the mafic rocks give an age of 289 ± 2 Ma (Keppie et al., 2004), whereas foliation-parallel muscovite in trondhjemite (1 km due SE) yield a $^{40}Ar/^{39}Ar$ age of 283 ± 1 Ma.

STOP 2-2 (W97.890711°, N18.208455°: Fig. 6)

Aplitic dikes intruding megacrystic hornblende diorite/ tonalite north of Santo Domingo Tonahuixtla. Dikes are mostly foliation-parallel, but are locally observed to cut the foliation at low angles. Some dikes contain an internal tectono-magmatic fabric parallel to the dike wall and dike-host contacts are sharp to irregular suggesting dike emplacement was syntectonic and occurred prior to complete crystallization of the host. The megacrystic hornblende-bearing rocks are laterally traceable. Whereas at this location, lineations are weakly developed or subhorizontal with sinistral kinematics, further east, between the villages of Tonahuixtla and Totoltepec, the rocks possess a strong down-dip mineral lineation and sigma-shaped tails on hornblende porphyroblasts suggest thrusting toward the south.

STOP 2-3 (W97.874964°, N18.207481°: Fig. 6)

Compositional/ textural banding in hornblende-bearing tonalites east of Tonahuixtla. Rocks at this stop have a mylonitic fabric and contain a conspicuous banding defined by a more or less rhythmic variation in grain size and modal proportions of feldspar and hornblende. Locally, these rocks exhibit gentle, ca. 2 m wavelength, fold-like structures resembling trough-banding characteristic of layered intrusions. These features indicate that the banding may have a complex, multi-stage history of development, involving magma chamber, injection as well as tectonic processes.

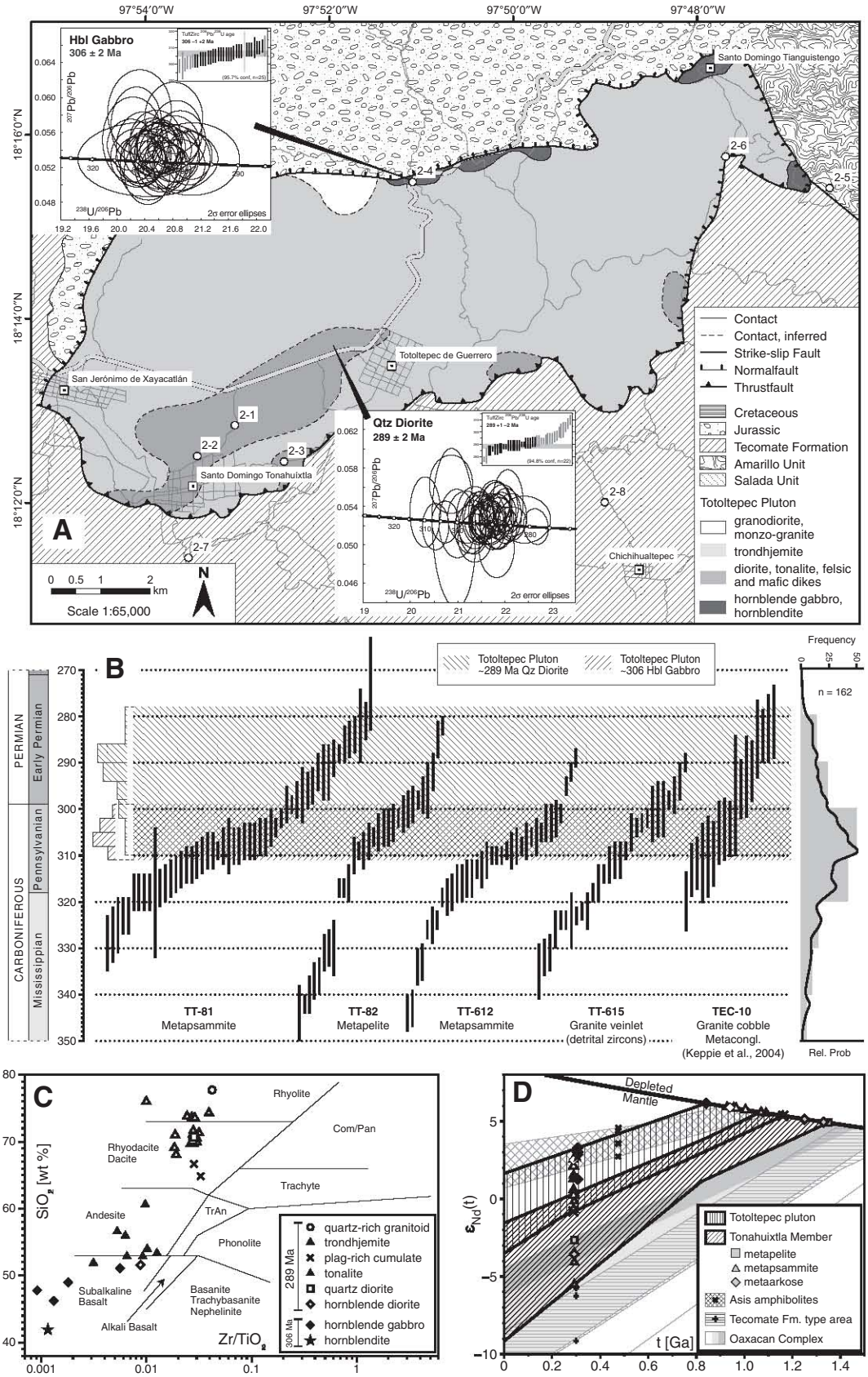

Figure 6. Stops 2-1 to 2-8: geological map of the Totoltepec pluton (after Kirsch et al., in press) showing field trip stops.

STOP 2-4 (W97.86816°, N18.218361°: Fig. 6)

Hornblende gabbro at the northern margin of the Totoltepec pluton in contact with Jurassic redbeds. This outcrop is located in one of three ca. 0.2–0.6 km^2, fault-bounded, precursor (306 ± 2 Ma) gabbroic phase, which is distributed along the northern and north-eastern margin of the pluton. Locally, these rocks are intruded by intensely deformed felsic dikes. To the north, the pluton is unconformably overlain by redbeds of inferred Jurassic age, which sit steeply against the pluton buttress due to a subsequent period of normal faulting.

STOP 2-5 (W97.851633°, N18.2581°: Fig. 6)

Amarillo Unit (new name), SE of Santo Domingo Tianguistengo. This unit is characterized by medium- to high-grade metasedimentary rocks locally intruded by amphibolite dikes. Youngest detrital zircons from a garnet schist sample indicate a maximum depositional age of 337 ± 4 Ma (Mississippian). The amphibolite dikes exhibit a MORB-like geochemistry with $\varepsilon_{Nd}(i)$ values of +5.2 to +7.6 and T_{DM} model ages between 333 and 433 Ma. These features are very similar to those documented in the Salada Unit (Morales-Gámez et al., 2008), on the western side of the Totoltepec pluton.

STOP 2-6 (W97.776016°, N18.257016°: Fig. 6)

Thrust contact between the Totoltepec pluton and the Tecomate Formation metasedimentary rocks. The exposed contact is a low-angle brittle-ductile thrust. At another location, this thrust is mylonitic and yielded a Middle Triassic $^{40}Ar/^{39}Ar$ age on muscovite. The contact is furthermore associated with a Fe-P-REE deposit containing the mineral association magnetite, apatite, barite, chlorite, quartz, chalcopyrite, and a cerium mineral. The mineralization is confined to two discrete, elongated bodies of ~100 m length coinciding with strong aeromagnetic anomalies.

STOP 2-7 (W97.794857°, N18.262697°: Fig. 6)

S-C fabrics in the Tecomate Formation ~1 km south of the margin of the Totoltepec pluton, indicating top-to-the-south thrusting. Thermochronological data from this area as well as other samples from the Tecomate Formation and Amarillo Unit reveal a regionally significant tectonothermal event of mid-Triassic age.

STOP 2-8 (W97.892266°, N18.190066°: Fig. 6)

Pebble metaconglomerates of the Tecomate Formation near Chichihualtepec. The pebbles from this outcrop, which are petrographically similar to the Totoltepec pluton trondhjemite, yielded zircons with ages between 320 and 264 Ma (Keppie et al., 2004). Morales-Gámez et al. (2009) conducted strain measurements in these rocks, documenting prolate spheroids typical of transtensional deformation. Rotated pebbles with asymmetric tails show top-to-the-south shear, which is consistent with other kinematic indicators in this area.

DAY 3

Gonzalo Galaz-Escanilla and J. Duncan Keppie

A High Pressure Zone within the Acatlán Complex: Uppermost Devonian: Lower Carboniferous Subduction and Extrusion under Extension during the Initial Stages of Pangea Amalgamation

Center of High Pressure Zone

Keppie, J.D., Nance, R.D., Dostal, J., Lee, J.K.W., and Ortega-Rivera, A. 2011 Constraints on the subduction erosion/extrusion cycle in the Paleozoic Acatlán Complex of southern Mexico: geochemistry and geochronology of the type Piaxtla Suite. Gondwana Research, doi:10.1016/j.gr.2011.07.020

ABSTRACT

The type high-pressure (HP) Piaxtla Suite in the Acatlán Complex of southern Mexico consists of retrogressed eclogite (amphibolite), megacrystic granitoids and high-grade metasedimentary rocks. Exhumation of these HP rocks has recently been interpreted as the result of extrusion into the upper plate, rather than by return flow up the subduction zone. Geochemical analyses of the retrograde eclogites indicate that they have a rift tholeiitic-transitional alkalic composition. These are closely associated with a megacrystic meta-granitoid that has yielded an intrusive age of 452 ± 6 Ma (concordant U-Pb zircon analyses) with inherited zircon populations at ca. 800–950 Ma and 1000–1200 Ma derived from the underlying basement, probably the Oaxacan Complex which borders the Acatlán Complex to the east. The bimodal nature of these igneous rocks and their close association with continentally-derived sedimentary rocks is similar to most HP rocks in the Acatlán Complex derived from a rifted passive margin. The youngest detrital zircon population in a metapsammite sample yielded an U-Pb age of 365 ± 15 Ma with older analyses distributed along a chord with an upper intercept of 1287 ± 29 Ma. The ca. 365 Ma age provides a maximum age for the time of deposition of this sample. $^{40}Ar/^{39}Ar$ ages from the retrogressed eclogites provided hornblende plateau ages of 342 ± 2 Ma and 344 ± 2 Ma, whereas muscovite from the granitoid and metapsammite yielded 334 ± 2 Ma plateau ages. These data constrain the subduction erosion-extrusion cycle to ≤35 my during which the rocks were taken to a depth of ca. 40 km at a rate of 2.7 km/my and back to the surface at 2.4 km/my. Such exhumation rates are slower than those in continent-continent collision zones, but similar to those in the Iberia-Czech Variscan belt where tectonic interpretation also suggests extrusion into the upper plate.

Western Boundary of High Pressure Zone: A High-Pressure Folded Klippe Explaced during the Lower Carboniferous at Tehuitzingo

Galaz E., Gonzalo, et al., in press. A high-pressure folded klippe at Tehuizingo on the western margin of an extrusion zone, Acatlán Complex, southern Mexico

ABSTRACT

The Acatlán Complex is divided into two blocks of low-grade metamorphic rocks by a central belt of high-pressure (HP) rocks, which at Tehuitzingo is composed of metabasites, serpentinite, granite and mica schist. 580–430 Ma detrital zircon ages indicate that these rocks were deposited adjacent or very close to the Gondwana supercontinent during the Early Paleozoic and are more consistent with a development on the southern margin of the Rheic Ocean rather than the Iapetus Ocean. These rocks were then removed by a subduction-erosion to depths of ~50km, reaching a metamorphic peak of ~16 kbar and 750 °C (eclogite facies). The HP rocks underwent rapid extrusion during a major Late Devonian-Pennsylvanian tectonothermal event indicated by $^{40}Ar/^{39}Ar$ analyses, which yielded ages of ~373 Ma (hornblende in metabasite) and of 328–317 Ma (muscovite in granite, mica schist and metabasite) that indicate cooling through ~570 °C and ~350 °C respectively, indicating a very high cooling rate of ~4.9–3.9 °C/m.y. During the extrusion process these rocks were affected by retrogression to amphibolite-epidote and green schist facies, and finally emplaced as a klippe on a greenschist facies psammite-pelite unit that constitutes the western block of the Acatlán Complex. Petrologic, deformational and geothermobarometric data suggest that west and east blocks belong to the same terrane, indicating that a subduction-erosion process and subsequent extrusion is more consistent with the genesis of the HP central belt than a collisional event as has been proposed. The P-T-t pattern of these HP rocks is consistent with subduction environments reported elsewhere in the world and suggests a serpentinite extrusion channel on the western margin of Pangea.

Eastern Boundary of High Pressure Zone: A Listric Normal Shear Zone Synchronous with Deposition of the Uppermost Devonian–Lower Permian Patlanoaya Group

Keppie, J.D., Nance, R.D., Ramos-Arias, M.A., Lee, J.K.W., Dostal, J., Ortega-Rivera, AQ., and Murphy, J.B. 2010. Late Paleozoic subduction and exhumation of Cambro-Ordovician passive margin and arc rocks in the northern Acatlán Complex, southern Mexico: geochronological constraints. Tectonophysics, v. 495, p. 213–229.

ABSTRACT

The origin and age of high pressure (HP) rocks is crucial for paleogeographic reconstruction because they either mark an oceanic suture or an extrusion zone within the upper plate. HP rocks in the San Miguel Las Minas area in the northern part of the complex has been inferred to be of early Paleozoic age and to mark oceanic sutures. However, blueschists in the northern part of the Acatlán Complex in southern Mexico have yielded Mississippian $^{40}Ar/^{39}Ar$ plateau ages of 344 ± 5 Ma for glaucophane and 338 ± 3 Ma and 337 ± 2 Ma for muscovite. These ages are slightly younger than recently published ages: a U-Pb zircon age of 353 ± 1 Ma from associated eclogite, and a 347 ± 3 Ma muscovite age from the tectonically overlying, greenschist facies Las Minas Unit. Taken together, these data indicate rapid cooling between 700° and 340°C in ca. 17 Myr. On the other hand, associated Ordovician Anacahuite Amphibolite cooled through ca. 500°C at 299 ± 6 Ma ($^{40}Ar/^{39}Ar$ on hornblende) suggesting a second, Permian period of exhumation. Protoliths of the high grade rocks include Cambrian-Ordovician, rift-passive margin, psammites, pelites, and tholeiitic dykes, an Ordovician mafic intrusion (Anacahuite Amphibolite dated at 470 ± 10 Ma: U-Pb zircon) and megacrystic granite (dated at 492 ± 12 Ma: U-Pb zircon), and arc-related mafic rocks of unknown age. These upper plate rocks are inferred to have been removed by subduction erosion and taken to depths between 35 and 55 km where they underwent blueschist-eclogite facies metamorphism. This was followed by rapid extrusion along a channel bounded by an easterly dipping, Mississippian, listric normal shear zone, and a thrust modified by a Permian dextral fault. Rocks above and below the extrusion zone are mainly Cambro-Ordovician rift-passive margin units, but a small vestige of the arc preserved as dikes cutting rocks lying unconformably beneath the fossiliferous latest Devonian-Lower Permian Patlanoaya Group. Since faunal data indicate that Pangea had amalgamated by the Mississippian, at which time the Acatlán Complex lay 1500–2000 km south of the Ouachita collisional orogen between Gondwana and Laurentia, it is inferred that subduction and extrusion of the high pressure rocks occurred on the active western margin of Pangea.

Ramos-Arias, M., Keppie, J.D., Ortega-Rivera, A., and Lee, J.W.K. 2008. Extensional late Paleozoic deformation on the western margin of Pangea, Patlanoaya area, Acatlán Complex, southern Mexico. Tectonophysics, v. 448, p. 60–76.

ABSTRACT

New mapping in the northern part of the Paleozoic Acatlán Complex (Patlanoaya area) records several ductile shear zones and brittle faults with normal kinematics (previously thought to be thrusts). These movement zones separate a variety of units that pass structurally upwards from: (i) blueschist-eclogitic metamorphic rocks (Piaxtla Suite) and mylonitic megacrystic granites (Columpio del Diablo granite ≡ Ordovician granites elsewhere in the complex); (ii) a gently E-dipping, listric, normal shear zone with top to the east kinematic indicators that formed under upper greenschist to lower amphibolite conditions; (iii) the Middle-Upper Ordovician Las Minas quartzite (upper greenschist facies psammites with minor interbedded pelites intruded by mafic dikes

and a leucogranite dike from the Columpio del Diablo granite) unconformably overlain by the Otate meta-arenite (lower greenschist facies psammites and pelites): roughly temporal equivalents are the Middle-Upper Ordovician Mal Paso unit and prelatest Devonian Ojo de Agua unit (interbedded metasandstone and slate, and metapelite and mafic minor intrusions, respectively)—the Otate and Mal Paso units are intruded by the massive, 461 ± 2 Ma, Palo Liso megacrystic granite: decussate, contact metamorphic muscovite yielded a $^{40}Ar/^{39}Ar$ plateau age of 440 ± 4 Ma; (iv) a steeply-moderately, E-dipping normal fault; (v) uppermost Devonian-Lower Permian sedimentary rocks (Patlanoaya Group: here elevated from formation status). The upward decrease in metamorphic grade is paralleled by a decrease in the number of penetrative fabrics, which varies from (i) three in the Piaxtla Suite, through (ii) two in the Las Minas unit (E-trending sheath folds deformed by NE-trending, subhorizontal folds with top to the southeast asymmetry, both associated with a solution cleavage), (iii) one in the Otate, Mal Paso, and Ojo de Agua units (steeply SE-dipping, NE-SW plunging, open-close folds), to (iv) none in the Patlanoaya Group. $^{40}Ar/^{39}Ar$ analyses of muscovite from the earliest cleavage in the Las Minas unit yielded a plateau age of 347 ± 3 Ma and show low temperature ages of ~260 Ma. Post-dating all of these structures and the Patlanoaya Group are NE-plunging, subvertical folds and kink bands. An E-W, vertical normal fault juxtaposes the low-grade rocks against the Anacahuite amphibolite that is cut by megacrystic granite sheets, both of which were deformed by two penetrative fabrics. Amphibole from this unit has yielded a $^{40}Ar/^{39}Ar$ plateau age of 299 ± 6 Ma, which records cooling through ~490 °C and is probably related to a Permo-Carboniferous reheating event during exhumation. The extensional deformation is inferred to have started in the latest Devonian (~360 Ma) during deposition of the basal Patlanoaya Group, lasting through the rapid exhumation of the Piaxtla Suite at ~350–340 Ma synchronous with cleavage development in the Las Minas unit, deposition of the Patlanoaya Group with active fault-related exhumation suggested by Mississippian and Early Permian conglomerates (~340 and 300 Ma, respectively), and continuing at least into the Middle Permian (≡ 260 Ma muscovite ages). The continuity of Mid-Continent Mississippian fauna from the USA to southern Mexico suggests that this extensional deformation occurred on the western margin of Pangea after closure of the Rheic Ocean.

STOP 3-1 (N18° 11.728′, W98° 14.690′ to N18° 11.652′, W98° 15.065′: Fig. 2)

Contact between a deformed, Ordovician megacrystic granitoid, a Tertiary dike, and the HP Piaxtla Suite at Piaxtla.

STOP 3-2 (UTM: 1405110/2023872: Fig. 7)

Thrust contact between Tehuitzingo serpentinite and polydeformed psammitic-pelitic rocks at Solozuchitl near Atopoltitlan.

The Piaxtla serpentinites are composed almost entirely of secondary minerals. Decussate, acicular and fibrous crystals serpentine aggregates make up 95% of the rock, magnetite, calcite, white mica and talc, and accessory chromite, clinochlore, undulose quartz, amphibole and epidote. This serpentinite are thrust over the low grade psammite-pelite unit along a gently NW-dipping thrust (320/15°), on which there are striae that plunge westwards (290/12°): associated recumbent folds, S-C fabrics and thrust horses indicate thrusting toward the west. Cutting across this thrust zone are several N-S vertical faults with subhorizontal striae.

The low grade psammite-pelite unit (498 ± 2 Ma, U-Pb detrital zircon; Galaz-Escanilla et al., in press) is composed mainly of primary minerals such as quartz, feldspar and zircon (accessory), which suggests a medium-grained quartz-arenitic (0.25–0.5 mm) and shaly (<0.06 mm grain size) protoliths respectively. The equilibrium secondary mineralogy is composed of quartz, albite ($Ab_{99–100}$), Mg-Fe-chlorite (ripidolite type), phengite, epidote, calcite and leucoxene, whose geothermobarometry indicated P-T conditions of ~2.7 kbar and ~350 °C (greenschist facies; Galaz-Escanilla and Keppie, in press).

STOP 3-3 (UTM: 140571085/2023811: Fig. 7)

Serpentinite, amphibolite, metabasite, Ordovician granitic and psammitic-pelitic rocks along the eastern margin of the Tehuitzingo serpentinite at Tecolutla.

In Tecolutla area outcrop a HP unit (eclogitic facies) that mainly consists of serpentinized harzburgite with small marginal fault blocks of metabasite, metagranitoid (485 ± 3 Ma, U-Pb zircon age: Galaz-Escanilla et al., in press) and mica schist (433 ± 3 Ma, U-Pb detrital zircon: Galaz-Escanilla et al., in press) juxtaposed by N-S structures. The serpentinized harzburgites contain elliptical metabasite lenses up to several meters in size, which have fine grained margins that may reflect an original intrusive relationship. The long axes of the elliptical lenses are parallel to the foliation indicating ductile deformation. On the other hand, the high-grade metasediments have a composite foliation where S_1 is parallel to a second S-C foliation with the S_2 planes subparallel to the border of the block and oriented ~128/27° (dip direction/dip angle), and C_2 planes oriented ~147/58°.

The HP unit is tectonically juxtaposed against a low grade psammite-pelitic unit along N-S structures. This unit has a planar fabric composed mainly of white mica and chlorite evidencing a low-temperature (greenschist) ductile deformation.

The geothermobarometry suggests a common prograde metamorphic history for the Tehuitzingo HP rocks: (a) a metamorphic peak eclogite facies of zoisite-amphibole, with a temperature of ~750 °C and a pressure of ~16 kbar; (b) retrogression to amphibolite-epidote facies, with a temperature of ~472 °C and variable pressures between ~7.1–3.4 kbar; (c) retrogression to greenschist facies with a temperature of ~360 °C and whose pressures were not obtained (Galaz-Escanilla et al., in press). The Piaxtla serpentinite contains three types of serpentine group minerals:

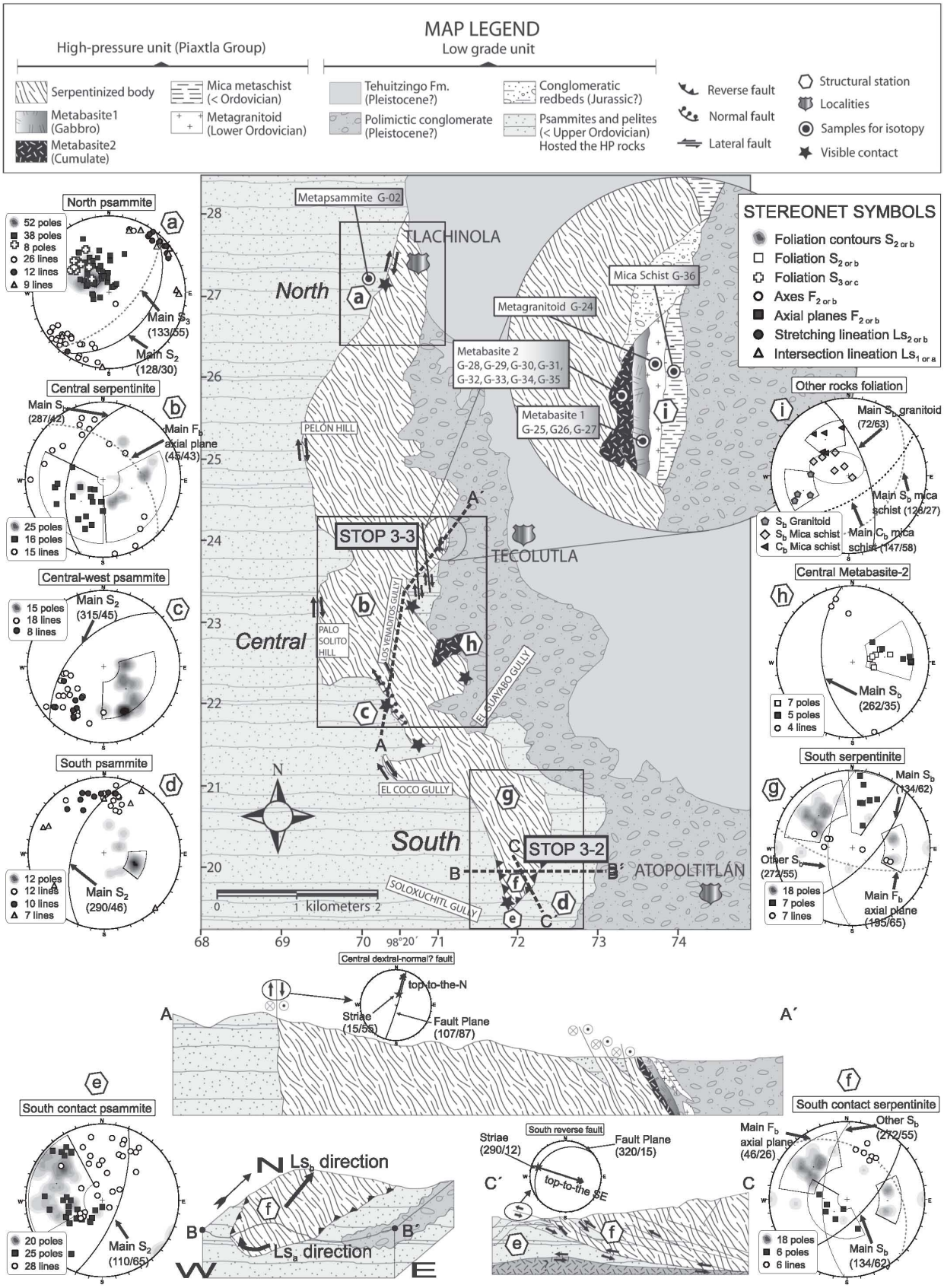

Figure 7. Stops 3-2 and 3-3: geological map, structural data, and section (after Galaz-Escanilla et al., in press).

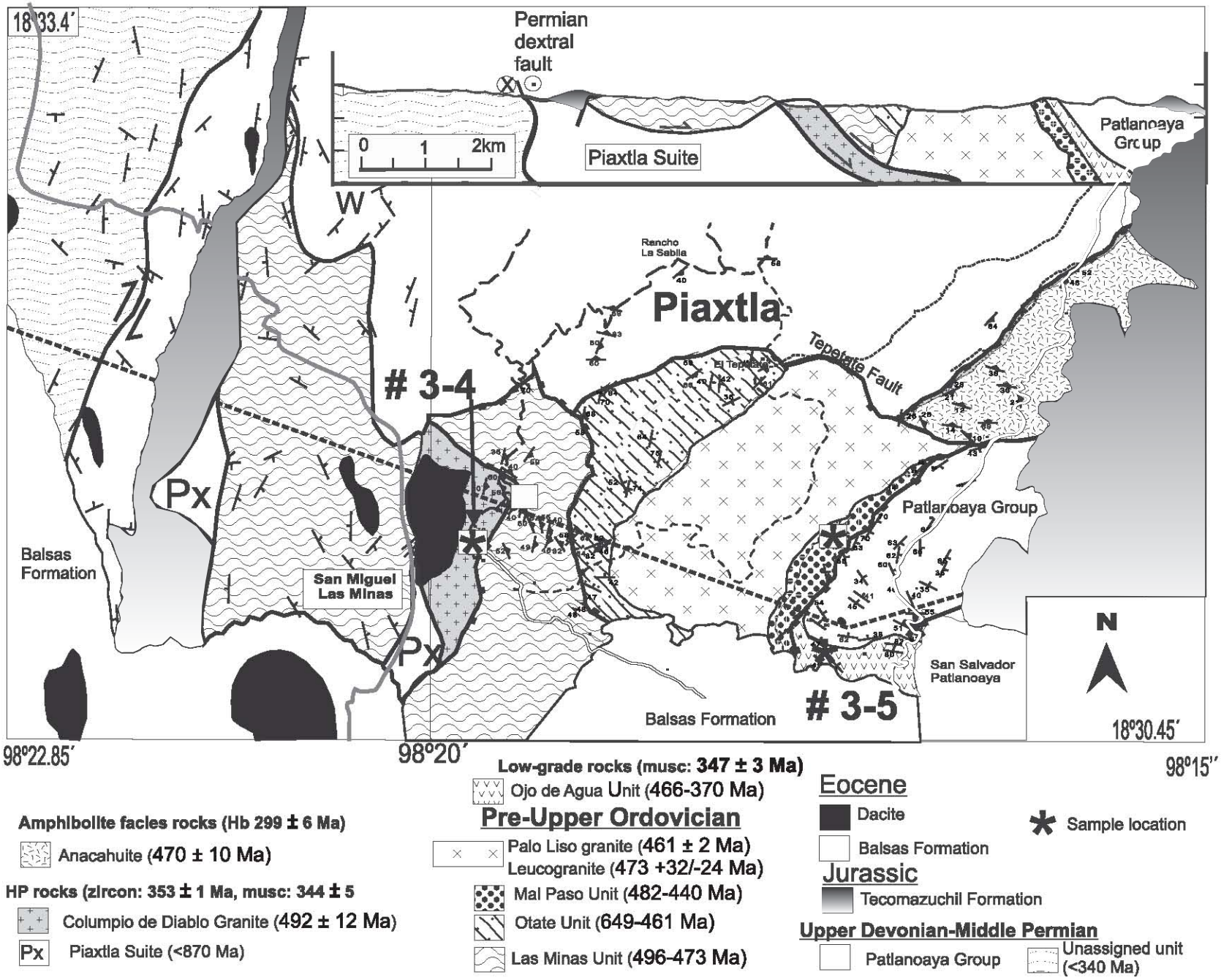

Figure 8. Stops 3-4, 3-5, 3-6 and 3-7: geological map and section (after Keppie et al., 2010).

chrysotile, lizardite and antigorite. Based on the stability field of the latter was estimated a P-T peak of ~550 °C and ~9 kbar (González-Mancera, 2001), however, has been reported in subduction zones antigorite reaching ~720 °C and high pressures of ~20 kbar (Ulmer and Trommsdorff, 1995).

The geochemistry data of the eclogitic mafic rocks indicate that these rocks have an arc affinity (author´s unpublished data). The P-T-t pattern of these rocks is consistent with subduction environments and serpentinite subduction channel exhumation (e.g., Guillot et al. 2009), where the driving forces for exhumation are a combination of buoyancy and channel flow coupled with underplating of slabs.

STOP 3-4 (N18° 31.051′, W98° 19.733′: Fig. 8)

Listric normal shear zone between megacrystic, Columpio del Diablo granitoid and Ordovician Las Minas unit.

The Columpio del Diablo megacrystic granite (492 ± 12 Ma, U-Pb zircon age: Keppie et al., 2010) consists of blastomylonitic granite containing quartz, K-feldspar (perthitic orthoclase), white mica, chlorite, epidote, and accessory opaque minerals. The megacrystic granite is cut by thin leucogranite sheets that consist mainly of quartz and potassium feldspar and are inferred to be a late differentiates of the granite. Structurally, the granite varies from an L-tectonite to an L-S tectonite with kinematic indicators, such as σ fabrics associated with the feldspars and generally vertical, extensional, quartz-filled fractures within the feldspars that indicate top-to-east movement along the contact with the Las Minas Unit: a minor, brittle fault has been superimposed on the contact. The Las Minas unit consists predominantly of polydeformed, low-grade psammites interbedded with thin pelitic phyllites, and intruded by many tholeiitic mafic dikes and sills (Keppie et al., 2008). The psammites consist mainly of quartz with minor muscovite, chlorite, and K-feldspar, and accessory zircon, whereas the phyllites are composed of muscovite, chlorite, quartz, and opaque minerals. The youngest concordant detrital zircon is dated at 496 ± 25 Ma (Keppie et al., 2008) The mafic intrusions contain amphibole (tremolite-actinolite), chlorite, epidote, quartz, plagioclase, muscovite, and accessory calcite, and opaque minerals. $^{40}Ar/^{39}Ar$ analyses of muscovite from the earliest cleavage in the Las Minas unit yielded a plateau age of 347 ± 3 Ma (Mississippian) and show low temperature ages of ~260 Ma.

STOP 3-5 (N18° 30.351′, W98° 17.57′: Fig. 8)

The Cerro Puntiagudo Formation of Strunian age (latest Devonian) is 63 m thick and consists of shale, sandstone, and limestone. It is overlain by conglomerates of the Potrerillo Formation (124 m thick) that consists of red sandstone with Oseagean fossils and conglomerate with large K-feldspar clasts: these clasts are inferred to have been derived from the nearby megacrystic granitoids. The Cerro Puntiagudo Formation rests unconformably upon the Ojo de Agua unit, which consists of finely bedded, black pelitic rocks intruded by green, fine grained, mafic dikes with an arc-related chemistry. These latter rocks are deformed by isoclinal, upright-steeply inclined, NE- and SE-trending, subhorizontal folds. The youngest detrital zircons in this unit are 466 ± 25 Ma (Keppie et al., 2008), abd 471 ± 9 Ma (Keppie et al., 2010).

STOP 3-6 (N18° 30.66′ W98° 17.78′: Fig. 8)

The La Junta Formation is a 126 m thick shale unit containing Missourian fossils; the Tepazulco Formation (193 m thick) is made up of interbedded limestone, shale, and sandstone and contains Virgilian-Missourian fossils. An Ordovician plug is faulted against the Patlanoaya Group at this locality.

STOP 3-7 (N18°31′, W°16.79′: Fig. 8)

The Lower Permian La Mesa, La Cuesta and La Cueva Formations consist of a conglomerate (45 m thick) and calcareous sandstone unit containing Wolfcampian fossils; interbedded shale and limestone with mid-Wolfcampian to middle Leonardian fossils; and sandstone (>280 m thick) containing late Leonardian fossils at its base.

REFERENCES CITED

Alva-Valdivia, L.M., Goguitchaichvli, A., Grajales, M., Flores de Dios, A., Urrutia-Fucugauchi, J., Rosales, C., and Morales, J., 2002, Further constraints for Permo-Carboniferous magnetostratigraphy: case study of the sedimentary sequence from San Salvador-Patlanoaya (Mexico): Comptes Rendus Geoscience, v. 334, p. 811–817, doi:10.1016/S1631-0713(02)01821-7.

Böhnel, H., 1999, Paleomagnetic study of Jurassic and Cretaceous rocks from the Mixteca terrane (Mexico): Journal of South American Earth Sciences, v. 12, no. 6, p. 545–556, doi:10.1016/S0895-9811(99)00038-3.

Bullard, E.C., et al., 1965, A symposium on continental drift-IV. The fit of the continents around the Atlantic: Philosophical Transactions of the Royal Society, v. 258, p. 41–51, doi:10.1098/rsta.1965.0020.

Fang, W., Van der Voo, R., Molina-Garza, R., Moran-Zenteno, D.J., and Urrutia-Fucugauchi, J., 1989, Paleomagnetism of the Acatlan terrane, southern Mexico: evidence for terrane rotation: Earth and Planetary Science Letters, v. 94, no. 1-2, p. 131–142, doi:10.1016/0012-821X(89)90089-7.

Galaz-Escanilla, G., Keppie, J.D., Lee, J.K.W., and Ortega-Rivera, A., in press, A high-pressure folded klippe at Tehuitzingo on the western margin of an extrusion zone, Acatlán Complex, southern Mexico: Gondwana Research.

González-Mancera, G., 2001, Mineralogía y petrología de las serpentinitas del cuerpo ultramáfico de Tehuitzingo, Estado de Puebla: Tesis de Maestría, Universidad Nacional Autónoma de México, 103p.

Guillot, S., Hattori, K., Agard, P., Schwartz, S., and Vidal, O., 2009, Exhumation Processes in Oceanic and Continental Subduction Contexts: A Review, *in* Lallemand, S., Funiciello, F., eds., Subduction Zone Geodynamics. Springer-Verlag Berlin Heidelberg, p. 175–205.

Helbig, M., Keppie, J.D., Murphy, B., and Solari, L., 2010, Jurassic Amphibolites of the Eastern Acatlan Complex (Southern Mexico) Related to Both Back-Arc Rifting and the Opening of the Gulf of Mexico?: Geological Society of America Abstracts with Programs, v. 42, no. 5, p. 679.

Irving, E., 1977, Drift of the major continents since the Devonian: Nature, v. 270, p. 304–309, doi:10.1038/270304a0.

Keppie, J.D., 2004, Terranes of Mexico revisited: A 1.3 billion year odyssey: International Geology Review, v. 46, no. 9, p. 765–794, doi:10.2747/0020-6814.46.9.765.

Keppie, D.F., and Keppie, J.D., in review, An alternative Pangean reconstruction for Middle America with the Chortis and Yucatan blocks in the Gulf of Mexico: implications for Mesozoic and Cenozoic tectonics: International Geology Review.

Keppie, J.D., Nance, R.D., Dostal, J., Ortega-Rivera, A., Miller, B.V., Fox, D., Powell, J., Mumma, S., and Lee, J.W.K., 2004, Mid-Jurassic Tectonothermal Event Superposed on a Paleozoic Geological Record in the Acatlán Complex of Southern Mexico: Hotspot Activity During the Breakup of Pangea: Gondwana Research, v. 7, p. 238–260, doi:10.1016/S1342-937X(05)70323-3.

Keppie, J.D., Dostal, J., Murphy, J.B., and Nance, R.D., 2008, Synthesis and tectonic interpretation of the westernmost Paleozoic Variscan orogen in southern Mexico: From rifted Rheic margin to active Pacific margin: Tectonophysics, v. 461, no. 1-4, p. 277–290, doi:10.1016/j.tecto.2008.01.012.

Keppie, J.D., Nance, R.D., Ramos-Arias, M.A., Lee, J.K.W., Dostal, J., Ortega-Rivera, A., and Murphy, J.B., 2010, Late Paleozoic subduction and exhumation of Cambro-Ordovician passive margin and arc rocks in the northern Acatlán Complex, southern Mexico: Geochronological constraints: Tectonophysics, v. 495, no. 3-4, p. 213–229, doi:10.1016/j.tecto.2010.09.019.

Kirsch, M., Keppie, J.D., Murphy, J.B., and Solari, L.A., in press, Permian–Carboniferous arc magmatism and basin evolution along the western margin of Pangea: geochemical and geochronological evidence from the eastern Acatlán Complex, southern Mexico: GSA Bulletin.

Malone, J., Nance, R.D., Keppie, J.D., and Dostal, J., 2002, Deformational history of part of the Acatlan Complex: Late Ordovician-early Silurian and early Permian orogenesis in southern Mexico: Journal of South American Earth Sciences, v. 15, no. 5, p. 511–524, doi:10.1016/S0895-9811(02)00080-9.

Morales-Gámez, M., Keppie, J.D., and Norman, M.D., 2008, Ordovician-Silurian rift-passive margin on the Mexican margin of the Rheic Ocean overlain by Carboniferous-Permian periarc rocks: Evidence from the eastern Acatlán Complex, southern Mexico: Tectonophysics, v. 461, p. 291–310, doi:10.1016/j.tecto.2008.01.014.

Morales-Gámez, M., Keppie, J.D., and Dostal, J., 2009, Carboniferous tholeiitic dikes in the Salada unit, Acatlán Complex, southern Mexico: a record of extension on the western margin of Pangea: Revista Mexicana De Ciencias Geológicas, v. 26, p. 133–142.

Pindell, J.L., and Dewey, J.F., 1982, Permo-Triassic reconstruction of western Pangaea and the evolution of the Gulf of Mexico/Caribbean region: Tectonics, v. 1, p. 179–211, doi:10.1029/TC001i002p00179.

Pindell, J.L., and Dewey, J.F., 1982, Permo-Triassic reconstruction of western Pangaea and the evolution of the Gulf of Mexico/Caribbean region: Tectonics, v. 1, p. 179–211, doi:10.1029/TC001i002p00179.

Smith, A.G., et al., 1981, Phanerozoic paleocontinental world maps. Cambridge University Press, Cambridge, 102 p.

Steiner, M.B., 2005, Pangean reconstruction of the Yucatan Block: Its Permian, Triassic, and Jurassic geologic and tectonic history, *in* Anderson, T.H., Nourse, J.A., McKee, J.W., and Steiner, M.B., eds. The Mojave-Sonora megashear hypothesis: Development, assessment, and alternatives. Geological Society of America Special Paper 393, p. 457–480. doi: 10.1130/2005.2393(17).

Talavera-Mendoza, O., Ruiz, J., Gehrels, G.E., Meza-Figueroa, D., Vega-Granillo, R., and Campa-Uranga, M., 2005, U-Pb geochronology of the Acatlán Complex and implications for the Paleozoic paleogeography and tectonic evolution of southern Mexico: Earth and Planetary Science Letters, v. 235, p. 682–699, doi:10.1016/j.epsl.2005.04.013.

Ulmer, P., and Trommsdorff, V., 1995, Serpentine Stability to Mantle Depths and Subduction-Related Magmatism: Science, v. 268, no. 5212, p. 858–861, doi:10.1126/science.268.5212.858.

Van der Voo, R., and French, R.B., 1974, Apparent polar wandering for the Atlantic-bordering continents: Late Carboniferous to Eocene: Earth-Science Reviews, v. 10, p. 99–119, doi:10.1016/0012-8252(74)90082-8.

Vega-Granillo, R., Meza-Figueroa, D., Ruiz, J., Talavera-Mendoza, O., and López-Martínez, M., 2009, Structural and tectonic evolution of the Acatlán Complex, southern Mexico: Its role in the collisional history of Laurentia and Gondwana: Tectonics, v. 28, no. 4, p. TC4008, doi:10.1029/2007TC002159.

Vega-Granillo, R., Talavera-Mendoza, O., Meza-Figueroa, D., Ruiz, J., Gehrels, G.E., and López-Martínez, M., 2007, Pressure-temperature-time evolution of Paleozoic high-pressure rocks of the Acatlán Complex (southern Mexico): Implications for the evolution of the Iapetus and Rheic Oceans: Geological Society of America Bulletin, v. 119, no. 9/10, p. 1249–1264, doi:10.1130/B226031.1.

Yañez, P., Patchett, P.J., Ortega-Gutierrez, F., and Gehrels, G.E., 1991, Isotopic studies of the Acatlán Complex, southern Mexico: Implications for Paleozoic North American Tectonics: Geological Society of America Bulletin, v. 103, no. 6, p. 817–828, doi:10.1130/0016-7606(1991)103<0817:ISOTAC>2.3.CO;2.

Printed in the U.S.A.

5

CONCLUSIONES

Los nuevos datos que fueron obtenidos en la presente tesis, plantean las siguientes conclusiones:

- El Litodema Chazumba, la Migmatita Magdalena, las rocas intrusivas de San Miguel, y los lentes máficos–ultramáficos de Tepejillo y lentes de Tultitlán, son unidades que anteriormente formaban parte del Grupo Petlalcingo dentro del Complejo Acatlán (Paleozoico); el presente trabajo permite reagrupar a estas unidades litológicas en un complejo nuevo, denominado Complejo Ayú, dado que las edades de sedimentación, de intrusión y de migmatización, respectivamente, posfechan las rocas del Complejo Acatlán.

- La Geocronología por LA-ICP-MS establece límites para el periodo de sedimentación de las rocas metasedimentarias del Complejo Ayú entre ca. 234-171 o 195-171 Ma, es decir entre el Triásico Tardío o Jurásico Inferior a Jurásico Medio, respectivamente. Los circones detríticos más jóvenes de las rocas metasedimentarias del Litodema Chazumba y del protolito de la Migmatita Magdalena muestran ambos procedencias similares sugiriendo que los dos protolitos clásticos pueden considerarse como una sola unidad, a saber, Litodema Chazumba. En cuanto a la distribución espacial, los datos geocronológicos indican que la deposición de las rocas metasedimentarias en la parte occidental del Litodema Chazumba comenzó sincrónicamente en el Jurásico Inferior. No obstante, debido a la deformación intensa de las rocas metasedimentarias, existe la posibilidad de que la sedimentación pudiera haber comenzado parcialmente en el Triásico.

- La Geoquímica y estudios isotópicos de Sm-Nd de las anfibolitas y rocas metasedimentarias del Complejo Ayú revelan que sus protolitos se formaron en un ambiente de trasarco. Las anfibolitas constan de un conjunto de basaltos alcalinos a basaltos transicionales y tholeiitas N-MORB, con una firma superpuesta de arco que es coherente con los valores Sm-Nd y documenta un adelgazamiento gradual de la litósfera continental con una edad de ca. 800 Ma que fue sustituida progresivamente por un manto más joven y evolucionado, un proceso típico de los regímenes extensivos.

- El Litodema Chazumba se infiere como un equivalente del abanico aluvial de Potosí el cuál fue depositado en el límite interior de una cuenca de trasarco en el margen rifteado occidental de los terrenos Oaxaquia y Mixteca durante el Triásico

Tardío–Jurásico Temprano. Las rocas sedimentarias del abanico Potosí son geoquímicamente muy similares a las del Litodema Chazumba, y en ambos casos se infieren tener fuentes de procedencia en el Complejo Oaxaqueño. La Geoquímica y isotopía de Sm-Nd de las rocas máficas del Gneis Francisco es más consistente con la firma de las anfibolitas del Litodema Chazumba. Las diferencias con otros conjuntos de rocas máficas triásicas correlacionadas con el abanico Potosí y la cuenca Arteaga se pueden explicar por variaciones laterales y transversaless en la cuenca de trascarco.

- Las rocas del Terreno Central no se encuentran a lo largo de la frontera oriental del sur del Terreno Compuesto Guerrero. Allá, un conjunto de arco cretácico separa el Terreno Zihuatanejo del Terreno Mixteca, lo que sugiere que el Litodema Chazumba es probablemente un vestigio de una porción del Terreno Central que fue desplazado por debajo de la margen continental de Pangea por erosión por subducción y fue exhumado por tectónica extensional en el Complejo Acatlán.

- La presente tesis representa una contribución a las reconstrucciones paleogeográficas para América Media durante el Mesozoico temprano. Los datos aquí presentados proporcionan evidencia de un escenario tectónico en las proximidades de una zona de subducción para el Triásico–Jurásico Inferior, y es compatible con una ubicación del terreno Mixteca en una configuración Pangea-A, a lo largo del margen occidental de América Media.

BIBLIOGRAFÍA

Andersen, T.H. Correction of common lead in U–Pb analyses that do not report 204Pb. *Chemical Geology* **192**(1-2):59–79 (2002)

Anderson, T.H., Jones, N.W., y McKee, J.W. The Taray Formation: Jurassic (?) mélange in northern Mexico—Tectonic implications. *Geological Society of America Special Paper* **393**:427–455 (2005)

Armstrong-Altrin, J. y Verma, S. Critical evaluation of six tectonic setting discrimination diagrams using geochemical data of Neogene sediments from known tectonic settings. *Sedimentary Geology* **177**(1-2):115–129 (2005)

Barboza-Gudiño, J.R., Orozco-Esquivel, M.T., Gómez-Anguiano, M., y Zavala-Monsiváis, A. The Early Mesozoic volcanic arc of western North America in northeastern Mexico. *Journal of South American Earth Sciences* **25**:49–63 (2008)

Barboza-Gudiño, J.R., Zavala-Monsiváis, A., Venegas-Rodríguez, G., y Barajas-Nigoche, L.D. Late Triassic stratigraphy and facies from northeastern Mexico: Tectonic setting and provenance. *Geosphere* **6**:621–640 (2010)

Bartolini, C., Lang, H., y Spell, T. Geochronology, geochemistry and tectonic setting of the Mesozoic Nazas arc in north-central Mexico, and its continuation to northern South America. En C. Bartolini, C. Buffler, y J. Blickwede (editores), *The Circum-Gulf of Mexico and the Caribbean: Hydrocarbon habitats, basin formation, and plate tectonics*, págs. 427–461. AAPG Memoir 79 (2003)

Bhatia, M. y Crook, K.A.W. Trace element characteristics of graywackes and tectonic setting discrimination of sedimentary basins. *Contributions To Mineralogy And Petrology* **92**(2):181–193 (1986)

Bhatia, M.R. Plate Tectonics and Geochemical Composition of Sandstones. *The Journal of Geology* **91**(6):611–627 (1983)

Cameron, K.L., López, R., Ortega-Gutiérrez, F., Solari, L.A., Keppie, J.D., y Schulze, C. U-Pb geochronology and Pb isotopic compositions of leached feldspars: Constraints on the origin and evolution of Grenvillian rocks eastern and southern Mexico. En *Proterozoic tectonic evolution of the Grenville orogen in North America*, págs. 755–770. Geological Society of America Memoir (2004)

Cardona, A., Chew, D., Valencia, V.A., Bayona, G., Mišković, A., y Ibañez-Mejía, M. Grenvillian remnants in the Northern Andes: Rodinian and Phanerozoic paleogeographic perspectives. *Journal of South American Earth Sciences* **29**(1):92–104 (2010)

Centeno-García, E. Review of Upper Paleozoic and Lower Mesozoic stratigraphy and depositional environments of central and west Mexico: Constraints on terrane analysis and paleogeography. En T.H. Anderson, J.A. Nourse, J.W. McKee, y M.B. Steiner (editores), *The Mojave-Sonora megashear hypothesis: Develop- ment, assessment, and alternatives*, págs. 233–258. Geological Society of America Special Paper 393 (2005)

Centeno-García, E. The Guerrero Composite Terrane of western Mexico: Collision and subsequent rifting in a supra-subduction zone. En A. Draut, P.D. Clift, y D. Scholl (editores), *Formation and Applications of the Sedimentary Record in Arc Collision Zones*, págs. 279–308. Geological Society of America Special Paper 436 (2008)

Centeno-García, E. y Silva-Romo, G. Petrogenesis and tectonic evolution of central Mexico during Triassic-Jurassic time. *Revista Mexicana de Ciencias Geológicas* **14**(2):244–260 (1997)

Cerca, M., Ferrari, L., López-Martínez, M., Martiny, B.M., y Iriondo, A. Late Cretaceous shortening and early Tertiary shearing in the central Sierra Madre del Sur, southern Mexico: Insights into the evolution of the Caribbean-North American plate interaction. *Tectonics* **26**(3):TC3007 (2007)

DePaolo, D.J. A Neodymium and Strontium Isotopic Studyof the Mesozoic Calc-Alkaline granitic batholiths of the Sierra Nevada and Peninsular Ranges, California. *Journal of Geophysical Research* **86**:10470–10488 (1981a)

DePaolo, D.J. Trace element and isotopic effects of combined wallrock assimilation and fractional crystallization. *Earth and Planetary Science Letters* **53**:189–202 (1981b)

DePaolo, D.J. *Neodymium Isotope Geochemistry*, *Minerals, Rocks and Mountains*, tomo 20. Springer, Berlin (1988)

Díaz-Salgado, C., Centeno-García, E., y Gehrels, G.E. Stratigraphy, Depositional Environments, and Tectonic Significance of the Taray Formation, Northern Zacatecas State, Mexico. *Geological Society of America Abstracts with Programs* **35**(4):71 (2003)

Dickinson, W.R. y Gehrels, G.E. Sediment delivery to the Cordilleran foreland basin: insights from U–Pb ages of detrital zircons in Upper Jurassic and Cretaceous strata of the Colorado Plateau. *American Journal of Science* **308**:1041–1082 (2008)

Dickinson, W.R. y Lawton, T.F. Carboniferous to Cretaceous assembly and fragmentation of Mexico. *Geological Society of America Bulletin* **113**(9):1142–1160 (2001)

Domeier, M., Van der Voo, R., y Torsvik, T.H. Paleomagnetism and Pangea: The road to reconciliation. *Tectonophysics* **514-517**(C):14–43 (2012)

Dostal, J., Baragar, W., y Dupuy, C. Petrogenesis of the Natkusiak continental basalts, Victoria Island, Northwest Territories, Canada. *Canadian Journal of Earth Sciences* **23**(5):622–632 (1986)

Dostal, J., Dupuy, C., y Caby, R. Geochemistry of the Neoproterozoic Tilemsi belt of Iforas (Mali, Sahara) : a crustal section of an oceanic island arc. *Precambrian Research* **65**:55–69 (1994)

Dowe, D.S., Nance, R.D., Keppie, J.D., Cameron, K.L., Ortega-Rivera, A., Ortega-Gutiérrez, F., y Lee, J.W.K. Deformational History of the Granjeno Schist, Ciudad Victoria, Mexico: Constraints on the Closure of the Rheic Ocean? *International Geology Review* **47**(9):920–937 (2005)

Elías-Herrera, M. y Ortega-Gutiérrez, F. Caltepec fault zone: An Early Permian dextral transpressional boundary between the Proterozoic Oaxacan and Paleozoic Acatlán complexes, southern Mexico, and regional tectonic implications. *Tectonics* **21**(3):1–18 (2002)

Elías-Herrera, M., Sánchez-Zavala, J.L., y Macías-Romo, C. Geologic and geochronologic data from the Guerrero terrane in the Tejupilco area, southern Mexico: new constraints on its tectonic interpretation. *Journal of South American Earth Sciences* **13**(4-5):355–375 (2000)

Elías-Herrera, M., Ortega-Gutiérrez, F., Sánchez-Zavala, J.L., y Macías-Romo, C. The real Guerrero terrane, southern Mexico: New insights from recent studies. *Geological Society of America Abstracts with Programs* **35** (2003)

Elías-Herrera, M., Ortega-Gutiérrez, F., Sánchez-Zavala, J.L., Macías-Romo, C., Ortega-Rivera, A., y Iriondo, A. La falla de Caltepec: raíces expuestas de una frontera tectónica de larga vida entre dos terrenos continentales del sur de México. *Grandes Fronteras Tectónicas de México: Boletín de la Sociedad Geológica Mexicana, Volumen Conmemorativo del Centenario* **57**(1):83–109 (2005)

Elías-Herrera, M., Ortega-Gutiérrez, F., Macías-Romo, C., Sánchez-Zavala, J.L., y Solari, L.A. *Colisión Oblicua Del Cisuraliano–Guadalopiano Entre Bloques Continentales en El Sur De México: Evidencias Estratigráfico-Estructurales Y Geocronológicas*. Simposio en Honor del Dr. Zoltan de Cserna. Libro de resúmenes, México, D.F. (2011)

Ferrari, L. Slab detachment control on mafic volcanic pulse and mantle heterogeneity in central Mexico. *Geology* **32**(1):77–80 (2004)

Ferrari, L., López-Martínez, M., Aguirre-Díaz, G., y Carrasco-Núñez, G. Space-time patterns of Cenozoic arc volcanism in central Mexico: from the Sierra Madre Occidental to the Mexican Volcanic Belt. *Geology* **27**(4):303–306 (1999)

Gehrels, G.E. Detrital zircon U-Pb geochronology: Current methods and new opportunities. En C. Busby y A. Azor-Pérez (editores), *Tectonics of Sedimentary Basins: Recent Advances*, págs. 45–62. John Wiley & Sons, Ltd. (2011)

Gehrels, G.E., Valencia, V.A., y Pullen, A. Detrital zircon geochronology by laser-ablation multicollector ICPMS at the Arizona Laserchron Center. En T. Olszewski (editor), *Geochronology: Emerging Opportunities, Paleontological Society Short Course, October 21, 2006, Philadelphia, PA*, págs. 67–76. Paleontological Society Papers (2006)

Godínez-Urban, A., Lawton, T.F., Molina Garza, R.S., Iriondo, A., Weber, B., y López-Martínez, M. Jurassic volcanic and sedimentary rocks of the La Silla and Todos Santos Formations, Chiapas: Record of Nazas arc magmatism and rift-basin formation prior to opening of the Gulf of Mexico. *Geosphere* **7**(1):121–144 (2011)

Goldstein, S.L., O'Nions, R.K., y Hamilton, P.J. A Sm-Nd isotopic study of atmospheric dusts and particulates from major river systems. *Earth and Planetary Science Letters* **70**(2):221–236 (1984)

Gómez-Tuena, A., Langmuir, C.H., Goldstein, S.L., Straub, S.M., y Ortega-Gutiérrez, F. Geochemical Evidence for Slab Melting in the Trans-Mexican Volcanic Belt. *Journal of Petrology* **48**(3):537–562 (2007)

Grajales-Nishimura, J.M., Centeno-García, E., Keppie, J.D., y Dostal, J. Geochemistry of Paleozoic basalts from the Juchatengo complex of southern Mexico: tectonic implications. *Journal of South American Earth Sciences* **12**(6):537–544 (1999)

Grodzicki, K.R., Nance, R.D., Keppie, J.D., y Dostal, J. Structural, geochemical and geochronological analysis of metasedimentary and metavolcanic rocks of the Coatlaco area, Acatlán Complex, southern Mexico. *Tectonophysics* **461**:311–323 (2008)

Harris, A.C., Allen, C.M., Bryan, S.E., Campbell, I.H., Holcombe, R.J., y Palin, J.M. ELA-ICP-MS U?Pb zircon geochronology of regional volcanism hosting the Bajo de la Alumbrera Cu?Au deposit: implications for porphyry-related mineralization. *Mineralium Deposita* **39**(1):46–67 (2004)

Helbig, M., Keppie, J.D., Murphy, J.B., y Solari, L.A. U–Pb geochronological constraints on the Triassic–Jurassic Ayú Complex, southern Mexico: Derivation from the western margin of Pangea-A. *Gondwana Research* **22**(3–4):910–927 (2012)

Helbig, M., Keppie, J.D., Murphy, J.B., y Solari, L.A. Exotic rifted passive margin of a back-arc basin off western Pangea: geochemical evidence from the Early Mesozoic Ayú Complex, southern Mexico. *International Geology Review* (2013)

Hinojosa-Prieto, H.R., Nance, R.D., Keppie, J.D., Dostal, J., Ortega-Rivera, A., y Lee, J.W.K. Ordovician and Late Paleozoic–Early Mesozoic tectonothermal history of the La Noria area, northern Acatlán Complex, southern Mexico: Record of convergence in the Rheic and paleo-Pacific Oceans. *Tectonophysics* **461**:324–342 (2008)

Hoskin, P.W.O. y Ireland, T. Rare earth element chemistry of zircon and its use as a provenance indicator. *Geology* **28**(7):627–630 (2000)

Hoskin, P.W.O. y Schaltegger, U. The composition of zircon and igneous and metamorphic petrogenesis. *Reviews in Mineralogy and Geochemistry* **53**(1):27–62 (2003)

Ibanez-Mejia, M., Ruiz, J., Valencia, V.A., Cardona, A., Gehrels, G.E., y Mora, A.R. The Putumayo Orogen of Amazonia and its implications for Rodinia reconstructions: New U–Pb geochronological insights into the Proterozoic tectonic evolution of northwestern South America. *Precambrian Research* **191**(1–2):58–77 (2011)

Jacobsen, S.B. y Wasserburg, G. Sm-Nd isotopic evolution of chondrites. *Earth and Planetary Science Letters* **50**:139–155 (1980)

Jeffries, T.E., Fernández-Suárez, J., Corfu, F., y Gutiérrez-Alonso, G. Advances in U-Pb geochronology using a frequency quintupled Nd:YAG based laser ablation system (lambda = 213 nm) and quadrupole based ICP-MS. *Journal of Analytical Atomic Spectrometry* **18**(8):847–855 (2003)

Jenner, G., Longerich, H., Jackson, S.E., y Fryer, B. ICP-MS—A powerful tool for high-precision trace-element analysis in Earth sciences: Evidence from analysis of selected U.S.G.S. reference samples. *Chemical Geology* **83**:133–148 (1990)

Keppie, D.F. y Keppie, J.D. An alternative Pangea reconstruction for Middle America with the Chortis Block in the Gulf of Mexico: tectonic implications. *International Geology Review* **54**(14):1685–1696 (2012)

Keppie, D.F., Hynes, A.J., Lee, J.W.K., y Norman, M. Oligocene-Miocene backthrusting in southern Mexico linked to the rapid subduction erosion of a large forearc block. *Tectonics* **31**(2):TC2008 (2012a)

Keppie, J.D. Terranes of Mexico revisited: A 1.3 billion year odyssey. *International Geology Review* **46**(9):765–794 (2004)

Keppie, J.D., Dostal, J., Ortega-Gutiérrez, F., y López, R. A Grenvillian arc on the margin of Amazonia: evidence from the southern Oaxacan Complex, southern Mexico. *Precambrian Research* **112**:165–181 (2001)

Keppie, J.D., Dostal, J., Cameron, K.L., Solari, L.A., Ortega-Gutiérrez, F., y López, R. Geochronology and geochemistry of Grenvillian igneous suites in the northern Oaxacan Complex, southern Mexico: tectonic implications. *Precambrian Research* **12**:365–389 (2003)

Keppie, J.D., Nance, R.D., Dostal, J., Ortega-Rivera, A., Miller, B.V., Fox, D., Powell, J., Mumma, S., y Lee, J.W.K. Mid-Jurassic Tectonothermal Event Superposed on a Paleozoic Geological Record in the Acatlán Complex of Southern Mexico: Hotspot Activity During the Breakup of Pangea. *Gondwana Research* **7**:239–260 (2004a)

Keppie, J.D., Sandberg, C., Miller, B.V., Sánchez-Zavala, J.L., Nance, R.D., y Poole, F.G. Implications of Latest Pennsylvanian to Middle Permian Paleontological and U-Pb SHRIMP Data from the Tecomate Formation to Re-dating Tectonothermal Events in the Acatlán Complex, Southern Mexico. *International Geology Review* **46**(8):745–753 (2004b)

Keppie, J.D., Dostal, J., Miller, B.V., Ortega-Rivera, A., Roldán-Quintana, J., y Lee, J.W.K. Geochronology and Geochemistry of the Francisco Gneiss: Triassic Continental Rift Tholeiites on the Mexican Margin of Pangea Metamorphosed and Exhumed in a Tertiary Core Complex. *International Geology Review* **48**(1):1–16 (2006a)

Keppie, J.D., Nance, R.D., Fernández-Suárez, J., Storey, C.D., Jeffries, T.E., y Murphy, J.B. Detrital Zircon Data from the Eastern Mixteca Terrane, Southern Mexico: Evidence for an Ordovician–Mississippian Continental Rise and a Permo-Triassic Clastic Wedge Adjacent to Oaxaquia. *International Geology Review* **48**:97–111 (2006b)

Keppie, J.D., Dostal, J., Miller, B.V., Ramos-Arias, M.A., Morales-Gámez, M., Nance, R.D., Murphy, J.B., Ortega-Rivera, A., Lee, J.W.K., Housh, T., y Cooper, P. Ordovician-earliest Silurian rift tholeiites in the Acatlán Complex, southern Mexico: Evidence of rifting on the southern margin of the Rheic Ocean. *Tectonophysics* **461**(1-4):130–156 (2008a)

Keppie, J.D., Dostal, J., Murphy, J.B., y Nance, R.D. Synthesis and tectonic interpretation of the westernmost Paleozoic Variscan orogen in southern Mexico: From rifted Rheic margin to active Pacific margin. *Tectonophysics* **461**(1-4):277–290 (2008b)

Keppie, J.D., Nance, R.D., Ramos-Arias, M.A., Lee, J.W.K., Dostal, J., Ortega-Rivera, A., y Murphy, J.B. Late Paleozoic subduction and exhumation of Cambro-Ordovician passive margin and arc rocks in the northern Acatlán Complex, southern Mexico: Geochronological constraints. *Tectonophysics* **495**(3-4):213–229 (2010)

Keppie, J.D., Galaz Escanilla, G., Helbig, M., y Kirsch, M. Amalgamation and Breakup of Pangæa: the type example of the supercontinent Cycle. En *International Geological Correlation Program Project #597: Late Paleozoic–Early Mesozoic of the Acatlán and Ayu complexes, southern Mexico: events on the periphery of Pangæa synchronous with amalgamation and breakup*, págs. 1–17. Geological Society of America, Cordilleran Section, 108th Annual Meeting (2012b)

Keppie, J.D., Nance, R.D., Dostal, J., Lee, J.W.K., y Ortega-Rivera, A. Constraints on the subduction erosion/extrusion cycle in the Paleozoic Acatlán Complex of southern Mexico: Geochemistry and geochronology of the type Piaxtla Suite. *Gondwana Research* **21**(4):1050–1065 (2012c)

Kerr, A., Jenner, G.A., y Fryer, B.J. Sm–Nd isotopic geochemistry of Precambrian to Paleozoic granitoid suites and the deep-crustal structure of the southeast margin of the Newfoundland Appalachians. *Canadian Journal of Earth Sciences* **32**(2):224–245 (1995)

Kirsch, M., Keppie, J.D., Murphy, J.B., y Lee, J.K.W. Arc plutonism in a transtensional regime: the late Palaeozoic Totoltepec pluton, Acatlán Complex, southern Mexico. *International Geology Review* (2012a)

Kirsch, M., Keppie, J.D., Murphy, J.B., y Solari, L.A. Permian–Carboniferous arc magmatism and basin evolution along the western margin of Pangea: geochemical and geochronological evidence from the eastern Acatlán Complex, southern Mexico. *Geological Society of America Bulletin* **124**(9/10):1607–1628 (2012b)

Levresse, G., Tritlla, J., Deloule, E., y Pinto-Linares, P. Is there a Grenvillian basement in the Guerrero-Morelos platform of Mexico? *Geologica Acta* **5**(2):167–175 (2007)

Li, Z.X., Bogdanova, S.V., Collins, A.S., Davidson, A., De Waele, B., Ernst, R.E., Fitzsimons, I.C.W., Fuck, R.A., Gladkochub, D.P., Jacobs, J., Karlstrom, K.E., Lu, S., Natapov, L.M., Pease, V., Pisarevsky, S.A., Thrane, K., y Vernikovsky, V. Assembly, configuration, and break-up history of Rodinia: A synthesis. *Precambrian Research* **160**(1-2):179–210 (2008)

Longerich, H., Jenner, G.A., Fryer, B.J., y Jackson, S.E. Inductively coupled plasma-mass spectrometric analysis of geological samples: A critical evaluation based on case studies. *Chemical Geology* **83**:105–118 (1990)

Ludwig, K. *User's Manual for Isoplot 3.70, A geochronological toolkit for Microsoft Excel*, tomo 4. Berkeley Geochronology Center Special Publication (2008)

Malone, J., Nance, R.D., Keppie, J.D., y Dostal, J. Deformational history of part of the Acatlán Complex: Late Ordovician-Early Silurian and Early Permian orogenesis in southern Mexico. *Journal of South American Earth Sciences* **15**(5):511–524 (2002)

Martini, M., Ferrari, L., López-Martínez, M., Cerca-Martínez, M., Valencia, V.A., y Serrano-Durán, L. Cretaceous–Eocene magmatism and Laramide deformation in southwestern Mexico: No role for terrane accretion. En S. Kay, V.A. Ramos, y W.R. Dickinson (editores), *Backbone of the Americas: Shallow Subduction, Plateau Uplift, and Ridge and Terrane Collision*, págs. 151–182. Geological Society of America Memoir 204 (2009)

Miller, B.V., Dostal, J., y Keppie, J.D. Ordovician calc-alkaline granitoids in the Acatlán Complex, southern México: Geochemical and geochronologic data and implications for the tectonics of the Gondwanan margin of the Rheic Ocean. En U. Linnemann, R.D. Nance, P. Kraft, y G. Zulauf (editores), *The evolution of the Rheic Ocean: From Avalonian-Cadomian active margin to Alleghenian-Variscan collision*, págs. 465–475. Geological Society of America Special Paper 423 (2007)

Morales-Gámez, M. y Keppie, J.D. Ordovician-Silurian rift-passive margin on the Mexican margin of the Rheic Ocean overlain by Carboniferous-Permian periarc rocks: evidence from the eastern Acatlán Complex, southern Mexico. *Tectonophysics* **461**:291–310 (2008)

Morales-Gámez, M., Keppie, J.D., Lee, J.W.K., y Ortega-Rivera, A. Palaeozoic structures in the Xayacatlán area, Acatlán Complex, southern Mexico: transtensional rift- and subduction-related deformation along the margin of Oaxaquia. *International Geology Review* **51**(4):279–303 (2009)

Morán-Zenteno, D.J., Caballero-Miranda, C., Silva-Romo, G., Ortega-Guerrero, B., y González-Torres, E. Jurassic-Cretaceous paleogeographic evolution of the northern Mixteca terrane, southern Mexico. *Geofísica Internacional* **32**(3):453–473 (1993)

Murphy, J.B., Keppie, J.D., Nance, R.D., Miller, B.V., Dostal, J., Middleton, M., Fernández-Suárez, J., Jeffries, T.E., y Storey, C.D. Geochemistry and U-Pb protolith ages of eclogitic rocks of the Asis Lithodeme, Piaxtla Suite, Acatlán Complex, southern Mexico: tectonothermal activity along the southern margin of the Rheic Ocean. *Journal of the Geological Society, London* **163**:683–695 (2006)

NACSN. North American commission on stratigraphic nomenclature. *American Association of Petroleum Geologists Bulletin* **89**(11):1547–1591 (2005)

Nance, R.D., Miller, B.V., Keppie, J.D., Murphy, J.B., y Dostal, J. Acatlán Complex, southern Mexico: Record spanning the assembly and breakup of Pangea. *Geology* **34**:857–860 (2006)

Nance, R.D., Fernández-Suárez, J., Keppie, J.D., Storey, C.D., y Jeffries, T.E. Provenance of the Granjeno Schist, Ciudad Victoria, México: Detrital zircon U-Pb age constraints and implications for the Paleozoic paleogeography of the Rheic Ocean. *The evolution of the Rheic Ocean: from Avalonian-Cadomian active margin to Alleghenian-Variscan collision* págs. 453–464 (2007)

Nesbitt, H. y Young, G. Early Proterozoic climates and plate motions inferred from major element chemistry of lutites. *Nature* **299**(21):715–717 (1982)

O'Nions, R.K., Hamilton, P.J., y Evensen, N.M. Variations in 143Nd/144Nd and 87Sr/86Sr ratios in oceanic basalts. *Earth and Planetary Science Letters* **34**(1):13–22 (1977)

Ortega-Gutiérrez, F. *The Pre-Mesozoic geology of the Acatlán area, south Mexico*. Tesis Doctoral, University of Leeds, Leeds (1975)

Ortega-Gutiérrez, F. Estratigrafía del Complejo Acatlán en la Mixteca Baja, Estados de Puebla y Oaxaca. *Universidad Nacional Autónoma de México, Instituto de Geología Revista* **2**(2):112–131 (1978)

Ortega-Gutiérrez, F. y Elías-Herrera, M. Wholesale melting of the southern Mixteco terrane and origin of the Xolapa Complex. *Geological Society of America Abstracts with Programs* **35** (2003)

Ortega-Gutiérrez, F. y Ruiz, J. Oaxaquia, a Proterozoic microcontinent accreted to North America during the late Paleozoic. *Geology* **23**(12):1127–1130 (1995)

Ortega-Gutiérrez, F., Elías-Herrera, M., Reyes-Salas, M., Macías-Romo, C., y López, R. Late Ordovician-Early Silurian continental collisional orogeny in southern Mexico and its bearing on Gondwana-Laurentia connections. *Geology* **27**(8):719–722 (1999)

Ortega-Obregón, C., Keppie, J.D., Murphy, J.B., Lee, J.W.K., y Ortega-Rivera, A. Geology and geochronology of Paleozoic rocks in western Acatlán Complex, southern Mexico: Evidence for contiguity across an extruded high-pressure belt and constraints on Paleozoic reconstructions. *Geological Society of America Bulletin* **121**(11-12):1678–1694 (2009)

Pérez-Gutiérrez, R., Solari, L.A., Gómez-Tuena, A., y Martens, U. Mesozoic geologic evolution of the Xolapa migmatitic complex north of Acapulco, southern Mexico: implications for paleogeographic reconstructions. *Revista Mexicana de Ciencias Geológicas* **26**(1):201–221 (2009)

Pindell, J.L., Maresch, W.V., Martens, U., y Stanek, K. The Greater Antillean Arc: Early Cretaceous origin and proposed relationship to Central American subduction mélanges: implications for models of Caribbean evolution. *International Geology Review* **54**(2):131–143 (2012)

Ramírez-Espinosa, J. *Tectono-magmatic evolution of the Paleozoic Acatlán Complex in southern Mexico, and its correlation with the Appalachian system*. Tesis Doctoral, University of Arizona, Tucson (2001)

Ramos, V.A. The Grenville-age basement of the Andes. *Journal of South American Earth Sciences* **29**(1):77–91 (2010)

Ramos-Arias, M.A. y Keppie, J.D. U-Pb Neoproterozoic-Ordovician protolith age constraints for high- to medium-pressure rocks thrust over low-grade metamorphic rocks in the Ixcamilpa area, Acatlán Complex, southern Mexico. *Canadian Journal of Earth Sciences* **48**(1):45–61 (2011)

Ramos-Arias, M.A., Keppie, J.D., Ortega-Rivera, A., y Lee, J.W.K. Extensional Late Paleozoic deformation on the western margin of Pangea, Patlanoaya area, Acatlán Complex, southern Mexico. *Tectonophysics* **448**(1-4):60–76 (2008)

Ramos-Arias, M.A., Keppie, J.D., Lee, J.W.K., y Ortega-Rivera, A. A Carboniferous high-pressure klippe in the western Acatlán Complex of southern Mexico: implications for the tectonothermal development and palaeogeography of Pangea. *International Geology Review* págs. 1–20 (2011)

Ratschbacher, L., Riller, U., Meschede, M., Herrmann, U., y Frisch, W. 2nd look at suspect terranes in southern Mexico. *Geology* **19**(12):1233–1236 (1991)

Ratschbacher, L., Franz, L., Min, M., Bachmann, R., Martens, U., Stanek, K.P., Stübner, K., Nelson, B.K., Herrmann, U., Weber, B., López-Martínez, M., Jonckheere, R., Sperner, B., Tichomirowa, M., McWilliams, M.O., Gordon, M., Meschede, M., y Bock, P. The North American–Caribbean Plate boundary in Mexico–Guatemala–Honduras. *Geological Society, London, Special Publications* **328**:219–293 (2009)

Riller, U., Ratschbacher, L., y Frisch, W. Left-lateral transtension along the Tierra Colorada deformation zone, northern margin of the Xolapa magmatic arc of southern Mexico. *Journal of South American Earth Sciences* **5**(3-4):237–249 (1992)

Rogers, R.D., Mann, P., y Emmet, P.A. Tectonic terranes of the Chortis block based on integration of regional aeromagnetic and geologic data. En P. Mann (editor), *Geologic and tectonic development of the Caribbean plate in northern Central America*, págs. 65–88. Geological Society of America Special Paper 428 (2007)

Roser, B. y Korsch, R.J. Provenance signatures of sandstone–mudstone suites determined using discriminant function analysis of major-element data. *Chemical Geology* **67**:119–139 (1988)

Ross, M.I. y Scotese, C.R. A hierarchical tectonic model of the Gulf of Mexico and Caribbean region. *Tectonophysics* **155**:139–168 (1988)

Sánchez-Zavala, J.L., Jenner, G., Belousova, E., y Macías-Romo, C. Ordovician and Mesoproterozoic Zircons from the Tecomate Formation and Esperanza Granitoids, Acatlán Complex, Southern Mexico: Local Provenance in the Acatlán and Oaxacan Complexes. *International Geology Review* **46**(11):1005–1021 (2004)

Schaaf, P., Morán-Zenteno, D.J., Hernández Bernal, M., Solís-Pichardo, G., Tolson, G., y Kohler, H. Paleogene continental margin truncation in southwestern Mexico: Geochronological evidence. *Tectonics* **14**(6):1339–1350 (1995)

Schaaf, P., Weber, B., Weis, P., Gross, A., Ortega-Gutiérrez, F., y Köhler, H. The Chiapas Massif (Mexico) revised: New geologic and isotopic data and basement

characteristics. *Neues Jahrbuch für Geologie und Paläontologie Abhandlungen* **255**:1–23 (2002)

Silva-Romo, G. The Guayape-Papalutla fault system: A continuous Cretaceous structure from southern Mexico to the Chortis block? Tectonic implications: COMMENT and REPLY: REPLY. *Geology* **36**(1):75–78 (2008)

Silva-Romo, G. y Mendoza-Rosales, C.C. La unidad Piedra Hueca secuencia clástica paleozoica (sur de Puebla). En *GEOS, 2a Reunión Nacional de Ciencias de la Tierra, Resúmenes y Programa*, pág. 325. Unión Geofísica Mexicana, Puerto Vallarta, Jalisco (2000)

Silva-Romo, G., Arellano-Gil, J., Mendoza-Rosales, C.C., y Nieto-Obregón, J. A submarine fan in the Mesa Central, Mexico. *Journal of South American Earth Sciences* **13**:429–442 (2000)

Silva-Romo, G., Mendoza-Rosales, C.C., Campos-Madrigal, E., y Centeno-García, E. Formación La Mora, unidad estratigráfica nueva del Triásico en el Terreno Mixteca (noroeste de Huajuapán de León, Oax., México): Sedimentología y su significado. En *Simposio en Honor del Dr. Zoltan de Cserna*, págs. 114–115. Instituto de Geología, Universidad Nacional Autónoma de México, México, D.F. (2011)

Sircombe, K.N. AgeDisplay: an EXCEL workbook to evaluate and display univariate geochronological data using binned frequency histograms and probability density distributions. *Computers and Geosciences* **30**(1):21–31 (2004)

Sláma, J., Košler, J., Condon, D., Crowley, J., Gerdes, A., Hanchar, J., Horstwood, M., Morris, G., Nasdala, L., Norberg, N., Schaltegger, U., Schoene, B., Tubrett, M., y Whitehouse, M.J. Plešovice zircon - A new natural reference material for U-Pb and Hf isotopic microanalysis. *Chemical Geology* **249**:1–35 (2008)

Solari, L.A. y Tanner, M. Fast reduction of U-Pb data using R. *Revista Mexicana de Ciencias Geológicas* **28**(1):83–91 (2011)

Solari, L.A., Keppie, J.D., Ortega-Gutiérrez, F., Cameron, K.L., López, R., y Hames, W. 990 and 1100 Ma Grenvillian tectonothermal events in the northern Oaxacan Complex, southern Mexico: roots of an orogen. *Tectonophysics* **365**(1-4):257–282 (2003)

Solari, L.A., de León, R.T., Pineda, G.H., Solé, J., Solís-Pichardo, G., y Hernandez-Treviño, T. Tectonic significance of Cretaceous-Tertiary magmatic and structural evolution of the northern margin of the Xolapa Complex, Tierra Colorada area, southern Mexico. *Geological Society of America Bulletin* **119**(9-10):1265–1279 (2007)

Solari, L.A., Gómez-Tuena, A., Bernal, J., Pérez-Arvizu, O., y Tanner, M. U-Pb zircon geochronology with an integrated LA-ICPMS microanalytical workstation: achievements in precision and accuracy. *Geostandards and Geoanalytical Research* **34**:5–18 (2010)

Steiger, R. y Jäger, E. Subcommission on geochronology: Convention on the use of decay constants in geo- and cosmochronology. *Earth and Planetary Science Letters* **36**:359–362 (1977)

Stern, R.J. Crustal evolution in the East African Orogen: a neodymium isotopic perspective. *Journal of African Earth Sciences* **34**:109–117 (2002)

Sun, S.S. y McDonough, W. Chemical and isotopic systematics of oceanic basalts: implications for mantle composition and processes. En A. Saunders y M. Norry (editores), *Magmatism in the Ocean Basins*, págs. 313–345. Geological Society Special Publication 42 (1989)

Talavera-Mendoza, O., Ruiz, J., Gehrels, G.E., Meza-Figueroa, D., Vega-Granillo, R., y Campa-Uranga, M.F. U-Pb geochronology of the Acatlán Complex and implications for the Paleozoic paleogeography and tectonic evolution of southern Mexico. *Earth and Planetary Science Letters* **235**:682–699 (2005)

Tanaka, T., Togashi, S., Kamioka, H., Amakawa, H., Kagami, H., Hamamoto, T., Yuhara, M., Orihashi, Y., Yoneda, S., Shimizu, H., Kunimaru, T., Takahashi, K., Yanagi, T., Nakano, T., Fujimaki, H., Shinjo, R., Asahara, Y., Tanimizu, M., y Dragusanu, C. JNdi-1: a neodymium isotopic reference in consistency with LaJolla neodymium. *Chemical Geology* **168**(3–4):279–281 (2000)

Tanner, M. y Solari, L.A. Fast reduction of U-Pb data using R. *Geochimica et Cosmochimica Acta Supplement* **73**:A1313 (2009)

Taylor, S.R. y McLennan, S.M. *The Continental Crust: its composition and evolution*. Blackwell, Oxford (1985)

Tera, F. y Wasserburg, G. U-Th-Pb systematics in three Apollo 14 basalts and the problem of initial Pb in lunar rocks. *Earth and Planetary Science Letters* **14**:281–304 (1972)

Tolson, G. La falla Chacalapa en el sur de Oaxaca. *Boletín de la Sociedad Geológica Mexicana* **57**(1):111–122 (2005)

Torres, R., Ruiz, J., y Patchett, P.J. Permo-Triassic continental arc in eastern Mexico: Tectonic implications for reconstructions of southern North America. *Geological Society of America Special Paper* **340**:191–196 (1999)

Torres de León, R., Solari, L.A., Ortega-Gutiérrez, F., y Martens, U. The Chortis Block–southwestern Mexico connections: U-Pb zircon geochronology constraints. *American Journal of Science* **312**(3):288–313 (2012)

Vega-Granillo, R., Talavera-Mendoza, O., Meza-Figueroa, D., Ruiz, J., Gehrels, G.E., y López-Martínez, M. Pressure-temperature-time evolution of Paleozoic high-pressure rocks of the Acatlán Complex (southern Mexico): Implications for the evolution of the Iapetus and Rheic Oceans. *Geological Society of America Bulletin* **119**(9/10):1249–1264 (2007)

Vega-Granillo, R., Meza-Figueroa, D., Ruiz, J., Talavera-Mendoza, O., y López-Martínez, M. Structural and tectonic evolution of the Acatlán Complex, southern Mexico: Its role in the collisional history of Laurentia and Gondwana. *Tectonics* **28**(4):1–25 (2009)

Weber, B. y Köhler, H. Sm-Nd, Rb-Sr and U-Pb geochronology of a Grenville terrane in southern Mexico: origin and geologic history of the Guichicovi complex. *Precambrian Research* **96**(3-4):245–262 (1999)

Weber, B., Cameron, K.L., Osorio, M., y Schaaf, P. A Late Permian tectonothermal event in Grenville crust of the southern Maya terrane: U-Pb zircon ages from the Chiapas Massif, southeastern Mexico. *International Geology Review* **47**:509–529 (2005)

Weber, B., Iriondo, A., Premo, W.R., Hecht, L., y Schaaf, P. New insights into the history and origin of the southern Maya block, SE Mexico: U-Pb-SHRIMP zircon geochronology from metamorphic rocks of the Chiapas massif. *International Journal of Earth Sciences* **96**(2):253–269 (2007)

Weber, B., Scherer, E.E., Schulze, C., Valencia, V.A., Montecinos, P., Mezger, K., y Ruiz, J. U–Pb and Lu–Hf isotope systematics of lower crust from central-southern Mexico – Geodynamic significance of Oaxaquia in a Rodinia Realm. *Precambrian Research* **182**(1–2):149–162 (2010)

Weber, B., Scherer, E.E., Martens, U.K., y Mezger, K. Where did the lower Paleozoic rocks of Yucatan come from? A U–Pb, Lu–Hf, and Sm–Nd isotope study. *Chemical Geology* **312–313**(0):1–17 (2012)

Weber, R. How old is the Triassic flora of Sonora and Tamaulipas and news on Leonardian flora in Puebla and Hidalgo, Mexico. *Revista Mexicana de Ciencias Geológicas* **14**:225–243 (1997)

Winchester, J. y Floyd, P. Geochemical discrimination of different magma series and their differentiation products using immobile elements. *Chemical Geology* **20**(4):325–343 (1977)

Yáñez, P., Patchett, P.J., Ortega-Gutiérrez, F., y Gehrels, G.E. Isotopic studies of the Acatlán Complex, southern Mexico: Implications for Paleozoic North American Tectonics. *Geological Society of America Bulletin* **103**(6):817–828 (1991)

Apéndices

A

GEOCRONOLOGÍA U–PB

A.1 FIELD RELATIONSHIPS

Samples collected beneath the thrust contact of the Tepejillo lens. TEP-474-3 is a psammitic micaceous schist and TEP-474-4 is a semipelitic micaceous schist that were collected from the same outcrop in order to sample a wider age spectrum. The rocks in this outcrop are cut by granitic, leucogranitic and aplitic dikes. 150 m away from the location of these samples a leucogranitic was sampled that cuts a tight, recumbent E-trending F_3 fold dike (MH-81, Fig. 5 on p. 916 in Helbig *et al.*, 2012). Small leucogranite veins that probably originate from the dike are parallel to the folded S_2 fabric. These relationships suggest that the intrusion was syn- to late-tectonic with respect to F_3.

Samples MH-49, 50, 53 and 59 were collected in the southern part of the Ayú Complex which is characterized by abundant migmatites. One leucogranite (MH-59) that cross-cuts the metasedimentary host rocks was sampled near Indixúa. Along a road section between the towns of Ayú and Ahuehuetitlán, the samples MH-49, 50, and 53 were collected in order to constrain the maximum depositional age of the protolith of the migmatite. At this locality, the paleosome, a semipelite (MH-50), is cut by a granitic dike (MH-49), which is folded by a moderately inclined, asymmetric F_3 fold (MH-81, Fig. 5 on p. 916 in Helbig *et al.*, 2012) suggesting syn- to late-tectonic intrusion with respect to F_3. MH-53 was collected nearby and is a psammitic garnet–biotite schist that also represents the paleosome. The more psammitic layers preserve a S_1–S_2 composite fabric with syntectonic garnet growth, whereas the more pelitic layers are overprinted by third deformational event with isoclinal to tight, upright to steeply inclined F_3 folds during D_3 producing co-axial planar cleavage S_3 in the more pelitic layers.

Three samples taken across a N–S section of the Providencia Shear Zone were analyzed to assign a northern limit to the Chazumba Lithodeme (Fig. 7 on p. 918 in Helbig *et al.*, 2012). The Providencia Shear Zone comprises mylonites that are strongly weathered. All three samples taken there are characterized by very small grain size, and relatively high amounts in graphite.

Tabla 1.: *Collected samples for U–Pb LA-ICP-MS zircon geochronology; location, rock type and number of analysed grains and of concordant analyses*

Sample	Longitude	Latitude	Unit	Rock type	NoA[a]	NoCo[b]	NoRej[c]
Igneous rocks							
MH-49	W97°47′16″	N17°56′19″	Magdalena Migmatite	granite dike	40	36	4
MH-59	W97°48′13″	N17°57′40″	Magdalena Migmatite	leucogranitic dike	40	36	4
MH-81	W97°49′39″	N18°03′09″	Chazumba Lithodeme	granite dike	39	33	6
Metasedimentary rocks							
MH-28	W97°44′41″	N18°10′56″	Chazumba Lithodeme	metapsammite	80	73	7
MH-50	W97°47′16″	N17°56′19″	Magdalena Migmatite	micaceous metapelite (paleosome)	82	61	21
MH-53	W97°47′19″	N17°56′20″	Magdalena Migmatite	msc–bt–grt schist (paleosome)	96	70	26
MH-73	W97°41′59″	N18°09′46″	Chazumba Lithodeme	micaceous schist (metapsammite)	95	87	8
MH-96	W97°53′57″	N18°07′09″	Providencia shearzone	mylonite	28	24	4
PET-480-1	W97°53′51″	N18°07′19″	Providencia shearzone	mylonite	32	19	13
PET-484-1	W97°53′58″	N18°06′51″	Providencia shearzone	mica schist (metapsammite)	37	16	21
TEP-474-3	W97°49′43″	N18°03′10″	Chazumba Lithodeme	mica schist (metapsammite)	99	96	3
TEP-474-4	W97°49′43″	N18°03′10″	Chazumba Lithodeme	mica schist (metapelite)	96	94	2

[a] Number of analysed grains

[b] Number of analyses within the 90 to 105 % concordance criterion

[c] Number of rejected analyses

A.2 ROCAS ÍGNEAS

Tabla 2.: *LA-ICP-MS U–Pb isotopic data for sample MH-49*

				Corrected isotopic ratios[a]									Corrected ages (Ma)[b]						Best age		
Zircon no.	U (ppm)	Th (ppm)	Th/U	$\frac{^{207}Pb}{^{206}Pb}$	1σ	$\frac{^{207}Pb}{^{235}U}$	1σ	$\frac{^{206}Pb}{^{238}U}$	1σ	$\frac{^{208}Pb}{^{232}Th}$	1σ	ρ^c	$\frac{^{206}Pb}{^{238}U}$	1σ	$\frac{^{207}Pb}{^{235}U}$	1σ	$\frac{^{207}Pb}{^{206}Pb}$	1σ	(Ma)	1σ	δ (%)[d]
Zircon_39_053	1497	417	0.24	0.05478	0.00077	0.18949	0.00326	0.02509	0.00025	0.00279	0.00013	0.58	160	2	176	3	403	30	160	2	9.1
Zircon_16_026	1106	7	0.01	0.05084	0.00091	0.18806	0.00394	0.02683	0.00029	0.00845	0.00040	0.52	171	2	175	3	234	39	171	2	2.3
Zircon_25_036	826	238	0.24	0.05033	0.00070	0.19437	0.00358	0.02798	0.00034	0.00831	0.00021	0.66	178	2	180	3	210	31	178	2	1.1
Zircon_10_018	1138	15	0.01	0.05292	0.00058	0.21336	0.00284	0.02926	0.00022	0.03928	0.00122	0.57	186	1	196	2	325	25	186	1	5.1
Zircon_19_029	821	31	0.03	0.05158	0.00067	0.21018	0.00325	0.02956	0.00025	0.01621	0.00037	0.54	188	2	194	3	267	29	188	2	3.1
Zircon_37_051	471	22	0.04	0.05487	0.00099	0.23622	0.00480	0.03117	0.00029	0.02148	0.00064	0.46	198	2	215	4	407	39	198	2	7.9
Zircon_36_050	1057	98	0.08	0.05847	0.00099	0.25861	0.00483	0.03207	0.00025	0.02231	0.00120	0.42	203	2	234	4	547	35	203	2	13.2
Zircon_12_021	743	76	0.09	0.05232	0.00094	0.23441	0.00459	0.03249	0.00025	0.01352	0.00024	0.40	206	2	214	4	299	42	206	2	3.7
Zircon_29_041	505	46	0.08	0.05216	0.00078	0.23843	0.00416	0.03317	0.00030	0.01770	0.00034	0.52	210	2	217	3	292	31	210	2	3.2
Zircon_30_042	410	36	0.07	0.05192	0.00083	0.24268	0.00427	0.03389	0.00025	0.02525	0.00250	0.42	215	2	221	3	282	35	215	2	2.7
Zircon_31_044	159	10	0.05	0.05092	0.00098	0.24384	0.00650	0.03473	0.00054	0.01094	0.00021	0.71	220	3	222	5	237	42	220	3	0.9
Zircon_23_034	1505	171	0.10	0.05157	0.00052	0.25303	0.00358	0.03558	0.00036	0.02486	0.00102	0.70	225	2	229	3	266	22	225	2	1.7
Zircon_40_054	388	41	0.09	0.05385	0.00075	0.26683	0.00419	0.03592	0.00026	0.01731	0.00031	0.46	227	2	240	3	365	30	227	2	5.4
Zircon_18_028	1033	643	0.53	0.05255	0.00058	0.26424	0.00379	0.03648	0.00034	0.01332	0.00017	0.64	231	2	238	3	309	24	231	2	2.9
Zircon_MH-49_1_008	321	73	0.19	0.05597	0.00112	0.28951	0.00618	0.03751	0.00028	0.01947	0.00055	0.35	237	2	258	5	451	43	237	2	8.1
Zircon_11_020	306	28	0.08	0.05335	0.00080	0.28020	0.00521	0.03811	0.00042	0.01841	0.00037	0.59	241	3	251	4	344	35	241	3	4.0
Zircon_26_038	350	28	0.07	0.05386	0.00065	0.28481	0.00443	0.03841	0.00038	0.02078	0.00056	0.63	243	2	254	4	365	25	243	2	4.3
Zircon_35_048	454	278	0.52	0.07743	0.00093	0.43297	0.00676	0.04104	0.00041	0.01234	0.00021	0.64	259	3	365	5	1132	23	259	3	29.0
Zircon_17_027	531	128	0.20	0.05279	0.00074	0.30011	0.00534	0.04120	0.00045	0.01503	0.00023	0.62	260	3	266	4	320	33	260	3	2.3
Zircon_9_017	348	108	0.26	0.05674	0.00125	0.33051	0.00799	0.04218	0.00042	0.01994	0.00054	0.41	266	3	290	6	481	47	266	3	8.3
Zircon_14_023	822	40	0.04	0.05930	0.00071	0.35384	0.00520	0.04297	0.00037	0.04208	0.00080	0.58	271	2	308	4	578	27	271	2	12.0
Zircon_8_016	497	245	0.42	0.05361	0.00059	0.31845	0.00428	0.04306	0.00033	0.01558	0.00022	0.57	272	2	281	3	355	24	272	2	3.2
Zircon_22_033	114	29	0.22	0.05875	0.00129	0.35564	0.00858	0.04397	0.00044	0.02023	0.00049	0.41	277	3	309	6	558	46	277	3	10.4
Zircon_20_030	348	202	0.49	0.05388	0.00097	0.32920	0.00678	0.04431	0.00044	0.01538	0.00023	0.49	279	3	289	5	366	39	279	3	3.5
Zircon_24_035	316	53	0.14	0.05477	0.00082	0.33537	0.00711	0.04436	0.00067	0.01753	0.00054	0.71	280	4	294	5	403	32	280	4	4.8
Zircon_27_039	581	399	0.58	0.05264	0.00068	0.32646	0.00493	0.04495	0.00035	0.01594	0.00021	0.52	283	2	287	4	313	28	283	2	1.4
Zircon_4_011	525	274	0.44	0.05404	0.00070	0.33507	0.00515	0.04508	0.00037	0.01650	0.00028	0.54	284	2	293	4	373	28	284	2	3.1
Zircon_5_012	185	118	0.54	0.05618	0.00118	0.37711	0.00894	0.04870	0.00054	0.01640	0.00069	0.46	307	3	325	7	459	45	307	3	5.5
Zircon_13_022	339	346	0.86	0.05510	0.00083	0.38880	0.00678	0.05121	0.00046	0.01619	0.00023	0.50	322	3	333	5	416	34	322	3	3.3
Zircon_6_014	272	305	0.95	0.05481	0.00071	0.40094	0.00608	0.05314	0.00041	0.01623	0.00021	0.52	334	3	342	4	404	28	334	3	2.3
Zircon_2_009	341	193	0.48	0.05480	0.00071	0.40845	0.00696	0.05408	0.00059	0.01730	0.00031	0.65	340	4	348	5	404	28	340	4	2.3
Zircon_21_032	423	446	0.89	0.05475	0.00077	0.40891	0.00649	0.05418	0.00041	0.01613	0.00021	0.46	340	3	348	5	402	30	340	3	2.3

(Continued)

Tabla 2 *(Continued)*

				Corrected isotopic ratios[a]									Corrected ages (Ma)[b]						Best age		
Zircon no.	U (ppm)	Th (ppm)	Th/U	$\frac{^{207}Pb}{^{206}Pb}$	1σ	$\frac{^{207}Pb}{^{235}U}$	1σ	$\frac{^{206}Pb}{^{238}U}$	1σ	$\frac{^{208}Pb}{^{232}Th}$	1σ	ρ^{c}	$\frac{^{206}Pb}{^{238}U}$	1σ	$\frac{^{207}Pb}{^{235}U}$	1σ	$\frac{^{207}Pb}{^{206}Pb}$	1σ	(Ma)	1σ	δ (%)[d]
Zircon_15_024	123	86	0.60	0.05712	0.00678	0.42735	0.05455	0.05426	0.00095	0.01685	0.00043	0.20	341	6	361	39	496	270	341	6	5.5
Zircon_3_010	234	155	0.56	0.05631	0.00118	0.42454	0.00975	0.05461	0.00051	0.01804	0.00031	0.41	343	3	359	7	465	44	343	3	4.5
Zircon_32_045	227	240	0.90	0.05368	0.00086	0.40892	0.00721	0.05528	0.00041	0.01649	0.00021	0.42	347	3	348	5	358	35	347	3	0.3
Zircon_33_046	312	99	0.27	0.05697	0.00057	0.56225	0.00727	0.07156	0.00059	0.02470	0.00035	0.63	446	4	453	5	490	21	446	4	1.5
Zircon_34_047	456	431	0.80	0.05875	0.00065	0.67682	0.01102	0.08340	0.00100	0.02650	0.00034	0.73	516	6	525	7	558	23	516	6	1.7
Zircon_38_052	381	92	0.20	0.06711	0.00083	1.15847	0.02298	0.12519	0.00147	0.03817	0.00045	0.77	760	8	781	11	841	25	760	8	2.7
Zircon_7_015	242	124	0.43	0.10220	0.00100	3.94720	0.05815	0.27954	0.00307	0.08009	0.00104	0.75	1589	15	1623	12	1664	17	1664	17	2.1
Zircon_28_040	162	70	0.37	0.13229	0.00122	6.76050	0.08377	0.37040	0.00307	0.10289	0.00134	0.67	2031	14	2081	11	2129	15	2129	15	2.4

[a] Absolute errors at 1-σ level
[b] Absolute errors (Ma) at 1-σ level
[c] Error correlation
[d] Discordance = $(\frac{^{207}Pb}{^{235}U} - \frac{^{206}Pb}{^{238}U}) / \frac{^{207}Pb}{^{235}U} \cdot 100$

Tabla 3.: *LA-ICP-MS U–Pb isotopic data for sample MH-59*

				Corrected isotopic ratios[a]									Corrected ages (Ma)[b]						Best age		
Zircon no.	U (ppm)	Th (ppm)	Th/U	$\frac{^{207}Pb}{^{206}Pb}$	1σ	$\frac{^{207}Pb}{^{235}U}$	1σ	$\frac{^{206}Pb}{^{238}U}$	1σ	$\frac{^{208}Pb}{^{232}Th}$	1σ	ρ^c	$\frac{^{206}Pb}{^{238}U}$	1σ	$\frac{^{207}Pb}{^{235}U}$	1σ	$\frac{^{207}Pb}{^{206}Pb}$	1σ	(Ma)	1σ	δ (%)[d]
Zircon_13_022	2246	51	0.02	0.05008	0.00047	0.17394	0.00194	0.02515	0.00016	0.00900	0.00017	0.54	160	1	163	2	199	22	160	1	1.8
Zircon_10_018	1477	33	0.02	0.05015	0.00046	0.17720	0.00216	0.02563	0.00018	0.00809	0.00006	0.58	163	1	166	2	202	21	163	1	1.8
Zircon_12_021	1364	30	0.02	0.04935	0.00048	0.18177	0.00216	0.02668	0.00018	0.00792	0.00022	0.57	170	1	170	2	164	23	170	1	0.0
Zircon_24_035	1044	15	0.01	0.05056	0.00056	0.19081	0.00251	0.02734	0.00020	0.01194	0.00027	0.54	174	1	177	2	221	25	174	1	1.7
Zircon_37_051	820	18	0.02	0.05197	0.00171	0.21080	0.00715	0.02931	0.00023	0.02067	0.00054	0.24	186	1	194	6	284	77	186	1	4.1
Zircon_14_023	775	16	0.02	0.05106	0.00061	0.21569	0.00322	0.03063	0.00027	0.01537	0.00037	0.60	194	2	198	3	244	27	194	2	2.0
Zircon_17_027	561	43	0.07	0.04066	0.00065	0.18845	0.00329	0.03357	0.00023	0.02773	0.00042	0.40	213	1	175	3	-252	37	213	1	-21.7
Zircon_32_045	493	12	0.02	0.05034	0.00079	0.23841	0.00437	0.03434	0.00029	0.01083	0.00014	0.53	218	2	217	4	211	36	218	2	-0.5
Zircon_19_029	808	17	0.02	0.05497	0.00066	0.28326	0.00429	0.03738	0.00030	0.01166	0.00031	0.62	237	2	253	3	411	27	237	2	6.3
Zircon_6_014	1608	38	0.02	0.05432	0.00063	0.32237	0.00457	0.04304	0.00038	0.01345	0.00015	0.65	272	2	284	4	385	27	272	2	4.2
Zircon_MH-59_1_008	894	45	0.05	0.05177	0.00065	0.32422	0.00537	0.04542	0.00047	0.01428	0.00017	0.71	286	3	285	4	275	30	286	3	-0.4
Zircon_25_036	543	18	0.03	0.05236	0.00063	0.33038	0.00544	0.04576	0.00047	0.01436	0.00016	0.67	288	3	290	4	301	27	288	3	0.7
Zircon_5_012	1249	42	0.03	0.05637	0.00061	0.36600	0.00484	0.04709	0.00037	0.01465	0.00022	0.66	297	2	317	4	467	24	297	2	6.3
Zircon_33_046	785	23	0.03	0.06230	0.00074	0.40679	0.00741	0.04735	0.00058	0.01456	0.00031	0.76	298	4	347	5	685	25	298	4	14.1
Zircon_15_024	779	25	0.03	0.05208	0.00071	0.34520	0.00600	0.04807	0.00045	0.01510	0.00020	0.61	303	3	301	5	289	31	303	3	-0.7
Zircon_3_010	421	24	0.05	0.05295	0.00066	0.36600	0.00572	0.05014	0.00040	0.01572	0.00015	0.58	315	2	317	4	327	28	315	2	0.6
Zircon_30_042	680	455	0.62	0.05348	0.00059	0.38943	0.00516	0.05270	0.00039	0.01552	0.00020	0.55	331	2	334	4	349	25	331	2	0.9
Zircon_23_034	331	89	0.25	0.05519	0.00066	0.42357	0.00648	0.05560	0.00053	0.02272	0.00034	0.62	349	3	359	5	420	26	349	3	2.8
Zircon_8_016	467	44	0.09	0.05351	0.00074	0.42538	0.00677	0.05765	0.00043	0.01805	0.00015	0.55	361	3	360	5	351	32	361	3	-0.3
Zircon_29_041	253	14	0.05	0.06042	0.00097	0.49018	0.00890	0.05862	0.00050	0.04221	0.00076	0.47	367	3	405	6	619	34	367	3	9.4
Zircon_26_038	294	247	0.78	0.05792	0.00075	0.52166	0.00959	0.06525	0.00085	0.01902	0.00063	0.71	407	5	426	6	527	28	407	5	4.5
Zircon_34_047	684	94	0.13	0.06690	0.00080	0.61314	0.01537	0.06623	0.00146	0.04095	0.00086	0.88	413	9	486	10	835	25	413	9	15.0
Zircon_35_048	1100	39	0.03	0.05472	0.00057	0.50345	0.00666	0.06673	0.00049	0.02083	0.00023	0.61	416	3	414	5	401	23	416	3	-0.5
Zircon_21_032	342	43	0.12	0.05802	0.00070	0.55947	0.01032	0.06972	0.00098	0.03177	0.00060	0.76	434	6	451	7	531	26	434	6	3.8
Zircon_28_040	253	53	0.19	0.05539	0.00066	0.54316	0.00763	0.07100	0.00052	0.02068	0.00035	0.53	442	3	441	5	428	26	442	3	-0.2
Zircon_7_015	391	230	0.55	0.05601	0.00062	0.55000	0.00895	0.07113	0.00085	0.02387	0.00048	0.73	443	5	445	6	453	25	443	5	0.4
Zircon_11_020	468	47	0.09	0.05572	0.00073	0.55987	0.01896	0.07288	0.00185	0.02270	0.00056	0.91	453	11	451	12	441	28	453	11	-0.4
Zircon_18_028	218	58	0.24	0.05710	0.00080	0.57897	0.00909	0.07341	0.00052	0.02282	0.00041	0.45	457	3	464	6	495	31	457	3	1.5
Zircon_22_033	232	5	0.02	0.05929	0.00065	0.63856	0.00854	0.07804	0.00059	0.06150	0.00154	0.57	484	4	501	5	578	24	484	4	3.4
Zircon_38_052	243	25	0.10	0.05796	0.00075	0.62723	0.01068	0.07821	0.00086	0.02424	0.00046	0.65	485	5	494	7	528	29	485	5	1.8
Zircon_4_011	465	47	0.09	0.06096	0.00078	0.70329	0.01061	0.08367	0.00063	0.02579	0.00023	0.59	518	4	541	6	638	28	518	4	4.3
Zircon_36_050	1179	117	0.09	0.06933	0.00086	0.85496	0.01344	0.08943	0.00073	0.02717	0.00044	0.71	552	4	627	7	909	26	552	4	12.0

(Continued)

Tabla 3 *(Continued)*

				Corrected isotopic ratios[a]									Corrected ages (Ma)[b]						Best age		
Zircon no.	U (ppm)	Th (ppm)	Th/U	$\frac{^{207}Pb}{^{206}Pb}$	1σ	$\frac{^{207}Pb}{^{235}U}$	1σ	$\frac{^{206}Pb}{^{238}U}$	1σ	$\frac{^{208}Pb}{^{232}Th}$	1σ	ρ^{c}	$\frac{^{206}Pb}{^{238}U}$	1σ	$\frac{^{207}Pb}{^{235}U}$	1σ	$\frac{^{207}Pb}{^{206}Pb}$	1σ	(Ma)	1σ	δ (%)[d]
Zircon_27_039	329	48	0.13	0.05816	0.00076	0.76546	0.01116	0.09467	0.00062	0.02657	0.00040	0.44	583	4	577	6	536	28	583	4	-1.0
Zircon_39_053	188	130	0.64	0.06090	0.00097	0.81819	0.01436	0.09704	0.00070	0.02558	0.00036	0.42	597	4	607	8	636	35	597	4	1.6
Zircon_31_044	606	132	0.20	0.06209	0.00082	0.90824	0.01872	0.10609	0.00123	0.03263	0.00037	0.73	650	7	656	10	677	28	650	7	0.9
Zircon_2_009	200	26	0.12	0.06851	0.00088	1.28980	0.02563	0.13654	0.00169	0.04153	0.00052	0.73	825	10	841	11	884	26	825	10	1.9
Zircon_16_026	83	21	0.23	0.06935	0.00090	1.51960	0.02447	0.15860	0.00151	0.04653	0.00079	0.59	949	8	938	10	909	27	949	8	-1.2
Zircon_20_030	153	31	0.19	0.07668	0.00077	1.80390	0.02255	0.16943	0.00127	0.05069	0.00076	0.60	1009	7	1047	8	1113	20	1113	20	3.6
Zircon_40_054	480	60	0.12	0.07902	0.00071	2.04500	0.02295	0.18715	0.00125	0.05755	0.00092	0.60	1106	7	1131	8	1173	18	1173	18	2.2
Zircon_9_017	397	134	0.31	0.07965	0.00072	2.10860	0.02304	0.19174	0.00119	0.05497	0.00071	0.56	1131	6	1152	8	1188	18	1188	18	1.8

[a] Absolute errors at 1-σ level
[b] Absolute errors (Ma) at 1-σ level
[c] Error correlation
[d] Discordance = $(\frac{^{207}Pb}{^{235}U} - \frac{^{206}Pb}{^{238}U}) / \frac{^{207}Pb}{^{235}U} \cdot 100$

Tabla 4.: *LA-ICP-MS U–Pb isotopic data for sample MH-81*

				Corrected isotopic ratios[a]									Corrected ages (Ma)[b]						Best age		
Zircon no.	U (ppm)	Th (ppm)	Th/U	$\frac{^{207}Pb}{^{206}Pb}$	1σ	$\frac{^{207}Pb}{^{235}U}$	1σ	$\frac{^{206}Pb}{^{238}U}$	1σ	$\frac{^{208}Pb}{^{232}Th}$	1σ	ρ^c	$\frac{^{206}Pb}{^{238}U}$	1σ	$\frac{^{207}Pb}{^{235}U}$	1σ	$\frac{^{207}Pb}{^{206}Pb}$	1σ	(Ma)	1σ	δ (%)[d]
Zircon_15_023	954	278	0.27	0.05025	0.00070	0.18288	0.00298	0.02642	0.00022	0.00736	0.00013	0.52	168	1	171	3	207	29	168	1	1.8
Zircon_24_033	817	160	0.18	0.05034	0.00070	0.19619	0.00328	0.02828	0.00026	0.00838	0.00026	0.56	180	2	182	3	211	29	180	2	1.1
Zircon_28_038	878	44	0.05	0.05064	0.00081	0.21086	0.00386	0.03023	0.00027	0.01071	0.00033	0.49	192	2	194	3	224	33	192	2	1.0
Zircon_20_029	307	79	0.24	0.08947	0.03579	0.44070	0.17636	0.03670	0.00044	0.02277	0.00068	0.03	232	3	371	124	1414	799	232	3	37.5
Zircon_22_031	909	254	0.26	0.05063	0.00076	0.26891	0.00453	0.03851	0.00030	0.01218	0.00018	0.45	244	2	242	4	224	31	244	2	-0.8
Zircon_19_028	221	71	0.30	0.06000	0.00120	0.36300	0.00829	0.04390	0.00048	0.01936	0.00039	0.48	277	3	314	6	604	38	277	3	11.8
Zircon_17_026	999	601	0.56	0.06520	0.00078	0.39830	0.00648	0.04424	0.00049	0.01020	0.00024	0.68	279	3	340	5	781	22	279	3	17.9
Zircon_32_043	715	49	0.06	0.05301	0.00192	0.32495	0.01297	0.04446	0.00043	0.01393	0.00021	0.58	280	3	286	10	329	73	280	3	2.1
Zircon_33_044	126	21	0.16	0.05485	0.00224	0.34513	0.01608	0.04563	0.00065	0.01424	0.00021	0.54	288	4	301	12	406	82	288	4	4.3
Zircon_38_050	235	78	0.31	0.05169	0.00114	0.32717	0.00780	0.04588	0.00042	0.01257	0.00020	0.38	289	3	287	6	272	52	289	3	-0.7
Zircon_9_016	207	116	0.52	0.04498	0.00090	0.28923	0.00638	0.04671	0.00043	0.01280	0.00019	0.42	294	3	258	5	-20	38	294	3	-14.0
Zircon_39_051	107	46	0.40	0.06416	0.00180	0.43537	0.01294	0.04927	0.00049	0.00517	0.00072	0.33	310	3	367	9	747	61	310	3	15.5
Zircon_13_021	281	145	0.48	0.05320	0.00090	0.36964	0.00709	0.05043	0.00045	0.01294	0.00019	0.47	317	3	319	5	337	34	317	3	0.6
Zircon_31_041	777	588	0.70	0.05250	0.00074	0.36822	0.00599	0.05087	0.00042	0.01554	0.00020	0.50	320	3	318	4	307	28	320	3	-0.6
Zircon_30_040	180	159	0.82	0.05420	0.00103	0.39919	0.00831	0.05348	0.00045	0.01497	0.00021	0.41	336	3	341	6	379	38	336	3	1.5
Zircon_23_032	908	250	0.25	0.07281	0.00087	0.99803	0.01491	0.09928	0.00088	0.02166	0.00035	0.60	610	5	703	8	1009	21	610	5	13.2
Zircon_Mh-81_008	173	44	0.24	0.06992	0.00112	1.14350	0.02220	0.11812	0.00130	0.05967	0.00113	0.57	720	7	774	11	926	34	720	7	7.0
Zircon_35_046	167	49	0.27	0.06750	0.00146	1.16831	0.03462	0.12552	0.00181	0.03824	0.00053	0.69	762	10	786	16	853	46	762	10	3.1
Zircon_2_009	636	185	0.27	0.07352	0.00221	1.29304	0.04282	0.12755	0.00143	0.03849	0.00044	0.33	774	8	843	19	1028	54	774	8	8.2
Zircon_16_025	355	37	0.10	0.06916	0.00090	1.22110	0.01988	0.12797	0.00125	0.02998	0.00072	0.60	776	7	810	9	904	24	776	7	4.2
Zircon_6_013	493	51	0.10	0.07339	0.00081	1.41810	0.02089	0.13991	0.00137	0.04092	0.00057	0.66	844	8	897	9	1025	23	844	8	5.9
Zircon_40_052	159	64	0.37	0.07235	0.00101	1.43210	0.02835	0.14335	0.00201	0.04074	0.00098	0.71	864	11	902	12	996	29	864	11	4.2
Zircon_8_015	410	154	0.35	0.06997	0.00138	1.38495	0.04710	0.14355	0.00266	0.04356	0.00076	0.85	865	15	883	20	928	41	865	15	2.0
Zircon_37_049	434	63	0.13	0.07305	0.00103	1.46757	0.02756	0.14571	0.00151	0.04400	0.00048	0.68	877	8	917	11	1015	29	877	8	4.4
Zircon_29_039	1345	204	0.14	0.07230	0.00080	1.52300	0.02045	0.15286	0.00118	0.04236	0.00055	0.57	917	7	940	8	994	20	917	7	2.4
Zircon_12_020	151	99	0.61	0.06977	0.00105	1.53050	0.02662	0.15895	0.00140	0.04410	0.00057	0.50	951	8	943	11	922	27	951	8	-0.8
Zircon_3_010	99	49	0.46	0.07310	0.00095	1.64920	0.02636	0.16350	0.00152	0.04558	0.00087	0.58	976	8	989	10	1017	23	976	8	1.3
Zircon_10_017	683	109	0.15	0.07077	0.00078	1.62940	0.02379	0.16703	0.00160	0.04496	0.00063	0.66	996	9	982	9	951	20	996	9	-1.4
Zircon_27_037	390	81	0.19	0.07478	0.00089	1.75812	0.02621	0.17052	0.00129	0.05137	0.00039	0.53	1015	7	1030	10	1063	21	1063	21	1.5
Zircon_41_053	170	161	0.87	0.07551	0.00091	2.05050	0.02957	0.19701	0.00158	0.04871	0.00068	0.55	1159	9	1132	10	1082	25	1082	25	-2.4
Zircon_7_014	382	101	0.24	0.07633	0.00092	2.00380	0.02846	0.19029	0.00145	0.05118	0.00067	0.53	1123	8	1117	10	1104	25	1104	25	-0.5
Zircon_11_019	159	56	0.33	0.07824	0.00110	2.10080	0.03441	0.19469	0.00165	0.05295	0.00069	0.51	1147	9	1149	11	1153	25	1153	25	0.2

(Continued)

Tabla 4 *(Continued)*

				Corrected isotopic ratios[a]									Corrected ages (Ma)[b]						Best age		
Zircon no.	U (ppm)	Th (ppm)	Th/U	$\frac{^{207}Pb}{^{206}Pb}$	1σ	$\frac{^{207}Pb}{^{235}U}$	1σ	$\frac{^{206}Pb}{^{238}U}$	1σ	$\frac{^{208}Pb}{^{232}Th}$	1σ	ρ^{c}	$\frac{^{206}Pb}{^{238}U}$	1σ	$\frac{^{207}Pb}{^{235}U}$	1σ	$\frac{^{207}Pb}{^{206}Pb}$	1σ	(Ma)	1σ	δ (%)[d]
Zircon_34_045	1021	540	0.49	0.07932	0.00087	1.99810	0.02718	0.18281	0.00146	0.05209	0.00063	0.59	1082	8	1115	9	1180	22	1180	22	3.0
Zircon_4_011	377	292	0.72	0.08023	0.00096	1.68340	0.02740	0.15218	0.00167	0.03862	0.00154	0.68	913	9	1002	10	1203	24	1203	24	8.9
Zircon_18_027	178	128	0.67	0.08185	0.00900	1.96470	0.21694	0.17489	0.00168	0.04919	0.00064	0.09	1039	9	1103	74	1242	196	1242	196	5.8
Zircon_26_035	552	282	0.47	0.08216	0.00090	2.00770	0.02828	0.17730	0.00156	0.04736	0.00071	0.63	1052	9	1118	10	1249	19	1249	19	5.9
Zircon_25_034	195	49	0.23	0.08277	0.00099	2.41100	0.03532	0.21131	0.00178	0.06269	0.00082	0.58	1236	9	1246	11	1264	21	1264	21	0.8
Zircon_36_047	610	163	0.25	0.08668	0.00095	2.34040	0.03986	0.19578	0.00255	0.05006	0.00110	0.77	1153	14	1225	12	1353	22	1353	22	5.9
Zircon_14_022	243	71	0.27	0.09477	0.00104	3.45750	0.04703	0.26463	0.00212	0.06897	0.00090	0.59	1513	11	1518	11	1524	18	1524	18	0.3

[a] Absolute errors at 1-σ level
[b] Absolute errors (Ma) at 1-σ level
[c] Error correlation
[d] Discordance = $(\frac{^{207}Pb}{^{235}U} - \frac{^{206}Pb}{^{238}U}) / \frac{^{207}Pb}{^{235}U} \cdot 100$

A.3 ROCAS METASEDIMENTARIAS

Tabla 5.: *LA-ICP-MS U–Pb isotopic data for sample MH-28*

				Corrected isotopic ratios[a]									Corrected ages (Ma)[b]						Best age		
Zircon no.	U (ppm)	Th (ppm)	Th/U	$^{207}Pb/^{206}Pb$	1σ	$^{207}Pb/^{235}U$	1σ	$^{206}Pb/^{238}U$	1σ	$^{208}Pb/^{232}Th$	1σ	ρ^c	$^{206}Pb/^{238}U$	1σ	$^{207}Pb/^{235}U$	1σ	$^{207}Pb/^{206}Pb$	1σ	(Ma)	1σ	δ (%)[d]
Zircon_5_012	597	552	0.87	0.06641	0.00166	0.31038	0.01076	0.03474	0.00083	0.01092	0.00038	0.69	220	5	274	8	819	53	220	5	19.7
Zircon_8_016	664	424	0.60	0.05545	0.00078	0.30183	0.00577	0.03947	0.00051	0.01292	0.00028	0.68	250	3	268	5	430	30	250	3	6.7
Zircon_15_024	634	604	0.89	0.05967	0.00449	0.33649	0.02815	0.04090	0.00059	0.01264	0.00016	0.45	258	4	295	21	592	158	258	4	12.5
Zircon_2_009	64	25	0.37	0.05609	0.00164	0.32120	0.01034	0.04153	0.00038	0.01293	0.00012	0.35	262	2	283	8	456	65	262	2	7.4
Zircon_10_018	1124	998	0.83	0.07956	0.00103	0.45438	0.00835	0.04195	0.00055	0.01947	0.00091	0.71	265	3	380	6	1186	26	265	3	30.3
Zircon_62_081	113	61	0.51	0.07375	0.01142	0.43177	0.06874	0.04246	0.00060	0.01281	0.00031	0.15	268	4	364	49	1035	315	268	4	26.4
Zircon_14_023	536	85	0.15	0.05294	0.00069	0.33703	0.00596	0.04608	0.00055	0.01396	0.00024	0.68	290	3	295	5	326	30	290	3	1.7
Zircon_41_056	237	106	0.42	0.05411	0.00076	0.35000	0.00553	0.04696	0.00034	0.01409	0.00021	0.46	296	2	305	4	376	32	296	2	3.0
Zircon_72_092	267	104	0.36	0.05328	0.00069	0.37697	0.00560	0.05126	0.00037	0.01616	0.00024	0.49	322	2	325	4	341	28	322	2	0.9
Zircon_6_014	720	439	0.57	0.05795	0.00064	0.47043	0.00684	0.05899	0.00056	0.01808	0.00029	0.65	369	3	391	5	528	23	369	3	5.6
Zircon_20_030	966	180	0.18	0.06941	0.00078	0.85861	0.01444	0.08972	0.00086	0.02725	0.00026	0.70	554	5	629	8	911	22	554	5	11.9
Zircon_68_088	63	33	0.49	0.06329	0.00101	0.83480	0.01490	0.09581	0.00076	0.02805	0.00048	0.45	590	4	616	8	718	32	590	4	4.2
Zircon_69_089	503	210	0.39	0.06085	0.00061	0.80353	0.00990	0.09579	0.00069	0.03122	0.00044	0.58	590	4	599	6	634	21	590	4	1.5
Zircon_3_010	800	71	0.08	0.06060	0.00061	0.82852	0.01011	0.09924	0.00069	0.03362	0.00040	0.57	610	4	613	6	625	22	610	4	0.5
Zircon_34_047	696	119	0.16	0.06577	0.00071	0.93592	0.01397	0.10320	0.00084	0.03154	0.00026	0.66	633	5	671	7	799	23	633	5	5.7
Zircon_42_057	73	46	0.59	0.06303	0.00113	0.90923	0.01753	0.10475	0.00072	0.03049	0.00043	0.37	642	4	657	9	709	38	642	4	2.3
Zircon_22_033	891	283	0.30	0.07147	0.00150	1.13515	0.02693	0.11519	0.00093	0.03487	0.00029	0.46	703	5	770	13	971	43	703	5	8.7
Zircon_11_020	615	162	0.25	0.07379	0.00075	1.53838	0.02019	0.15121	0.00105	0.04561	0.00031	0.60	908	6	946	8	1036	20	908	6	4.0
Zircon_45_060	343	86	0.24	0.07127	0.00066	1.59320	0.01913	0.16205	0.00123	0.04709	0.00057	0.64	968	7	968	7	965	19	968	7	0.0
Zircon_67_087	178	37	0.19	0.07137	0.00090	1.60246	0.02717	0.16284	0.00138	0.04931	0.00041	0.60	973	8	971	11	968	24	973	8	-0.2
Zircon_76_097	184	58	0.30	0.07231	0.00072	1.72390	0.02155	0.17290	0.00130	0.05341	0.00069	0.60	1028	7	1017	8	995	19	995	19	-1.1
Zircon_79_100	138	55	0.37	0.07230	0.00087	1.66670	0.02324	0.16727	0.00119	0.04896	0.00059	0.51	997	7	996	9	994	23	997	7	-0.1
Zircon_16_026	74	32	0.41	0.07245	0.00247	1.68496	0.06421	0.16868	0.00153	0.05099	0.00047	0.38	1005	8	1003	24	999	66	999	66	-0.2
Zircon_80_101	215	70	0.30	0.07302	0.00080	1.67310	0.02173	0.16642	0.00115	0.05004	0.00060	0.54	992	6	998	8	1015	21	1015	21	0.6
Zircon_54_071	380	111	0.28	0.07329	0.00071	1.88310	0.02479	0.18646	0.00166	0.05640	0.00068	0.68	1102	9	1075	9	1022	20	1022	20	-2.5
Zircon_MH28_1_008	148	57	0.36	0.07348	0.00081	1.76520	0.02302	0.17438	0.00122	0.05089	0.00061	0.53	1036	7	1033	8	1027	21	1027	21	-0.3
Zircon_50_066	518	59	0.11	0.07356	0.00066	1.70400	0.02063	0.16811	0.00136	0.05052	0.00066	0.67	1002	8	1010	8	1029	18	1029	18	0.8
Zircon_39_053	161	49	0.28	0.07360	0.00088	1.68360	0.02365	0.16586	0.00121	0.04927	0.00059	0.52	989	7	1002	9	1031	24	1031	24	1.3
Zircon_7_015	191	22	0.11	0.07386	0.00081	2.05020	0.04325	0.20148	0.00363	0.05729	0.00086	0.85	1183	19	1132	14	1038	21	1038	21	-4.5
Zircon_75_095	115	63	0.52	0.07436	0.00097	1.76760	0.03250	0.17284	0.00225	0.05443	0.00147	0.70	1028	12	1034	12	1051	25	1051	25	0.6
Zircon_4_011	313	112	0.34	0.07471	0.00102	1.64778	0.02973	0.15997	0.00130	0.04819	0.00038	0.59	957	7	989	11	1061	28	1061	28	3.2
Zircon_46_062	92	61	0.63	0.07483	0.00157	1.70980	0.03796	0.16559	0.00119	0.04824	0.00058	0.33	988	7	1012	14	1064	43	1064	43	2.4

(Continued)

Tabla 5 *(Continued)*

				Corrected isotopic ratios[a]									Corrected ages (Ma)[b]						Best age		
Zircon no.	U (ppm)	Th (ppm)	Th/U	$\frac{^{207}Pb}{^{206}Pb}$	1σ	$\frac{^{207}Pb}{^{235}U}$	1σ	$\frac{^{206}Pb}{^{238}U}$	1σ	$\frac{^{208}Pb}{^{232}Th}$	1σ	ρ^c	$\frac{^{206}Pb}{^{238}U}$	1σ	$\frac{^{207}Pb}{^{235}U}$	1σ	$\frac{^{207}Pb}{^{206}Pb}$	1σ	(Ma)	1σ	δ (%)[d]
Zircon_55_072	46	22	0.45	0.07486	0.00112	1.68860	0.02810	0.16368	0.00118	0.04840	0.00063	0.44	977	7	1004	11	1065	30	1065	30	2.7
Zircon_35_048	90	24	0.25	0.07514	0.00098	1.82660	0.02723	0.17614	0.00129	0.05759	0.00098	0.48	1046	7	1055	10	1072	26	1072	26	0.9
Zircon_18_028	561	85	0.14	0.07559	0.00070	1.92580	0.02219	0.18479	0.00126	0.05404	0.00065	0.60	1093	7	1090	8	1084	19	1084	19	-0.3
Zircon_29_041	175	49	0.26	0.07570	0.00091	1.85930	0.02789	0.17804	0.00160	0.05271	0.00074	0.60	1056	9	1067	10	1087	24	1087	24	1.0
Zircon_51_068	261	55	0.20	0.07587	0.00074	1.89430	0.02238	0.18110	0.00120	0.05556	0.00067	0.56	1073	7	1079	8	1092	20	1092	20	0.6
Zircon_12_021	76	28	0.35	0.07675	0.00137	2.00527	0.04224	0.18950	0.00139	0.05692	0.00041	0.41	1119	8	1117	14	1115	34	1115	34	-0.2
Zircon_57_075	401	78	0.18	0.07679	0.00071	2.04520	0.02418	0.19312	0.00141	0.05962	0.00078	0.62	1138	8	1131	8	1116	19	1116	19	-0.6
Zircon_65_084	266	74	0.26	0.07710	0.00073	1.93020	0.02255	0.18157	0.00123	0.05217	0.00063	0.59	1076	7	1092	8	1124	18	1124	18	1.5
Zircon_58_076	601	159	0.25	0.07752	0.00091	1.90717	0.02972	0.17844	0.00146	0.05354	0.00043	0.59	1058	8	1084	10	1135	23	1135	23	2.4
Zircon_48_064	187	55	0.28	0.07758	0.00078	1.95780	0.02532	0.18325	0.00150	0.05632	0.00073	0.63	1085	8	1101	9	1136	20	1136	20	1.5
Zircon_70_090	1088	142	0.12	0.07760	0.00065	1.94820	0.02081	0.18211	0.00120	0.05477	0.00071	0.62	1078	7	1098	7	1137	16	1137	16	1.8
Zircon_9_017	707	67	0.09	0.07766	0.00072	1.98460	0.02546	0.18535	0.00142	0.05560	0.00042	0.62	1096	8	1110	9	1138	17	1138	17	1.3
Zircon_28_040	236	93	0.37	0.07769	0.00071	2.10680	0.02344	0.19631	0.00126	0.05795	0.00070	0.57	1155	7	1151	8	1139	18	1139	18	-0.3
Zircon_32_045	615	15	0.02	0.07771	0.00071	2.05090	0.02447	0.19152	0.00146	0.06149	0.00086	0.64	1130	8	1133	8	1139	18	1139	18	0.3
Zircon_66_086	603	111	0.17	0.07769	0.00068	2.14310	0.02462	0.20000	0.00150	0.05516	0.00061	0.65	1175	8	1163	8	1139	17	1139	17	-1.0
Zircon_77_098	67	39	0.55	0.07788	0.00093	2.25830	0.03244	0.21035	0.00166	0.06047	0.00079	0.56	1231	9	1199	10	1144	23	1144	23	-2.7
Zircon_49_065	259	77	0.28	0.07812	0.00078	2.08720	0.02524	0.19377	0.00132	0.05760	0.00069	0.56	1142	7	1145	8	1150	20	1150	20	0.3
Zircon_53_070	241	78	0.30	0.07811	0.00105	2.04369	0.03374	0.18976	0.00134	0.05689	0.00039	0.50	1120	7	1130	11	1150	27	1150	27	0.9
Zircon_59_077	566	97	0.16	0.07831	0.00071	2.18410	0.02590	0.20262	0.00154	0.06194	0.00081	0.64	1189	8	1176	8	1155	18	1155	18	-1.1
Zircon_63_082	938	154	0.15	0.07832	0.00068	2.04960	0.02315	0.18987	0.00137	0.05157	0.00067	0.64	1121	7	1132	8	1155	16	1155	16	1.0
Zircon_44_059	1129	233	0.19	0.07847	0.00077	1.87500	0.03053	0.17344	0.00225	0.04472	0.00192	0.80	1031	12	1072	11	1159	20	1159	20	3.8
Zircon_64_083	215	68	0.30	0.07846	0.00078	2.13130	0.02589	0.19701	0.00136	0.05750	0.00069	0.57	1159	7	1159	8	1159	19	1159	19	0.0
Zircon_43_058	45	32	0.67	0.07873	0.00134	2.16880	0.04132	0.20015	0.00172	0.05757	0.00081	0.45	1176	9	1171	13	1165	34	1165	34	-0.4
Zircon_19_029	206	58	0.27	0.07890	0.00077	2.25440	0.03000	0.20735	0.00187	0.05934	0.00077	0.68	1215	10	1198	9	1170	19	1170	19	-1.4
Zircon_17_027	1052	39	0.03	0.07894	0.00065	2.01476	0.02263	0.18510	0.00154	0.05543	0.00046	0.72	1095	8	1120	8	1171	16	1171	16	2.2
Zircon_26_038	488	140	0.27	0.07907	0.00070	2.14030	0.02450	0.19639	0.00141	0.05700	0.00074	0.63	1156	8	1162	8	1174	18	1174	18	0.5
Zircon_13_022	175	41	0.22	0.07910	0.00079	2.32380	0.03095	0.21300	0.00187	0.06711	0.00114	0.66	1245	10	1220	9	1175	20	1175	20	-2.0
Zircon_37_051	31	14	0.44	0.07957	0.00127	2.11760	0.03973	0.19307	0.00189	0.06030	0.00096	0.53	1138	10	1155	13	1186	32	1186	32	1.5
Zircon_74_094	66	37	0.52	0.07966	0.00112	2.20670	0.03526	0.20105	0.00155	0.05839	0.00076	0.48	1181	8	1183	11	1189	26	1189	26	0.2
Zircon_73_093	370	86	0.22	0.07978	0.00076	2.12390	0.02481	0.19272	0.00131	0.05831	0.00082	0.58	1136	7	1157	8	1192	18	1192	18	1.8
Zircon_27_039	925	231	0.23	0.07983	0.00069	2.00430	0.02130	0.18210	0.00111	0.05542	0.00061	0.58	1078	6	1117	7	1193	17	1193	17	3.5
Zircon_56_074	935	270	0.27	0.07986	0.00079	1.64890	0.04587	0.14818	0.00385	0.04640	0.00097	0.93	891	22	989	18	1194	20	1194	20	9.9
Zircon_52_069	339	92	0.26	0.08018	0.00078	2.20630	0.02614	0.19963	0.00136	0.05742	0.00069	0.57	1173	7	1183	8	1201	19	1201	19	0.8

(Continued)

Tabla 5 *(Continued)*

				Corrected isotopic ratios[a]									Corrected ages (Ma)[b]						Best age		
Zircon no.	U (ppm)	Th (ppm)	Th/U	$\frac{^{207}Pb}{^{206}Pb}$	1σ	$\frac{^{207}Pb}{^{235}U}$	1σ	$\frac{^{206}Pb}{^{238}U}$	1σ	$\frac{^{208}Pb}{^{232}Th}$	1σ	ρ[c]	$\frac{^{206}Pb}{^{238}U}$	1σ	$\frac{^{207}Pb}{^{235}U}$	1σ	$\frac{^{207}Pb}{^{206}Pb}$	1σ	(Ma)	1σ	δ (%)[d]
Zircon_60_078	153	54	0.33	0.08037	0.00080	2.40630	0.02937	0.21715	0.00152	0.05705	0.00068	0.58	1267	8	1244	9	1206	19	1206	19	-1.8
Zircon_40_054	776	59	0.07	0.08042	0.00075	2.31440	0.02736	0.20887	0.00152	0.06238	0.00081	0.61	1223	8	1217	8	1207	19	1207	19	-0.5
Zircon_78_099	889	122	0.13	0.08091	0.00074	2.27562	0.03090	0.20399	0.00168	0.06092	0.00051	0.67	1197	9	1205	10	1219	17	1219	17	0.7
Zircon_31_044	975	67	0.06	0.08101	0.00072	1.72390	0.01931	0.15423	0.00105	0.03562	0.00057	0.61	925	6	1017	7	1222	18	1222	18	9.0
Zircon_36_050	656	76	0.11	0.08140	0.00072	2.21600	0.02496	0.19758	0.00136	0.06002	0.00066	0.62	1162	7	1186	8	1231	17	1231	17	2.0
Zircon_23_034	317	95	0.28	0.08145	0.00075	2.45010	0.02862	0.21820	0.00157	0.06418	0.00071	0.62	1272	8	1257	8	1232	18	1232	18	-1.2
Zircon_25_036	165	52	0.29	0.08160	0.00082	2.30110	0.03254	0.20452	0.00205	0.06704	0.00080	0.70	1200	11	1213	10	1236	20	1236	20	1.1
Zircon_61_080	406	279	0.65	0.08182	0.00074	2.26150	0.02592	0.20045	0.00142	0.05558	0.00067	0.61	1178	8	1200	8	1241	17	1241	17	1.8
Zircon_33_046	252	88	0.33	0.08227	0.00082	2.39580	0.02938	0.21130	0.00150	0.06177	0.00074	0.58	1236	8	1241	9	1252	20	1252	20	0.4
Zircon_21_032	465	311	0.63	0.08380	0.00071	2.41950	0.02619	0.20946	0.00140	0.06111	0.00067	0.62	1226	7	1248	8	1288	16	1288	16	1.8
Zircon_38_052	258	88	0.32	0.08480	0.00078	2.53110	0.03053	0.21619	0.00169	0.06193	0.00074	0.65	1262	9	1281	9	1311	18	1311	18	1.5
Zircon_81_103	165	70	0.40	0.08491	0.00085	2.48350	0.03308	0.21223	0.00187	0.06244	0.00069	0.66	1241	10	1267	10	1313	18	1313	18	2.1
Zircon_47_063	643	195	0.28	0.09016	0.00144	1.56680	0.06750	0.12936	0.00517	0.07140	0.00193	0.93	784	30	957	27	1429	29	1429	29	18.1
Zircon_24_035	357	63	0.16	0.09045	0.00089	2.29137	0.04104	0.18373	0.00234	0.05422	0.00068	0.82	1087	13	1210	13	1435	19	1435	19	10.2
Zircon_30_042	87	27	0.29	0.10088	0.00111	4.01770	0.05946	0.28855	0.00286	0.08544	0.00120	0.67	1634	14	1638	12	1640	19	1640	19	0.2

[a] Absolute errors at 1-σ level
[b] Absolute errors (Ma) at 1-σ level
[c] Error correlation
[d] Discordance = $(\frac{^{207}Pb}{^{235}U} - \frac{^{206}Pb}{^{238}U}) / \frac{^{207}Pb}{^{235}U} \cdot 100$

Tabla 6.: *LA-ICP-MS U–Pb isotopic data for sample MH-50*

				Corrected isotopic ratios[a]									Corrected ages (Ma)[b]						Best age		
Zircon no.	U (ppm)	Th (ppm)	Th/U	$\frac{^{207}Pb}{^{206}Pb}$	1σ	$\frac{^{207}Pb}{^{235}U}$	1σ	$\frac{^{206}Pb}{^{238}U}$	1σ	$\frac{^{208}Pb}{^{232}Th}$	1σ	ρ^c	$\frac{^{206}Pb}{^{238}U}$	1σ	$\frac{^{207}Pb}{^{235}U}$	1σ	$\frac{^{207}Pb}{^{206}Pb}$	1σ	(Ma)	1σ	δ (%)[d]
Zircon_76_099	3766	297	0.09	0.06508	0.00223	0.19015	0.00697	0.02119	0.00019	0.00648	0.00018	0.34	135	1	177	6	777	71	135	1	23.7
Zircon_77_100	2340	74	0.03	0.05149	0.00095	0.15662	0.00347	0.02206	0.00021	0.00694	0.00027	0.59	141	1	148	3	263	42	141	1	4.7
Zircon_13_023	2020	149	0.08	0.05600	0.00117	0.19116	0.00523	0.02476	0.00033	0.00771	0.00014	0.61	158	2	178	4	453	47	158	2	11.2
Zircon_78_101	4899	188	0.04	0.05470	0.00136	0.19349	0.00754	0.02565	0.00061	0.00801	0.00030	0.77	163	4	180	6	400	55	163	4	9.4
Zircon_53_071	923	84	0.10	0.05969	0.00129	0.24078	0.01098	0.02925	0.00091	0.00904	0.00028	0.91	186	6	219	9	593	47	186	6	15.1
Zircon_54_072	1291	5	0.00	0.05079	0.00072	0.21652	0.00386	0.03092	0.00029	0.00974	0.00092	0.59	196	2	199	3	232	30	196	2	1.5
Zircon_61_081	836	14	0.02	0.04941	0.00052	0.21318	0.00330	0.03129	0.00032	0.00989	0.00017	0.74	199	2	196	3	167	24	199	2	-1.5
Zircon_11_021	570	438	0.85	0.07588	0.00152	0.35756	0.00816	0.03400	0.00037	0.00750	0.00033	0.48	216	2	310	6	1092	40	216	2	30.3
Zircon_88_113	3120	177	0.06	0.05171	0.00052	0.24660	0.00529	0.03457	0.00066	0.01762	0.00097	0.88	219	4	224	4	273	23	219	4	2.2
Zircon_71_093	879	20	0.02	0.05031	0.00052	0.24707	0.00420	0.03562	0.00042	0.01123	0.00018	0.79	226	3	224	3	209	23	226	3	-0.9
Zircon_16_027	633	52	0.09	0.06192	0.00080	0.31604	0.00487	0.03703	0.00031	0.02993	0.00126	0.54	234	2	279	4	671	28	234	2	16.1
Zircon_12_022	537	25	0.05	0.05893	0.00077	0.30439	0.00494	0.03745	0.00036	0.03350	0.00224	0.59	237	2	270	4	565	29	237	2	12.2
Zircon_85_109	924	251	0.30	0.06188	0.00068	0.31956	0.00444	0.03769	0.00032	0.01806	0.00033	0.61	238	2	282	3	670	23	238	2	15.6
Zircon_8_017	321	43	0.15	0.05309	0.00090	0.27476	0.00530	0.03780	0.00034	0.01965	0.00045	0.48	239	2	246	4	333	38	239	2	2.8
Zircon_7_016	512	60	0.13	0.06642	0.00073	0.34735	0.00674	0.03796	0.00061	0.02486	0.00037	0.82	240	4	303	5	820	22	240	4	20.8
Zircon_70_091	553	341	0.68	0.07308	0.00095	0.38317	0.00628	0.03870	0.00039	0.00758	0.00014	0.61	245	2	329	5	1016	25	245	2	25.5
Zircon_21_033	1794	2014	1.23	0.05958	0.00054	0.32461	0.00413	0.03955	0.00036	0.01255	0.00015	0.70	250	2	285	3	588	20	250	2	12.3
Zircon_47_064	626	89	0.16	0.06253	0.00069	0.35480	0.00485	0.04126	0.00033	0.02539	0.00030	0.59	261	2	308	4	692	24	261	2	15.3
Zircon_22_034	636	25	0.04	0.05798	0.00064	0.33465	0.00465	0.04175	0.00035	0.04491	0.00085	0.61	264	2	293	4	529	23	264	2	9.9
Zircon_39_054	381	177	0.51	0.06176	0.00099	0.35547	0.00665	0.04186	0.00041	0.01715	0.00022	0.52	264	3	309	5	666	33	264	3	14.6
Zircon_34_048	357	87	0.27	0.05498	0.00066	0.31715	0.00481	0.04198	0.00039	0.01663	0.00023	0.61	265	2	280	4	411	26	265	2	5.4
Zircon_42_058	582	77	0.15	0.05384	0.00059	0.31188	0.00485	0.04203	0.00046	0.01604	0.00022	0.71	265	3	276	4	364	25	265	3	4.0
Zircon_56_075	549	266	0.53	0.05398	0.00065	0.31583	0.00559	0.04247	0.00055	0.01452	0.00022	0.73	268	3	279	4	370	28	268	3	3.9
Zircon_52_070	280	82	0.32	0.05723	0.00086	0.33756	0.00670	0.04283	0.00056	0.01718	0.00027	0.65	270	3	295	5	500	34	270	3	8.5
Zircon_38_053	833	1074	1.42	0.05438	0.00053	0.32648	0.00406	0.04357	0.00034	0.01496	0.00025	0.62	275	2	287	3	387	21	275	2	4.2
Zircon_75_097	521	75	0.16	0.05913	0.00098	0.35486	0.01023	0.04353	0.00076	0.01346	0.00023	0.80	275	5	308	8	572	36	275	5	10.7
Zircon_91_117	748	85	0.12	0.05337	0.00080	0.34347	0.00948	0.04668	0.00081	0.01462	0.00026	0.85	294	5	300	7	344	33	294	5	2.0
Zircon_46_063	345	74	0.24	0.05200	0.00145	0.33807	0.01086	0.04715	0.00049	0.01481	0.00015	0.53	297	3	296	8	286	65	297	3	-0.3
Zircon_66_087	1210	424	0.39	0.06035	0.00060	0.38833	0.00497	0.04710	0.00038	0.01803	0.00020	0.63	297	2	333	4	616	21	297	2	10.8
Zircon_59_078	147	79	0.59	0.07406	0.00126	0.49201	0.01053	0.04827	0.00063	0.02019	0.00028	0.61	304	4	406	7	1043	33	304	4	25.1
Zircon_33_047	282	126	0.49	0.05732	0.00080	0.39259	0.00645	0.04976	0.00043	0.01541	0.00018	0.53	313	3	336	5	504	30	313	3	6.8
Zircon_55_073	345	57	0.18	0.06023	0.00129	0.42502	0.01177	0.05118	0.00067	0.01580	0.00020	0.68	322	4	360	8	612	47	322	4	10.6

(Continued)

Tabla 6 *(Continued)*

				Corrected isotopic ratios[a]									Corrected ages (Ma)[b]						Best age		
Zircon no.	U (ppm)	Th (ppm)	Th/U	$\frac{^{207}Pb}{^{206}Pb}$	1σ	$\frac{^{207}Pb}{^{235}U}$	1σ	$\frac{^{206}Pb}{^{238}U}$	1σ	$\frac{^{208}Pb}{^{232}Th}$	1σ	ρ^c	$\frac{^{206}Pb}{^{238}U}$	1σ	$\frac{^{207}Pb}{^{235}U}$	1σ	$\frac{^{207}Pb}{^{206}Pb}$	1σ	(Ma)	1σ	δ (%)[d]
Zircon_67_088	177	68	0.42	0.05241	0.00128	0.37456	0.01296	0.05183	0.00071	0.01627	0.00020	0.71	326	4	323	10	304	54	326	4	-0.9
Zircon_73_095	666	17	0.03	0.05516	0.00161	0.40340	0.02095	0.05304	0.00166	0.01654	0.00126	0.93	333	10	344	15	419	59	333	10	3.2
Zircon_2_010	125	219	1.92	0.05920	0.00142	0.44047	0.01295	0.05411	0.00092	0.01765	0.00021	0.58	340	6	371	9	574	53	340	6	8.4
Zircon_40_055	99	238	2.64	0.06206	0.00124	0.46985	0.01009	0.05549	0.00043	0.01759	0.00025	0.37	348	3	391	7	676	41	348	3	11.0
Zircon_44_060	750	38	0.06	0.06136	0.00110	0.47241	0.01650	0.05583	0.00135	0.01720	0.00054	0.89	350	8	393	11	652	39	350	8	10.9
Zircon_89_114	181	32	0.20	0.05396	0.00151	0.42145	0.02126	0.05665	0.00168	0.01772	0.00050	0.80	355	10	357	15	369	62	355	10	0.6
Zircon_48_065	788	54	0.08	0.06836	0.00068	0.53549	0.01056	0.05674	0.00096	0.05853	0.00082	0.86	356	6	435	7	879	21	356	6	18.2
Zircon_65_085	481	189	0.43	0.05636	0.00062	0.44350	0.00690	0.05718	0.00063	0.01972	0.00026	0.71	358	4	373	5	467	24	358	4	4.0
Zircon_45_061	53	25	0.52	0.05391	0.00209	0.43317	0.01999	0.05828	0.00081	0.01823	0.00023	0.48	365	5	365	14	367	89	365	5	0.0
Zircon_37_052	150	52	0.38	0.05772	0.00150	0.47066	0.01388	0.05914	0.00045	0.01835	0.00013	0.37	370	3	392	10	519	55	370	3	5.6
Zircon_79_102	248	205	0.91	0.05525	0.00066	0.46782	0.00936	0.06162	0.00099	0.01720	0.00021	0.80	385	6	390	6	422	26	385	6	1.3
Zircon_23_035	462	67	0.16	0.05469	0.00085	0.47519	0.00948	0.06302	0.00052	0.01968	0.00019	0.64	394	3	395	7	400	34	394	3	0.3
Zircon_26_039	133	81	0.67	0.05892	0.00112	0.51310	0.01531	0.06413	0.00147	0.01850	0.00024	0.77	401	9	421	10	564	40	401	9	4.8
Zircon_90_115	62	33	0.58	0.05954	0.00426	0.52829	0.04250	0.06436	0.00109	0.01989	0.00030	0.39	402	7	431	28	587	156	402	7	6.7
Zircon_86_111	542	68	0.14	0.05722	0.00055	0.50796	0.00824	0.06445	0.00084	0.02536	0.00038	0.81	403	5	417	6	500	21	403	5	3.4
Zircon_68_089	699	480	0.76	0.05709	0.00057	0.51285	0.00656	0.06520	0.00053	0.02005	0.00024	0.63	407	3	420	4	495	21	407	3	3.1
Zircon_36_051	216	50	0.25	0.05728	0.00080	0.52299	0.00828	0.06626	0.00049	0.02488	0.00030	0.47	414	3	427	6	502	30	414	3	3.0
Zircon_69_090	365	39	0.12	0.05632	0.00067	0.54923	0.01279	0.07073	0.00113	0.02201	0.00034	0.84	441	7	444	8	465	25	441	7	0.7
Zircon_49_066	436	16	0.04	0.06228	0.00090	0.64798	0.01240	0.07546	0.00076	0.02320	0.00061	0.67	469	5	507	8	684	28	469	5	7.5
Zircon_5_013	407	66	0.18	0.07401	0.00081	0.79896	0.01618	0.07745	0.00132	0.05728	0.00109	0.84	481	8	596	9	1042	22	481	8	19.3
Zircon_41_057	373	131	0.39	0.05762	0.00058	0.62120	0.00819	0.07772	0.00067	0.02481	0.00032	0.65	482	4	491	5	515	22	482	4	1.8
Zircon_14_024	411	47	0.12	0.05602	0.00104	0.61807	0.01743	0.08002	0.00123	0.02491	0.00044	0.76	496	7	489	11	453	37	496	7	-1.4
Zircon_60_079	313	144	0.51	0.06066	0.00117	0.73830	0.01900	0.08827	0.00084	0.02722	0.00023	0.62	545	5	561	11	627	40	545	5	2.9
Zircon_80_103	415	52	0.14	0.06230	0.00127	0.76683	0.03301	0.08927	0.00246	0.02745	0.00076	0.92	551	15	578	19	684	43	551	15	4.7
Zircon_63_083	452	58	0.14	0.06235	0.00062	0.81317	0.01010	0.09442	0.00071	0.02996	0.00051	0.60	582	4	604	6	686	21	582	4	3.6
Zircon_72_094	451	78	0.19	0.06137	0.00055	0.81868	0.00974	0.09690	0.00077	0.03039	0.00036	0.66	596	5	607	5	652	19	596	5	1.8
Zircon_15_025	345	71	0.22	0.06528	0.00109	0.89026	0.02584	0.09891	0.00165	0.03025	0.00048	0.87	608	10	647	14	783	35	608	10	6.0
Zircon_19_030	203	97	0.53	0.06454	0.00090	0.97900	0.01645	0.10996	0.00102	0.03189	0.00041	0.56	673	6	693	8	759	30	673	6	2.9
Zircon_64_084	397	97	0.27	0.06298	0.00061	0.96855	0.01170	0.11160	0.00080	0.03388	0.00044	0.60	682	5	688	6	708	20	682	5	0.9
Zircon_29_042	368	129	0.39	0.07054	0.00071	1.14840	0.01884	0.11796	0.00153	0.04506	0.00054	0.79	719	9	776	9	944	20	719	9	7.3
Zircon_27_040	635	67	0.12	0.07043	0.00073	1.15234	0.02022	0.11866	0.00141	0.03598	0.00042	0.79	723	8	778	10	941	20	723	8	7.1
Zircon_30_043	219	43	0.21	0.06672	0.00124	1.11897	0.03380	0.12164	0.00197	0.03711	0.00061	0.83	740	11	762	16	829	38	740	11	2.9
Zircon_28_041	221	63	0.31	0.06352	0.00191	1.08516	0.03918	0.12390	0.00133	0.03801	0.00055	0.67	753	8	746	19	726	57	753	8	-0.9

(Continued)

Tabla 6 *(Continued)*

				Corrected isotopic ratios[a]									Corrected ages (Ma)[b]						Best age		
Zircon no.	U (ppm)	Th (ppm)	Th/U	$\frac{^{207}Pb}{^{206}Pb}$	1σ	$\frac{^{207}Pb}{^{235}U}$	1σ	$\frac{^{206}Pb}{^{238}U}$	1σ	$\frac{^{208}Pb}{^{232}Th}$	1σ	ρ^{c}	$\frac{^{206}Pb}{^{238}U}$	1σ	$\frac{^{207}Pb}{^{235}U}$	1σ	$\frac{^{207}Pb}{^{206}Pb}$	1σ	(Ma)	1σ	δ (%)[d]
Zircon_50_067	184	35	0.21	0.07220	0.00169	1.25843	0.04001	0.12641	0.00172	0.03823	0.00068	0.73	767	10	827	18	992	43	767	10	7.3
Zircon_51_069	200	62	0.34	0.06662	0.00092	1.20396	0.02190	0.13107	0.00108	0.03999	0.00031	0.59	794	6	802	10	826	29	794	6	1.0
Zircon_6_015	496	142	0.31	0.07135	0.00064	1.43210	0.02148	0.14559	0.00175	0.04381	0.00057	0.80	876	10	902	9	967	18	876	10	2.9
Zircon_57_076	515	66	0.14	0.07035	0.00070	1.41660	0.01805	0.14571	0.00115	0.04525	0.00059	0.62	877	6	896	8	939	21	877	6	2.1
Zircon_31_045	553	56	0.11	0.07391	0.00067	1.50831	0.01864	0.14801	0.00103	0.04464	0.00032	0.64	890	6	934	8	1039	18	890	6	4.7
Zircon_35_049	205	170	0.91	0.07178	0.00079	1.59510	0.02267	0.16130	0.00145	0.04437	0.00058	0.63	964	8	968	9	980	22	964	8	0.4
Zircon_83_107	612	72	0.13	0.07097	0.00066	1.59208	0.02196	0.16271	0.00142	0.04930	0.00043	0.67	972	8	967	9	956	19	972	8	-0.5
Zircon_82_106	530	130	0.27	0.07327	0.00063	1.64640	0.02847	0.16301	0.00245	0.04863	0.00058	0.87	973	14	988	11	1021	17	973	14	1.5
Zircon_18_029	95	41	0.48	0.07247	0.00094	1.63820	0.02581	0.16395	0.00146	0.04794	0.00067	0.57	979	8	985	10	999	27	979	8	0.6
Zircon_43_059	425	100	0.26	0.07229	0.00071	1.65196	0.02447	0.16574	0.00141	0.05011	0.00041	0.70	989	8	990	9	994	20	989	8	0.1
Zircon_32_046	250	51	0.22	0.07399	0.00091	1.70046	0.03271	0.16669	0.00184	0.05027	0.00054	0.74	994	10	1009	12	1041	24	1041	24	1.5
Zircon_81_105	301	309	1.13	0.07456	0.00075	1.87580	0.02640	0.18253	0.00181	0.05071	0.00056	0.70	1081	10	1073	9	1057	20	1057	20	-0.7
Zircon_58_077	691	76	0.12	0.07484	0.00062	1.76950	0.02193	0.17105	0.00157	0.05304	0.00095	0.74	1018	9	1034	8	1064	16	1064	16	1.5
Zircon_74_096	255	76	0.33	0.07575	0.00095	1.82145	0.03725	0.17440	0.00196	0.05246	0.00056	0.74	1036	11	1053	13	1088	23	1088	23	1.6
Zircon_17_028	145	34	0.25	0.07688	0.00085	2.04500	0.02645	0.19275	0.00131	0.05398	0.00081	0.52	1136	7	1131	9	1118	22	1118	22	-0.4
Zircon_92_118	110	45	0.45	0.10450	0.00101	4.69630	0.06057	0.32551	0.00277	0.08963	0.00117	0.66	1817	13	1767	11	1706	16	1706	16	-2.8
Zircon_62_082	406	83	0.22	0.12391	0.00151	3.34953	0.05521	0.19605	0.00159	0.05601	0.00076	0.68	1154	9	1493	13	2013	20	2013	20	22.7

[a] Absolute errors at 1-σ level
[b] Absolute errors (Ma) at 1-σ level
[c] Error correlation
[d] Discordance = $(\frac{^{207}Pb}{^{235}U} - \frac{^{206}Pb}{^{238}U}) / \frac{^{207}Pb}{^{235}U} \cdot 100$

Tabla 7.: *LA-ICP-MS U–Pb isotopic data for sample MH-53*

				Corrected isotopic ratios[a]									Corrected ages (Ma)[b]						Best age		
Zircon no.	U (ppm)	Th (ppm)	Th/U	$\frac{^{207}Pb}{^{206}Pb}$	1σ	$\frac{^{207}Pb}{^{235}U}$	1σ	$\frac{^{206}Pb}{^{238}U}$	1σ	$\frac{^{208}Pb}{^{232}Th}$	1σ	ρ^c	$\frac{^{206}Pb}{^{238}U}$	1σ	$\frac{^{207}Pb}{^{235}U}$	1σ	$\frac{^{207}Pb}{^{206}Pb}$	1σ	(Ma)	1σ	δ (%)[d]
Zircon_94_116	1579	116	0.07	0.05034	0.00151	0.23457	0.00763	0.03379	0.00031	0.01066	0.00012	0.38	214	2	214	6	211	72	214	2	0.0
Zircon_78_097	606	12	0.02	0.06175	0.00099	0.28873	0.00561	0.03395	0.00037	0.08195	0.00746	0.56	215	2	258	4	665	36	215	2	16.7
Zircon_36_047	646	76	0.11	0.05545	0.00089	0.27849	0.00650	0.03638	0.00062	0.04162	0.00458	0.73	230	4	249	5	430	35	230	4	7.6
Zircon_75_093	567	131	0.21	0.05935	0.00089	0.30258	0.00601	0.03700	0.00048	0.01645	0.00023	0.66	234	3	268	5	580	34	234	3	12.7
Zircon_32_042	850	48	0.05	0.05416	0.00119	0.27737	0.00683	0.03715	0.00029	0.01161	0.00045	0.53	235	2	249	5	378	48	235	2	5.6
Zircon_76_095	454	112	0.23	0.08538	0.00290	0.43785	0.01579	0.03730	0.00045	0.03545	0.00245	0.34	236	3	369	11	1324	68	236	3	36.0
Zircon_99_122	315	80	0.24	0.05350	0.00080	0.28844	0.00676	0.03899	0.00070	0.01556	0.00030	0.77	247	4	257	5	350	34	247	4	3.9
Zircon_MH-53_1_008	352	81	0.21	0.05307	0.00090	0.28932	0.00540	0.03957	0.00030	0.01641	0.00031	0.42	250	2	258	4	332	39	250	2	3.1
Zircon_54_068	221	73	0.31	0.06298	0.00132	0.34387	0.00773	0.03966	0.00032	0.01702	0.00039	0.36	251	2	300	6	708	46	251	2	16.3
Zircon_50_063	149	9	0.06	0.06219	0.00283	0.34690	0.01679	0.04046	0.00040	0.01244	0.00073	0.38	256	2	302	13	681	99	256	2	15.2
Zircon_83_103	154	33	0.20	0.06205	0.00112	0.34836	0.00700	0.04077	0.00036	0.02016	0.00040	0.44	258	2	303	5	676	39	258	2	14.9
Zircon_10_018	313	39	0.11	0.06539	0.00183	0.37024	0.01143	0.04102	0.00053	0.03456	0.00211	0.42	259	3	320	8	787	60	259	3	19.1
Zircon_38_049	566	299	0.49	0.05780	0.00087	0.32955	0.00582	0.04130	0.00038	0.01492	0.00019	0.52	261	2	289	4	522	32	261	2	9.7
Zircon_77_096	427	67	0.15	0.05618	0.00132	0.33288	0.01102	0.04297	0.00071	0.01337	0.00022	0.69	271	4	292	8	459	53	271	4	7.2
Zircon_93_115	697	405	0.53	0.05410	0.00134	0.32051	0.01134	0.04297	0.00061	0.01343	0.00017	0.76	271	4	282	9	375	57	271	4	3.9
Zircon_65_081	219	56	0.23	0.05166	0.00113	0.30842	0.00830	0.04330	0.00043	0.01361	0.00013	0.52	273	3	273	6	270	52	273	3	0.0
Zircon_91_113	197	47	0.22	0.05899	0.00130	0.35356	0.00870	0.04333	0.00048	0.02569	0.00385	0.44	273	3	307	7	567	49	273	3	11.1
Zircon_52_066	189	79	0.39	0.06030	0.00109	0.36150	0.00728	0.04341	0.00039	0.01682	0.00032	0.44	274	2	313	5	614	40	274	2	12.5
Zircon_98_121	251	97	0.36	0.06317	0.00139	0.37988	0.00892	0.04358	0.00036	0.02004	0.00118	0.35	275	2	327	7	714	49	275	2	15.9
Zircon_88_109	609	226	0.34	0.05913	0.00083	0.35899	0.00639	0.04380	0.00048	0.01768	0.00030	0.61	276	3	311	5	572	31	276	3	11.3
Zircon_34_044	208	41	0.18	0.06342	0.00108	0.38377	0.00719	0.04386	0.00035	0.02189	0.00039	0.42	277	2	330	5	722	35	277	2	16.1
Zircon_80_099	325	173	0.49	0.05942	0.00119	0.35945	0.00777	0.04392	0.00036	0.01665	0.00053	0.38	277	2	312	6	583	44	277	2	11.2
Zircon_100_123	412	110	0.25	0.05165	0.00110	0.31322	0.00807	0.04398	0.00043	0.01383	0.00013	0.49	277	3	277	6	270	50	277	3	0.0
Zircon_39_050	336	150	0.41	0.05627	0.00079	0.34360	0.00591	0.04425	0.00044	0.01560	0.00027	0.58	279	3	300	4	463	30	279	3	7.0
Zircon_16_023	267	92	0.32	0.05810	0.00093	0.35961	0.00643	0.04489	0.00036	0.02028	0.00089	0.45	283	2	312	5	534	34	283	2	9.3
Zircon_72_090	436	359	0.76	0.05427	0.00071	0.33520	0.00521	0.04486	0.00038	0.01494	0.00045	0.54	283	2	294	4	382	30	283	2	3.7
Zircon_41_053	197	67	0.31	0.05771	0.00092	0.35811	0.00641	0.04498	0.00036	0.01734	0.00029	0.45	284	2	311	5	519	34	284	2	8.7
Zircon_57_072	127	56	0.41	0.06202	0.00112	0.38508	0.00812	0.04508	0.00050	0.01787	0.00027	0.52	284	3	331	6	675	40	284	3	14.2
Zircon_87_108	376	158	0.39	0.05447	0.00071	0.34248	0.00549	0.04552	0.00043	0.01778	0.00037	0.58	287	3	299	4	391	30	287	3	4.0
Zircon_89_110	441	221	0.46	0.05468	0.00066	0.34279	0.00516	0.04547	0.00041	0.01572	0.00022	0.60	287	3	299	4	399	27	287	3	4.0
Zircon_95_117	236	48	0.19	0.10390	0.00301	0.66027	0.02025	0.04583	0.00046	0.05880	0.00200	0.33	289	3	515	12	1695	56	289	3	43.9
Zircon_47_060	153	36	0.22	0.05259	0.00300	0.33501	0.02078	0.04620	0.00051	0.01449	0.00029	0.47	291	3	293	16	311	126	291	3	0.7

(Continued)

Tabla 7 *(Continued)*

Zircon no.	U (ppm)	Th (ppm)	Th/U	Corrected isotopic ratios[a]									Corrected ages (Ma)[b]						Best age		
				$\frac{^{207}Pb}{^{206}Pb}$	1σ	$\frac{^{207}Pb}{^{235}U}$	1σ	$\frac{^{206}Pb}{^{238}U}$	1σ	$\frac{^{208}Pb}{^{232}Th}$	1σ	ρ^c	$\frac{^{206}Pb}{^{238}U}$	1σ	$\frac{^{207}Pb}{^{235}U}$	1σ	$\frac{^{207}Pb}{^{206}Pb}$	1σ	(Ma)	1σ	δ (%)[d]
Zircon_84_104	288	217	0.69	0.05216	0.00138	0.33631	0.01199	0.04676	0.00058	0.01468	0.00016	0.65	295	4	294	9	293	61	295	4	-0.3
Zircon_86_107	207	99	0.44	0.06689	0.00100	0.43694	0.00764	0.04739	0.00043	0.02020	0.00053	0.52	298	3	368	5	834	32	298	3	19.0
Zircon_90_111	264	157	0.55	0.05461	0.00076	0.35708	0.00610	0.04734	0.00046	0.01665	0.00027	0.58	298	3	310	5	396	32	298	3	3.9
Zircon_40_051	247	98	0.36	0.05366	0.00080	0.35476	0.00613	0.04792	0.00041	0.01695	0.00056	0.51	302	3	308	5	357	33	302	3	1.9
Zircon_45_057	96	29	0.28	0.05804	0.00151	0.38575	0.01075	0.04821	0.00048	0.01953	0.00049	0.36	304	3	331	8	531	55	304	3	8.2
Zircon_85_105	138	43	0.29	0.05305	0.00134	0.35295	0.01105	0.04825	0.00058	0.01512	0.00017	0.52	304	4	307	8	331	58	304	4	1.0
Zircon_68_085	218	28	0.12	0.05899	0.00130	0.39517	0.01502	0.04838	0.00150	0.03977	0.00676	0.81	305	9	338	11	567	50	305	9	9.8
Zircon_79_098	274	151	0.51	0.05653	0.00096	0.37901	0.00748	0.04855	0.00049	0.01708	0.00024	0.51	306	3	326	6	473	38	306	3	6.1
Zircon_82_102	202	91	0.42	0.05398	0.00103	0.36602	0.00902	0.04917	0.00046	0.01538	0.00013	0.55	309	3	317	7	370	44	309	3	2.5
Zircon_9_017	184	70	0.35	0.05516	0.00131	0.37474	0.01059	0.04927	0.00048	0.01537	0.00014	0.44	310	3	323	8	419	54	310	3	4.0
Zircon_31_041	274	153	0.51	0.05357	0.00117	0.36806	0.00977	0.04983	0.00041	0.01560	0.00012	0.46	313	3	318	7	353	48	313	3	1.6
Zircon_42_054	62	23	0.34	0.05510	0.00170	0.38647	0.01325	0.05087	0.00049	0.01587	0.00015	0.32	320	3	332	10	416	67	320	3	3.6
Zircon_30_039	283	201	0.65	0.05407	0.00173	0.37959	0.01472	0.05092	0.00058	0.01592	0.00016	0.45	320	4	327	11	374	73	320	4	2.1
Zircon_5_012	123	49	0.37	0.05335	0.00116	0.37833	0.01025	0.05143	0.00049	0.01611	0.00014	0.56	323	3	326	8	344	51	323	3	0.9
Zircon_51_065	212	127	0.55	0.05624	0.00202	0.39826	0.01665	0.05136	0.00053	0.01598	0.00015	0.48	323	3	340	12	462	83	323	3	5.0
Zircon_62_078	348	232	0.61	0.05626	0.00090	0.40190	0.00854	0.05143	0.00072	0.02072	0.00095	0.66	323	4	343	6	463	37	323	4	5.8
Zircon_19_026	276	185	0.62	0.07807	0.00515	0.56048	0.03820	0.05187	0.00088	0.02411	0.00157	0.25	326	5	452	25	1149	128	326	5	27.9
Zircon_97_120	243	51	0.19	0.04684	0.00108	0.33592	0.00922	0.05224	0.00078	0.01727	0.00026	0.54	328	5	294	7	41	50	328	5	-11.6
Zircon_4_011	275	193	0.65	0.05322	0.00075	0.38506	0.00623	0.05243	0.00042	0.01669	0.00022	0.49	329	3	331	5	338	31	329	3	0.6
Zircon_69_086	150	69	0.43	0.05835	0.00292	0.42213	0.02147	0.05249	0.00049	0.01681	0.00025	0.18	330	3	358	15	543	114	330	3	7.8
Zircon_81_101	169	98	0.53	0.05416	0.00124	0.39283	0.01111	0.05260	0.00049	0.01644	0.00014	0.50	330	3	336	8	378	52	330	3	1.8
Zircon_64_080	131	75	0.53	0.05681	0.00108	0.41252	0.00864	0.05268	0.00046	0.01683	0.00025	0.42	331	3	351	6	484	43	331	3	5.7
Zircon_58_073	270	204	0.69	0.06173	0.00093	0.45345	0.00771	0.05314	0.00043	0.01626	0.00023	0.46	334	3	380	5	665	33	334	3	12.1
Zircon_63_079	195	130	0.61	0.05559	0.00158	0.40822	0.01410	0.05326	0.00053	0.01660	0.00015	0.52	335	3	348	10	436	65	335	3	3.7
Zircon_71_089	135	65	0.44	0.05941	0.00107	0.43696	0.01052	0.05327	0.00085	0.01918	0.00102	0.66	335	5	368	7	582	40	335	5	9.0
Zircon_59_074	489	257	0.48	0.05828	0.00468	0.42962	0.03618	0.05346	0.00052	0.01657	0.00019	0.15	336	3	363	26	540	186	336	3	7.4
Zircon_35_045	170	109	0.59	0.05702	0.00091	0.42053	0.00774	0.05372	0.00049	0.01659	0.00025	0.50	337	3	356	6	492	34	337	3	5.3
Zircon_8_016	128	89	0.64	0.05607	0.00112	0.41551	0.00915	0.05364	0.00049	0.01676	0.00025	0.42	337	3	353	7	455	45	337	3	4.5
Zircon_55_069	437	345	0.73	0.05391	0.00065	0.40035	0.00708	0.05391	0.00070	0.01698	0.00020	0.73	338	4	342	5	367	28	338	4	1.2
Zircon_74_092	205	145	0.65	0.05370	0.00091	0.40043	0.00751	0.05407	0.00043	0.01616	0.00021	0.43	339	3	342	5	358	40	339	3	0.9
Zircon_24_032	374	320	0.79	0.05766	0.00364	0.43032	0.02951	0.05412	0.00057	0.01679	0.00017	0.31	340	4	363	21	517	135	340	4	6.3
Zircon_25_033	77	39	0.47	0.05506	0.00215	0.41133	0.01818	0.05418	0.00064	0.01690	0.00019	0.36	340	4	350	13	415	85	340	4	2.9
Zircon_49_062	162	133	0.76	0.06085	0.00110	0.45503	0.00918	0.05420	0.00049	0.01949	0.00035	0.44	340	3	381	6	634	38	340	3	10.8

(Continued)

Tabla 7 *(Continued)*

Zircon no.	U (ppm)	Th (ppm)	Th/U	Corrected isotopic ratios[a]									Corrected ages (Ma)[b]						Best age		
				$\frac{^{207}Pb}{^{206}Pb}$	1σ	$\frac{^{207}Pb}{^{235}U}$	1σ	$\frac{^{206}Pb}{^{238}U}$	1σ	$\frac{^{208}Pb}{^{232}Th}$	1σ	ρ^c	$\frac{^{206}Pb}{^{238}U}$	1σ	$\frac{^{207}Pb}{^{235}U}$	1σ	$\frac{^{207}Pb}{^{206}Pb}$	1σ	(Ma)	1σ	δ (%)[d]
Zircon_33_043	103	73	0.65	0.05592	0.00112	0.41915	0.00909	0.05428	0.00046	0.01661	0.00025	0.38	341	3	355	7	449	43	341	3	3.9
Zircon_43_055	238	148	0.57	0.06008	0.00102	0.45297	0.00998	0.05438	0.00076	0.01953	0.00037	0.64	341	5	379	7	606	36	341	5	10.0
Zircon_96_119	114	74	0.60	0.05741	0.00126	0.43159	0.01024	0.05460	0.00049	0.01632	0.00023	0.38	343	3	364	7	507	49	343	3	5.8
Zircon_2_009	59	37	0.58	0.05449	0.00206	0.41225	0.01952	0.05487	0.00083	0.01714	0.00023	0.54	344	5	350	14	391	83	344	5	1.7
Zircon_37_048	237	188	0.73	0.05381	0.00081	0.40731	0.00687	0.05484	0.00042	0.01614	0.00021	0.45	344	3	347	5	363	33	344	3	0.9
Zircon_6_014	228	196	0.79	0.05691	0.00148	0.43009	0.01166	0.05477	0.00042	0.01620	0.00019	0.28	344	3	363	8	488	60	344	3	5.2
Zircon_44_056	282	244	0.80	0.05305	0.00069	0.40235	0.00616	0.05503	0.00045	0.01599	0.00022	0.53	345	3	343	4	331	29	345	3	-0.6
Zircon_60_075	46	23	0.46	0.06019	0.00419	0.45648	0.03387	0.05500	0.00068	0.01698	0.00022	0.23	345	4	382	24	611	158	345	4	9.7
Zircon_17_024	123	94	0.70	0.06101	0.00104	0.46512	0.00915	0.05529	0.00055	0.01790	0.00084	0.50	347	3	388	6	640	35	347	3	10.6
Zircon_23_031	133	109	0.76	0.06640	0.00173	0.50590	0.01392	0.05533	0.00050	0.01754	0.00030	0.32	347	3	416	9	819	53	347	3	16.6
Zircon_3_010	182	132	0.67	0.05406	0.00092	0.41279	0.00774	0.05528	0.00044	0.01602	0.00021	0.42	347	3	351	6	374	37	347	3	1.1
Zircon_61_077	262	215	0.75	0.05424	0.00081	0.41323	0.00699	0.05532	0.00043	0.01638	0.00021	0.47	347	3	351	5	381	35	347	3	1.1
Zircon_20_027	265	320	1.11	0.05511	0.00094	0.42080	0.00828	0.05548	0.00055	0.01590	0.00030	0.50	348	3	357	6	417	37	348	3	2.5
Zircon_56_071	643	1116	1.60	0.05338	0.00064	0.40965	0.00667	0.05541	0.00061	0.01654	0.00035	0.68	348	4	349	5	345	28	348	4	0.3
Zircon_21_029	155	69	0.41	0.05613	0.00107	0.43201	0.00928	0.05580	0.00056	0.01745	0.00026	0.46	350	3	365	7	458	41	350	3	4.1
Zircon_48_061	278	179	0.59	0.05550	0.00160	0.42669	0.01438	0.05576	0.00050	0.01738	0.00014	0.40	350	3	361	10	433	63	350	3	3.0
Zircon_18_025	161	136	0.78	0.05919	0.00148	0.46028	0.01225	0.05629	0.00051	0.01707	0.00024	0.34	353	3	384	9	574	52	353	3	8.1
Zircon_15_021	95	91	0.89	0.05685	0.00108	0.44241	0.00938	0.05639	0.00053	0.01692	0.00024	0.44	354	3	372	7	486	40	354	3	4.8
Zircon_46_059	186	138	0.68	0.05472	0.00082	0.42720	0.00720	0.05661	0.00044	0.01630	0.00023	0.46	355	3	361	5	401	33	355	3	1.7
Zircon_67_084	48	23	0.43	0.06092	0.00171	0.47719	0.01419	0.05681	0.00057	0.01800	0.00041	0.33	356	3	396	10	636	63	356	3	10.1
Zircon_29_038	239	218	0.84	0.05599	0.00084	0.43960	0.00754	0.05688	0.00047	0.01648	0.00021	0.48	357	3	370	5	452	32	357	3	3.5
Zircon_53_067	103	87	0.78	0.05391	0.00102	0.42351	0.00894	0.05698	0.00052	0.01613	0.00023	0.44	357	3	359	6	367	44	357	3	0.6
Zircon_70_087	167	133	0.73	0.05707	0.00108	0.45051	0.00967	0.05728	0.00057	0.01843	0.00029	0.47	359	3	378	7	494	43	359	3	5.0
Zircon_7_015	54	39	0.67	0.06114	0.00165	0.48528	0.01377	0.05753	0.00050	0.01831	0.00044	0.31	361	3	402	9	644	60	361	3	10.2
Zircon_27_036	84	37	0.41	0.05864	0.00117	0.47028	0.01205	0.05795	0.00093	0.01756	0.00032	0.63	363	6	391	8	554	42	363	6	7.2
Zircon_66_083	55	30	0.51	0.06020	0.00169	0.47861	0.01423	0.05805	0.00058	0.01706	0.00034	0.33	364	4	397	10	611	63	364	4	8.3
Zircon_73_091	62	34	0.51	0.05723	0.00235	0.45784	0.02064	0.05803	0.00057	0.01802	0.00017	0.26	364	3	383	14	500	94	364	3	5.0
Zircon_92_114	75	62	0.75	0.06012	0.00126	0.48049	0.01081	0.05808	0.00047	0.01730	0.00057	0.36	364	3	398	7	608	46	364	3	8.5
Zircon_12_020	74	54	0.67	0.05460	0.00120	0.44225	0.01056	0.05888	0.00055	0.01838	0.00033	0.39	369	3	372	7	396	47	369	3	0.8
Zircon_28_037	62	27	0.40	0.07023	0.01405	0.59354	0.11892	0.06031	0.00072	0.01804	0.00036	0.05	378	4	473	76	935	418	378	4	20.1
Zircon_22_030	58	29	0.46	0.05576	0.00212	0.47043	0.02174	0.06118	0.00096	0.01906	0.00028	0.42	383	6	391	15	443	82	383	6	2.0

[a] Absolute errors at 1-σ level
[b] Absolute errors (Ma) at 1-σ level

[c] Error correlation

[d] Discordance = $\left(\frac{^{207}Pb}{^{235}U} - \frac{^{206}Pb}{^{238}U}\right) / \frac{^{207}Pb}{^{235}U} \cdot 100$

Tabla 8.: *LA-ICP-MS U–Pb isotopic data for sample MH-73*

				Corrected isotopic ratios[a]									Corrected ages (Ma)[b]						Best age		
Zircon no.	U (ppm)	Th (ppm)	Th/U	$\frac{^{207}Pb}{^{206}Pb}$	1σ	$\frac{^{207}Pb}{^{235}U}$	1σ	$\frac{^{206}Pb}{^{238}U}$	1σ	$\frac{^{208}Pb}{^{232}Th}$	1σ	ρ^c	$\frac{^{206}Pb}{^{238}U}$	1σ	$\frac{^{207}Pb}{^{235}U}$	1σ	$\frac{^{207}Pb}{^{206}Pb}$	1σ	(Ma)	1σ	δ (%)[d]
Zircon_77_099	176	181	1.00	0.06026	0.00133	0.30931	0.00727	0.03735	0.00031	0.01198	0.00028	0.34	236	2	274	6	613	46	236	2	13.9
Zircon_72_093	707	235	0.32	0.05495	0.00131	0.30766	0.00871	0.04061	0.00035	0.01267	0.00010	0.50	257	2	272	7	410	51	257	2	5.5
Zircon_8_016	79	39	0.48	0.05889	0.00258	0.35180	0.01709	0.04332	0.00045	0.01341	0.00013	0.29	273	3	306	13	563	93	273	3	10.8
Zircon_MH-73_008	214	56	0.26	0.05507	0.00134	0.34456	0.00975	0.04538	0.00039	0.01416	0.00012	0.45	286	2	301	7	415	53	286	2	5.0
Zircon_48_064	208	88	0.41	0.05516	0.00167	0.34991	0.01265	0.04601	0.00051	0.01435	0.00015	0.47	290	3	305	10	419	65	290	3	4.9
Zircon_34_047	424	61	0.14	0.05282	0.00087	0.34354	0.00673	0.04717	0.00035	0.01479	0.00011	0.44	297	2	300	5	321	33	297	2	1.0
Zircon_58_076	141	41	0.29	0.05415	0.00103	0.36591	0.00822	0.04907	0.00059	0.01477	0.00043	0.53	309	4	317	6	377	41	309	4	2.5
Zircon_94_119	208	100	0.47	0.06061	0.00364	0.42743	0.02863	0.05114	0.00062	0.01578	0.00021	0.46	322	4	361	20	626	127	322	4	10.8
Zircon_38_052	206	91	0.43	0.05651	0.00102	0.40041	0.00824	0.05144	0.00051	0.01608	0.00040	0.48	323	3	342	6	472	39	323	3	5.6
Zircon_60_078	1324	585	0.43	0.08476	0.00119	0.83287	0.01536	0.07139	0.00086	0.01884	0.00049	0.65	445	5	615	9	1310	24	445	5	27.6
Zircon_44_059	1690	231	0.13	0.07639	0.00107	0.95053	0.01592	0.09039	0.00083	0.02662	0.00067	0.55	558	5	678	8	1105	24	558	5	17.7
Zircon_67_087	1228	563	0.45	0.06997	0.00098	1.16910	0.01835	0.12132	0.00086	0.03343	0.00087	0.45	738	5	786	9	927	25	738	5	6.1
Zircon_42_057	734	31	0.04	0.07180	0.00095	1.40142	0.02540	0.14156	0.00154	0.04283	0.00047	0.65	853	9	890	11	980	24	853	9	4.2
Zircon_10_018	287	33	0.11	0.07172	0.00125	1.40577	0.03117	0.14216	0.00163	0.04302	0.00051	0.60	857	9	891	13	978	36	857	9	3.8
Zircon_76_098	344	193	0.54	0.07314	0.00102	1.54120	0.02501	0.15309	0.00126	0.04573	0.00105	0.51	918	7	947	10	1018	27	918	7	3.1
Zircon_9_017	52	15	0.28	0.07021	0.00147	1.78280	0.03994	0.18509	0.00144	0.05886	0.00147	0.36	1095	8	1039	15	935	41	935	41	-5.4
Zircon_74_095	337	72	0.21	0.07166	0.00100	1.88840	0.03054	0.19150	0.00155	0.05937	0.00142	0.51	1129	8	1077	11	976	27	976	27	-4.8
Zircon_51_068	131	50	0.37	0.07269	0.00124	1.75320	0.03279	0.17540	0.00137	0.05116	0.00118	0.41	1042	8	1028	12	1005	30	1005	30	-1.4
Zircon_17_027	68	17	0.24	0.07303	0.00131	1.74730	0.03381	0.17381	0.00123	0.05027	0.00121	0.38	1033	7	1026	12	1015	36	1015	36	-0.7
Zircon_55_072	461	177	0.37	0.07323	0.00103	1.75210	0.02799	0.17381	0.00134	0.05219	0.00120	0.47	1033	7	1028	10	1020	25	1020	25	-0.5
Zircon_3_010	270	55	0.20	0.07354	0.00103	1.71580	0.02750	0.16952	0.00132	0.05112	0.00112	0.49	1009	7	1014	10	1029	25	1029	25	0.5
Zircon_11_020	106	26	0.24	0.07364	0.00118	1.73860	0.03235	0.17145	0.00163	0.05307	0.00249	0.51	1020	9	1023	12	1032	32	1032	32	0.3
Zircon_21_032	321	55	0.17	0.07405	0.00104	1.64740	0.02656	0.16150	0.00129	0.04597	0.00110	0.49	965	7	989	10	1043	28	1043	28	2.4
Zircon_45_060	126	24	0.19	0.07439	0.00119	1.71930	0.03123	0.16796	0.00144	0.05121	0.00138	0.47	1001	8	1016	12	1052	28	1052	28	1.5
Zircon_68_088	86	31	0.35	0.07444	0.00134	1.89270	0.03655	0.18481	0.00129	0.05500	0.00132	0.36	1093	7	1079	13	1053	32	1053	32	-1.3
Zircon_54_071	864	49	0.05	0.07457	0.00097	1.66434	0.02546	0.16187	0.00109	0.04877	0.00033	0.47	967	6	995	10	1057	23	1057	23	2.8
Zircon_15_024	242	49	0.20	0.07468	0.00112	1.64890	0.02819	0.16061	0.00132	0.05058	0.00116	0.48	960	7	989	11	1060	30	1060	30	2.9
Zircon_56_074	62	17	0.26	0.07471	0.00127	1.66270	0.03089	0.16192	0.00121	0.05534	0.00421	0.40	967	7	994	12	1061	30	1061	30	2.7
Zircon_79_101	68	28	0.39	0.07504	0.00135	1.82680	0.03555	0.17736	0.00131	0.05239	0.00126	0.38	1053	7	1055	13	1070	35	1070	35	0.2
Zircon_37_051	257	79	0.30	0.07533	0.00125	1.74823	0.03469	0.16833	0.00115	0.05066	0.00033	0.42	1003	6	1027	13	1077	29	1077	29	2.3
Zircon_22_033	67	14	0.21	0.07546	0.00121	1.83180	0.03381	0.17642	0.00162	0.05066	0.00122	0.50	1047	9	1057	12	1081	32	1081	32	0.9
Zircon_35_048	70	18	0.25	0.07594	0.00191	1.79143	0.04900	0.17110	0.00123	0.05145	0.00037	0.27	1018	7	1042	18	1093	44	1093	44	2.3

(Continued)

Tabla 8 *(Continued)*

				Corrected isotopic ratios[a]									Corrected ages (Ma)[b]						Best age		
Zircon no.	U (ppm)	Th (ppm)	Th/U	$\frac{^{207}Pb}{^{206}Pb}$	1σ	$\frac{^{207}Pb}{^{235}U}$	1σ	$\frac{^{206}Pb}{^{238}U}$	1σ	$\frac{^{208}Pb}{^{232}Th}$	1σ	ρ^c	$\frac{^{206}Pb}{^{238}U}$	1σ	$\frac{^{207}Pb}{^{235}U}$	1σ	$\frac{^{207}Pb}{^{206}Pb}$	1σ	(Ma)	1σ	δ (%)[d]
Zircon_62_081	534	147	0.27	0.07602	0.00106	1.98160	0.03176	0.18943	0.00148	0.05556	0.00128	0.49	1118	8	1109	11	1096	24	1096	24	-0.8
Zircon_14_023	153	27	0.17	0.07620	0.00175	1.71530	0.04373	0.16548	0.00182	0.05192	0.00426	0.43	987	10	1014	16	1100	46	1100	46	2.7
Zircon_85_108	284	67	0.23	0.07618	0.00152	1.92380	0.04302	0.18376	0.00184	0.05449	0.00136	0.45	1087	10	1089	15	1100	38	1100	38	0.2
Zircon_12_021	407	137	0.33	0.07628	0.00114	1.76270	0.02972	0.16780	0.00129	0.05194	0.00140	0.46	1000	7	1032	11	1102	30	1102	30	3.1
Zircon_40_054	141	72	0.49	0.07625	0.00114	2.21500	0.03648	0.21080	0.00143	0.06079	0.00134	0.42	1233	8	1186	12	1102	26	1102	26	-4.0
Zircon_32_045	121	38	0.31	0.07649	0.00130	2.27880	0.06702	0.21522	0.00517	0.06439	0.00225	0.82	1257	27	1206	21	1108	30	1108	30	-4.2
Zircon_92_117	639	32	0.05	0.07650	0.00107	1.94380	0.03096	0.18440	0.00140	0.05923	0.00178	0.48	1091	8	1096	11	1108	27	1108	27	0.5
Zircon_69_089	564	83	0.14	0.07654	0.00105	1.93000	0.03131	0.18288	0.00118	0.05495	0.00035	0.44	1083	6	1092	11	1109	24	1109	24	0.8
Zircon_96_122	364	106	0.28	0.07665	0.00115	2.16780	0.03837	0.20570	0.00193	0.06077	0.00140	0.53	1206	10	1171	12	1112	29	1112	29	-3.0
Zircon_73_094	452	159	0.34	0.07677	0.00107	1.94700	0.03467	0.18412	0.00203	0.05373	0.00118	0.62	1089	11	1097	12	1115	27	1115	27	0.7
Zircon_90_114	474	106	0.22	0.07718	0.00108	1.98750	0.03076	0.18683	0.00123	0.05445	0.00120	0.43	1104	7	1111	10	1126	27	1126	27	0.6
Zircon_27_039	46	20	0.42	0.07733	0.00147	1.85870	0.03790	0.17488	0.00129	0.05346	0.00128	0.36	1039	7	1067	13	1130	38	1130	38	2.6
Zircon_20_030	170	30	0.17	0.07745	0.00139	2.21050	0.04663	0.20673	0.00227	0.05760	0.00144	0.53	1211	12	1184	15	1133	36	1133	36	-2.3
Zircon_49_065	255	77	0.29	0.07760	0.00178	1.95070	0.04696	0.18270	0.00130	0.05341	0.00117	0.30	1082	7	1099	16	1137	40	1137	40	1.5
Zircon_95_120	166	60	0.35	0.07766	0.00116	2.19230	0.03667	0.20491	0.00152	0.05803	0.00128	0.45	1202	8	1179	12	1138	29	1138	29	-2.0
Zircon_65_084	321	99	0.30	0.07788	0.00109	2.03430	0.03140	0.18975	0.00123	0.05544	0.00128	0.42	1120	7	1127	11	1144	24	1144	24	0.6
Zircon_33_046	485	121	0.24	0.07797	0.00117	1.58310	0.03832	0.14752	0.00280	0.03304	0.00129	0.78	887	16	964	15	1146	29	1146	29	8.0
Zircon_19_029	52	27	0.50	0.07805	0.00133	1.81660	0.03390	0.16941	0.00130	0.05324	0.00133	0.41	1009	7	1051	12	1148	34	1148	34	4.0
Zircon_71_092	367	90	0.24	0.07811	0.00109	2.19120	0.03410	0.20378	0.00139	0.05828	0.00128	0.44	1196	7	1178	11	1150	27	1150	27	-1.5
Zircon_81_104	812	215	0.26	0.07816	0.00109	1.72190	0.02776	0.15995	0.00128	0.04386	0.00101	0.50	956	7	1017	10	1151	27	1151	27	6.0
Zircon_43_058	1409	27	0.02	0.07820	0.00109	2.04400	0.03327	0.18969	0.00157	0.06982	0.00209	0.52	1120	9	1130	11	1152	24	1152	24	0.9
Zircon_75_096	402	131	0.32	0.07820	0.00109	2.15470	0.03382	0.20016	0.00142	0.05705	0.00126	0.46	1176	8	1167	11	1152	27	1152	27	-0.8
Zircon_93_118	143	42	0.28	0.07819	0.00117	2.49170	0.04157	0.23178	0.00169	0.07073	0.00191	0.44	1344	9	1270	12	1152	29	1152	29	-5.8
Zircon_91_116	1350	173	0.12	0.07830	0.00102	2.09670	0.03234	0.19451	0.00161	0.05629	0.00129	0.54	1146	9	1148	11	1154	25	1154	25	0.2
Zircon_2_009	96	43	0.44	0.07833	0.00329	1.96800	0.08445	0.18309	0.00161	0.05352	0.00123	0.20	1084	9	1105	29	1155	84	1155	84	1.9
Zircon_86_110	205	38	0.18	0.07841	0.00118	1.89840	0.03245	0.17572	0.00144	0.05344	0.00123	0.47	1044	8	1081	11	1157	29	1157	29	3.4
Zircon_57_075	313	84	0.26	0.07849	0.00110	2.06710	0.03264	0.19114	0.00140	0.05532	0.00122	0.46	1128	8	1138	11	1159	24	1159	24	0.9
Zircon_36_050	217	45	0.20	0.07862	0.00110	2.08610	0.03518	0.19259	0.00181	0.05952	0.00161	0.56	1135	10	1144	12	1163	24	1163	24	0.8
Zircon_24_035	678	54	0.08	0.07881	0.00110	2.14730	0.03484	0.19785	0.00162	0.06041	0.00139	0.51	1164	9	1164	11	1167	28	1167	28	0.0
Zircon_78_100	44	16	0.36	0.07878	0.00291	1.93610	0.07363	0.17867	0.00157	0.05439	0.00136	0.24	1060	9	1094	25	1167	71	1167	71	3.1
Zircon_46_062	249	83	0.32	0.07884	0.00110	2.17940	0.03421	0.20093	0.00143	0.05749	0.00126	0.46	1180	8	1174	11	1168	24	1168	24	-0.5
Zircon_25_036	439	179	0.40	0.07895	0.00142	1.99390	0.04058	0.18352	0.00174	0.05387	0.00140	0.47	1086	9	1113	14	1171	36	1171	36	2.4
Zircon_26_038	295	33	0.11	0.07929	0.00115	2.15562	0.04381	0.19717	0.00243	0.05901	0.00073	0.68	1160	13	1167	14	1179	29	1179	29	0.6

(Continued)

Tabla 8 *(Continued)*

				Corrected isotopic ratios[a]									Corrected ages (Ma)[b]						Best age		
Zircon no.	U (ppm)	Th (ppm)	Th/U	$\frac{^{207}Pb}{^{206}Pb}$	1σ	$\frac{^{207}Pb}{^{235}U}$	1σ	$\frac{^{206}Pb}{^{238}U}$	1σ	$\frac{^{208}Pb}{^{232}Th}$	1σ	ρ^c	$\frac{^{206}Pb}{^{238}U}$	1σ	$\frac{^{207}Pb}{^{235}U}$	1σ	$\frac{^{207}Pb}{^{206}Pb}$	1σ	(Ma)	1σ	δ (%)[d]
Zircon_16_026	693	26	0.04	0.07945	0.00111	1.88470	0.03356	0.17275	0.00190	0.04849	0.00136	0.62	1027	10	1076	12	1183	28	1183	28	4.6
Zircon_7_015	43	15	0.33	0.06019	0.00175	1.65900	0.04995	0.20136	0.00163	0.05864	0.00152	0.26	1183	9	993	19	610	61	1183	9	-19.1
Zircon_23_034	231	72	0.30	0.07947	0.00111	2.15110	0.03557	0.19676	0.00173	0.06132	0.00215	0.54	1158	9	1165	11	1184	28	1184	28	0.6
Zircon_13_022	8	3	0.35	0.07951	0.00286	2.08970	0.08150	0.19118	0.00287	0.06951	0.01390	0.39	1128	16	1145	27	1185	72	1185	72	1.5
Zircon_4_011	451	81	0.17	0.08004	0.00112	2.12020	0.05004	0.19189	0.00365	0.05861	0.00135	0.81	1132	20	1155	16	1198	24	1198	24	2.0
Zircon_63_082	187	57	0.30	0.08027	0.00120	2.43550	0.04391	0.22022	0.00220	0.06168	0.00148	0.56	1283	12	1253	13	1204	26	1204	26	-2.4
Zircon_82_105	886	244	0.27	0.08039	0.00113	1.65320	0.03048	0.14939	0.00179	0.03236	0.00126	0.65	898	10	991	12	1207	27	1207	27	9.4
Zircon_30_042	330	57	0.17	0.08059	0.00126	2.12300	0.04134	0.19106	0.00158	0.05708	0.00046	0.53	1127	9	1156	13	1212	27	1212	27	2.5
Zircon_97_123	111	33	0.29	0.08062	0.00121	2.42010	0.04092	0.21805	0.00170	0.06294	0.00138	0.46	1272	9	1249	12	1212	28	1212	28	-1.8
Zircon_70_090	340	166	0.47	0.08089	0.00113	2.37470	0.03749	0.21323	0.00156	0.05697	0.00125	0.47	1246	8	1235	11	1219	26	1219	26	-0.9
Zircon_39_053	87	33	0.37	0.08105	0.00421	2.01510	0.10638	0.17863	0.00163	0.05643	0.00203	0.18	1059	9	1121	36	1223	89	1223	89	5.5
Zircon_83_106	59	39	0.64	0.08131	0.00321	1.94547	0.09772	0.17352	0.00290	0.05179	0.00078	0.57	1031	16	1097	34	1229	75	1229	75	6.0
Zircon_53_070	700	165	0.23	0.08147	0.00176	2.00036	0.04810	0.17808	0.00131	0.05314	0.00039	0.33	1056	7	1116	16	1233	37	1233	37	5.4
Zircon_66_086	61	18	0.30	0.08147	0.00139	2.45760	0.04835	0.21955	0.00217	0.07157	0.00172	0.50	1279	11	1260	14	1233	29	1233	29	-1.5
Zircon_18_028	301	83	0.27	0.08181	0.00115	2.25740	0.04019	0.20039	0.00220	0.05919	0.00136	0.61	1177	12	1199	13	1241	28	1241	28	1.8
Zircon_50_066	419	108	0.25	0.08209	0.00140	1.79200	0.03629	0.15880	0.00175	0.04711	0.00443	0.54	950	10	1043	13	1248	29	1248	29	8.9
Zircon_28_040	311	78	0.24	0.08218	0.00132	2.39349	0.04657	0.21122	0.00177	0.06297	0.00053	0.52	1235	9	1241	14	1250	32	1250	32	0.5
Zircon_64_083	200	58	0.28	0.08226	0.00132	2.38410	0.05229	0.21124	0.00317	0.06865	0.00165	0.68	1235	17	1238	16	1252	27	1252	27	0.2
Zircon_84_107	149	81	0.53	0.08276	0.00124	2.48690	0.04096	0.21817	0.00148	0.06133	0.00282	0.42	1272	8	1268	12	1264	28	1264	28	-0.3
Zircon_52_069	251	68	0.26	0.08281	0.00116	2.72580	0.04279	0.23854	0.00169	0.07558	0.00219	0.45	1379	9	1336	12	1265	24	1265	24	-3.2
Zircon_6_014	592	67	0.11	0.08292	0.00133	2.48090	0.04681	0.21484	0.00215	0.07864	0.00204	0.53	1255	11	1266	14	1267	27	1267	27	0.9
Zircon_80_102	145	39	0.26	0.08293	0.00116	2.50340	0.03988	0.21936	0.00167	0.06471	0.00149	0.48	1278	9	1273	12	1268	26	1268	26	-0.4
Zircon_31_044	50	18	0.34	0.08319	0.00341	2.26220	0.09425	0.19773	0.00146	0.05928	0.00148	0.18	1163	8	1201	29	1274	70	1274	70	3.2
Zircon_88_112	106	35	0.32	0.08344	0.00275	2.32790	0.07858	0.20315	0.00144	0.06084	0.00140	0.22	1192	8	1221	24	1280	62	1280	62	2.4
Zircon_47_063	109	30	0.27	0.08510	0.00128	2.82930	0.04906	0.24148	0.00210	0.06519	0.00150	0.50	1394	11	1363	13	1318	25	1318	25	-2.3
Zircon_5_012	202	70	0.34	0.08561	0.00120	2.65220	0.04517	0.22500	0.00218	0.06942	0.00180	0.57	1308	11	1315	13	1329	24	1329	24	0.5
Zircon_29_041	93	40	0.41	0.08591	0.00137	2.30960	0.04240	0.19580	0.00176	0.05619	0.00129	0.50	1153	9	1215	13	1336	31	1336	31	5.1
Zircon_41_056	174	64	0.36	0.08616	0.00121	2.72340	0.04577	0.22986	0.00214	0.06117	0.00147	0.55	1334	11	1335	12	1342	24	1342	24	0.1
Zircon_61_080	261	60	0.22	0.09087	0.00136	3.35120	0.06041	0.26448	0.00264	0.07443	0.00171	0.56	1513	13	1493	14	1444	25	1444	25	-1.3
Zircon_98_124	191	53	0.27	0.09514	0.00143	2.93370	0.05132	0.22380	0.00201	0.10053	0.00221	0.51	1302	11	1391	13	1531	27	1531	27	6.4

[a] Absolute errors at 1-σ level
[b] Absolute errors (Ma) at 1-σ level
[c] Error correlation

[d] Discordance = $\left(\frac{^{207}Pb}{^{235}U} - \frac{^{206}Pb}{^{238}U}\right) / \frac{^{207}Pb}{^{235}U} \cdot 100$

Tabla 9.: *LA-ICP-MS U–Pb isotopic data for sample MH-96*

				Corrected isotopic ratios[a]									Corrected ages (Ma)[b]						Best age		
Zircon no.	U (ppm)	Th (ppm)	Th/U	$\frac{^{207}Pb}{^{206}Pb}$	1σ	$\frac{^{207}Pb}{^{235}U}$	1σ	$\frac{^{206}Pb}{^{238}U}$	1σ	$\frac{^{208}Pb}{^{232}Th}$	1σ	ρ^{c}	$\frac{^{206}Pb}{^{238}U}$	1σ	$\frac{^{207}Pb}{^{235}U}$	1σ	$\frac{^{207}Pb}{^{206}Pb}$	1σ	(Ma)	1σ	δ (%)[d]
Zircon_14_023	190	46	0.23	0.05550	0.00133	0.33988	0.00852	0.04454	0.00032	0.01362	0.00025	0.29	281	2	297	6	432	50	281	2	5.4
Zircon_5_012	368	204	0.54	0.05631	0.00113	0.36287	0.00866	0.04687	0.00061	0.01461	0.00031	0.54	295	4	314	6	465	45	295	4	6.1
Zircon_30_040	78	19	0.23	0.06248	0.01029	0.49313	0.10489	0.05724	0.00449	0.01760	0.00172	0.66	359	27	407	71	691	355	359	27	11.8
Zircon_9_017	309	100	0.31	0.05795	0.00093	0.62709	0.01085	0.07850	0.00052	0.02309	0.00046	0.37	487	3	494	7	528	35	487	3	1.4
Zircon_MH-76_1_008	715	164	0.22	0.08004	0.00136	0.90671	0.01940	0.08215	0.00107	0.02128	0.00038	0.61	509	6	655	10	1198	34	509	6	22.3
Zircon_26_036	411	163	0.39	0.07612	0.00137	1.12580	0.02500	0.10718	0.00139	0.02127	0.00057	0.59	656	8	766	12	1098	34	656	8	14.4
Zircon_15_024	338	38	0.11	0.07508	0.00198	1.40919	0.04282	0.13612	0.00150	0.04098	0.00046	0.45	823	9	893	18	1071	49	823	9	7.8
Zircon_16_026	516	43	0.08	0.07346	0.00116	1.49521	0.03645	0.14763	0.00233	0.04456	0.00069	0.71	888	13	928	15	1027	30	888	13	4.3
Zircon_13_022	215	88	0.40	0.07324	0.00117	1.73370	0.03021	0.17181	0.00119	0.05107	0.00128	0.40	1022	7	1021	11	1021	30	1021	30	-0.1
Zircon_17_027	191	13	0.07	0.07420	0.00193	1.69720	0.04791	0.16552	0.00182	0.04960	0.00084	0.39	987	10	1007	18	1047	49	1047	49	2.0
Zircon_22_032	361	91	0.24	0.07458	0.00172	1.79570	0.04931	0.17319	0.00260	0.04541	0.00127	0.54	1030	14	1044	18	1057	47	1057	47	1.3
Zircon_8_016	333	95	0.28	0.07487	0.00121	1.65809	0.03358	0.16062	0.00144	0.04838	0.00042	0.45	960	8	993	13	1065	32	1065	32	3.3
Zircon_4_011	47	13	0.27	0.07536	0.00151	1.99150	0.04207	0.19166	0.00130	0.05491	0.00181	0.32	1130	7	1113	14	1078	40	1078	40	-1.5
Zircon_11_020	220	33	0.15	0.07631	0.00122	1.97720	0.03639	0.18798	0.00171	0.05879	0.00088	0.50	1110	9	1108	12	1103	30	1103	30	-0.2
Zircon_21_031	233	46	0.19	0.07732	0.00124	1.93300	0.03539	0.18137	0.00161	0.05604	0.00078	0.48	1074	9	1093	12	1129	30	1129	30	1.7
Zircon_12_021	647	29	0.04	0.07763	0.00124	2.05190	0.03592	0.19182	0.00136	0.06699	0.00623	0.41	1131	7	1133	12	1137	30	1137	30	0.2
Zircon_29_039	335	71	0.21	0.07773	0.00132	1.72940	0.04037	0.16141	0.00258	0.04844	0.00073	0.69	965	14	1020	15	1140	34	1140	34	5.4
Zircon_18_028	396	23	0.06	0.07874	0.00126	2.02810	0.04312	0.18679	0.00262	0.05509	0.00099	0.66	1104	14	1125	14	1166	30	1166	30	1.9
Zircon_3_010	204	90	0.43	0.08020	0.00225	2.30350	0.06627	0.20845	0.00138	0.05692	0.00080	0.22	1221	7	1213	20	1202	55	1202	55	-0.7
Zircon_28_038	144	56	0.38	0.08068	0.00137	2.18870	0.04112	0.19660	0.00157	0.05777	0.00075	0.43	1157	8	1177	13	1214	33	1214	33	1.7
Zircon_24_033	399	103	0.25	0.08081	0.00129	2.06440	0.03702	0.18518	0.00150	0.07034	0.00120	0.46	1095	8	1137	12	1217	29	1217	29	3.7
Zircon_7_015	326	56	0.17	0.08178	0.00131	2.51520	0.04325	0.22316	0.00141	0.06193	0.00087	0.36	1299	7	1276	12	1240	31	1240	31	-1.8
Zircon_27_037	294	62	0.20	0.08269	0.00132	2.45300	0.04628	0.21529	0.00215	0.06070	0.00085	0.53	1257	11	1258	14	1262	31	1262	31	0.1
Zircon_6_014	336	208	0.60	0.08304	0.00133	2.63050	0.04615	0.22967	0.00165	0.06265	0.00081	0.41	1333	9	1309	13	1270	31	1270	31	-1.8
Zircon_25_034	75	43	0.55	0.08471	0.00144	2.57330	0.04999	0.22056	0.00207	0.06505	0.00299	0.48	1285	11	1293	14	1309	31	1309	31	0.6
Zircon_2_009	807	60	0.07	0.08864	0.00142	1.79540	0.04460	0.14661	0.00279	0.03726	0.00075	0.76	882	16	1044	16	1396	29	1396	29	15.5
Zircon_10_018	285	82	0.28	0.09187	0.00147	3.41510	0.05937	0.26967	0.00183	0.07389	0.00096	0.39	1539	9	1508	14	1465	28	1465	28	-2.1
Zircon_20_029	314	67	0.21	0.10519	0.00168	4.07240	0.07684	0.28069	0.00281	0.08226	0.00115	0.53	1595	14	1649	15	1718	27	1718	27	3.3

[a] Absolute errors at 1-σ level
[b] Absolute errors (Ma) at 1-σ level
[c] Error correlation
[d] Discordance = $(\frac{^{207}Pb}{^{235}U} - \frac{^{206}Pb}{^{238}U}) / \frac{^{207}Pb}{^{235}U} \cdot 100$

Tabla 10.: *LA-ICP-MS U–Pb isotopic data for sample PET-480-1*

				Corrected isotopic ratios[a]									Corrected ages (Ma)[b]						Best age		
Zircon no.	U (ppm)	Th (ppm)	Th/U	$\frac{^{207}Pb}{^{206}Pb}$	1σ	$\frac{^{207}Pb}{^{235}U}$	1σ	$\frac{^{206}Pb}{^{238}U}$	1σ	$\frac{^{208}Pb}{^{232}Th}$	1σ	ρ^c	$\frac{^{206}Pb}{^{238}U}$	1σ	$\frac{^{207}Pb}{^{235}U}$	1σ	$\frac{^{207}Pb}{^{206}Pb}$	1σ	(Ma)	1σ	δ (%)[d]
Zircon_31_044	1090	273	0.23	0.06719	0.00167	0.20609	0.00739	0.02225	0.00038	0.00678	0.00012	0.68	142	2	190	6	844	51	142	2	25.3
Zircon_29_041	430	126	0.26	0.08477	0.00161	0.26319	0.00671	0.02247	0.00038	0.01595	0.00024	0.67	143	2	237	5	1310	36	143	2	39.7
Zircon_23_034	527	219	0.38	0.08713	0.00139	0.34844	0.00788	0.02919	0.00047	0.01841	0.00024	0.71	185	3	304	6	1363	28	185	3	39.1
Zircon_34_047	428	291	0.61	0.07242	0.00145	0.30759	0.00769	0.03095	0.00046	0.00799	0.00026	0.60	196	3	272	6	998	40	196	3	27.9
Zircon_28_040	685	1025	1.35	0.06296	0.00062	0.41339	0.00518	0.04772	0.00037	0.00644	0.00012	0.62	301	2	351	4	707	21	301	2	14.2
Zircon_26_038	704	477	0.61	0.05773	0.00063	0.39662	0.00499	0.04986	0.00030	0.01045	0.00018	0.50	314	2	339	4	520	24	314	2	7.4
Zircon_7_015	227	140	0.56	0.05589	0.00089	0.40247	0.00781	0.05238	0.00058	0.01629	0.00021	0.57	329	4	343	6	448	35	329	4	4.1
Zircon_36_049	745	652	0.79	0.07187	0.00079	0.52255	0.01285	0.05308	0.00117	0.00850	0.00029	0.89	333	7	427	9	982	22	333	7	22.0
Zircon_2_009	203	222	0.98	0.05530	0.00088	0.41075	0.00847	0.05393	0.00070	0.01612	0.00023	0.64	339	4	349	6	424	33	339	4	2.9
Zircon_21_032	321	119	0.33	0.06399	0.00148	0.47931	0.01238	0.05432	0.00037	0.01665	0.00011	0.30	341	2	398	8	741	45	341	2	14.3
Zircon_3_010	696	283	0.37	0.06899	0.00076	0.57074	0.00808	0.06015	0.00054	0.01243	0.00019	0.63	377	3	458	5	898	22	377	3	17.7
Zircon_32_045	375	144	0.35	0.07023	0.00119	0.59214	0.01296	0.06115	0.00054	0.01855	0.00016	0.59	383	3	472	8	935	34	383	3	18.9
Zircon_4_011	290	160	0.50	0.06445	0.00103	0.54642	0.01008	0.06173	0.00057	0.01154	0.00032	0.50	386	3	443	7	756	33	386	3	12.9
Zircon_19_029	454	286	0.57	0.05970	0.00060	0.58055	0.00680	0.07064	0.00043	0.01598	0.00022	0.51	440	3	465	4	593	20	440	3	5.4
Zircon_22_033	660	189	0.26	0.06304	0.00057	0.65102	0.00768	0.07514	0.00056	0.01767	0.00032	0.64	467	3	509	5	710	18	467	3	8.3
Zircon_6_014	391	167	0.38	0.06572	0.00159	0.78417	0.02783	0.08654	0.00133	0.02645	0.00038	0.81	535	8	588	16	797	50	535	8	9.0
Zircon_9_017	265	152	0.52	0.05877	0.00071	0.71557	0.00917	0.08831	0.00040	0.02542	0.00031	0.33	546	2	548	5	559	25	546	2	0.4
Zircon_10_018	241	171	0.64	0.06018	0.00066	0.75624	0.01015	0.09115	0.00070	0.02889	0.00035	0.58	562	4	572	6	610	22	562	4	1.7
Zircon_24_035	345	126	0.33	0.06246	0.00069	0.78988	0.00975	0.09176	0.00051	0.02440	0.00037	0.45	566	3	591	6	690	23	566	3	4.2
Zircon_11_020	334	79	0.21	0.06461	0.00071	0.88796	0.01069	0.09966	0.00049	0.02718	0.00049	0.41	612	3	645	6	762	21	612	3	5.1
Zircon_33_046	783	182	0.21	0.06043	0.00050	0.84267	0.00780	0.10113	0.00043	0.03040	0.00036	0.45	621	3	621	4	619	18	621	3	0.0
Zircon_25_036	629	227	0.33	0.06060	0.00047	0.87747	0.00778	0.10499	0.00046	0.03173	0.00035	0.48	644	3	640	4	625	16	644	3	-0.6
Zircon_12_021	345	321	0.84	0.06171	0.00059	0.92905	0.00977	0.10920	0.00049	0.03224	0.00035	0.42	668	3	667	5	664	19	668	3	-0.1
Zircon_18_028	1197	615	0.46	0.06865	0.00054	1.05720	0.01095	0.11165	0.00075	0.01685	0.00039	0.65	682	4	732	5	888	15	682	4	6.8
Zircon_17_027	1450	355	0.22	0.08023	0.00059	1.34340	0.01178	0.12139	0.00057	0.02602	0.00036	0.54	739	3	865	5	1203	13	739	3	14.6
Zircon_15_024	200	169	0.76	0.06576	0.00072	1.16670	0.01387	0.12863	0.00058	0.03820	0.00042	0.39	780	3	785	6	799	21	780	3	0.6
Zircon_16_026	217	90	0.37	0.07381	0.00067	1.55960	0.01700	0.15324	0.00092	0.04212	0.00080	0.55	919	5	954	7	1036	17	919	5	3.7
Zircon_35_048	166	71	0.39	0.07180	0.00072	1.57530	0.01741	0.15918	0.00075	0.05051	0.00061	0.42	952	4	961	7	980	20	952	4	0.9
Zircon_5_012	296	147	0.45	0.08300	0.00091	1.49510	0.02662	0.13044	0.00183	0.04025	0.00181	0.79	790	10	928	11	1269	21	1269	21	14.9
Zircon_14_023	15	11	0.66	0.09055	0.00222	2.97547	0.08642	0.23832	0.00204	0.07032	0.00055	0.37	1378	11	1401	22	1437	43	1437	43	1.6
Zircon_13_022	112	48	0.38	0.12841	0.00103	6.76470	0.06311	0.38200	0.00183	0.10497	0.00115	0.51	2086	9	2081	8	2076	13	2076	13	-0.2
Zircon_27_039	234	169	0.65	0.14802	0.00184	6.39238	0.11771	0.31321	0.00270	0.08793	0.00084	0.71	1756	13	2031	16	2323	21	2323	21	13.5

[a] Absolute errors at 1-σ level
[b] Absolute errors (Ma) at 1-σ level
[c] Error correlation
[d] Discordance = $\left(\frac{^{207}Pb}{^{235}U} - \frac{^{206}Pb}{^{238}U}\right) / \frac{^{207}Pb}{^{235}U} \cdot 100$

Tabla 11.: *LA-ICP-MS U–Pb isotopic data for sample PET-484-1*

				Corrected isotopic ratios[a]									Corrected ages (Ma)[b]						Best age		
Zircon no.	U (ppm)	Th (ppm)	Th/U	$\frac{^{207}Pb}{^{206}Pb}$	1σ	$\frac{^{207}Pb}{^{235}U}$	1σ	$\frac{^{206}Pb}{^{238}U}$	1σ	$\frac{^{208}Pb}{^{232}Th}$	1σ	ρ^c	$\frac{^{206}Pb}{^{238}U}$	1σ	$\frac{^{207}Pb}{^{235}U}$	1σ	$\frac{^{207}Pb}{^{206}Pb}$	1σ	(Ma)	1σ	δ (%)[d]
Zircon_15_024	1979	450	0.23	0.06264	0.00081	0.18660	0.00343	0.02153	0.00028	0.71	137	2	174	3	696	25	214	3	137	2	21.3
Zircon_11_020	1488	379	0.26	0.05666	0.00182	0.17125	0.00672	0.02192	0.00028	0.63	140	2	161	6	478	64	137	2	140	2	13.0
Zircon_26_038	2309	451	0.20	0.07626	0.00114	0.25284	0.00519	0.02414	0.00034	0.69	154	2	229	4	1102	29	335	5	154	2	32.8
Zircon_21_032	1426	218	0.16	0.05494	0.00159	0.18479	0.00623	0.02439	0.00025	0.61	155	2	172	5	410	64	153	3	155	2	9.9
Zircon_4_011	420	171	0.42	0.06070	0.00227	0.23776	0.01261	0.02841	0.00060	0.72	181	4	217	10	629	78	176	3	181	4	16.6
Zircon_28_040	460	279	0.63	0.06836	0.00235	0.27935	0.01327	0.02964	0.00055	0.63	188	3	250	11	879	70	181	3	188	3	24.8
Zircon_31_044	1057	351	0.34	0.06140	0.00139	0.25137	0.00885	0.02969	0.00053	0.71	189	3	228	7	653	48	184	3	189	3	17.1
Zircon_17_027	593	233	0.41	0.05309	0.00146	0.21946	0.00711	0.02998	0.00028	0.48	190	2	201	6	333	56	189	2	190	2	5.5
Zircon_37_051	565	157	0.29	0.05234	0.00137	0.21883	0.00662	0.03032	0.00025	0.45	193	2	201	6	300	57	191	2	193	2	4.0
Zircon_2_009	409	113	0.29	0.07670	0.00215	0.35188	0.01118	0.03308	0.00050	0.47	210	3	306	8	1113	54	389	7	210	3	31.4
Zircon_6_014	734	246	0.35	0.07119	0.00121	0.33187	0.00798	0.03382	0.00057	0.71	214	4	291	6	963	33	345	20	214	4	26.5
Zircon_24_035	568	266	0.48	0.06353	0.00149	0.30931	0.00991	0.03531	0.00045	0.65	224	3	274	8	726	49	218	3	224	3	18.2
Zircon_25_036	943	439	0.48	0.05894	0.00077	0.28901	0.00492	0.03550	0.00039	0.64	225	2	258	4	565	28	218	3	225	2	12.8
Zircon_38_052	774	331	0.44	0.05920	0.00095	0.29403	0.00730	0.03586	0.00068	0.76	227	4	262	6	574	34	189	3	227	4	13.4
Zircon_10_018	200	140	0.73	0.05755	0.00249	0.29021	0.01700	0.03657	0.00073	0.61	232	5	259	13	513	86	228	4	232	5	10.4
Zircon_3_010	821	268	0.34	0.05279	0.00107	0.26821	0.00697	0.03685	0.00035	0.67	233	2	241	6	320	45	232	2	233	2	3.3
Zircon_16_026	583	276	0.49	0.06943	0.00111	0.36455	0.00688	0.03797	0.00038	0.53	240	2	316	5	912	29	362	13	240	2	24.1
Zircon_18_028	375	186	0.51	0.06581	0.00230	0.34983	0.01393	0.03870	0.00074	0.48	245	5	305	10	800	66	322	6	245	5	19.7
Zircon_5_012	757	265	0.36	0.06683	0.00100	0.36122	0.00741	0.03919	0.00055	0.68	248	3	313	6	832	30	337	6	248	3	20.8
Zircon_19_029	258	226	0.91	0.06356	0.00114	0.37330	0.00731	0.04271	0.00033	0.40	270	2	322	5	727	37	255	4	270	2	16.1
Zircon_13_022	843	623	0.76	0.06427	0.00071	0.38230	0.00553	0.04290	0.00040	0.65	271	2	329	4	751	21	355	6	271	2	17.6
Zircon_20_030	500	205	0.42	0.05671	0.00085	0.34427	0.00550	0.04398	0.00024	0.35	277	1	300	4	480	32	309	4	277	1	7.7
Zircon_12_021	453	389	0.89	0.05261	0.00167	0.32008	0.01182	0.04413	0.00035	0.42	278	2	282	9	312	65	278	2	278	2	1.4
Zircon_40_054	371	161	0.45	0.06169	0.00086	0.38799	0.00656	0.04562	0.00043	0.57	288	3	333	5	663	29	372	6	288	3	13.5
Zircon_9_017	426	185	0.45	0.05996	0.00090	0.38692	0.00675	0.04673	0.00042	0.51	294	3	332	5	602	31	344	5	294	3	11.4
Zircon_33_046	135	45	0.35	0.05329	0.00192	0.35686	0.01576	0.04857	0.00071	0.54	306	4	310	12	341	81	305	4	306	4	1.3
Zircon_29_041	555	230	0.43	0.05605	0.00078	0.37967	0.00752	0.04923	0.00069	0.71	310	4	327	6	454	30	343	5	310	4	5.2
Zircon_41_055	486	168	0.36	0.05291	0.00116	0.36141	0.00961	0.04954	0.00043	0.50	312	3	313	7	325	48	312	2	312	3	0.3
Zircon_1_PET-484-1_008	404	234	0.60	0.05324	0.00121	0.36978	0.00914	0.05037	0.00023	0.25	317	1	319	7	339	46	316	1	317	1	0.6
Zircon_23_034	98	63	0.66	0.06741	0.00204	0.46950	0.01635	0.05051	0.00046	0.36	318	3	391	11	851	62	309	3	318	3	18.7
Zircon_30_042	178	141	0.82	0.05911	0.00130	0.41436	0.00947	0.05078	0.00031	0.27	319	2	352	7	571	47	323	5	319	2	9.4
Zircon_22_033	471	669	1.47	0.05565	0.00083	0.39020	0.00681	0.05084	0.00045	0.52	320	3	335	5	438	32	332	4	320	3	4.5

(Continued)

Tabla 11 *(Continued)*

				Corrected isotopic ratios[a]									Corrected ages (Ma)[b]						Best age		
Zircon no.	U (ppm)	Th (ppm)	Th/U	$\frac{^{207}Pb}{^{206}Pb}$	1σ	$\frac{^{207}Pb}{^{235}U}$	1σ	$\frac{^{206}Pb}{^{238}U}$	1σ	$\frac{^{208}Pb}{^{232}Th}$	1σ	ρ^c	$\frac{^{206}Pb}{^{238}U}$	1σ	$\frac{^{207}Pb}{^{235}U}$	1σ	$\frac{^{207}Pb}{^{206}Pb}$	1σ	(Ma)	1σ	δ (%)[d]
Zircon_7_015	251	160	0.66	0.04902	0.00441	0.34729	0.03323	0.05138	0.00041	0.13	323	2	303	25	149	191	326	13	323	2	-6.6
Zircon_34_047	798	1063	1.38	0.05424	0.00071	0.38734	0.00712	0.05173	0.00067	0.70	325	4	332	5	381	29	326	7	325	4	2.1
Zircon_8_016	240	121	0.52	0.05500	0.00190	0.40368	0.01641	0.05323	0.00056	0.45	334	3	344	12	412	74	333	3	334	3	2.9
Zircon_39_053	802	886	1.14	0.05426	0.00060	0.40336	0.00478	0.05383	0.00024	0.36	338	1	344	3	382	24	329	4	338	1	1.7
Zircon_14_023	221	178	0.83	0.05473	0.00088	0.41029	0.00690	0.05434	0.00028	0.29	341	2	349	5	401	32	339	5	341	2	2.3

[a] Absolute errors at 1-σ level
[b] Absolute errors (Ma) at 1-σ level
[c] Error correlation
[d] Discordance = $(\frac{^{207}Pb}{^{235}U} - \frac{^{206}Pb}{^{238}U}) / \frac{^{207}Pb}{^{235}U} \cdot 100$

Tabla 12.: *LA-ICP-MS U–Pb isotopic data for sample TEP-474-3*

				Corrected isotopic ratios[a]									Corrected ages (Ma)[b]						Best age		
Zircon no.	U (ppm)	Th (ppm)	Th/U	$\frac{^{207}Pb}{^{206}Pb}$	1σ	$\frac{^{207}Pb}{^{235}U}$	1σ	$\frac{^{206}Pb}{^{238}U}$	1σ	$\frac{^{208}Pb}{^{232}Th}$	1σ	ρ^c	$\frac{^{206}Pb}{^{238}U}$	1σ	$\frac{^{207}Pb}{^{235}U}$	1σ	$\frac{^{207}Pb}{^{206}Pb}$	1σ	(Ma)	1σ	δ (%)[d]
Zircon_15_024	548	486	0.80	0.06686	0.00100	0.34741	0.00569	0.03769	0.00025	0.00983	0.00015	0.41	238	2	303	4	833	32	238	2	21.5
Zircon_85_108	209	117	0.51	0.05134	0.00098	0.28510	0.00569	0.04036	0.00025	0.01072	0.00018	0.29	255	2	255	4	256	45	255	2	0.0
Zircon_31_044	100	67	0.61	0.06707	0.00168	0.37856	0.01034	0.04135	0.00045	0.01284	0.00026	0.40	261	3	326	8	840	48	261	3	19.9
Zircon_56_074	103	50	0.44	0.05425	0.00141	0.31266	0.00836	0.04199	0.00026	0.01124	0.00021	0.23	265	2	276	6	381	60	265	2	4.0
Zircon_61_080	94	53	0.51	0.05393	0.00151	0.31550	0.00914	0.04274	0.00032	0.01179	0.00028	0.26	270	2	278	7	368	65	270	2	2.9
Zircon_93_118	169	70	0.38	0.05785	0.00127	0.34080	0.00775	0.04285	0.00024	0.01327	0.00027	0.26	270	1	298	6	524	49	270	1	9.4
Zircon_37_051	181	112	0.56	0.05058	0.00096	0.30766	0.00610	0.04420	0.00025	0.01149	0.00022	0.29	279	2	272	5	222	41	279	2	-2.6
Zircon_84_107	196	99	0.46	0.05619	0.00112	0.34281	0.00717	0.04442	0.00027	0.01328	0.00025	0.30	280	2	299	5	460	45	280	2	6.4
Zircon_43_058	263	128	0.44	0.05218	0.00089	0.32019	0.00569	0.04463	0.00023	0.01189	0.00019	0.28	281	1	282	4	293	36	281	1	0.4
Zircon_42_057	375	264	0.64	0.05177	0.00083	0.31923	0.00540	0.04483	0.00025	0.01191	0.00018	0.32	283	2	281	4	275	34	283	2	-0.7
Zircon_97_123	196	86	0.40	0.06078	0.00159	0.37780	0.01052	0.04508	0.00023	0.01390	0.00008	0.21	284	1	325	8	632	58	284	1	12.6
Zircon_69_089	43	20	0.42	0.05923	0.00267	0.38116	0.01748	0.04675	0.00041	0.01345	0.00048	0.18	295	3	328	13	576	101	295	3	10.1
Zircon_10_018	180	118	0.60	0.05199	0.00099	0.36218	0.00722	0.05061	0.00030	0.01301	0.00020	0.30	318	2	314	5	285	43	318	2	-1.3
Zircon_29_041	79	48	0.55	0.06799	0.00170	0.50983	0.01331	0.05444	0.00041	0.01708	0.00029	0.29	342	3	418	9	868	53	342	3	18.2
Zircon_46_062	53	38	0.65	0.06167	0.00265	0.76983	0.03348	0.09056	0.00059	0.02326	0.00042	0.15	559	3	580	19	663	85	559	3	3.6
Zircon_72_093	99	140	1.28	0.06187	0.00118	0.89439	0.01785	0.10506	0.00064	0.02714	0.00038	0.29	644	4	649	10	670	42	644	4	0.8
Zircon_70_090	253	136	0.49	0.06581	0.00092	0.97380	0.01538	0.10721	0.00078	0.03252	0.00049	0.47	657	5	690	8	800	30	657	5	4.8
Zircon_83_106	738	96	0.12	0.06645	0.00071	1.03556	0.01355	0.11302	0.00067	0.03450	0.00024	0.53	690	4	722	7	821	23	690	4	4.4
Zircon_25_036	2968	245	0.07	0.06723	0.00062	1.22580	0.01240	0.13239	0.00056	0.03187	0.00051	0.41	801	3	812	6	845	18	801	3	1.4
Zircon_34_047	218	97	0.40	0.06985	0.00077	1.43040	0.01717	0.14877	0.00071	0.04266	0.00064	0.40	894	4	902	7	924	21	894	4	0.9
Zircon_41_056	328	47	0.13	0.06605	0.00073	1.35520	0.01637	0.14900	0.00075	0.03805	0.00061	0.40	895	4	870	7	808	21	895	4	-2.9
Zircon_2_009	129	31	0.22	0.07336	0.00128	1.50896	0.02996	0.14918	0.00113	0.04503	0.00034	0.40	896	6	934	12	1024	33	896	6	4.1
Zircon_49_065	528	101	0.17	0.07266	0.00072	1.50420	0.01612	0.15037	0.00062	0.04372	0.00157	0.38	903	3	932	7	1004	19	903	3	3.1
Zircon_91_116	623	221	0.32	0.07431	0.00071	1.57360	0.01682	0.15375	0.00072	0.03930	0.00055	0.45	922	4	960	7	1050	20	922	4	4.0
Zircon_90_114	702	192	0.25	0.06942	0.00067	1.47870	0.01563	0.15462	0.00065	0.03984	0.00056	0.41	927	4	922	6	911	20	927	4	-0.5
Zircon_26_038	239	66	0.25	0.06972	0.00077	1.49220	0.01797	0.15550	0.00076	0.04051	0.00061	0.40	932	4	927	7	920	21	932	4	-0.5
Zircon_74_095	140	79	0.51	0.07079	0.00106	1.55920	0.02465	0.15999	0.00080	0.04172	0.00063	0.32	957	4	954	10	951	31	957	4	-0.3
Zircon_23_034	244	76	0.28	0.07154	0.00079	1.57730	0.01852	0.16023	0.00066	0.04258	0.00064	0.34	958	4	961	7	973	21	958	4	0.3
Zircon_62_081	115	37	0.29	0.06883	0.00089	1.52700	0.02101	0.16108	0.00072	0.04139	0.00062	0.34	963	4	941	8	894	27	963	4	-2.3
Zircon_48_064	749	167	0.20	0.06981	0.00070	1.55650	0.01713	0.16176	0.00074	0.04318	0.00078	0.41	967	4	953	7	923	19	967	4	-1.5
Zircon_99_125	213	55	0.23	0.07131	0.00086	1.59210	0.02024	0.16224	0.00068	0.04427	0.00066	0.32	969	4	967	8	966	25	969	4	-0.2
Zircon_11_020	79	37	0.43	0.07243	0.00101	1.62120	0.02416	0.16271	0.00083	0.04129	0.00066	0.35	972	5	978	9	998	28	972	5	0.6

(Continued)

Tabla 12 *(Continued)*

Zircon no.	U (ppm)	Th (ppm)	Th/U	Corrected isotopic ratios[a]									Corrected ages (Ma)[b]						Best age		
				$\frac{^{207}Pb}{^{206}Pb}$	1σ	$\frac{^{207}Pb}{^{235}U}$	1σ	$\frac{^{206}Pb}{^{238}U}$	1σ	$\frac{^{208}Pb}{^{232}Th}$	1σ	ρ[c]	$\frac{^{206}Pb}{^{238}U}$	1σ	$\frac{^{207}Pb}{^{235}U}$	1σ	$\frac{^{207}Pb}{^{206}Pb}$	1σ	(Ma)	1σ	δ (%)[d]
Zircon_89_113	153	46	0.27	0.07268	0.00087	1.63280	0.02098	0.16328	0.00075	0.04698	0.00070	0.36	975	4	983	8	1005	25	975	4	0.8
Zircon_1_TEP-474-3_008	90	24	0.24	0.07052	0.00099	1.58750	0.02365	0.16366	0.00083	0.04373	0.00079	0.33	977	5	965	9	944	28	977	5	-1.2
Zircon_71_092	205	52	0.23	0.06800	0.00082	1.53240	0.01953	0.16363	0.00070	0.04101	0.00066	0.32	977	4	943	8	869	26	977	4	-3.6
Zircon_78_100	75	11	0.13	0.07088	0.00092	1.59810	0.02275	0.16372	0.00095	0.04257	0.00106	0.41	977	5	969	9	954	27	977	5	-0.8
Zircon_28_040	74	23	0.28	0.07243	0.00094	1.63510	0.02314	0.16398	0.00092	0.04526	0.00077	0.40	979	5	984	9	998	24	979	5	0.5
Zircon_98_124	310	125	0.37	0.07084	0.00071	1.60130	0.01737	0.16410	0.00069	0.04302	0.00060	0.38	980	4	971	7	953	21	980	4	-0.9
Zircon_53_070	294	95	0.29	0.06948	0.00076	1.57200	0.01899	0.16430	0.00082	0.04148	0.00062	0.42	981	5	959	7	913	23	981	5	-2.3
Zircon_52_069	70	17	0.22	0.06991	0.00112	1.59770	0.02683	0.16593	0.00085	0.04251	0.00072	0.30	990	5	969	10	926	34	990	5	-2.2
Zircon_100_126	151	56	0.34	0.07188	0.00079	1.64470	0.02677	0.16614	0.00199	0.04420	0.00066	0.74	991	11	988	10	983	22	991	11	-0.3
Zircon_92_117	277	72	0.23	0.07221	0.00072	1.74200	0.01857	0.17513	0.00065	0.04509	0.00068	0.35	1040	4	1024	7	992	21	992	21	-1.6
Zircon_4_011	467	61	0.12	0.07087	0.00069	1.62550	0.01733	0.16651	0.00070	0.04270	0.00064	0.41	993	4	980	7	954	18	993	4	-1.3
Zircon_86_110	89	46	0.47	0.07222	0.00094	1.65860	0.02316	0.16689	0.00085	0.04354	0.00065	0.36	995	5	993	9	992	27	995	5	-0.2
Zircon_16_026	45	15	0.29	0.07236	0.00109	1.78910	0.02884	0.17990	0.00106	0.04611	0.00083	0.36	1066	6	1041	10	996	30	996	30	-2.4
Zircon_63_082	54	42	0.71	0.07235	0.00130	1.70400	0.03217	0.17114	0.00098	0.04352	0.00070	0.31	1018	5	1010	12	996	37	996	37	-0.8
Zircon_50_066	117	62	0.49	0.07060	0.00099	1.62620	0.02391	0.16722	0.00075	0.04209	0.00063	0.30	997	4	980	9	946	29	997	4	-1.7
Zircon_44_059	145	72	0.45	0.07242	0.00094	1.67940	0.02305	0.16865	0.00074	0.04476	0.00067	0.33	1005	4	1001	9	998	24	998	24	-0.4
Zircon_40_054	67	26	0.35	0.07078	0.00113	1.63260	0.02723	0.16755	0.00079	0.04135	0.00066	0.29	999	4	983	11	951	30	999	4	-1.6
Zircon_6_014	156	77	0.45	0.07198	0.00086	1.66180	0.02154	0.16780	0.00082	0.04367	0.00061	0.39	1000	5	994	8	985	25	1000	5	-0.6
Zircon_94_119	152	72	0.43	0.07111	0.00078	1.64760	0.01940	0.16828	0.00071	0.04300	0.00060	0.36	1003	4	989	7	961	23	1003	4	-1.4
Zircon_87_111	286	95	0.30	0.06961	0.00077	1.62120	0.01966	0.16916	0.00086	0.04330	0.00065	0.41	1007	5	978	8	917	23	1007	5	-3.0
Zircon_67_087	111	52	0.42	0.07304	0.00088	1.75880	0.02300	0.17462	0.00091	0.04450	0.00067	0.39	1038	5	1030	8	1015	25	1015	25	-0.8
Zircon_75_096	197	76	0.35	0.07324	0.00088	1.68410	0.02164	0.16718	0.00077	0.04560	0.00073	0.35	997	4	1003	8	1021	25	1021	25	0.6
Zircon_59_077	148	39	0.24	0.07329	0.00088	1.78870	0.02274	0.17725	0.00074	0.04854	0.00073	0.33	1052	4	1041	8	1022	25	1022	25	-1.1
Zircon_30_042	91	31	0.31	0.06765	0.00088	1.60210	0.02204	0.17192	0.00077	0.04302	0.00065	0.33	1023	4	971	9	858	25	1023	4	-5.4
Zircon_95_120	163	46	0.25	0.07332	0.00081	1.71500	0.02072	0.16986	0.00085	0.04462	0.00067	0.40	1011	5	1014	8	1023	23	1023	23	0.3
Zircon_76_098	91	25	0.25	0.07342	0.00117	1.69900	0.02853	0.16841	0.00086	0.04416	0.00079	0.32	1003	5	1008	11	1026	33	1026	33	0.5
Zircon_21_032	43	6	0.12	0.07402	0.00144	1.76982	0.03703	0.17341	0.00105	0.05229	0.00036	0.32	1031	6	1034	14	1042	40	1042	40	0.3
Zircon_65_084	138	101	0.66	0.07437	0.00104	1.72920	0.02532	0.16922	0.00073	0.04400	0.00062	0.30	1008	4	1019	9	1052	29	1052	29	1.1
Zircon_39_053	567	150	0.24	0.07510	0.00074	2.00490	0.02122	0.19394	0.00078	0.04984	0.00070	0.37	1143	4	1117	7	1071	18	1071	18	-2.3
Zircon_13_022	238	70	0.27	0.07530	0.00279	1.77350	0.06602	0.17107	0.00070	0.04412	0.00066	0.10	1018	4	1036	24	1077	73	1077	73	1.7
Zircon_20_030	200	108	0.49	0.07574	0.00091	2.04700	0.02616	0.19641	0.00086	0.04966	0.00070	0.34	1156	5	1131	9	1088	22	1088	22	-2.2
Zircon_5_012	458	76	0.15	0.07576	0.00076	1.95850	0.02460	0.18774	0.00143	0.05157	0.00088	0.60	1109	8	1101	8	1089	21	1089	21	-0.7
Zircon_32_045	389	103	0.24	0.07582	0.00076	2.05700	0.02215	0.19686	0.00079	0.04985	0.00070	0.37	1158	4	1135	7	1090	19	1090	19	-2.0

(Continued)

Tabla 12 *(Continued)*

Zircon no.	U (ppm)	Th (ppm)	Th/U	Corrected isotopic ratios[a]									Corrected ages (Ma)[b]						Best age		
				$\frac{^{207}Pb}{^{206}Pb}$	1σ	$\frac{^{207}Pb}{^{235}U}$	1σ	$\frac{^{206}Pb}{^{238}U}$	1σ	$\frac{^{208}Pb}{^{232}Th}$	1σ	ρ^c	$\frac{^{206}Pb}{^{238}U}$	1σ	$\frac{^{207}Pb}{^{235}U}$	1σ	$\frac{^{207}Pb}{^{206}Pb}$	1σ	(Ma)	1σ	δ (%)[d]
Zircon_58_076	439	113	0.23	0.07634	0.00076	2.01740	0.02741	0.19180	0.00176	0.04995	0.00085	0.68	1131	10	1121	9	1104	20	1104	20	-0.9
Zircon_64_083	255	73	0.26	0.07640	0.00076	2.00610	0.02234	0.19068	0.00093	0.04953	0.00074	0.45	1125	5	1118	8	1106	20	1106	20	-0.6
Zircon_96_122	155	73	0.43	0.07669	0.00092	2.03490	0.02661	0.19282	0.00100	0.04969	0.00075	0.40	1137	5	1127	9	1113	24	1113	24	-0.9
Zircon_36_050	461	120	0.24	0.07700	0.00075	2.01090	0.02136	0.18960	0.00078	0.04690	0.00070	0.40	1119	4	1119	7	1121	18	1121	18	0.0
Zircon_57_075	305	77	0.23	0.07700	0.00076	1.96380	0.02136	0.18518	0.00083	0.05308	0.00080	0.42	1095	5	1103	7	1121	20	1121	20	0.7
Zircon_47_063	117	49	0.38	0.07707	0.00108	1.82160	0.02684	0.17236	0.00079	0.05089	0.00112	0.31	1025	4	1053	10	1123	26	1123	26	2.7
Zircon_66_086	362	124	0.31	0.07706	0.00077	1.96630	0.02133	0.18524	0.00078	0.04794	0.00067	0.39	1096	4	1104	7	1123	20	1123	20	0.7
Zircon_55_072	147	48	0.29	0.07723	0.00129	1.82325	0.03386	0.17123	0.00085	0.05139	0.00026	0.33	1019	5	1054	12	1127	34	1127	34	3.3
Zircon_88_112	114	51	0.41	0.07733	0.00101	2.09350	0.02880	0.19671	0.00089	0.05129	0.00077	0.31	1158	5	1147	9	1130	27	1130	27	-1.0
Zircon_51_068	44	16	0.33	0.07745	0.00186	1.81140	0.04464	0.16957	0.00095	0.04976	0.00134	0.22	1010	5	1050	16	1133	49	1133	49	3.8
Zircon_22_033	646	247	0.35	0.07762	0.00076	2.08190	0.02196	0.19475	0.00076	0.04907	0.00069	0.37	1147	4	1143	7	1137	18	1137	18	-0.3
Zircon_68_088	278	105	0.34	0.07773	0.00076	2.22480	0.02458	0.20773	0.00106	0.05206	0.00073	0.47	1217	6	1189	8	1140	20	1140	20	-2.4
Zircon_18_028	73	31	0.38	0.07777	0.00109	2.02820	0.03043	0.18972	0.00102	0.05073	0.00081	0.36	1120	6	1125	10	1141	26	1141	26	0.4
Zircon_38_052	58	25	0.39	0.07798	0.00125	1.90050	0.03192	0.17743	0.00090	0.05114	0.00097	0.30	1053	5	1081	11	1146	30	1146	30	2.6
Zircon_17_027	61	27	0.40	0.07800	0.00109	2.13180	0.03191	0.19881	0.00105	0.05144	0.00087	0.36	1169	6	1159	10	1147	27	1147	27	-0.9
Zircon_7_015	156	69	0.40	0.07810	0.00086	2.09810	0.02486	0.19525	0.00086	0.04972	0.00090	0.37	1150	5	1148	8	1149	22	1149	22	-0.2
Zircon_60_078	149	46	0.28	0.07818	0.00094	2.19810	0.02841	0.20453	0.00098	0.05458	0.00087	0.37	1200	5	1180	9	1151	24	1151	24	-1.7
Zircon_27_039	80	42	0.48	0.07825	0.00110	2.13290	0.03208	0.19801	0.00109	0.05181	0.00083	0.36	1165	6	1160	10	1153	26	1153	26	-0.4
Zircon_73_094	126	46	0.33	0.07828	0.00094	2.10070	0.02707	0.19498	0.00092	0.05241	0.00084	0.36	1148	5	1149	9	1154	24	1154	24	0.1
Zircon_77_099	649	269	0.38	0.07827	0.00074	2.20540	0.02291	0.20456	0.00086	0.05170	0.00072	0.41	1200	5	1183	7	1154	19	1154	19	-1.4
Zircon_80_102	87	36	0.38	0.07829	0.00102	2.17760	0.03057	0.20207	0.00107	0.05293	0.00085	0.37	1186	6	1174	10	1154	26	1154	26	-1.0
Zircon_3_010	256	86	0.31	0.07848	0.00078	2.19840	0.02368	0.20342	0.00081	0.05212	0.00073	0.39	1194	4	1181	8	1159	18	1159	18	-1.1
Zircon_24_035	76	44	0.52	0.07876	0.00102	2.13210	0.02926	0.19675	0.00087	0.04806	0.00072	0.33	1158	5	1159	9	1166	24	1166	24	0.1
Zircon_79_101	702	202	0.26	0.07908	0.00074	2.32100	0.02341	0.21306	0.00083	0.05384	0.00075	0.37	1245	4	1219	7	1174	19	1174	19	-2.1
Zircon_35_048	395	90	0.21	0.07915	0.00079	2.08660	0.02324	0.19149	0.00094	0.05712	0.00086	0.44	1129	5	1144	8	1176	20	1176	20	1.3
Zircon_12_021	102	81	0.72	0.07956	0.00095	2.33690	0.03047	0.21322	0.00109	0.05254	0.00074	0.40	1246	6	1224	9	1186	23	1186	23	-1.8
Zircon_8_016	82	42	0.46	0.08535	0.00102	2.65570	0.03473	0.22587	0.00117	0.05569	0.00084	0.41	1313	6	1316	10	1324	24	1324	24	0.2
Zircon_14_023	235	91	0.35	0.08660	0.00087	2.93020	0.03276	0.24557	0.00123	0.06078	0.00085	0.44	1416	6	1390	8	1352	19	1352	19	-1.9
Zircon_54_071	40	18	0.41	0.08676	0.00191	2.52390	0.05827	0.21228	0.00149	0.05666	0.00261	0.30	1241	8	1279	17	1355	43	1355	43	3.0
Zircon_19_029	129	74	0.52	0.08742	0.00105	2.83080	0.04246	0.23510	0.00212	0.05922	0.00089	0.60	1361	11	1364	11	1370	21	1370	21	0.2
Zircon_33_046	48	33	0.63	0.08753	0.00114	2.40120	0.03418	0.19959	0.00116	0.05582	0.00089	0.40	1173	6	1243	10	1372	23	1372	23	5.6
Zircon_45_060	117	57	0.44	0.08953	0.00107	2.64550	0.03381	0.21440	0.00094	0.05644	0.00085	0.35	1252	5	1313	9	1416	21	1416	21	4.6
Zircon_82_105	416	154	0.34	0.08966	0.00085	3.07140	0.03143	0.24865	0.00094	0.06194	0.00087	0.38	1432	5	1426	8	1418	18	1418	18	-0.4

(Continued)

Tabla 12 *(Continued)*

				Corrected isotopic ratios[a]									Corrected ages (Ma)[b]						Best age		
Zircon no.	U (ppm)	Th (ppm)	Th/U	$\frac{^{207}Pb}{^{206}Pb}$	1σ	$\frac{^{207}Pb}{^{235}U}$	1σ	$\frac{^{206}Pb}{^{238}U}$	1σ	$\frac{^{208}Pb}{^{232}Th}$	1σ	ρ^{c}	$\frac{^{206}Pb}{^{238}U}$	1σ	$\frac{^{207}Pb}{^{235}U}$	1σ	$\frac{^{207}Pb}{^{206}Pb}$	1σ	(Ma)	1σ	δ (%)[d]
Zircon_9_017	310	307	0.90	0.09739	0.00093	3.58390	0.03847	0.26691	0.00133	0.06871	0.00089	0.46	1525	7	1546	9	1575	18	1575	18	1.4

[a] Absolute errors at 1-σ level
[b] Absolute errors (Ma) at 1-σ level
[c] Error correlation
[d] Discordance = $(\frac{^{207}Pb}{^{235}U} - \frac{^{206}Pb}{^{238}U}) / \frac{^{207}Pb}{^{235}U} \cdot 100$

Tabla 13.: *LA-ICP-MS U–Pb isotopic data for sample TEP-474-4*

				Corrected isotopic ratios[a]									Corrected ages (Ma)[b]						Best age		
Zircon no.	U (ppm)	Th (ppm)	Th/U	$\frac{^{207}Pb}{^{206}Pb}$	1σ	$\frac{^{207}Pb}{^{235}U}$	1σ	$\frac{^{206}Pb}{^{238}U}$	1σ	$\frac{^{208}Pb}{^{232}Th}$	1σ	ρ^c	$\frac{^{206}Pb}{^{238}U}$	1σ	$\frac{^{207}Pb}{^{235}U}$	1σ	$\frac{^{207}Pb}{^{206}Pb}$	1σ	(Ma)	1σ	δ (%)[d]
Zircon_80_102	90	41	0.41	0.05587	0.00151	0.31569	0.00873	0.04105	0.00025	0.01245	0.00024	0.21	259	2	279	7	447	59	259	2	7.2
Zircon_51_068	98	39	0.36	0.05617	0.00188	0.31956	0.01258	0.04126	0.00051	0.01284	0.00015	0.45	261	3	282	10	459	69	261	3	7.4
Zircon_87_111	187	143	0.69	0.05696	0.00125	0.33353	0.00762	0.04248	0.00026	0.01311	0.00025	0.28	268	2	292	6	490	45	268	2	8.2
Zircon_47_063	178	93	0.47	0.05526	0.00126	0.34692	0.00947	0.04553	0.00040	0.01420	0.00012	0.42	287	2	302	7	423	51	287	2	5.0
Zircon_19_029	206	76	0.33	0.05480	0.00108	0.34996	0.00753	0.04632	0.00022	0.01446	0.00007	0.25	292	1	305	6	404	42	292	1	4.3
Zircon_65_084	118	145	1.10	0.05254	0.00116	0.34011	0.00786	0.04708	0.00033	0.01390	0.00019	0.30	297	2	297	6	309	49	297	2	0.0
Zircon_72_093	417	370	0.80	0.05619	0.00073	0.37921	0.00531	0.04915	0.00026	0.01465	0.00028	0.37	309	2	326	4	460	27	309	2	5.2
Zircon_99_125	122	93	0.69	0.05938	0.00229	0.41372	0.01725	0.05053	0.00035	0.01562	0.00010	0.25	318	2	352	12	581	78	318	2	9.7
Zircon_46_062	348	90	0.23	0.06026	0.00072	0.49630	0.00713	0.05962	0.00047	0.01769	0.00067	0.56	373	3	409	5	613	24	373	3	8.8
Zircon_38_052	92	70	0.69	0.05994	0.00156	0.61044	0.01801	0.07386	0.00054	0.02281	0.00016	0.33	459	3	484	11	602	56	459	3	5.2
Zircon_68_088	330	351	0.96	0.05709	0.00069	0.58909	0.00751	0.07487	0.00032	0.02242	0.00025	0.32	465	2	470	5	495	26	465	2	1.1
Zircon_22_033	176	19	0.10	0.06866	0.00103	0.74205	0.01523	0.07715	0.00108	0.05580	0.00123	0.68	479	6	564	9	889	29	479	6	15.1
Zircon_7_015	635	38	0.05	0.06431	0.00071	0.70616	0.01371	0.07811	0.00125	0.02144	0.00088	0.82	485	7	542	8	752	23	485	7	10.5
Zircon_49_065	802	87	0.10	0.06465	0.00067	0.83945	0.00980	0.09417	0.00041	0.02883	0.00018	0.42	580	2	619	5	763	22	580	2	6.3
Zircon_53_070	162	30	0.16	0.06506	0.00152	1.00519	0.02512	0.11205	0.00051	0.03428	0.00030	0.31	685	3	706	13	776	46	685	3	3.0
Zircon_29_041	66	18	0.25	0.06147	0.00178	0.98702	0.04383	0.11647	0.00262	0.03587	0.00078	0.79	710	15	697	22	656	62	710	15	-1.9
Zircon_79_101	280	60	0.19	0.06533	0.00085	1.17295	0.02574	0.13022	0.00176	0.03982	0.00052	0.79	789	10	788	12	785	27	789	10	-0.1
Zircon_23_034	1519	123	0.07	0.07188	0.00056	1.31635	0.01369	0.13281	0.00080	0.04018	0.00024	0.57	804	5	853	6	983	15	804	5	5.7
Zircon_9_017	727	64	0.08	0.07166	0.00065	1.31551	0.01579	0.13314	0.00094	0.04029	0.00029	0.63	806	5	853	7	976	17	806	5	5.5
Zircon_20_030	331	67	0.18	0.06877	0.00080	1.29339	0.01932	0.13641	0.00097	0.04147	0.00029	0.51	824	5	843	9	892	23	824	5	2.3
Zircon_27_039	745	94	0.11	0.07510	0.00069	1.41554	0.01707	0.13671	0.00089	0.04116	0.00026	0.56	826	5	895	7	1071	18	826	5	7.7
Zircon_67_087	581	75	0.12	0.07167	0.00068	1.48594	0.01564	0.15036	0.00064	0.04551	0.00020	0.43	903	4	925	6	977	19	903	4	2.4
Zircon_35_048	228	36	0.14	0.07149	0.00070	1.51350	0.01665	0.15368	0.00077	0.04720	0.00066	0.46	922	4	936	7	971	20	922	4	1.5
Zircon_15_024	269	54	0.18	0.07297	0.00073	1.55200	0.01749	0.15428	0.00080	0.04724	0.00061	0.46	925	4	951	7	1013	19	925	4	2.7
Zircon_30_042	142	71	0.45	0.07287	0.00101	1.55243	0.02473	0.15451	0.00076	0.04667	0.00022	0.40	926	4	951	10	1010	28	926	4	2.6
Zircon_12_021	665	223	0.30	0.07406	0.00064	1.60720	0.01546	0.15743	0.00065	0.04711	0.00052	0.44	942	4	973	6	1043	17	942	4	3.2
Zircon_58_076	186	50	0.24	0.07355	0.00101	1.59963	0.02435	0.15774	0.00073	0.04760	0.00026	0.39	944	4	970	10	1029	28	944	4	2.7
Zircon_56_074	193	78	0.36	0.07310	0.00105	1.60433	0.02608	0.15917	0.00077	0.04807	0.00026	0.40	952	4	972	10	1017	29	952	4	2.1
Zircon_77_099	296	127	0.39	0.07181	0.00095	1.58516	0.02381	0.16010	0.00076	0.04844	0.00022	0.41	957	4	964	9	981	26	957	4	0.7
Zircon_50_066	97	36	0.33	0.07279	0.00095	1.61650	0.02257	0.16125	0.00082	0.04775	0.00067	0.36	964	5	977	9	1008	26	964	5	1.3
Zircon_24_035	145	37	0.23	0.07320	0.00082	1.63266	0.02173	0.16176	0.00086	0.04884	0.00025	0.41	967	5	983	8	1020	22	967	5	1.6
Zircon_21_032	184	129	0.63	0.07307	0.00080	1.64290	0.01953	0.16324	0.00073	0.04935	0.00054	0.39	975	4	987	8	1016	21	975	4	1.2

(Continued)

Tabla 13 *(Continued)*

Zircon no.	U (ppm)	Th (ppm)	Th/U	Corrected isotopic ratios[a]									Corrected ages (Ma)[b]						Best age		
				$\frac{^{207}Pb}{^{206}Pb}$	1σ	$\frac{^{207}Pb}{^{235}U}$	1σ	$\frac{^{206}Pb}{^{238}U}$	1σ	$\frac{^{208}Pb}{^{232}Th}$	1σ	ρ^c	$\frac{^{206}Pb}{^{238}U}$	1σ	$\frac{^{207}Pb}{^{235}U}$	1σ	$\frac{^{207}Pb}{^{206}Pb}$	1σ	(Ma)	1σ	δ (%)[d]
Zircon_6_014	82	34	0.38	0.07131	0.00126	1.62481	0.03176	0.16526	0.00094	0.05004	0.00028	0.33	986	5	980	12	966	35	986	5	-0.6
Zircon_93_118	65	25	0.35	0.07217	0.00108	1.73330	0.02769	0.17457	0.00096	0.05213	0.00073	0.35	1037	5	1021	10	991	28	991	28	-1.6
Zircon_74_095	320	194	0.55	0.07235	0.00069	1.67220	0.01737	0.16774	0.00070	0.04820	0.00053	0.40	1000	4	998	7	996	19	1000	4	-0.2
Zircon_98_124	119	57	0.43	0.07249	0.00080	1.74200	0.02070	0.17444	0.00078	0.04988	0.00065	0.37	1037	4	1024	8	1000	21	1000	21	-1.3
Zircon_62_081	732	355	0.44	0.07222	0.00058	1.67610	0.01522	0.16843	0.00072	0.04951	0.00050	0.47	1003	4	1000	6	992	16	1003	4	-0.3
Zircon_64_083	265	291	0.99	0.07264	0.00068	1.80380	0.01865	0.18022	0.00077	0.04944	0.00054	0.42	1068	4	1047	7	1004	19	1004	19	-2.0
Zircon_33_046	590	299	0.46	0.07275	0.00065	1.67980	0.01632	0.16757	0.00065	0.04998	0.00050	0.39	999	4	1001	6	1007	18	1007	18	0.2
Zircon_96_122	153	89	0.53	0.07127	0.00078	1.66350	0.02076	0.16940	0.00100	0.04905	0.00054	0.48	1009	6	995	8	965	21	1009	6	-1.4
Zircon_60_078	218	50	0.21	0.07298	0.00070	1.69850	0.02018	0.16891	0.00118	0.05000	0.00060	0.59	1006	7	1008	8	1013	19	1013	19	0.2
Zircon_3_010	128	45	0.32	0.07308	0.00080	1.74240	0.02105	0.17288	0.00086	0.05425	0.00065	0.42	1028	5	1024	8	1016	22	1016	22	-0.4
Zircon_26_038	250	113	0.41	0.07327	0.00073	1.69410	0.01822	0.16762	0.00070	0.04684	0.00066	0.38	999	4	1006	7	1021	19	1021	19	0.7
Zircon_48_064	100	27	0.25	0.07346	0.00081	1.71040	0.02026	0.16907	0.00074	0.04968	0.00079	0.37	1007	4	1012	8	1027	22	1027	22	0.5
Zircon_54_071	138	48	0.31	0.07353	0.00081	1.80620	0.02175	0.17841	0.00087	0.05185	0.00062	0.40	1058	5	1048	8	1029	22	1029	22	-1.0
Zircon_73_094	144	49	0.31	0.07386	0.00096	1.74990	0.02407	0.17179	0.00077	0.05041	0.00091	0.33	1022	4	1027	9	1038	26	1038	26	0.5
Zircon_1_TEP-474-4_008	258	86	0.30	0.07396	0.00078	1.82307	0.02362	0.17878	0.00091	0.05392	0.00027	0.45	1060	5	1054	8	1040	20	1040	20	-0.6
Zircon_5_012	296	214	0.65	0.07399	0.00069	1.67490	0.01689	0.16424	0.00064	0.04887	0.00054	0.38	980	4	999	6	1041	19	1041	19	1.9
Zircon_42_057	191	26	0.12	0.07404	0.00079	1.79011	0.02172	0.17535	0.00089	0.05288	0.00029	0.45	1042	5	1042	8	1043	21	1043	21	0.0
Zircon_75_096	98	48	0.44	0.07420	0.00111	1.86820	0.02931	0.18292	0.00084	0.05378	0.00075	0.30	1083	5	1070	10	1047	30	1047	30	-1.2
Zircon_25_036	230	98	0.38	0.07427	0.00082	1.71280	0.02070	0.16762	0.00084	0.05103	0.00066	0.41	999	5	1013	8	1049	21	1049	21	1.4
Zircon_57_075	184	52	0.25	0.07445	0.00094	1.75458	0.02584	0.17093	0.00101	0.05151	0.00031	0.43	1017	6	1029	10	1054	25	1054	25	1.2
Zircon_92_117	304	107	0.32	0.07449	0.00074	1.71310	0.01863	0.16699	0.00075	0.05043	0.00061	0.41	996	4	1013	7	1055	19	1055	19	1.7
Zircon_63_082	294	94	0.29	0.07465	0.00084	1.76549	0.02266	0.17153	0.00081	0.05168	0.00024	0.40	1021	4	1033	8	1059	22	1059	22	1.2
Zircon_84_107	55	27	0.45	0.07475	0.00170	1.73666	0.04464	0.16851	0.00132	0.05076	0.00039	0.36	1004	7	1022	17	1062	45	1062	45	1.8
Zircon_86_110	122	44	0.32	0.07487	0.00098	1.78251	0.02616	0.17268	0.00075	0.05201	0.00022	0.35	1027	4	1039	10	1065	25	1065	25	1.2
Zircon_18_028	300	69	0.21	0.07525	0.00074	1.84670	0.02008	0.17799	0.00080	0.05831	0.00076	0.43	1056	4	1062	7	1075	19	1075	19	0.6
Zircon_90_114	454	38	0.07	0.07524	0.00066	1.82860	0.01753	0.17649	0.00067	0.05986	0.00084	0.40	1048	4	1056	6	1075	16	1075	16	0.8
Zircon_8_016	264	50	0.17	0.07530	0.00075	1.80660	0.01980	0.17401	0.00082	0.05265	0.00063	0.42	1034	5	1048	7	1077	20	1077	20	1.3
Zircon_40_054	666	159	0.22	0.07604	0.00064	1.83240	0.01705	0.17486	0.00070	0.05313	0.00058	0.43	1039	4	1057	6	1096	17	1096	17	1.7
Zircon_95_120	105	60	0.51	0.07632	0.00182	1.86274	0.04972	0.17701	0.00114	0.05320	0.00032	0.34	1051	6	1068	18	1104	44	1104	44	1.6
Zircon_52_069	755	139	0.17	0.07638	0.00066	1.82244	0.02051	0.17305	0.00103	0.05200	0.00031	0.60	1029	6	1054	7	1105	17	1105	17	2.4
Zircon_71_092	223	107	0.43	0.07638	0.00099	1.85652	0.02791	0.17628	0.00089	0.05298	0.00026	0.42	1047	5	1066	10	1105	25	1105	25	1.8
Zircon_81_104	20	11	0.49	0.07646	0.00184	1.82750	0.04584	0.17337	0.00127	0.05024	0.00095	0.28	1031	7	1055	16	1107	47	1107	47	2.3
Zircon_16_026	121	20	0.15	0.07652	0.00084	2.02110	0.02394	0.19167	0.00084	0.05482	0.00093	0.38	1130	5	1123	8	1109	21	1109	21	-0.6

(Continued)

Tabla 13 *(Continued)*

Zircon no.	U (ppm)	Th (ppm)	Th/U	Corrected isotopic ratios[a]									Corrected ages (Ma)[b]						Best age		
				$\frac{^{207}Pb}{^{206}Pb}$	1σ	$\frac{^{207}Pb}{^{235}U}$	1σ	$\frac{^{206}Pb}{^{238}U}$	1σ	$\frac{^{208}Pb}{^{232}Th}$	1σ	ρ^c	$\frac{^{206}Pb}{^{238}U}$	1σ	$\frac{^{207}Pb}{^{235}U}$	1σ	$\frac{^{207}Pb}{^{206}Pb}$	1σ	(Ma)	1σ	δ (%)[d]
Zircon_41_056	665	159	0.22	0.07680	0.00062	1.95240	0.01747	0.18442	0.00070	0.05387	0.00059	0.43	1091	4	1099	6	1116	16	1116	16	0.7
Zircon_17_027	163	14	0.08	0.07687	0.00092	2.10800	0.02847	0.19856	0.00123	0.06584	0.00132	0.46	1168	7	1151	9	1118	23	1118	23	-1.5
Zircon_82_105	208	106	0.46	0.07694	0.00073	1.96660	0.02035	0.18557	0.00076	0.05489	0.00060	0.40	1097	4	1104	7	1120	19	1120	19	0.6
Zircon_78_100	93	50	0.49	0.07721	0.00143	1.90670	0.04899	0.17911	0.00212	0.05376	0.00060	0.59	1062	12	1083	17	1127	36	1127	36	1.9
Zircon_13_022	632	112	0.16	0.07725	0.00064	1.78410	0.01660	0.16760	0.00070	0.04711	0.00057	0.46	999	4	1040	6	1128	16	1128	16	3.9
Zircon_37_051	117	48	0.37	0.07806	0.00086	2.04540	0.02431	0.18999	0.00085	0.05587	0.00067	0.38	1121	5	1131	8	1148	22	1148	22	0.9
Zircon_76_098	98	27	0.25	0.07832	0.00086	2.02470	0.02438	0.18786	0.00092	0.06474	0.00091	0.41	1110	5	1124	8	1155	21	1155	21	1.2
Zircon_83_106	530	285	0.49	0.07832	0.00068	1.97150	0.01969	0.18271	0.00090	0.05037	0.00060	0.49	1082	5	1106	7	1155	17	1155	17	2.2
Zircon_91_116	473	314	0.60	0.07845	0.00070	1.97900	0.01923	0.18317	0.00071	0.05261	0.00058	0.40	1084	4	1108	7	1158	16	1158	16	2.2
Zircon_61_080	120	64	0.48	0.07893	0.00087	2.17370	0.02626	0.19980	0.00100	0.05793	0.00070	0.41	1174	5	1173	8	1170	21	1170	21	-0.1
Zircon_28_040	77	29	0.34	0.07901	0.00112	2.13749	0.03499	0.19620	0.00106	0.05875	0.00031	0.35	1155	6	1161	11	1172	27	1172	27	0.5
Zircon_88_112	194	76	0.35	0.07902	0.00079	2.15590	0.02364	0.19814	0.00089	0.06035	0.00072	0.41	1165	5	1167	8	1173	18	1173	18	0.2
Zircon_32_045	175	102	0.53	0.07910	0.00227	1.85739	0.05586	0.17031	0.00086	0.05099	0.00032	0.22	1014	5	1066	20	1175	57	1175	57	4.9
Zircon_69_089	271	89	0.30	0.07924	0.00083	2.10736	0.02578	0.19288	0.00093	0.05773	0.00027	0.46	1137	5	1151	8	1178	20	1178	20	1.2
Zircon_70_090	753	125	0.15	0.07944	0.00076	2.15331	0.02429	0.19659	0.00103	0.05883	0.00033	0.51	1157	6	1166	8	1183	19	1183	19	0.8
Zircon_94_119	330	106	0.29	0.07945	0.00071	2.20410	0.02294	0.20145	0.00109	0.05770	0.00069	0.51	1183	6	1182	7	1183	16	1183	16	-0.1
Zircon_14_023	241	121	0.45	0.08010	0.00097	2.11030	0.03185	0.19108	0.00104	0.05713	0.00029	0.49	1127	6	1152	10	1199	23	1199	23	2.2
Zircon_89_113	630	334	0.48	0.08013	0.00069	2.09930	0.02121	0.19011	0.00101	0.05492	0.00060	0.52	1122	5	1149	7	1200	16	1200	16	2.3
Zircon_43_058	264	113	0.39	0.08031	0.00078	2.25490	0.02375	0.20382	0.00084	0.06282	0.00069	0.39	1196	4	1198	7	1205	19	1205	19	0.2
Zircon_10_018	353	107	0.27	0.08067	0.00072	2.25560	0.02220	0.20268	0.00085	0.05816	0.00064	0.42	1190	5	1199	7	1213	17	1213	17	0.8
Zircon_4_011	535	101	0.17	0.08083	0.00068	2.34790	0.02165	0.21062	0.00080	0.06033	0.00066	0.41	1232	4	1227	7	1217	17	1217	17	-0.4
Zircon_59_077	1004	583	0.52	0.08102	0.00066	2.32340	0.02188	0.20820	0.00100	0.06128	0.00061	0.50	1219	5	1219	7	1222	16	1222	16	0.0
Zircon_44_059	182	51	0.25	0.08157	0.00081	2.29940	0.02510	0.20470	0.00094	0.06354	0.00083	0.42	1201	5	1212	8	1235	19	1235	19	0.9
Zircon_39_053	536	220	0.37	0.08162	0.00086	1.98751	0.02478	0.17661	0.00079	0.05269	0.00024	0.47	1048	4	1111	8	1236	21	1236	21	5.7
Zircon_66_086	362	135	0.34	0.08199	0.00086	2.26433	0.02689	0.20031	0.00080	0.05974	0.00024	0.39	1177	4	1201	8	1245	20	1245	20	2.0
Zircon_2_009	339	266	0.71	0.08232	0.00072	2.35620	0.02246	0.20765	0.00081	0.06136	0.00067	0.40	1216	4	1229	7	1253	16	1253	16	1.1
Zircon_85_108	563	214	0.34	0.08371	0.00073	2.36760	0.02308	0.20532	0.00090	0.06124	0.00080	0.45	1204	5	1233	7	1286	16	1286	16	2.4
Zircon_11_020	600	221	0.33	0.08512	0.00072	2.67600	0.02467	0.22802	0.00087	0.06566	0.00066	0.40	1324	5	1322	7	1318	16	1318	16	-0.2
Zircon_97_123	719	284	0.36	0.08568	0.00069	2.72960	0.02516	0.23128	0.00102	0.06600	0.00066	0.49	1341	5	1337	7	1331	15	1331	15	-0.3
Zircon_36_050	1032	399	0.35	0.08624	0.00068	2.10420	0.01924	0.17695	0.00081	0.05083	0.00061	0.51	1050	4	1150	6	1344	15	1344	15	8.7
Zircon_34_047	108	69	0.57	0.08888	0.00124	2.71600	0.04148	0.22156	0.00135	0.06526	0.00078	0.41	1290	7	1333	11	1402	27	1402	27	3.2

[a] Absolute errors at 1-σ level
[b] Absolute errors (Ma) at 1-σ level

[c] Error correlation

[d] Discordance = $\left(\frac{^{207}Pb}{^{235}U} - \frac{^{206}Pb}{^{238}U}\right) / \frac{^{207}Pb}{^{235}U} \cdot 100$

A.4 TABLAS ELEMENTOS TRAZA MEDIDOS POR LA-ICP-MS

Tabla 14.: *LA-ICP-MS trace element abundances (ppm) for zircons of sample MH-28*

Zircon no.	P	Ti	Y	Zr	Nb	La	Ce	Pr	Nd	Sm	Eu	Gd	Tb	Dy	Ho	Er	Yb	Lu	Hf	Th	U
Zircon_5_012	805.50	6.42	2914.67	410 238.79	5.45	16.26	105.40	8.71	49.47	31.18	8.84	78.58	27.19	302.99	99.83	441.11	868.55	162.66	9263.92	575.83	629.14
Zircon_8_016	133.29	0.64	1101.53	417 062.90	2.77	4.69	58.57	2.77	15.00	9.29	2.72	21.35	7.06	82.46	32.30	170.62	510.81	125.73	10 937.91	441.98	699.04
Zircon_15_024	245.35	8.73	2391.66	392 006.92	5.82	3.93	110.09	2.14	15.66	13.79	3.46	54.67	18.03	206.92	78.19	362.80	800.33	162.74	8729.00	630.12	668.08
Zircon_2_009	565.52	–3.48	512.93	296 333.55	1.64	0.06	14.89	0.07	0.91	1.31	0.58	7.60	2.76	36.11	15.70	80.99	208.53	47.39	6463.56	26.44	67.53
Zircon_10_018	910.33	5.46	4469.43	375 032.05	4.30	72.58	256.05	31.33	159.75	81.03	23.00	156.58	52.06	542.50	160.55	643.08	1168.30	207.99	9760.19	1041.65	1184.01
Zircon_62_081	230.71	51.36	738.42	414 305.81	0.69	1.13	11.08	0.72	4.84	4.79	1.49	18.01	6.15	68.90	24.90	112.78	241.23	50.72	8934.44	63.97	118.94
Zircon_14_023	69.26	9.77	913.01	385 942.71	3.63	0.89	7.33	0.54	4.13	3.95	1.13	16.05	5.71	70.16	27.79	141.00	349.43	74.80	9352.74	88.38	564.59
Zircon_41_056	242.97	4.79	632.98	412 027.82	1.00	0.05	10.82	0.08	1.18	2.45	0.84	14.24	4.62	56.02	21.54	99.78	207.33	43.87	9773.63	111.00	249.71
Zircon_72_092	610.94	2.88	1442.05	425 143.82	2.40	0.06	9.24	0.08	1.42	2.48	0.25	18.37	7.71	110.44	49.42	247.02	560.44	118.85	10 169.17	108.20	281.29
Zircon_6_014	337.19	7.68	1369.55	405 573.42	3.18	22.72	183.12	12.37	66.32	32.10	8.86	57.14	16.14	152.17	46.57	186.43	361.17	65.16	8973.09	458.05	758.88
Zircon_20_030	255.27	73.07	1114.34	373 474.97	12.29	3.88	44.93	2.36	13.24	7.71	3.02	18.43	6.85	84.18	34.17	189.87	532.06	119.37	10 780.93	188.19	1017.85
Zircon_68_088	223.22	6.60	531.20	423 417.42	3.09	0.04	9.73	0.08	1.16	1.70	0.61	10.90	3.84	48.67	19.48	90.58	181.19	36.97	8931.72	34.55	66.36
Zircon_69_089	249.55	9.23	766.29	419 742.59	1.12	0.10	22.17	0.58	7.77	9.90	2.01	34.26	9.28	87.42	26.85	102.88	160.83	28.86	9168.75	219.45	529.49
Zircon_3_010	473.27	6.02	749.79	457 575.96	1.83	0.31	3.24	0.22	2.06	2.05	0.25	10.13	4.44	61.22	24.49	121.00	269.20	52.49	12 786.17	73.61	842.76
Zircon_34_047	273.18	22.12	698.93	390 535.51	5.36	5.71	13.26	1.68	8.62	3.77	1.29	13.53	4.68	58.70	23.81	113.45	240.07	47.92	10 136.83	124.66	733.75
Zircon_42_057	418.45	19.57	824.25	421 273.33	1.45	0.10	3.47	0.40	6.32	7.34	0.95	28.75	8.57	87.89	29.37	121.88	207.29	38.30	8785.02	48.05	76.96
Zircon_22_033	442.63	22.46	1607.04	364 289.82	4.96	3.58	22.84	2.01	12.07	9.47	2.15	33.80	12.34	148.72	53.81	236.89	422.26	77.92	9319.81	294.96	938.47
Zircon_11_020	781.10	57.83	1739.75	373 991.92	1.99	2.94	7.49	0.86	7.21	8.99	1.78	41.37	13.35	154.13	58.19	255.57	457.65	85.85	8812.50	169.27	647.87
Zircon_45_060	582.64	–0.22	1072.58	417 695.91	1.49	0.06	2.93	0.10	1.60	2.92	0.10	18.93	7.08	89.15	36.66	169.39	334.69	65.25	10 558.80	89.72	361.50
Zircon_67_087	429.98	1.22	719.71	430 328.28	1.54	0.12	2.64	0.15	1.70	2.41	0.23	13.71	5.06	62.95	25.13	116.91	236.94	47.69	10 891.92	38.42	187.02
Zircon_76_097	155.00	1.81	553.63	432 663.16	5.13	0.09	10.11	0.15	2.54	3.52	0.25	17.04	5.20	58.80	20.68	86.70	151.85	28.82	9932.67	60.89	193.73
Zircon_79_100	251.02	7.80	735.23	454 828.46	2.22	0.06	11.14	0.10	2.03	3.40	0.40	17.86	6.02	71.00	26.23	115.91	219.37	42.22	10 161.68	57.26	145.69
Zircon_16_026	4.54	37.61	422.05	377 321.95	1.75	0.78	7.32	0.24	2.68	3.20	0.50	12.95	3.83	41.71	14.50	61.87	111.56	21.02	7241.46	33.27	77.79
Zircon_80_101	286.87	4.05	599.07	420 465.49	3.61	0.04	11.07	0.08	1.48	2.53	0.18	13.38	4.73	57.10	21.24	95.80	181.10	34.60	9585.25	72.77	226.56
Zircon_54_071	789.34	–3.72	1336.73	391 980.18	1.61	4.44	7.66	1.12	6.90	5.47	0.55	26.32	9.40	115.89	44.38	202.68	379.65	71.81	9880.30	116.26	400.44
Zircon_MH28_1_008	40.40	3.12	1250.77	384 791.59	3.47	0.12	9.58	0.53	8.31	12.24	1.01	47.27	13.56	137.10	44.55	175.09	273.91	48.10	7790.96	59.51	155.78
Zircon_50_066	62.45	14.98	132.17	412 417.22	0.57	0.98	6.50	0.14	1.47	1.31	0.37	4.45	1.21	13.20	4.49	19.23	38.04	7.67	9186.95	61.75	545.21
Zircon_39_053	332.15	14.07	540.18	416 628.08	2.81	0.05	14.68	0.13	1.77	2.30	0.39	11.50	4.15	50.06	18.89	88.32	194.14	38.71	10 178.27	50.84	169.59
Zircon_7_015	211.54	1.65	529.42	373 144.11	1.41	0.05	2.89	0.09	1.74	3.11	0.46	15.74	4.97	54.36	18.76	78.34	131.26	25.61	7684.76	23.18	201.30
Zircon_75_095	284.42	11.74	775.76	425 563.88	2.81	1.10	10.13	0.46	5.47	6.72	0.77	26.38	7.78	83.15	27.73	115.07	195.71	36.87	8475.79	66.24	120.72
Zircon_4_011	8719.97	18.72	1300.96	415 695.65	1.81	175.89	443.95	58.01	270.35	57.90	1.46	72.39	13.75	126.69	43.38	184.75	329.40	62.43	9249.30	116.41	329.28
Zircon_46_062	168.86	6.67	841.04	414 140.49	1.35	0.32	15.10	0.41	5.86	7.72	1.46	28.32	8.59	88.71	30.20	124.52	219.08	40.26	8006.81	64.12	96.92
Zircon_55_072	277.35	13.12	774.60	422 799.27	0.65	0.07	4.26	0.42	7.17	9.00	1.45	33.97	9.04	87.87	28.29	109.54	172.62	31.45	8151.01	22.91	48.48
Zircon_35_048	150.08	25.76	331.23	364 951.26	1.79	0.08	4.73	0.13	2.02	2.39	0.23	10.88	3.25	34.46	11.88	49.05	83.54	15.49	7346.72	24.81	95.26
Zircon_18_028	1619.77	5.46	2436.78	371 954.49	1.69	1.80	6.20	0.86	5.39	4.58	0.09	28.52	13.17	186.90	79.03	386.35	782.49	148.28	10 239.54	88.33	591.36
Zircon_29_041	328.96	13.24	1215.93	415 681.14	3.53	0.13	4.82	0.22	3.52	5.86	1.35	30.69	10.05	116.92	43.47	193.77	368.59	73.79	6924.20	50.73	184.52
Zircon_51_068	128.70	10.60	234.67	414 873.54	0.88	0.04	3.16	0.06	0.82	0.58	0.06	2.94	1.16	16.44	7.58	40.69	96.04	23.38	10 189.43	57.31	274.98
Zircon_12_021	129.04	3023.63	566.83	346 808.14	12.14	1.99	10.61	1.48	9.81	5.26	0.45	17.05	5.02	54.01	19.26	83.70	146.50	27.81	7121.09	29.67	80.04
Zircon_57_075	733.17	17.53	1147.57	418 908.00	1.34	0.25	2.56	0.18	1.99	2.95	0.11	18.72	7.14	93.55	38.24	183.83	377.86	73.40	11 265.34	80.89	422.93
Zircon_65_084	617.20	–0.52	1166.97	429 304.32	1.09	0.05	2.16	0.09	1.59	3.36	0.10	22.36	8.21	104.29	40.52	182.51	337.24	65.42	10 608.97	77.57	280.33
Zircon_58_076	609.59	21.46	1241.35	408 060.30	9.06	0.79	16.01	0.48	3.99	3.66	0.69	18.52	7.18	97.35	40.72	202.41	460.74	93.54	10 314.58	166.16	632.94
Zircon_48_064	371.54	3.71	646.12	411 642.47	5.30	0.06	27.13	0.10	1.42	2.13	0.24	11.51	4.06	54.48	21.86	105.46	237.01	48.76	10 458.26	57.49	197.33
Zircon_70_090	412.49	11.16	1055.83	408 967.54	4.40	0.41	15.55	0.26	2.67	3.78	1.06	21.42	7.68	92.36	34.86	157.96	336.19	72.09	11 882.32	147.80	1146.25
Zircon_9_017	277.84	5.50	567.06	364 053.01	1.39	0.17	2.23	0.12	1.19	1.59	0.15	9.07	3.76	47.63	18.28	86.01	178.62	35.82	7708.18	70.32	745.03
Zircon_28_040	488.53	7.86	770.55	395 552.43	2.05	7.98	27.89	2.18	11.61	6.19	0.51	21.55	6.55	73.01	26.77	116.91	214.68	40.50	8603.35	96.96	248.31
Zircon_32_045	49.54	2.42	354.48	409 302.19	8.47	0.05	6.78	0.06	0.85	0.89	0.25	5.68	2.27	28.27	10.98	49.31	95.15	18.65	9135.60	15.87	647.77

(Continued)

Tabla 14 *(Continued)*

Zircon no.	P	Ti	Y	Zr	Nb	La	Ce	Pr	Nd	Sm	Eu	Gd	Tb	Dy	Ho	Er	Yb	Lu	Hf	Th	U
Zircon_66_086	313.76	8.57	784.04	418 023.16	2.39	0.37	4.24	0.15	1.44	2.15	0.19	13.03	5.03	64.47	26.47	128.51	268.67	54.25	10 453.46	115.90	635.34
Zircon_77_098	398.25	5.07	1180.95	430 345.42	0.97	0.29	4.82	0.53	7.50	10.34	0.99	41.53	12.05	126.38	42.68	172.36	284.21	52.14	8571.49	41.19	70.79
Zircon_49_065	133.74	3.05	499.48	415 745.47	1.66	0.03	6.26	0.08	1.40	2.15	0.13	10.68	3.62	45.73	17.32	77.89	153.20	29.36	10 116.98	80.32	273.29
Zircon_53_070	1501.00	230.70	2034.96	383 396.72	1.79	3.22	11.47	1.78	13.57	11.20	0.41	50.02	16.41	190.78	71.40	317.80	571.31	109.85	9086.74	81.07	254.08
Zircon_59_077	342.51	0.31	573.79	418 851.30	2.45	0.24	6.84	0.16	1.36	1.38	0.09	8.39	3.33	44.21	18.82	96.62	228.57	47.16	10 741.88	101.56	596.46
Zircon_63_082	293.78	8.59	1091.63	422 591.58	3.48	0.65	6.49	0.37	4.15	5.31	0.33	27.96	9.27	106.18	38.02	165.28	290.60	54.43	10 738.97	160.49	987.72
Zircon_44_059	2315.29	16.07	1294.86	411 711.57	6.21	8.04	38.97	5.52	36.64	18.44	2.23	37.46	10.26	112.13	41.55	198.25	429.02	88.62	10 362.99	242.88	1189.05
Zircon_64_083	696.58	6.62	1256.74	427 563.08	1.10	0.05	2.43	0.13	2.28	4.53	0.29	26.56	9.28	113.03	42.98	193.82	358.86	67.68	10 099.30	71.16	226.38
Zircon_43_058	571.77	12.49	760.57	410 065.21	1.94	3.36	29.08	1.07	7.40	6.11	1.61	23.33	7.24	77.43	27.16	114.93	206.00	39.45	7497.83	33.08	47.01
Zircon_19_029	73.33	3.70	645.78	386 062.57	0.98	0.06	4.10	0.09	1.28	2.01	0.14	12.37	4.52	55.91	21.54	98.80	186.02	35.53	9448.89	60.77	216.98
Zircon_17_027	39.01	8.93	465.89	380 885.61	36.92	1.60	11.05	0.71	4.30	3.04	0.69	7.72	2.82	34.92	14.62	79.41	249.16	58.09	10 451.67	40.82	1108.62
Zircon_26_038	10.79	6.86	201.52	412 334.70	0.88	0.03	17.16	0.13	1.76	2.09	1.11	6.76	1.78	17.83	6.07	27.56	61.80	13.74	7708.84	146.17	514.02
Zircon_13_022	–32.06	11.03	211.05	380 912.19	1.19	0.14	6.68	0.11	1.32	0.87	0.29	3.31	1.14	14.45	6.16	31.99	87.44	20.49	8103.66	42.44	184.20
Zircon_37_051	249.88	8.20	641.29	413 454.88	1.24	0.05	3.59	0.14	2.48	4.03	0.48	19.11	5.73	62.87	22.67	96.93	172.06	32.67	8485.70	14.89	32.24
Zircon_74_094	229.04	6.34	753.98	426 686.50	1.07	0.05	6.26	0.40	6.18	8.26	1.74	30.31	8.33	82.46	27.47	111.79	187.57	35.21	8039.51	38.28	70.00
Zircon_73_093	559.83	162.13	951.34	399 538.45	1.73	0.79	4.37	0.26	2.19	2.78	0.08	15.66	6.11	81.55	32.77	155.83	310.28	59.95	10 577.56	89.28	389.92
Zircon_27_039	1309.27	59.47	1405.44	409 848.07	19.67	0.52	17.59	0.47	5.15	6.45	1.00	29.65	10.67	132.99	49.97	227.12	428.03	79.80	10 520.09	240.87	974.20
Zircon_56_074	6394.31	20.29	2019.81	397 811.77	10.42	100.67	185.16	19.03	81.72	23.83	4.37	56.94	17.75	197.55	71.82	320.67	613.44	117.20	10 624.44	282.00	985.46
Zircon_52_069	217.07	3.29	1064.35	421 758.60	1.03	0.04	2.07	0.13	2.88	5.02	0.29	25.80	8.52	99.75	36.85	162.01	296.52	56.38	8845.02	96.33	356.71
Zircon_60_078	207.03	6.06	634.45	411 166.80	3.83	0.04	8.39	0.14	2.55	3.79	0.26	18.46	5.78	64.04	22.68	98.01	171.03	32.20	9435.12	56.82	161.25
Zircon_40_054	183.30	5.38	568.20	407 843.77	1.45	0.04	2.55	0.06	0.96	1.18	0.09	7.09	2.96	41.62	18.03	95.40	228.37	47.93	11 623.19	62.05	817.55
Zircon_78_099	243.27	3.85	1411.99	412 340.00	4.91	0.38	12.86	0.28	3.37	4.96	0.24	27.62	9.72	122.71	49.44	233.73	463.76	95.66	10 753.78	127.25	936.37
Zircon_31_044	99.58	12.09	471.54	397 029.27	8.51	0.32	4.36	0.17	1.40	0.93	0.13	4.61	2.03	30.06	14.77	88.28	269.47	65.91	9955.86	69.49	1026.72
Zircon_36_050	1460.24	3.80	2459.74	409 017.19	1.57	0.31	2.69	0.25	2.43	3.75	0.10	29.28	13.08	188.90	81.66	407.74	862.58	167.89	11 203.91	79.02	691.34
Zircon_23_034	708.56	15.19	1404.73	380 939.23	1.76	2.62	9.96	1.11	7.68	5.83	0.25	28.59	9.97	122.45	47.47	215.52	403.13	77.93	8667.38	99.25	334.19
Zircon_25_036	490.25	3.52	920.14	377 895.51	1.62	0.14	4.76	0.27	3.24	4.34	0.52	20.85	6.93	82.68	31.29	139.34	266.14	50.30	7734.18	53.81	174.26
Zircon_61_080	1020.36	79.94	1596.42	424 590.48	3.61	0.47	49.36	0.27	2.99	4.87	1.22	26.51	9.91	128.89	53.14	268.00	640.51	133.49	10 216.37	291.64	427.21
Zircon_33_046	1632.46	2.73	1219.12	405 364.02	1.63	16.60	40.05	4.38	21.53	7.53	0.24	30.17	9.69	115.35	43.01	186.34	324.88	61.70	9383.98	91.93	265.90
Zircon_21_032	370.17	10.32	1396.19	371 012.36	0.93	0.24	5.80	0.32	4.01	6.27	0.33	31.52	10.48	122.09	47.06	206.99	343.72	64.39	8371.79	324.09	490.11
Zircon_38_052	1633.93	7.54	595.31	401 840.01	2.12	11.70	38.08	2.89	13.58	4.56	1.55	17.39	5.10	54.43	19.72	86.05	166.13	33.15	8058.33	92.04	271.94
Zircon_81_103	486.75	3.50	1159.47	425 861.51	3.91	7.12	19.36	2.42	13.81	8.34	1.99	30.11	9.17	105.46	40.19	185.11	368.38	73.72	9497.21	72.94	173.53
Zircon_47_063	583.94	4.63	1864.98	415 577.68	2.51	36.10	141.77	15.06	78.94	34.42	8.17	71.06	20.00	191.96	61.82	256.28	471.46	88.73	10 322.83	202.96	677.16
Zircon_24_035	209.41	7.91	452.04	370 728.39	2.25	0.67	10.97	0.65	4.93	3.16	1.64	8.05	2.81	35.02	13.92	69.62	166.42	34.05	7896.88	65.39	375.82
Zircon_30_042	1028.08	9.88	1576.39	425 583.96	0.97	0.20	3.79	0.16	2.10	3.69	0.29	23.60	9.63	126.33	51.59	249.06	510.77	99.71	9914.39	28.02	91.32

Tabla 15.: *LA-ICP-MS trace element abundances (ppm) for zircons of sample MH-50*

Zircon no.	P	Ti	Y	Zr	Nb	La	Ce	Pr	Nd	Sm	Eu	Gd	Tb	Dy	Ho	Er	Yb	Lu	Hf	Th	U
Zircon_76_099	1809.63	66.82	5907.38	423 737.06	9.20	21.39	139.56	25.65	170.30	143.48	69.48	279.32	82.28	765.27	190.83	707.91	1345.50	252.08	10 237.55	338.51	4315.39
Zircon_77_100	771.87	26.57	3371.74	445 061.74	10.38	7.13	55.83	9.28	66.45	58.34	31.16	128.81	38.35	348.77	97.86	382.06	716.55	136.14	9835.40	83.88	2681.97
Zircon_13_023	861.02	30.23	3256.88	456 970.17	6.48	7.87	87.97	11.45	81.72	72.55	39.70	155.58	44.04	380.20	97.76	339.64	591.36	115.24	8669.37	170.20	2314.70
Zircon_78_101	1627.39	71.02	6148.40	456 645.19	10.10	14.73	154.19	27.09	186.32	160.17	81.57	307.99	90.40	794.93	195.46	688.61	1238.87	241.58	9342.22	214.76	5613.79
Zircon_53_071	637.96	26.61	2194.87	467 775.60	4.53	5.44	48.96	7.36	51.58	45.36	22.70	93.92	27.91	256.62	68.26	246.69	429.47	76.16	8644.14	95.60	1058.21
Zircon_54_072	419.92	16.72	1047.08	477 639.16	3.42	1.11	4.61	0.50	3.44	2.54	1.24	8.26	4.06	65.62	31.42	179.78	544.85	134.09	11 150.52	5.88	1479.67
Zircon_61_081	565.62	7.49	988.90	459 833.49	2.10	0.11	6.53	0.18	1.80	1.96	0.79	10.52	5.10	78.06	33.35	156.99	332.21	66.54	11 170.66	15.96	957.78
Zircon_11_021	3526.20	30.22	1849.04	469 344.81	7.57	14.42	107.82	9.12	57.37	39.11	14.21	85.29	23.73	219.34	63.19	236.72	375.25	69.05	8132.00	499.46	653.16
Zircon_88_113	376.52	14.60	1946.92	447 114.39	12.75	5.92	40.03	2.04	15.36	15.88	4.50	57.71	17.12	182.87	65.51	291.00	624.07	146.60	9205.63	201.40	3575.14
Zircon_71_093	443.59	7.18	1156.63	462 156.68	3.22	0.77	21.36	1.16	9.98	10.83	5.12	32.03	9.91	108.39	37.24	160.83	332.11	69.02	9599.86	22.30	1007.59
Zircon_16_027	614.38	34.67	1194.37	476 935.26	4.19	13.19	35.15	4.40	23.75	13.59	5.38	34.77	10.95	113.95	37.76	167.61	409.84	83.15	11 308.44	58.98	725.68
Zircon_12_022	387.96	50.57	919.49	481 559.94	2.43	0.60	4.49	0.54	4.46	5.18	1.81	21.04	6.93	81.01	29.66	138.52	305.11	60.14	10 242.34	28.39	615.24
Zircon_85_109	451.87	21.09	1830.65	491 454.49	31.19	45.47	138.12	6.56	26.63	12.00	4.11	33.69	11.74	142.38	57.01	279.35	622.10	132.98	9177.68	286.62	1058.77
Zircon_8_017	529.28	12.89	1057.83	455 571.93	3.46	4.44	125.73	1.62	10.55	8.52	2.72	32.97	9.83	105.66	36.89	153.55	271.58	53.55	8540.94	48.51	367.89
Zircon_7_016	369.09	55.99	1260.66	461 728.26	8.17	1.07	26.14	1.81	14.13	14.55	6.17	39.27	12.18	125.81	41.85	179.48	368.20	73.75	7886.06	67.94	587.25
Zircon_70_091	544.40	26.18	2304.55	455 137.12	5.62	3.67	68.10	5.21	40.46	37.54	18.40	97.67	28.19	270.61	78.20	290.39	461.39	83.83	7953.29	389.18	634.05
Zircon_21_033	635.99	29.44	2932.12	445 001.89	64.85	6.38	90.45	5.45	39.06	34.15	18.30	79.04	24.94	248.69	81.59	369.21	889.01	179.13	14 790.82	2295.15	2056.39
Zircon_47_064	544.12	38.04	1428.88	469 609.71	3.41	2.62	16.70	1.41	8.71	7.21	3.48	25.66	9.50	117.63	47.08	223.60	482.78	96.23	11 782.56	101.78	717.74
Zircon_22_034	333.82	20.19	829.35	459 288.00	2.96	2.02	3.79	0.32	3.38	3.33	0.87	14.15	5.11	68.13	26.97	131.86	279.14	56.68	11 222.41	28.55	728.67
Zircon_39_054	535.65	28.66	2199.22	465 712.20	19.76	0.82	44.85	1.38	14.74	17.71	8.53	68.91	21.08	222.66	74.88	298.25	478.76	89.21	7592.01	201.57	436.81
Zircon_34_048	330.61	2.34	1508.10	464 431.21	1.59	1.88	8.21	0.61	4.97	6.95	2.02	33.86	11.52	135.05	51.98	228.91	432.02	88.17	8590.88	99.09	409.40
Zircon_42_058	155.12	394.54	1284.25	464 413.23	22.18	0.20	17.97	0.32	4.40	7.10	1.24	30.40	9.62	110.99	41.97	198.65	440.28	105.38	7996.62	88.26	667.41
Zircon_56_075	1489.87	22.57	2273.56	452 449.06	21.44	3.07	40.82	2.33	21.14	22.83	3.74	85.24	24.06	245.49	81.20	323.94	534.36	104.08	8045.26	302.99	629.52
Zircon_52_070	284.01	31.70	1622.12	491 190.73	9.38	0.19	33.19	0.60	8.83	12.40	5.61	53.17	15.23	159.48	54.86	228.94	419.18	87.91	8979.29	93.06	321.09
Zircon_38_053	231.82	76.98	1134.57	441 376.94	34.57	0.51	57.10	0.55	5.18	5.70	1.60	21.26	7.33	89.31	35.49	175.31	402.36	87.19	9934.74	1224.51	954.97
Zircon_75_097	270.13	28.78	1894.91	476 607.09	4.42	1.54	21.40	2.98	24.33	25.83	10.71	71.58	21.33	208.98	63.99	247.54	426.90	81.91	8095.41	85.51	597.03
Zircon_91_117	435.83	31.94	1197.56	459 635.27	11.58	3.49	18.83	2.53	17.41	14.54	7.49	33.87	10.70	109.32	36.27	175.23	511.81	101.55	10 891.76	96.74	857.02
Zircon_46_063	214.56	44.10	1200.79	451 271.51	3.22	0.25	7.18	0.30	4.03	6.19	0.91	29.25	9.44	111.15	42.74	189.23	367.46	74.39	9494.41	84.83	395.92
Zircon_66_087	1664.40	8.33	3186.06	462 289.53	55.75	80.91	267.00	29.70	139.38	51.24	14.49	108.82	32.47	323.90	103.43	419.55	748.97	141.65	9554.51	482.96	1386.71
Zircon_59_078	138.26	12.99	840.39	477 145.45	3.35	0.39	33.33	0.64	6.80	6.99	3.91	24.90	7.36	77.90	27.20	115.79	216.79	42.73	7183.55	89.80	168.14
Zircon_33_047	273.35	8.28	817.47	465 364.95	1.96	1.25	18.41	0.57	4.60	4.28	1.43	16.98	5.74	69.01	26.23	121.30	249.15	50.00	9593.97	143.64	323.01
Zircon_55_073	311.46	27.49	1030.07	439 754.59	7.32	0.52	42.76	0.99	8.22	8.90	4.16	29.55	9.45	101.85	34.75	148.42	278.43	55.27	7544.06	65.36	395.47
Zircon_67_088	211.11	21.28	1431.30	465 030.09	7.33	0.71	38.92	0.72	8.51	10.83	4.20	43.87	13.12	138.99	48.91	202.06	337.62	65.04	6966.20	77.68	203.24
Zircon_73_095	312.61	58.52	745.21	460 261.72	3.16	0.21	2.66	0.19	2.04	2.26	0.58	11.20	4.41	59.65	24.91	123.32	295.26	60.57	10 533.77	19.00	762.97
Zircon_2_010	150.57	23.74	674.16	469 624.00	3.55	0.61	45.53	0.44	4.95	4.58	2.29	18.62	5.57	61.69	22.17	96.21	185.58	37.19	6789.06	249.91	143.63
Zircon_40_055	16.24	21.11	559.82	482 772.72	2.66	0.07	19.27	0.26	3.08	3.01	2.08	12.45	3.77	43.12	16.75	80.13	185.71	39.86	6110.25	270.83	113.54
Zircon_44_060	319.16	8.20	701.04	466 830.47	3.47	0.85	6.69	0.61	4.04	3.17	1.14	10.28	4.62	57.48	22.81	107.43	233.22	47.13	12 353.18	42.85	859.94
Zircon_89_114	308.14	17.26	901.87	475 699.58	3.57	2.14	22.38	0.93	6.93	7.88	2.86	30.03	9.20	94.94	31.38	124.64	204.41	38.13	8201.32	36.84	206.95
Zircon_48_065	462.54	13.82	987.09	463 098.50	1.91	0.43	5.56	0.26	2.71	3.33	0.49	14.93	6.11	84.95	34.04	156.84	301.79	58.58	11 203.50	61.63	903.54
Zircon_65_085	410.65	7.84	1909.33	452 165.96	29.70	0.48	33.27	0.83	8.39	10.75	3.11	46.85	16.15	181.04	64.14	270.56	494.07	94.32	8832.75	215.74	551.19
Zircon_45_061	334.77	27.57	819.72	489 469.77	3.34	0.36	27.86	0.50	5.78	6.63	3.02	29.55	8.54	89.34	29.18	113.24	173.59	32.19	8024.36	28.77	60.87
Zircon_37_052	829.97	26.72	1475.11	475 833.50	7.02	0.56	14.40	1.59	15.77	13.06	2.82	48.61	14.37	154.00	52.33	210.58	335.87	62.01	7851.99	59.60	172.21
Zircon_79_102	61.01	215.43	1086.62	474 140.79	6.10	0.16	40.68	0.37	5.41	5.92	3.13	23.80	7.48	86.41	33.59	159.27	335.61	73.65	7121.06	233.82	284.04
Zircon_23_035	911.32	19.40	1201.52	464 751.91	6.67	31.13	84.06	11.24	55.35	18.26	2.99	35.95	9.95	107.82	38.21	175.01	376.95	73.03	10 588.36	76.14	528.91
Zircon_26_039	101.28	29.03	1045.42	456 838.55	3.78	2.68	38.63	1.24	10.35	8.92	4.51	31.21	9.00	96.58	33.83	144.48	261.71	52.44	6814.80	92.73	152.29
Zircon_90_115	243.34	15.79	1016.14	470 884.67	4.90	1.02	20.75	0.60	6.06	7.22	2.46	29.36	9.06	100.85	35.80	150.34	264.62	52.49	7314.34	37.45	71.56

(Continued)

Tabla 15 *(Continued)*

Zircon no.	P	Ti	Y	Zr	Nb	La	Ce	Pr	Nd	Sm	Eu	Gd	Tb	Dy	Ho	Er	Yb	Lu	Hf	Th	U
Zircon_86_111	1503.91	7.78	2835.60	476 818.92	3.01	3.80	34.51	1.01	6.32	5.96	1.39	32.88	15.24	216.46	90.87	446.70	985.78	189.34	13 320.25	76.97	621.43
Zircon_68_089	266.73	−0.06	971.15	468 727.76	3.19	0.68	19.77	0.55	4.78	5.18	1.59	21.27	7.10	84.14	31.70	142.08	275.75	53.79	10 401.54	547.12	800.79
Zircon_36_051	191.13	5.44	679.04	457 957.70	4.57	0.07	12.49	0.13	2.01	3.34	0.18	17.59	5.67	64.81	23.60	100.08	172.62	33.00	10 341.62	56.49	247.10
Zircon_69_090	155.45	10.48	611.89	450 390.99	5.15	0.09	2.69	0.16	2.22	3.34	0.34	14.47	4.76	55.07	20.97	94.74	208.84	41.50	12 235.76	44.31	417.95
Zircon_49_066	605.71	9.66	1172.66	466 322.52	0.62	6.25	12.67	1.50	7.78	5.50	0.41	23.54	8.85	106.27	39.47	168.60	305.11	59.44	11 355.92	18.26	500.04
Zircon_5_013	436.97	15.89	1584.93	463 335.38	3.65	1.74	58.82	0.92	6.77	6.15	1.71	27.75	9.89	123.07	50.06	243.96	525.11	110.91	9089.37	74.96	465.95
Zircon_41_057	314.56	20.22	1051.16	470 765.02	3.67	0.22	15.09	0.24	2.62	3.86	0.84	20.00	7.08	88.22	35.95	167.46	356.53	74.90	10 462.66	149.00	427.89
Zircon_14_024	346.36	4.28	2073.77	489 475.47	4.34	0.33	15.79	0.65	8.28	11.73	1.25	58.59	18.48	207.24	73.89	302.89	460.56	82.03	9224.43	53.18	470.59
Zircon_60_079	661.61	8.54	1393.38	467 642.79	1.75	0.28	10.31	0.86	10.85	14.24	1.53	55.60	15.28	152.33	48.26	187.62	283.92	52.43	8843.70	163.95	358.45
Zircon_80_103	329.41	47.68	976.61	463 164.14	4.57	0.59	7.05	0.68	5.32	5.71	2.32	21.22	7.25	85.00	31.79	151.71	340.54	69.88	10 852.28	59.18	475.34
Zircon_63_083	1242.84	16.23	2400.52	475 474.37	1.41	8.40	22.98	2.81	13.09	5.74	0.15	31.96	14.88	200.85	75.31	322.30	579.96	109.45	12 803.10	66.55	517.69
Zircon_72_094	293.11	9.77	762.72	463 432.02	2.40	0.07	4.46	0.12	2.09	3.59	0.13	19.18	6.44	74.02	26.90	113.61	197.27	37.66	10 162.33	88.49	516.92
Zircon_15_025	215.19	27.22	1212.88	465 523.49	8.94	4.62	23.04	2.13	13.13	8.80	2.04	31.35	10.05	114.14	40.63	181.54	375.68	75.70	11 555.72	80.42	395.62
Zircon_19_030	365.20	8.38	1055.17	465 681.52	3.74	0.05	13.26	0.11	1.79	3.80	0.21	21.30	7.55	92.05	35.22	155.49	281.79	53.54	11 778.54	110.95	232.42
Zircon_64_084	372.22	15.05	1058.21	466 875.64	2.21	0.18	5.88	0.19	2.73	4.46	0.15	23.19	7.94	95.80	36.07	156.87	280.23	54.38	9625.22	110.46	454.77
Zircon_29_042	744.17	9.71	433.24	457 460.66	1.83	0.22	13.14	0.45	3.71	2.41	0.72	8.32	2.61	31.83	13.21	67.41	182.96	42.48	11 686.51	146.92	421.28
Zircon_27_040	804.71	15.16	1838.49	451 300.73	1.68	0.66	2.15	0.33	3.35	7.02	1.89	45.19	16.26	180.99	61.02	251.23	439.39	83.29	11 267.24	76.26	727.95
Zircon_30_043	177.73	88.63	736.18	463 909.65	5.40	0.53	8.54	0.27	2.53	2.85	0.57	13.42	5.06	62.79	25.09	115.25	232.93	47.18	10 353.96	48.68	250.54
Zircon_28_041	357.01	23.53	732.79	467 485.97	2.68	0.61	7.98	0.50	4.55	4.45	1.23	16.34	5.26	63.39	24.26	113.03	253.94	53.04	11 326.17	72.07	253.06
Zircon_50_067	212.39	14.53	1197.92	494 554.38	3.71	0.32	4.65	0.39	3.70	5.22	1.46	25.22	8.95	110.65	41.00	176.33	332.17	64.28	10 026.65	40.45	211.41
Zircon_51_069	485.58	17.22	1195.32	470 767.48	1.98	0.07	3.35	0.09	1.88	3.57	0.30	24.66	8.50	107.07	41.60	185.07	355.35	70.62	11 902.49	71.08	229.51
Zircon_6_015	367.19	22.48	737.49	477 824.86	3.23	0.12	4.97	0.23	2.67	3.24	0.54	14.32	5.08	60.98	22.91	106.05	219.18	42.11	11 910.16	161.52	568.00
Zircon_57_076	230.05	42.56	1127.85	469 504.17	5.50	0.31	13.13	0.58	7.31	9.74	2.13	37.24	10.78	109.98	38.22	164.51	339.79	67.79	9355.52	75.68	590.14
Zircon_31_045	85.00	24.13	233.74	461 820.61	1.38	0.05	1.92	0.09	1.17	1.22	0.31	5.25	1.70	19.30	7.26	33.15	68.61	14.07	9936.59	63.50	633.29
Zircon_35_049	490.54	3.56	2195.19	471 077.73	1.64	0.83	7.93	0.27	4.77	8.13	1.17	46.94	16.23	201.01	76.88	332.16	550.87	102.59	9397.11	193.47	235.11
Zircon_83_107	77.80	7.05	205.95	467 042.41	0.89	0.02	3.20	0.05	0.68	0.49	0.19	2.29	0.93	13.51	6.19	33.78	95.61	24.14	9744.62	81.88	701.44
Zircon_82_106	59.44	10.04	257.76	475 294.44	1.50	0.02	15.71	0.06	0.89	0.92	0.42	4.81	1.58	19.65	8.08	40.39	108.79	24.17	10 517.17	147.96	607.47
Zircon_18_029	131.32	3.65	365.47	475 162.25	1.57	0.04	8.96	0.13	1.75	2.30	0.21	9.34	3.08	33.73	12.49	54.87	104.12	20.63	9617.99	46.87	108.97
Zircon_43_059	627.51	1.69	1321.47	468 633.72	2.52	0.16	8.27	0.19	1.76	2.90	0.41	20.54	8.18	103.95	41.95	195.38	422.81	89.75	12 743.01	114.15	486.50
Zircon_32_046	1517.30	5.57	1635.37	475 274.54	3.28	2.08	9.27	1.13	7.84	6.27	1.09	32.45	11.59	145.06	57.37	251.46	482.12	95.64	9734.74	57.88	286.49
Zircon_81_105	774.07	8.71	1286.53	458 202.10	1.65	7.55	62.61	2.25	12.44	8.00	2.35	33.42	10.21	113.37	41.58	185.54	364.95	74.89	9816.29	352.45	344.66
Zircon_58_077	347.30	4.81	1039.60	456 966.45	7.65	0.08	9.26	0.09	1.23	2.10	0.26	14.75	6.03	81.89	35.12	169.71	361.54	74.55	12 455.02	86.40	792.36
Zircon_74_096	358.94	11.84	1538.19	465 252.08	2.20	0.24	26.49	0.46	6.61	10.25	2.82	44.88	14.00	155.17	53.18	222.24	390.40	75.38	8771.02	86.17	292.10
Zircon_17_028	106.83	8.83	501.63	478 320.02	0.76	0.10	3.08	0.12	1.60	2.08	0.67	11.37	3.58	43.32	16.72	78.10	157.23	32.92	7216.33	38.31	166.23
Zircon_92_118	195.91	0.94	549.59	478 077.43	2.96	0.06	10.67	0.07	0.95	1.33	0.25	9.63	3.47	44.79	18.40	86.38	179.92	38.07	10 462.19	51.20	126.22
Zircon_62_082	401.78	8.57	1135.74	464 788.21	4.23	0.52	10.70	0.46	4.42	5.43	1.46	23.30	8.01	97.98	37.61	171.78	348.69	68.66	10 780.77	94.32	464.84

Tabla 16.: *LA-ICP-MS trace element abundances (ppm) for zircons of sample MH-53*

Zircon no.	P	Ti	Y	Zr	Nb	La	Ce	Pr	Nd	Sm	Eu	Gd	Tb	Dy	Ho	Er	Yb	Lu	Hf	Th	U
Zircon_94_116	929.84	36.08	1965.88	469 042.87	8.06	1.63	17.33	0.94	7.77	6.85	3.36	28.98	10.99	149.84	62.33	315.00	831.38	192.76	11 589.59	121.90	1678.39
Zircon_78_097	374.89	132.43	1144.13	479 424.77	11.07	3.70	2.14	1.67	9.31	5.81	3.24	20.49	5.73	72.66	32.96	196.52	686.96	184.41	11 473.64	12.92	644.03
Zircon_36_047	2563.50	46.22	1835.75	450 491.19	9.28	5.79	15.53	2.85	18.71	12.96	3.94	46.53	13.24	153.92	58.31	269.36	615.79	135.40	9228.10	80.52	686.51
Zircon_75_093	1498.53	6.14	927.45	482 510.18	4.77	21.20	58.24	4.49	20.10	8.37	4.16	22.07	6.81	81.96	30.00	145.84	389.48	89.85	10 701.70	138.07	602.32
Zircon_32_042	299.99	41.57	938.05	408 043.76	13.33	3.02	2.07	0.64	3.64	2.12	0.90	9.25	3.84	60.92	27.98	142.24	355.74	78.58	10 130.88	50.75	903.59
Zircon_76_095	534.75	208.93	1289.96	448 752.67	12.27	1.86	5.47	0.77	5.57	4.68	1.82	19.33	6.67	87.94	38.85	215.26	673.21	174.89	10 508.23	118.31	482.28
Zircon_99_122	380.94	71.09	1574.02	464 369.90	6.28	0.14	7.81	0.25	3.71	5.71	1.40	32.35	10.61	130.45	52.74	254.67	562.06	117.64	9436.32	84.75	334.57
Zircon_MH-53_1_008	216.34	36.80	728.17	398 414.32	4.56	0.09	12.70	0.13	1.68	2.12	0.72	10.92	3.98	53.81	22.77	119.86	371.63	94.55	8521.62	84.91	374.36
Zircon_54_068	1639.75	31.14	1086.81	460 038.89	6.73	7.59	23.25	2.64	14.87	6.43	1.08	21.54	6.87	85.48	35.42	178.77	464.87	110.15	9870.48	77.02	234.66
Zircon_50_063	186.01	577.70	232.11	431 985.53	4.12	0.14	0.49	0.15	1.70	1.71	0.70	5.60	1.62	17.43	6.92	39.05	163.98	46.79	10 433.39	9.79	158.22
Zircon_83_103	1186.95	22.39	1091.76	471 665.73	4.33	1.68	9.41	1.25	9.00	7.38	1.91	28.83	8.66	97.16	37.20	170.77	357.89	76.47	9020.12	35.09	163.93
Zircon_10_018	265.51	90.43	1150.03	379 710.04	12.63	10.89	4.12	2.31	13.44	6.79	2.46	21.89	6.38	78.52	34.31	191.90	619.55	139.89	8864.44	40.98	332.87
Zircon_38_049	1055.95	37.59	1440.81	443 330.97	5.41	4.94	44.05	2.43	17.86	14.00	7.49	47.23	12.65	132.90	44.42	195.68	427.35	97.64	9238.63	315.03	601.73
Zircon_77_096	2573.99	21.81	1292.17	459 827.74	4.04	3.63	12.71	1.96	12.83	8.98	2.32	31.50	9.81	116.27	43.80	197.18	412.12	89.13	9280.21	70.89	453.88
Zircon_93_115	551.27	11.49	1739.35	461 442.19	3.81	1.74	34.31	1.29	11.60	12.29	5.86	45.66	14.08	154.98	53.85	247.87	533.14	117.13	9783.07	426.49	741.03
Zircon_65_081	2795.25	6.44	1490.47	466 759.18	3.94	4.32	18.44	2.48	16.11	9.86	1.49	36.44	11.45	135.46	50.93	224.43	427.78	87.80	8431.75	58.72	232.69
Zircon_91_113	263.84	32.75	1349.06	463 994.46	14.55	0.27	8.08	0.28	3.71	5.77	1.46	28.62	8.59	104.50	43.22	225.89	594.81	129.82	10 374.77	49.63	209.56
Zircon_52_066	283.31	56.46	2134.20	458 696.33	6.90	0.10	5.27	0.31	4.91	8.06	1.64	46.91	14.87	180.97	71.03	324.03	672.97	147.90	8430.67	83.62	200.96
Zircon_98_121	2947.93	16.93	2012.72	466 228.28	14.12	4.85	19.19	2.65	17.35	13.86	3.35	51.85	15.04	174.88	65.14	302.86	679.02	148.86	9350.96	102.52	266.70
Zircon_88_109	623.00	5.68	938.59	469 162.56	6.58	4.29	39.32	1.32	7.08	4.89	1.77	19.25	6.31	77.09	30.11	145.58	365.64	86.05	10 516.93	237.92	647.57
Zircon_34_044	2462.05	207.61	2172.18	408 256.48	7.84	8.96	14.97	3.99	25.17	17.73	5.44	61.60	18.42	203.36	73.56	334.49	679.79	146.69	8424.22	43.25	221.27
Zircon_80_099	338.50	165.81	1455.71	452 334.46	10.18	0.24	10.43	0.36	4.17	5.58	2.05	25.90	8.41	106.34	44.82	228.88	564.23	128.32	10 347.70	181.86	345.80
Zircon_100_123	302.76	123.61	1535.17	476 982.21	15.27	0.29	13.83	0.17	2.09	3.13	0.62	18.71	7.28	101.32	48.04	270.00	681.77	148.38	11 243.62	115.47	437.82
Zircon_39_050	552.11	9.74	809.46	420 297.83	2.69	3.44	28.78	1.05	7.06	5.49	2.12	21.04	6.29	71.74	26.31	122.25	280.49	62.19	8507.02	158.34	356.91
Zircon_16_023	321.86	39.90	1845.13	400 828.65	10.79	0.29	11.46	0.49	4.88	6.57	1.14	37.66	12.86	157.68	59.78	272.81	548.06	113.97	9411.88	96.37	283.39
Zircon_72_090	765.53	34.67	4284.47	454 802.77	9.85	0.39	21.18	0.75	9.57	18.81	3.02	104.42	34.41	401.18	147.43	637.74	1112.44	220.93	8893.16	378.37	463.23
Zircon_41_053	643.60	25.21	1887.24	435 443.45	7.52	3.64	16.03	1.51	10.38	8.23	1.68	40.79	13.63	163.83	63.30	292.00	564.19	116.29	8817.01	70.54	209.35
Zircon_57_072	263.74	58.89	834.31	465 221.28	3.05	0.38	14.22	0.43	4.75	5.66	2.16	22.16	6.29	72.73	27.15	126.07	267.15	58.88	9384.29	59.12	135.01
Zircon_87_108	1272.25	13.48	1021.59	468 084.71	3.28	6.90	38.20	1.78	10.32	6.03	2.19	22.82	7.40	87.44	33.59	161.64	415.20	94.76	9937.10	166.50	399.49
Zircon_89_110	444.76	46.48	891.90	467 233.54	7.19	0.19	27.00	0.25	2.80	3.19	1.27	15.95	5.17	64.40	28.42	146.99	382.92	91.43	9918.81	233.11	469.25
Zircon_95_117	747.95	209.92	2038.19	468 834.19	6.96	21.24	7.75	7.70	48.69	27.38	13.89	76.35	19.42	184.26	61.98	283.68	619.65	135.16	8596.41	50.19	251.18
Zircon_47_060	381.73	535.05	982.04	430 871.70	11.81	0.93	5.84	0.45	3.75	3.75	1.17	18.49	6.01	76.78	32.29	161.61	376.86	82.95	7991.48	38.19	162.61
Zircon_84_104	1174.00	4.37	2096.14	478 337.56	6.27	4.02	22.96	1.46	9.67	8.32	1.57	46.44	15.84	191.62	71.92	315.57	581.96	114.07	9269.81	228.86	306.53
Zircon_86_107	462.40	119.54	2304.61	469 815.21	9.50	0.91	11.67	0.59	7.09	11.21	2.71	57.83	18.76	217.82	80.86	354.26	661.10	135.33	9189.61	104.04	220.22
Zircon_90_111	282.97	16.14	945.82	462 964.98	2.75	0.24	25.55	0.40	5.57	6.15	2.29	27.59	8.11	89.58	31.88	140.18	300.90	65.88	9100.16	165.73	281.00
Zircon_40_051	345.56	12.33	823.97	418 723.49	2.55	0.11	10.15	0.21	2.93	3.96	1.90	18.54	5.79	67.46	26.13	122.41	266.04	58.74	7651.83	102.85	263.00
Zircon_45_057	211.93	4.78	758.92	429 845.81	4.99	0.66	9.43	0.36	2.96	3.38	0.98	17.01	5.46	67.41	25.94	122.47	252.83	50.31	9197.92	30.25	101.71
Zircon_85_105	1998.57	16.50	1038.95	474 024.23	4.00	3.23	12.55	1.32	8.68	5.37	1.34	19.56	6.22	80.13	33.69	166.86	381.92	82.44	8822.80	45.34	146.35
Zircon_68_085	227.12	51.19	1178.91	443 907.64	5.54	0.14	3.58	0.17	2.41	2.92	0.67	16.99	5.86	78.92	35.98	194.36	466.30	104.91	8538.28	29.32	232.06
Zircon_79_098	1025.21	20.39	4723.43	472 613.85	15.85	7.62	36.18	3.84	29.82	29.55	5.95	145.83	44.33	495.23	173.24	708.64	1150.13	209.68	9054.40	159.22	291.42
Zircon_82_102	305.86	71.17	1628.91	457 280.18	14.25	1.69	8.38	0.56	5.17	5.91	1.52	30.45	10.06	128.36	53.55	248.83	493.64	102.64	8945.36	95.86	214.61
Zircon_9_017	2839.34	50.80	1397.22	378 782.97	13.40	4.28	19.43	2.31	13.91	7.64	1.38	24.82	8.05	103.68	43.52	210.05	425.37	88.46	6895.56	73.36	195.61
Zircon_31_041	2873.01	54.40	658.08	423 527.22	5.30	3.40	29.41	1.55	9.30	5.51	1.08	15.29	4.64	51.27	20.61	104.05	272.75	63.56	9081.29	161.17	290.90
Zircon_42_054	189.10	7.45	634.01	443 470.71	3.79	0.13	6.08	0.11	1.80	2.76	0.60	12.68	4.25	51.76	20.84	102.99	233.61	51.20	8417.82	24.03	66.02
Zircon_30_039	8411.03	27.37	1645.28	409 966.40	6.06	6.46	49.72	3.31	20.88	15.09	4.36	48.97	14.13	155.10	54.35	242.14	475.35	102.03	7927.64	211.54	300.42
Zircon_5_012	103.19	7.12	1484.14	364 755.61	6.27	0.24	6.09	0.19	3.08	5.60	1.16	34.09	11.43	140.13	52.52	222.35	375.25	71.33	8456.02	51.49	130.61

(Continued)

Tabla 16 *(Continued)*

Zircon no.	P	Ti	Y	Zr	Nb	La	Ce	Pr	Nd	Sm	Eu	Gd	Tb	Dy	Ho	Er	Yb	Lu	Hf	Th	U
Zircon_51_065	1220.50	30.16	1591.39	442 759.18	5.30	1.65	19.26	0.83	6.62	6.89	1.32	33.64	11.54	140.04	53.22	240.13	480.16	100.16	9831.82	133.20	225.25
Zircon_62_078	475.28	55.29	2264.34	454 978.34	13.51	0.07	23.10	0.30	5.11	8.68	2.11	48.79	15.84	190.89	74.54	349.50	734.38	148.98	9813.64	244.59	369.81
Zircon_19_026	2257.96	30.77	2314.41	396 223.06	8.00	4.33	29.19	2.27	15.84	12.78	2.21	54.95	17.82	201.42	78.21	350.89	694.62	145.07	8504.93	194.38	292.98
Zircon_97_120	375.96	10.94	1502.65	464 262.29	4.85	0.27	4.40	0.27	3.63	4.92	1.33	29.42	10.42	129.41	50.83	232.18	465.94	95.51	8589.09	53.62	258.49
Zircon_4_011	121.54	4.65	752.17	393 234.30	3.13	0.09	25.12	0.22	3.40	4.25	1.39	16.91	5.07	58.62	23.20	111.54	282.20	65.97	8112.84	203.00	291.90
Zircon_69_086	151.21	21.23	2381.44	450 040.03	9.61	0.04	5.72	0.24	4.47	8.06	1.82	52.63	17.73	219.35	83.60	367.32	634.30	119.61	8796.30	73.01	159.02
Zircon_81_101	2403.78	11.10	634.03	458 445.07	2.24	1.42	22.37	0.81	6.14	5.77	1.65	21.26	6.21	64.33	21.49	91.43	190.24	40.22	9549.96	102.94	179.29
Zircon_64_080	190.34	18.61	985.69	450 701.31	7.22	0.04	14.37	0.13	2.41	4.16	1.11	20.89	6.91	84.61	32.92	154.50	344.47	73.93	8712.03	79.25	138.82
Zircon_58_073	9441.94	12.84	1490.22	466 226.94	7.99	4.03	29.41	3.14	26.88	14.92	3.84	45.11	13.65	139.08	53.07	226.61	467.45	94.79	8870.00	214.30	286.80
Zircon_63_079	1262.36	79.39	1524.90	444 905.36	9.23	4.50	21.86	2.06	13.96	8.70	1.37	36.64	11.64	135.14	51.98	227.92	436.64	86.46	8108.51	136.37	207.10
Zircon_71_089	210.81	1.82	1646.07	457 072.43	9.70	0.06	9.76	0.14	2.91	5.38	1.13	33.56	11.57	148.87	57.14	257.10	462.60	91.46	8685.42	68.28	143.79
Zircon_59_074	409.00	524.08	1375.97	456 196.48	17.29	0.92	48.24	0.57	6.18	4.74	1.65	28.32	10.07	121.23	44.75	199.16	387.72	77.43	10 627.04	270.78	520.20
Zircon_35_045	2572.38	10.18	510.16	415 784.86	2.83	24.61	68.82	5.63	25.72	7.21	1.55	17.37	4.68	48.10	16.70	74.21	166.39	36.71	8700.29	114.48	180.90
Zircon_8_016	292.61	16.81	1698.37	380 313.82	3.35	1.18	11.77	0.68	7.42	10.25	2.67	50.95	15.34	169.45	59.20	246.06	435.33	83.43	6960.66	93.39	136.18
Zircon_55_069	323.65	7.29	940.76	442 222.61	5.01	0.12	38.39	0.27	3.42	4.50	1.59	19.63	6.40	77.01	29.42	139.93	336.07	72.82	9398.89	363.63	464.52
Zircon_74_092	349.85	2.71	423.99	479 202.71	2.93	1.58	27.04	0.42	3.03	2.37	0.64	8.89	2.92	35.09	13.64	65.21	158.00	34.76	10 162.97	152.94	217.49
Zircon_24_032	697.57	18.45	2985.78	402 047.37	29.83	26.67	107.84	8.78	46.73	21.54	2.12	88.77	26.74	301.13	105.52	430.52	684.72	129.24	8071.61	336.90	397.86
Zircon_25_033	3896.48	19.00	1881.76	408 514.63	7.48	6.24	26.38	3.62	24.50	17.13	2.39	58.83	17.79	193.66	68.39	280.14	447.08	82.70	7491.58	41.38	82.35
Zircon_49_062	210.78	15.18	800.25	432 194.81	3.96	0.45	21.35	0.35	3.83	4.66	2.10	20.46	6.02	69.13	25.18	118.10	263.38	57.47	9307.32	140.48	171.92
Zircon_33_043	350.42	9.62	907.75	421 599.81	4.02	0.12	11.97	0.27	3.97	4.78	1.11	23.79	7.40	86.35	32.19	139.24	259.08	52.47	7833.43	76.47	109.40
Zircon_43_055	217.60	118.72	751.74	428 266.72	2.78	0.16	15.80	0.25	3.69	4.35	1.33	19.81	6.07	69.20	25.05	110.79	232.38	48.22	9184.58	155.40	252.96
Zircon_96_119	1121.77	5.69	911.11	481 147.42	6.09	0.54	11.43	0.47	4.30	5.03	0.96	23.07	7.33	87.37	32.52	144.35	265.78	51.90	8435.81	77.72	121.38
Zircon_2_009	108.48	10.24	883.18	399 281.43	1.80	0.13	7.07	0.20	3.56	5.73	1.73	25.81	7.80	85.90	30.64	129.21	224.81	44.04	6929.43	38.96	62.70
Zircon_37_048	861.97	8.59	510.23	427 942.70	3.00	12.90	49.29	2.52	10.02	3.29	0.94	11.66	3.60	42.56	16.31	77.32	184.28	40.02	9282.96	198.11	252.17
Zircon_6_014	447.65	1.35	578.18	374 765.51	3.08	0.22	26.32	0.35	3.10	2.91	0.96	12.87	4.00	47.34	18.21	85.62	196.60	41.35	7655.98	206.22	242.35
Zircon_44_056	831.61	32.48	824.83	421 957.69	4.25	2.89	42.14	1.20	8.27	6.43	1.97	22.80	6.76	73.37	27.26	122.11	257.09	54.02	8615.12	256.76	299.89
Zircon_60_075	331.65	10.25	798.15	478 080.82	1.87	0.13	4.62	0.11	1.53	2.53	0.62	15.43	5.30	67.40	27.01	127.38	252.56	52.41	8042.95	24.40	48.97
Zircon_17_024	2585.64	6.92	1242.33	404 658.90	5.65	5.56	17.53	2.45	15.92	10.33	1.77	33.15	9.93	115.65	42.63	186.49	345.59	66.60	7361.64	98.57	130.79
Zircon_23_031	2285.23	15.67	2352.35	389 721.44	5.14	13.40	38.35	4.12	24.59	14.32	2.77	62.20	19.83	229.54	82.36	344.98	594.11	110.27	7035.54	115.03	141.47
Zircon_3_010	189.23	4.88	388.62	407 706.01	2.65	2.24	25.05	0.54	2.90	1.95	0.63	7.93	2.58	30.77	12.03	58.26	139.97	30.91	8353.35	139.32	193.76
Zircon_61_077	446.90	739.23	612.66	466 440.78	7.49	2.85	40.14	0.68	4.13	3.17	1.09	13.55	4.24	51.33	19.69	92.24	212.63	46.07	9822.56	226.30	278.99
Zircon_20_027	980.70	6.64	900.30	402 316.39	4.72	16.00	69.26	3.28	14.46	6.55	1.89	24.56	7.24	79.46	29.83	130.06	270.29	56.00	7737.52	337.24	281.29
Zircon_56_071	327.79	12.70	1569.04	478 006.01	8.90	0.13	85.19	0.62	8.65	11.27	2.91	45.68	13.33	143.76	50.65	220.61	438.11	86.03	9610.70	1174.95	683.11
Zircon_21_029	150.37	7.65	419.96	410 542.54	1.64	0.11	13.01	0.14	1.83	2.13	0.76	9.34	2.84	34.06	13.09	64.30	155.25	35.12	9321.12	72.55	165.00
Zircon_48_061	9661.91	−1.22	761.06	450 817.44	5.15	136.54	305.96	28.46	107.87	19.01	3.06	30.12	7.47	74.53	25.16	110.30	236.93	50.55	9279.35	188.76	295.69
Zircon_18_025	2496.13	4.56	2241.81	395 451.48	12.64	3.66	36.48	2.91	21.41	17.36	2.44	67.65	20.25	228.11	79.92	326.79	530.57	97.31	7496.77	143.12	171.09
Zircon_15_021	218.27	5.98	1017.04	396 811.70	3.76	0.07	8.74	0.20	2.72	4.82	1.20	25.52	8.39	97.44	35.72	149.58	266.51	50.45	6826.91	96.29	100.90
Zircon_46_059	231.26	2.84	2167.18	439 390.87	14.32	0.05	13.50	0.20	3.64	7.43	1.63	47.82	16.42	206.26	76.87	327.71	554.67	101.06	8138.46	144.94	198.14
Zircon_67_084	360.07	9.51	1130.27	456 010.90	3.39	0.26	4.28	0.27	3.27	4.93	1.11	27.41	9.04	107.05	40.67	178.49	319.64	62.39	7950.25	24.07	51.46
Zircon_29_038	1125.74	4.92	582.91	408 402.96	3.54	9.38	45.97	2.14	10.27	4.44	1.04	13.63	4.18	48.12	18.11	85.67	197.38	42.59	8393.21	229.37	254.41
Zircon_53_067	252.28	11.39	685.88	453 658.20	2.26	0.03	19.71	0.22	3.39	4.39	1.41	19.95	5.90	66.54	23.71	102.42	193.33	37.80	8647.91	91.90	109.86
Zircon_70_087	362.96	13.35	1292.17	451 006.41	6.86	0.26	17.25	0.27	4.20	6.88	1.53	33.55	10.39	120.72	43.85	189.06	356.25	70.94	8421.39	140.02	177.44
Zircon_7_015	1476.44	9.34	1431.92	392 906.38	3.42	27.59	70.35	9.63	51.27	17.52	2.55	49.03	13.34	144.77	50.01	209.17	355.19	65.94	6554.58	41.47	57.59
Zircon_27_036	899.54	10.12	889.90	407 122.15	2.89	1.93	9.03	0.79	5.28	4.23	0.82	19.54	6.58	80.43	31.03	138.92	265.50	52.81	7020.42	39.38	89.06
Zircon_66_083	594.08	5.28	1241.73	466 197.30	5.24	7.85	25.46	2.84	16.64	8.01	1.52	32.73	10.40	122.04	45.56	191.23	335.77	64.80	8110.43	31.77	58.33
Zircon_73_091	243.72	10.66	887.66	472 357.09	1.63	0.11	7.33	0.09	1.26	2.11	0.87	14.91	5.64	74.48	30.34	138.86	270.95	55.88	8246.28	36.31	66.17
Zircon_92_114	488.25	8.56	1544.55	461 833.83	4.37	0.28	5.92	0.27	3.08	5.36	1.13	32.96	11.17	142.11	54.37	238.50	426.20	82.70	8070.91	64.80	79.88
Zircon_12_020	126.33	2.99	383.86	393 703.13	1.54	0.04	11.84	0.08	1.28	1.82	0.79	8.86	2.76	33.14	12.13	56.52	127.65	26.41	7663.28	57.26	79.13

(Continued)

Tabla 16 *(Continued)*

Zircon no.	P	Ti	Y	Zr	Nb	La	Ce	Pr	Nd	Sm	Eu	Gd	Tb	Dy	Ho	Er	Yb	Lu	Hf	Th	U
Zircon_28_037	367.83	2.87	2012.91	413 904.13	2.79	0.05	2.39	0.17	2.99	5.24	0.97	40.05	14.29	176.93	69.00	302.83	544.17	105.38	7297.61	28.69	65.87
Zircon_22_030	2214.58	-1.62	293.20	403 985.88	0.67	0.37	6.64	0.28	2.30	1.90	0.78	7.18	2.21	25.07	9.48	43.15	99.27	22.35	8051.05	30.22	61.12

Tabla 17.: *LA-ICP-MS trace element abundances (ppm) for zircons of sample PET-484-1*

Zircon no.	P	Ti	Y	Nb	La	Ce	Pr	Nd	Sm	Eu	Gd	Tb	Dy	Ho	Er	Yb	Lu	Hf	Th	U
Zircon_15_024	1099.92	328.03	6239.59	11.81	21.41	170.32	29.62	189.74	138.95	47.60	300.49	86.11	773.68	216.06	852.99	1735.87	321.33	11939.36	469.18	2084.14
Zircon_11_020	1370.44	433.94	5960.92	7.76	20.23	138.29	28.65	191.20	146.54	49.42	306.74	84.76	754.92	210.86	787.24	1518.62	278.87	11294.35	395.93	1567.56
Zircon_26_038	1894.70	419.50	7865.40	13.48	38.03	219.15	42.50	265.40	187.20	61.91	392.51	111.02	994.49	270.11	1032.45	1934.55	394.33	11752.74	470.30	2432.44
Zircon_21_032	1315.37	101.38	5310.60	5.35	19.80	112.81	25.86	164.38	127.16	41.56	260.81	84.40	694.18	190.73	747.81	1487.72	299.76	11056.53	227.52	1501.69
Zircon_4_011	362.19	152.06	1908.57	3.63	6.29	41.13	7.61	49.80	35.86	12.37	83.78	24.82	225.68	66.39	265.26	530.78	102.60	11484.93	178.92	442.36
Zircon_28_040	437.44	115.91	1843.02	5.43	12.32	46.45	6.78	39.98	25.83	8.26	68.01	20.04	197.93	62.97	272.61	541.34	111.72	11864.93	290.75	485.04
Zircon_31_044	1435.76	90.26	4096.72	7.26	122.93	153.90	54.00	150.67	84.55	31.75	214.51	58.44	512.47	137.83	538.54	1189.89	270.04	9979.72	366.71	1113.41
Zircon_17_027	432.60	55.18	2270.08	4.82	5.98	53.90	7.48	48.56	37.70	12.77	89.83	26.92	256.72	78.77	324.47	660.47	129.26	11976.90	243.44	624.72
Zircon_37_051	556.98	177.34	2623.45	4.02	5.74	39.59	7.58	50.24	37.76	13.58	96.88	29.18	284.25	89.32	376.11	778.92	160.01	11859.32	163.97	594.67
Zircon_2_009	566.81	88.36	2529.70	2.10	4.63	31.59	6.45	43.82	37.86	12.98	97.21	27.96	268.10	83.44	342.42	667.88	137.31	9327.44	118.43	430.66
Zircon_6_014	447.87	251.11	1859.56	7.17	8.45	63.95	9.71	59.69	40.75	14.54	88.08	24.98	226.35	64.03	254.79	542.22	107.99	10695.60	256.96	773.34
Zircon_24_035	606.65	192.48	2164.55	6.99	6.15	56.66	7.57	50.53	46.72	14.24	120.81	32.71	300.00	79.00	309.57	610.36	114.38	11567.75	277.23	598.12
Zircon_25_036	467.19	155.28	2533.28	7.99	6.01	60.18	8.41	59.04	46.52	18.31	125.66	32.95	292.55	85.07	356.24	789.08	168.42	13144.88	457.91	993.86
Zircon_38_052	783.18	108.79	2737.44	5.07	8.22	63.97	10.17	65.37	52.50	19.21	130.33	38.14	346.60	97.50	377.76	751.04	150.47	12523.03	344.99	814.81
Zircon_10_018	285.26	22.29	1461.74	2.10	2.66	20.55	3.21	23.99	18.58	6.15	54.31	15.44	161.26	51.33	212.84	414.87	78.04	11343.38	146.39	210.23
Zircon_3_010	461.17	354.13	2246.04	10.68	5.67	61.96	7.42	48.04	38.38	13.49	92.37	26.32	252.18	75.70	308.83	630.37	127.40	12274.94	279.57	864.45
Zircon_16_026	677.13	33.86	2152.26	5.84	6.97	66.64	6.37	44.61	39.74	14.34	109.30	29.48	260.21	73.81	295.64	618.19	130.64	11827.31	287.86	614.20
Zircon_18_028	884.54	24.73	3128.22	3.17	4.42	31.43	6.31	77.47	49.99	20.34	151.67	38.40	330.30	101.27	400.10	771.81	161.65	10674.97	193.74	395.36
Zircon_5_012	388.40	97.38	1724.59	7.32	3.21	47.13	4.53	29.70	24.09	7.94	53.90	16.35	167.74	55.85	262.67	666.76	150.87	11657.35	277.05	797.18
Zircon_19_029	280.48	14.22	2006.76	4.24	1.69	23.55	2.08	17.40	14.37	5.25	51.69	16.92	189.74	68.50	300.40	581.31	112.25	11291.44	235.51	271.49
Zircon_13_022	485.38	27.78	2777.64	12.06	4.63	77.17	5.38	38.66	33.36	11.92	103.27	30.30	296.70	92.87	368.60	668.41	134.45	13495.72	650.32	888.16
Zircon_20_030	590.54	25.82	1934.83	6.92	1.85	45.57	2.60	21.49	21.96	8.25	71.02	20.02	203.50	66.08	280.76	602.13	129.74	12685.53	213.56	526.81
Zircon_12_021	636.84	19.67	2399.70	5.02	8.84	74.38	4.39	32.61	30.97	11.58	112.43	29.70	268.55	81.90	327.86	586.52	123.58	10429.68	405.84	477.59
Zircon_40_054	279.59	77.81	1081.76	3.63	1.38	31.91	2.12	19.14	15.00	5.50	41.80	11.55	111.93	36.79	161.48	356.37	73.49	13167.34	168.10	391.23
Zircon_9_017	141.54	34.75	1226.74	6.97	2.04	35.43	1.72	12.19	11.54	4.02	37.20	12.11	120.80	40.53	174.08	372.56	76.65	13070.88	192.86	448.91
Zircon_33_046	217.10	19.43	817.37	1.48	1.02	12.24	1.33	9.22	8.42	2.79	23.30	7.25	79.46	27.86	129.19	272.00	56.60	12166.56	47.40	142.05
Zircon_29_041	273.60	89.68	1723.46	9.44	12.35	59.44	3.51	21.19	15.65	5.53	52.08	16.32	173.22	58.11	254.36	542.16	109.62	12926.78	240.35	584.68
Zircon_41_055	251.17	155.41	1157.27	9.22	1.35	34.55	1.70	12.18	10.31	3.72	33.19	10.27	111.02	38.88	174.77	391.43	79.70	13760.96	175.42	511.52
Zircon_1_PET-484-1_008	240.63	20.41	1496.52	8.47	0.91	40.82	1.41	11.74	11.41	4.56	43.07	12.76	140.96	49.21	213.95	435.95	85.16	10066.13	244.18	425.23
Zircon_23_034	248.31	16.79	887.19	1.88	1.96	12.90	0.91	5.35	4.55	1.65	19.25	6.45	79.26	30.06	140.40	309.60	64.12	11452.98	65.40	103.28
Zircon_30_042	73.58	19.35	1101.61	2.06	0.31	18.36	0.44	5.50	7.00	3.12	31.86	9.66	105.16	36.56	159.68	316.18	65.25	12068.65	146.68	187.04
Zircon_22_033	227.73	9.71	1998.75	3.30	1.12	61.25	2.70	27.62	24.38	10.55	72.35	19.85	196.62	64.40	273.90	581.44	115.32	9129.71	697.99	496.40
Zircon_7_015	153.86	−0.96	918.61	3.50	0.83	36.66	1.34	12.79	11.66	3.42	31.74	8.71	89.91	29.76	130.23	273.45	54.65	12379.56	167.11	264.89
Zircon_34_047	759.53	0.94	2757.22	22.71	2.64	122.40	3.86	19.07	24.42	9.14	99.73	28.08	287.82	93.81	376.96	673.22	124.41	12115.95	1109.40	840.94
Zircon_8_016	51.64	54.27	820.14	4.64	3.23	29.27	0.78	6.15	6.19	2.05	23.83	7.01	76.42	26.65	119.54	253.53	51.50	11202.18	126.18	252.82
Zircon_39_053	587.48	11.59	2013.81	10.26	8.91	84.50	2.35	13.91	11.96	3.60	51.29	15.95	183.31	67.24	301.21	630.99	125.07	12502.88	924.20	844.53
Zircon_14_023	144.82	8.56	703.67	3.54	0.05	26.51	0.19	2.72	3.51	1.12	16.06	5.13	60.84	22.88	108.39	249.86	52.13	12456.37	185.32	232.52

Tabla 18.: *LA-ICP-MS trace element abundances (ppm) for zircons of sample TEP-474-3*

Zircon no.	P	Ti	Y	Nb	La	Ce	Pr	Nd	Sm	Eu	Gd	Tb	Dy	Ho	Er	Yb	Lu	Hf	Th	U
Zircon_15_024	24 037.57	31.09	2425.88	1.84	18.46	68.33	9.25	49.51	29.63	5.04	61.84	21.51	242.20	83.85	370.11	785.84	143.24	10 715.19	596.50	656.16
Zircon_85_108	1979.45	4.07	909.07	1.87	0.27	26.04	0.18	2.66	3.59	1.04	17.74	6.00	74.88	29.72	143.05	336.77	72.41	12 534.08	120.05	214.92
Zircon_31_044	1101.83	9.65	893.74	1.31	0.04	11.62	0.14	2.73	4.16	0.80	19.96	6.55	79.39	29.88	136.74	269.25	55.09	9635.92	67.64	101.25
Zircon_56_074	2602.21	8.27	941.71	2.21	0.07	11.83	0.13	1.95	2.99	0.82	14.91	5.22	68.95	29.60	153.87	399.42	90.21	10 506.26	51.15	104.74
Zircon_61_080	2665.55	11.63	710.92	1.37	0.05	17.57	0.13	1.95	2.77	0.69	14.32	4.92	59.68	23.75	113.91	259.91	54.12	10 800.41	53.90	95.69
Zircon_93_118	–	6.22	535.66	1.10	1.81	14.60	0.47	3.33	2.16	0.84	10.60	3.30	40.89	16.44	83.08	216.96	52.33	12 281.32	71.51	173.01
Zircon_37_051	–	4.87	838.38	1.42	0.05	23.14	0.11	1.73	3.12	1.99	21.06	6.82	75.67	26.77	120.41	268.72	60.74	10 905.55	106.03	179.12
Zircon_84_107	2942.01	161.49	777.07	3.05	0.33	26.77	0.30	2.46	2.61	0.98	13.34	4.55	59.68	24.73	128.64	323.15	71.19	11 679.92	101.03	199.22
Zircon_43_058	976.19	1.96	693.59	1.31	0.06	9.78	0.11	1.80	2.25	0.67	12.28	4.18	53.79	22.12	108.72	267.29	58.68	10 432.64	130.17	268.58
Zircon_42_057	1793.48	9.01	1305.52	1.97	0.06	26.12	0.11	2.38	4.78	1.60	28.88	9.63	115.65	43.84	197.23	400.15	84.58	11 134.01	268.71	382.63
Zircon_97_123	1344.92	−2.52	581.30	1.65	0.08	15.20	0.09	1.42	1.61	0.73	9.22	3.15	41.79	18.06	95.89	262.87	61.33	12 596.06	87.60	199.74
Zircon_69_089	6473.12	−2.39	330.65	0.42	0.20	5.08	0.22	2.26	1.72	0.60	7.30	2.39	27.95	10.82	52.97	129.66	30.07	11 691.04	21.14	45.97
Zircon_10_018	3209.46	−5.71	1663.49	1.76	0.09	6.96	0.13	2.16	3.70	0.64	26.20	10.19	138.15	58.11	282.31	584.63	118.45	9351.13	119.86	183.45
Zircon_29_041	1467.77	−5.33	974.40	1.87	0.05	10.56	0.12	2.04	3.18	0.41	17.37	6.17	81.07	33.44	156.79	330.34	66.94	9817.12	53.04	84.17
Zircon_46_062	5781.18	15.93	1064.79	0.97	0.04	6.05	0.14	2.46	4.56	0.93	24.40	8.37	101.64	37.86	166.47	312.56	60.00	10 132.61	38.54	53.80
Zircon_72_093	3550.18	34.01	719.99	1.64	0.12	11.81	0.49	7.83	11.43	0.71	38.28	9.80	88.55	25.92	96.15	150.59	26.41	12 142.05	141.30	100.17
Zircon_70_090	738.74	13.09	854.28	2.22	0.04	14.08	0.15	2.66	3.82	1.22	15.78	5.07	63.33	26.26	132.71	346.11	80.51	11 711.56	139.17	258.17
Zircon_83_106	6041.04	121.56	976.81	2.26	2.98	12.25	1.35	9.55	10.69	1.97	44.20	12.09	112.22	31.42	109.18	165.13	28.83	13 099.81	96.91	745.36
Zircon_25_036	7310.17	10.59	1916.84	86.59	2.48	47.19	4.61	30.96	25.35	3.51	51.38	18.34	206.70	70.92	363.36	1203.84	272.10	18 905.57	250.56	3037.94
Zircon_34_047	1740.83	−2.75	591.98	1.93	0.05	9.25	0.16	2.32	3.20	0.87	14.24	4.60	52.12	19.32	88.45	191.19	38.50	10 147.11	97.53	221.85
Zircon_41_056	1036.51	11.78	171.23	0.76	0.02	2.15	0.14	2.13	3.74	0.15	13.52	3.02	22.04	5.61	18.75	29.79	5.98	13 620.24	48.15	333.80
Zircon_2_009	189.97	10.11	454.03	2.82	0.27	8.84	0.24	3.20	3.78	0.40	14.01	4.27	47.27	16.32	69.89	122.77	22.59	6892.64	31.87	130.82
Zircon_49_065	3832.06	5.02	839.62	1.59	0.15	5.87	0.18	2.12	2.86	0.35	16.80	5.77	71.94	28.42	131.19	268.00	54.55	11 442.77	102.64	538.44
Zircon_91_116	12 950.14	19.69	1877.87	3.00	6.41	22.14	2.74	16.91	10.87	0.74	45.37	15.25	180.53	66.84	296.39	542.77	103.35	11 169.57	225.75	636.84
Zircon_90_114	3794.50	−1.69	1143.34	14.48	8.62	36.11	2.86	16.11	7.74	0.70	30.79	9.70	112.87	40.81	180.75	337.70	63.38	11 527.63	195.52	715.36
Zircon_26_038	35.87	−0.33	455.02	1.55	0.08	8.79	0.15	2.20	2.75	0.49	11.81	3.74	42.85	15.78	70.57	143.97	28.94	10 454.20	67.36	244.03
Zircon_74_095	–	48.92	642.88	1.40	0.04	9.07	0.18	3.34	4.46	1.18	17.49	5.17	55.93	20.61	93.15	190.24	37.81	10 032.83	80.73	142.96
Zircon_23_034	14 278.56	18.21	597.04	2.98	6.64	29.65	3.21	18.30	7.00	0.49	16.55	5.01	56.86	20.86	93.89	191.88	37.27	10 916.50	77.35	249.02
Zircon_62_081	2629.25	4.33	623.18	2.73	0.02	6.17	0.11	1.77	2.62	0.26	14.82	5.10	61.00	22.03	96.00	172.58	32.53	10 861.99	38.10	118.28
Zircon_48_064	6413.17	3.94	1088.90	2.18	0.05	3.49	0.11	2.04	4.57	0.19	26.53	9.16	103.02	35.96	149.47	257.71	47.86	15 569.67	168.90	761.62
Zircon_99_125	2087.41	−6.21	494.12	1.84	0.01	7.16	0.09	1.73	2.13	0.37	10.88	3.70	44.58	16.89	79.48	170.51	34.22	11 213.95	56.10	217.47
Zircon_11_020	–	10.69	767.67	2.33	0.07	7.08	0.29	5.10	7.01	0.94	28.27	7.97	84.50	28.00	111.94	187.12	33.79	9183.00	38.38	81.27
Zircon_89_113	1633.48	9.20	613.76	4.82	80.73	147.39	14.59	59.80	11.11	0.89	20.62	5.70	62.27	22.44	94.93	169.35	31.43	11 667.44	46.54	157.10
Zircon_1_TEP-474-3_008	–	−4.87	329.08	1.76	0.03	3.78	0.07	1.37	1.74	0.12	7.73	2.67	30.48	11.37	50.18	94.75	18.05	9724.60	24.56	91.98
Zircon_71_092	1986.26	−0.28	617.55	1.71	0.05	4.53	0.12	2.97	4.58	0.32	19.93	6.00	66.13	22.55	92.82	156.53	28.75	10 873.80	52.44	208.98
Zircon_78_100	3215.36	10.01	408.87	2.16	0.05	3.90	0.10	1.58	1.84	0.36	10.24	3.51	40.49	14.61	62.68	124.19	23.94	9922.69	11.17	76.40
Zircon_28_040	1889.60	20.96	514.80	2.11	0.04	3.57	0.09	1.77	2.47	0.27	12.60	4.14	50.93	18.45	79.64	143.20	27.34	9788.82	23.45	75.73
Zircon_98_124	1777.33	10.97	860.78	1.91	0.07	6.90	0.28	4.30	6.57	0.20	27.55	8.38	91.63	31.09	128.68	218.38	39.81	11 609.86	125.91	314.77
Zircon_53_070	22 078.54	−3.75	1606.15	4.38	76.56	188.50	24.70	117.20	31.03	2.06	62.58	16.77	173.23	59.15	243.10	411.33	75.28	11 211.92	96.86	299.69
Zircon_52_069	1486.00	3.00	342.97	1.57	0.04	3.64	0.09	1.39	1.57	0.14	7.69	2.78	31.76	12.14	53.49	102.50	19.57	10 997.02	16.96	71.62
Zircon_100_126	9258.76	16.49	595.34	2.20	12.55	41.42	4.11	20.08	6.67	0.62	16.12	5.02	58.40	21.14	95.85	195.82	38.55	12 173.92	57.21	154.33
Zircon_92_117	3437.95	8.66	941.59	33.91	0.03	112.20	0.10	1.88	2.83	0.17	16.00	5.89	76.38	30.91	150.01	340.78	70.33	12 079.20	73.26	283.62
Zircon_4_011	312.04	0.03	228.87	0.88	0.06	2.78	0.09	0.91	0.69	0.19	2.82	1.00	13.51	6.13	34.16	94.68	21.16	8895.31	61.23	472.03
Zircon_86_110	3829.92	17.27	804.24	1.55	3.80	16.49	1.34	9.80	8.54	1.17	29.32	8.65	91.14	29.89	121.08	205.34	37.69	10 278.70	47.25	90.79
Zircon_16_026	1260.00	35.63	627.32	2.59	0.07	3.25	0.20	2.98	4.26	0.43	18.86	5.69	62.50	22.26	92.26	165.77	31.08	9350.73	15.01	46.48
Zircon_63_082	4469.09	28.41	556.96	1.77	0.30	18.57	0.30	3.86	4.67	1.35	17.86	5.13	54.56	19.03	82.06	158.97	31.27	9693.27	42.67	54.70

(Continued)

Tabla 18 *(Continued)*

Zircon no.	P	Ti	Y	Nb	La	Ce	Pr	Nd	Sm	Eu	Gd	Tb	Dy	Ho	Er	Yb	Lu	Hf	Th	U
Zircon_50_066	1021.56	11.79	1183.65	1.90	0.05	11.31	0.30	4.93	8.40	1.44	37.00	11.38	123.22	42.44	175.31	293.33	54.93	10 251.93	63.75	119.29
Zircon_44_059	2229.56	10.90	1117.42	0.96	1.97	11.98	0.87	9.44	11.26	1.85	44.76	12.30	123.85	40.12	158.58	254.14	46.47	9641.38	73.90	148.77
Zircon_40_054	1286.91	−4.45	849.27	1.56	0.08	3.82	0.30	5.04	7.20	0.91	28.73	8.68	91.74	30.88	124.76	206.20	38.31	9892.84	26.43	67.89
Zircon_6_014	–	8.93	927.91	3.38	0.17	7.01	0.26	4.11	6.07	0.50	28.50	8.71	95.49	33.06	136.35	230.58	42.74	9610.69	77.72	158.44
Zircon_94_119	3679.73	4.91	960.59	1.98	0.08	11.32	0.42	5.89	8.67	1.09	33.27	10.03	105.10	35.32	143.12	246.02	45.29	10 065.75	73.04	155.47
Zircon_87_111	1661.88	7.62	980.41	1.70	0.07	4.38	0.30	4.86	7.29	0.50	34.36	10.13	106.76	35.72	141.41	217.63	39.08	10 179.98	96.67	290.56
Zircon_67_087	3072.78	15.96	949.21	1.24	0.09	8.80	0.42	6.53	8.43	1.33	33.16	9.52	99.47	34.04	136.64	221.33	40.72	9784.23	52.75	113.15
Zircon_75_096	7757.43	8.66	1327.46	1.24	0.24	2.80	0.22	3.25	6.36	0.35	34.19	11.20	129.74	47.30	200.51	348.85	64.64	10 929.78	77.63	199.14
Zircon_59_077	2825.14	2.34	1040.69	1.74	0.11	4.68	0.40	6.73	9.77	0.91	39.33	11.20	114.10	37.31	148.38	239.37	44.56	10 203.01	39.53	151.05
Zircon_30_042	226.62	7.36	390.77	1.96	0.06	9.61	0.10	1.76	2.18	0.31	9.84	3.31	37.89	13.61	60.70	116.56	22.53	10 569.20	31.52	92.21
Zircon_95_120	4555.63	10 142.22	829.98	16.96	0.14	2.24	0.17	1.85	2.81	0.10	15.76	5.78	73.46	28.60	129.59	251.09	47.85	12 156.03	46.13	165.48
Zircon_76_098	2289.15	16.53	565.53	2.70	0.05	6.52	0.16	2.32	3.50	0.45	15.69	4.81	55.92	20.32	86.97	161.34	30.64	11 324.85	25.40	94.60
Zircon_21_032	–	12.09	358.96	2.60	0.03	3.25	0.07	1.32	1.98	0.29	8.66	3.07	35.86	13.08	56.25	105.95	20.48	9940.39	5.73	43.32
Zircon_65_084	–	14.18	229.55	2.72	0.05	39.80	0.06	0.98	0.85	0.30	4.21	1.34	17.40	7.19	37.00	95.76	20.13	10 408.17	101.59	139.72
Zircon_39_053	5527.74	5.37	1410.25	1.82	0.84	6.58	0.23	2.78	4.52	0.27	26.60	9.70	121.29	47.50	217.03	413.03	78.89	11 809.87	153.45	581.85
Zircon_13_022	7735.82	9.42	1507.18	1.10	0.10	2.35	0.13	2.40	4.15	0.14	28.43	10.62	133.72	51.68	233.87	429.79	81.42	11 246.25	71.78	244.52
Zircon_20_030	2593.06	14.69	1269.17	2.00	0.09	10.06	0.49	7.54	10.23	0.92	42.50	12.29	129.80	45.01	183.18	300.21	54.48	9901.14	111.03	205.35
Zircon_5_012	4118.78	9.54	999.80	2.70	6.39	18.96	1.96	9.32	4.02	0.21	15.27	6.11	80.87	33.46	164.97	385.53	78.46	11 262.42	77.15	466.55
Zircon_32_045	1108.07	5.48	539.85	1.33	0.06	2.40	0.13	1.70	2.38	0.16	11.61	3.95	46.38	17.67	82.73	179.02	36.51	10 582.31	104.73	396.62
Zircon_58_076	4726.95	0.92	1614.43	1.54	0.09	2.82	0.21	3.58	6.42	0.43	35.08	11.99	147.32	56.42	250.69	471.66	91.70	10 976.85	115.80	451.41
Zircon_64_083	2217.85	4.11	659.62	1.14	0.01	5.36	0.09	1.36	1.98	0.15	11.60	4.58	56.73	22.48	103.29	199.13	38.65	12 984.34	74.08	260.27
Zircon_96_122	870.33	3.24	884.46	1.82	0.76	9.05	0.32	4.42	6.05	0.59	26.41	8.28	90.76	31.76	132.63	232.68	43.41	10 307.57	74.44	159.34
Zircon_36_050	6867.80	11.64	1377.03	4.12	0.04	6.19	0.10	1.47	3.03	0.09	21.39	9.00	119.49	46.34	210.89	428.06	84.05	13 066.59	122.70	469.73
Zircon_57_075	2801.53	7.20	1164.80	2.00	0.04	9.06	0.12	2.29	4.48	1.22	27.16	9.00	106.66	39.43	170.74	328.55	65.46	10 930.79	78.40	310.85
Zircon_47_063	1586.44	5.70	608.24	2.00	0.06	10.67	0.18	2.84	4.28	0.50	18.24	5.63	62.70	21.71	93.20	170.65	31.67	10 650.32	49.49	118.89
Zircon_66_086	8916.97	13.29	1847.85	1.64	0.07	3.44	0.19	3.61	6.46	0.26	38.93	13.82	170.21	64.48	287.36	523.70	99.50	12 517.18	126.70	370.68
Zircon_55_072	1129.19	8.15	826.43	2.08	0.18	5.08	0.27	3.65	5.73	0.57	24.11	7.53	82.73	29.33	123.57	218.94	40.75	10 630.54	48.13	149.36
Zircon_88_112	4669.77	12.75	707.76	2.90	4.80	27.72	1.32	7.17	3.77	0.66	15.42	5.13	63.48	24.62	114.94	247.75	49.09	11 005.26	52.44	117.86
Zircon_51_068	30 833.26	17.35	518.41	1.76	15.96	65.64	9.05	49.10	14.41	2.16	26.09	6.51	60.26	19.00	74.28	124.38	22.57	10 822.59	16.13	44.16
Zircon_22_033	2654.70	12.47	1879.79	2.08	0.06	6.51	0.23	3.73	6.95	0.22	38.75	13.76	169.54	65.25	289.96	518.18	96.63	11 471.54	253.65	663.02
Zircon_68_088	31 262.24	3.16	1371.03	1.17	6.95	35.64	5.96	36.55	14.76	0.59	40.77	11.81	131.38	47.89	205.96	355.00	66.01	11 249.76	106.38	281.19
Zircon_18_028	1243.31	14.78	1000.63	1.23	0.05	3.48	0.25	5.08	7.68	0.64	31.81	9.61	101.70	35.60	149.40	260.06	48.47	9899.10	31.43	75.10
Zircon_38_052	4391.19	8.31	658.68	1.25	0.04	7.14	0.27	4.50	5.69	1.20	23.56	6.78	71.31	23.60	95.90	167.22	30.94	9622.29	25.20	58.52
Zircon_17_027	1707.73	9.74	955.39	2.08	0.04	4.67	0.17	2.77	4.53	0.36	24.00	7.83	92.72	34.05	146.46	254.64	46.81	10 001.02	27.25	62.21
Zircon_7_015	2746.55	1197.54	1221.62	2.64	5.81	21.88	3.19	18.74	9.54	1.05	34.86	10.50	118.28	43.20	182.85	327.04	61.96	8134.19	70.12	159.58
Zircon_60_078	2388.83	5.81	869.62	2.04	0.07	5.61	0.13	2.57	4.23	0.35	21.17	7.18	82.18	30.61	133.93	245.57	46.28	11 070.56	46.84	151.64
Zircon_27_039	1731.84	6.41	583.29	2.55	0.03	5.93	0.11	2.11	3.00	0.23	15.47	5.11	57.88	21.33	91.33	166.29	31.41	10 482.18	42.49	80.98
Zircon_73_094	38 361.58	73.74	804.34	2.30	30.05	122.27	21.58	127.79	36.04	1.95	47.57	9.39	87.15	28.68	118.90	209.06	38.92	10 682.77	46.41	128.94
Zircon_77_099	11 004.84	11.60	3119.58	2.04	0.05	4.72	0.42	6.96	13.24	0.43	75.47	25.76	303.28	112.57	477.51	802.26	147.08	11 634.82	277.91	669.09
Zircon_80_102	2043.59	−4.94	699.08	1.46	0.03	7.59	0.10	2.09	3.15	0.44	16.97	5.34	64.31	24.22	109.67	221.85	44.36	11 497.74	36.64	88.12
Zircon_3_010	1458.83	12.65	1127.36	1.38	0.08	3.14	0.16	2.61	4.59	0.21	23.81	8.43	101.96	38.89	172.06	310.59	57.54	9818.16	88.33	262.28
Zircon_24_035	3633.19	6.30	1435.28	1.22	0.12	6.91	0.58	9.50	14.00	1.60	54.98	15.68	160.41	51.71	205.79	327.94	57.83	9844.39	44.47	77.75
Zircon_79_101	3488.69	−6.55	3133.15	31.81	0.67	28.02	0.60	5.62	9.34	0.98	63.72	24.01	304.03	116.15	509.10	852.43	152.96	12 526.58	205.14	716.07
Zircon_35_048	6840.88	3.47	1301.83	1.84	0.05	13.33	0.11	1.94	3.20	0.57	21.60	8.37	111.83	45.86	222.36	510.39	105.62	12 414.61	91.97	410.74
Zircon_12_021	1398.60	15.67	1036.93	1.40	1.87	29.14	0.90	9.16	10.22	3.25	38.24	10.55	108.29	36.57	148.17	253.83	47.63	8362.94	82.63	104.78
Zircon_8_016	1998.57	27.00	567.01	1.98	0.44	13.19	0.20	2.08	2.17	0.29	10.82	3.86	48.60	19.23	92.18	202.94	40.09	9595.27	42.13	83.05
Zircon_14_023	6388.82	25.40	1703.83	2.64	9.78	36.35	3.51	18.42	7.94	0.51	32.59	11.45	147.53	59.24	273.22	526.67	102.27	9990.25	92.03	237.01
Zircon_54_071	–	12.02	904.59	1.20	0.04	5.84	0.18	4.20	6.23	0.97	27.67	8.53	95.01	33.66	145.94	270.16	54.58	8227.16	18.39	40.67

(Continued)

Tabla 18 *(Continued)*

Zircon no.	P	Ti	Y	Nb	La	Ce	Pr	Nd	Sm	Eu	Gd	Tb	Dy	Ho	Er	Yb	Lu	Hf	Th	U
Zircon_19_029	2723.59	13.56	769.55	2.47	0.10	25.17	0.13	2.03	2.83	0.54	14.18	5.22	66.29	25.89	125.30	277.26	55.15	10 335.36	75.39	130.97
Zircon_33_046	230.42	0.74	644.70	0.74	0.13	3.70	0.62	8.44	8.82	1.69	30.92	7.68	72.61	23.29	91.40	149.94	28.09	8210.78	33.45	48.52
Zircon_45_060	1363.75	6.52	523.25	1.62	0.04	10.80	0.08	1.37	1.76	0.22	9.70	3.48	44.58	17.96	85.39	174.91	34.52	11 311.31	57.80	119.60
Zircon_82_105	2677.43	-5.20	907.15	2.25	0.04	5.50	0.12	1.79	3.19	0.10	18.66	6.44	82.04	31.90	143.77	270.27	50.92	12 137.77	155.78	423.11
Zircon_9_017	12 657.96	14.44	3268.34	6.67	0.12	12.80	0.62	10.10	15.93	2.75	88.61	28.28	321.13	117.40	486.94	792.40	146.68	8841.52	313.91	307.03

B

TABLAS GEOQUÍMICA

Tabla 19.: *Sample list of amphibolite for XRF, ICP-MS, and Sm-Nd isotopic analyses*

Sample	Longitude	Latitude	Rock type	XRF	ICP-MS	Sm–Nd
AYU-457-3	W97°47′14″	N17°56′20″	retrogr. amphibolite	•		
AYU-458-1	W97°47′44″	N17°57′42″	amphibolite	•		
AYU-458-2	W97°47′44″	N17°57′42″	Pl-amphibolite	•	•	•
AYU-458-3	W97°47′44″	N17°57′42″	Pl-amphibolite	•		
AYU-458-4	W97°47′44″	N17°57′42″	Pl-amphibolite	•		
AYU-459-1	W97°47′42″	N17°57′41″	amphibolite	•		
AYU-460-2	W97°47′41″	N17°57′43″	retrogr. amphibolite	•	•	•
AYU-462-1	W97°47′29″	N17°57′43″	amphibolite	•	•	•
AYU-462-2	W97°47′29″	N17°57′43″	amphibolite	•	•	•
AYU-464-1	W97°47′26″	N17°57′42″	Qtz-amphibolite	•	•	
AYU-464-2	W97°47′26″	N17°57′42″	amphibolite	•		
AYU-465-1	W97°47′20″	N17°57′40″	amphibolite	•		
AYU-466-1	W97°47′15″	N17°57′39″	amphibolite	•	•	•
AYU-468-1	W97°45′55″	N17°59′26″	amphibolite	•		
AYU-469-1	W97°48′38″	N18°00′01″	amphibolite	•		
AYU-469-2	W97°48′38″	N18°00′01″	amphibolite	•	•	•
MH-5	W97°44′58″	N18°10′58″	retrogr. Qtz-amphibolite	•		
MH-6	W97°47′16″	N17°56′19″	Pl-amphibolite	•		
MH-17	W97°45′38″	N18°09′19″	Pl-amphibolite	•	•	
MH-18	W97°44′58″	N18°10′58″	amphibolite	•	•	
MH-30	W97°47′20″	N17°57′41″	Qtz-amphibolite	•	•	•
MH-32	W97°47′15″	N17°57′40″	Qtz-amphibolite	•	•	•
MH-48	W97°44′56″	N18°10′55″	amphibolite	•	•	•
MH-75	W97°45′38″	N18°09′19″	retrogr. Pl-amphibolite	•	•	•

Tabla 20.: *Sample locations of metasedimentary rocks for XRF, ICP-MS, and Sm-Nd isotopic analyses*

Sample	Longitude	Latitude	Rock type	XRF	ICP-MS	Sm–Nd
AYU-456-1	W97°47′09″	N17°56′13″	metapsammite	•		
AYU-456-2	W97°47′09″	N17°56′13″	metapelite	•		
AYU-460-1	W97°47′41″	N17°57′43″	semi-pelite	•	•	
AYU-461-1	W97°47′39″	N17°57′43″	Hbl-Bt schist	•		
AYU-M4-1	W97°49′56″	N18°02′32″	metapelite	•	•	
AYU-M4-2	W97°49′56″	N18°02′32″	semipelite	•	•	
MH-2	W97°47′11″	N17°56′11″	metapsammite	•	•	
MH-4	W97°45′51″	N18°10′13″	psammite	•	•	

(Continued)

Tabla 20 *(Continued)*

Sample	Longitude	Latitude	Rock type	XRF	ICP-MS	Sm–Nd
MH-7	W97°44′14″	N18°10′30″	semipelite	•	•	
MH-37	W97°43′35″	N18°10′19″	metapsammite	•	•	
MH-41	W97°47′13″	N17°56′13″	metapelite	•	•	•
MH-42	W97°47′12″	N17°56′12″	metapsammite	•	•	•
MH-46	W97°47′11″	N17°56′11″	metapelite	•	•	
MH-50	W97°47′16″	N17°56′19″	psammite	•	•	
MH-53	W97°47′20″	N17°56′20″	psammite	•	•	•
MH-56	W97°48′08″	N17°57′50″	metapelite	•	•	
MH-68	W97°40′47″	N18°11′02″	metapsammite	•	•	
MH-69	W97°40′47″	N18°11′02″	metapsammite	•		
MH-71	W97°41′59″	N18°10′26″	Bt-schist	•		
MH-73	W97°41′58″	N18°09′47″	metapsammite	•	•	•
MH-74	W97°42′10″	N18°09′36″	metapelite	•	•	
MH-78	W97°46′32″	N18°05′49″	metapelite	•		
MH-79	W97°46′39″	N18°05′40″	Bt-schist	•		
MH-80	W97°46′39″	N18°05′40″	Fsp-rich mylonite	•		
MH-83	W97°49′38″	N18°03′10″	metapsammite	•		
MH-84	W97°49′38″	N18°03′10″	metapelite	•		
MH-85	W97°51′20″	N18°06′49″	metapsammite	•	•	•
MH-87	W97°48′18″	N18°04′49″	metapelite	•	•	
MH-95	W97°53′59″	N18°06′51″	mylonite	•	•	
PET-484-1	W97°53′59″	N18°06′51″	metapelite	•	•	
TEP-474-1	W97°49′43″	N18°03′10″	metapelite	•		
TEP-474-2	W97°49′43″	N18°03′10″	metapsammite	•		
TEP-474-3	W97°49′43″	N18°03′10″	metapsammite	•	•	•
TEP-474-4	W97°49′43″	N18°03′10″	metapelite	•	•	
TEP-478-1	W97°48′55″	N18°03′55″	metapelite	•		
TEP-478-2	W97°48′55″	N18°03′55″	metapsammite	•		
TUT-477-1	W97°47′47″	N18°04′24″	quarzite	•		
TUT-477-2	W97°47′47″	N18°04′24″	metapelite	•		

Tabla 21.: *Whole-rock geochemistry of amphibolites from the Chazumba Lithodeme*

Sample	AYU-457-3	AYU-458-1	AYU-458-2	AYU-458-3	AYU-458-4	AYU-459-1	AYU-460-2	AYU-462-1
Major element abundances (wt %)								
SiO_2	49.00	49.12	47.06	47.79	47.98	46.65	53.32	48.33
TiO_2	1.91	3.17	2.73	1.73	1.90	3.04	1.19	3.36
Al_2O_3	14.55	12.61	14.21	13.93	13.67	13.65	16.37	16.18
Fe_2O_3	13.50	15.74	14.57	14.09	15.19	15.20	11.55	13.77
FeO_t[a]	12.15	14.16	13.11	12.68	13.67	13.68	10.39	12.39
MnO	0.22	0.21	0.19	0.21	0.26	0.20	0.18	0.18
MgO	5.78	5.23	6.15	7.65	7.27	6.52	5.64	4.59
CaO	9.49	10.38	11.77	10.77	9.86	10.95	10.34	7.77
Na_2O	1.62	1.97	2.05	2.09	1.44	2.73	0.63	0.69
K_2O	1.26	0.85	0.75	1.02	0.82	0.83	0.27	2.41
P_2O_5	0.22	0.35	0.28	0.16	0.20	0.33	0.44	0.62
LOI[b]	2.09	1.05	0.69	1.10	1.12	0.70	0.58	2.69
Total	99.64	100.68	100.45	100.53	99.71	100.79	100.51	100.59
Mg#[c]	32.24	26.97	31.93	37.63	34.72	32.28	35.18	27.03
CIA[d]	54.05	48.86	49.37	50.09	53.01	48.47	59.29	59.82
Trace element abundances (ppm)								
V	382.6	395.1	359.6	369.3	381.8	417.8	199.2	288.9
Cr	158.8	109.0	241.4	286.7	266.1	231.0	169.3	16.4
Co	43.1	44.8	40.4	46.1	43.4	43.3	32.9	33.5
Ni	67.2	67.0	91.5	92.1	75.8	97.0	54.6	10.5
Cu	32.3	156.2	64.7	81.9	5.2	165.8	4.8	11.4
Zn	106.2	123.1	67.9	97.5	112.8	131.7	120.7	104.8
Ga	20.2	21.7	22.1	18.1	20.6	21.7	20.6	22.6
Rb	20.2	13.3	8.1	23.3	17.6	11.1	5.1	93.8
Sr	179.5	280.6	300.0	216.2	132.4	273.5	161.2	322.6
Pb	8.5	8.3	12.70	12.4	13.8	10.3	12.10	3.90
U	6.9	0.5	1.80	0.0	7.7	0.0	2.90	2.20
Cs	0.0	0.0	0.00	0.0	0.0	0.0	0.90	0.40
Y	33.4	32.2	26.791	30.5	33.3	31.4	33.930	31.495
Zr	131.6	202.1	228.022	102.7	104.1	196.1	321.680	444.569
Nb	12.9	22.6	19.583	7.5	9.9	20.9	27.944	66.608
Ba	215.9	115.5	105.727	145.2	173.4	152.2	79.440	1063.631
La			16.294				22.382	58.586
Ce			38.324				46.226	119.466
Pr			5.307				5.727	14.216
Nd			24.660				23.754	56.268
Sm			5.925				5.380	10.368
Eu			1.951				1.605	2.822
Gd			5.788				5.404	7.717
Tb			0.960				0.992	1.141
Dy			5.573				6.008	6.883
Ho			1.132				1.311	1.268
Er			2.906				3.931	3.240
Tm			0.410				0.581	0.414
Yb			2.458				4.088	2.626
Lu			0.316				0.580	0.356
Hf			5.053				5.930	9.328
Ta			0.842				1.084	3.071
Th			1.756				1.699	7.556
Eu/Eu*[e]			1.019				0.910	0.964
$(La/Yb)_N$[f]			4.755				3.927	16.006
$(La/Sm)_N$[g]			1.775				2.685	3.648
$(Gd/Yb)_N$[h]			1.948				1.093	2.432

Table 21 (continued)

Sample	AYU-462-2	AYU-464-1	AYU-464-2	AYU-465-1	AYU-466-1	AYU-468-1	AYU-469-1	AYU-469-2
Major element abundances (wt %)								
SiO_2	44.03	55.84	45.98	45.40	47.16	44.89	48.10	45.71
TiO_2	3.73	1.52	1.58	1.41	1.81	1.72	1.09	1.10
Al_2O_3	15.96	13.30	15.48	15.20	15.18	10.46	16.50	15.57
Fe_2O_3	13.83	11.77	13.81	14.73	14.05	13.19	11.33	12.45
FeO_t[a]	12.44	10.59	12.43	13.25	12.64	11.87	10.19	11.20
MnO	0.22	0.14	0.22	0.23	0.20	0.23	0.19	0.18
MgO	6.08	6.43	8.70	8.29	7.99	10.93	7.52	8.85
CaO	11.88	7.18	10.68	11.23	10.82	15.06	10.66	11.82
Na_2O	1.01	2.00	2.16	1.79	1.24	0.95	2.72	2.22
K_2O	1.08	1.06	0.78	0.72	0.74	0.58	1.51	1.17
P_2O_5	0.70	0.08	0.12	0.15	0.16	0.19	0.11	0.10
LOI[b]	1.46	0.93	1.29	1.20	1.19	1.89	1.20	0.89
Total	99.97	100.25	100.80	100.34	100.54	100.09	100.93	100.06
Mg#[c]	32.82	37.78	41.18	38.48	38.73	47.94	42.45	44.13
CIA[d]	53.32	56.50	53.20	52.52	54.25	38.67	52.56	50.58
Trace element abundances (ppm)								
V	305.4	319.4	342.9	365.1	397.3	270.4	226.7	215.0
Cr	64.1	123.6	271.4	231.9	289.6	1632.1	475.5	545.3
Co	32.8	31.2	51.7	52.3	47.0	69.1	42.2	53.9
Ni	32.7	49.3	108.1	105.1	130.9	503.4	235.6	265.8
Cu	136.3	119.6	111.5	157.5	206.6	33.4	10.7	50.1
Zn	103.8	95.2	87.6	89.6	84.4	96.1	94.2	83.7
Ga	20.7	17.7	17.0	17.1	18.7	14.4	17.4	15.4
Rb	34.4	27.7	17.0	19.8	19.8	10.4	31.3	15.3
Sr	509.3	132.9	266.5	214.9	263.7	207.0	305.8	223.4
Pb	7.50	10.20	8.3	7.4	4.50	5.0	4.8	7.20
U	1.60	1.30	0.0	1.1	4.70	0.0	2.8	0.40
Cs	0.00	1.00	0.0	0.0	0.80	6.7	0.0	1.00
Y	29.363	30.438	30.8	27.9	25.500	17.6	25.0	23.677
Zr	449.316	174.644	80.7	82.1	129.608	126.7	89.4	91.672
Nb	65.582	12.024	6.0	5.4	6.106	13.8	3.1	1.968
Ba	336.091	567.819	213.7	94.4	171.058	305.5	144.6	136.158
La	65.319	10.788			5.930			3.262
Ce	131.187	24.707			15.806			8.595
Pr	15.174	3.679			2.518			1.532
Nd	58.822	16.891			12.669			8.086
Sm	10.469	4.691			3.654			2.817
Eu	3.288	1.371			1.349			1.044
Gd	7.620	4.827			4.304			3.361
Tb	1.208	0.822			0.755			0.619
Dy	6.846	5.589			5.038			4.559
Ho	1.171	1.203			1.008			0.955
Er	3.318	3.536			3.004			2.958
Tm	0.449	0.531			0.393			0.432
Yb	2.691	3.526			2.780			2.857
Lu	0.342	0.535			0.405			0.422
Hf	9.555	4.234			2.946			2.070
Ta	2.922	0.431			0.241			0.088
Th	8.403	1.313			0.716			0.305
Eu/Eu*[e]	1.125	0.881			1.040			1.037
$(La/Yb)_N$[f]	17.412	2.195			1.530			0.819
$(La/Sm)_N$[g]	4.028	1.485			1.048			0.748
$(Gd/Yb)_N$[h]	2.343	1.133			1.280			0.973

Table 21 (continued)

Sample	MH-5	MH-6	MH-17	MH-18	MH-30	MH-32	MH-48	MH-75
Major element abundances (wt %)								
SiO_2	46.23	47.46	47.32	46.67	51.05	48.93	46.55	48.56
TiO_2	1.45	1.76	1.37	1.28	1.39	1.81	2.84	1.35
Al_2O_3	17.60	15.11	14.57	14.53	15.44	14.75	13.57	17.09
Fe_2O_3	11.89	13.87	13.78	13.71	10.91	13.27	14.54	10.94
FeO_t[a]	10.70	12.48	12.40	12.34	9.82	11.94	13.08	9.84
MnO	0.19	0.22	0.22	0.22	0.19	0.21	0.23	0.18
MgO	5.82	9.15	8.01	8.47	6.49	8.36	6.41	5.06
CaO	10.93	9.61	10.87	10.22	8.34	7.79	10.72	9.48
Na_2O	3.21	1.36	1.66	1.16	2.57	1.18	0.99	3.44
K_2O	0.59	0.57	0.67	1.07	0.72	0.58	1.24	0.57
P_2O_5	0.22	0.14	0.13	0.12	0.14	0.16	0.31	0.17
LOI[b]	1.89	1.40	1.21	1.18	1.19	2.37	1.76	2.10
Total	100.02	100.65	99.81	98.62	98.44	99.40	99.16	98.94
Mg#[c]	35.23	42.30	39.25	40.71	39.80	41.18	32.88	33.95
CIA[d]	54.44	56.70	52.47	53.85	57.04	60.70	51.17	55.89
Trace element abundances (ppm)								
V	301.8	333.4	342.4	337.1	271.8	335.8	402.0	253.1
Cr	659.9	412.2	243.3	265.5	383.0	329.3	217.4	555.4
Co	55.8	48.1	52.6	53.7	45.7	47.2	45.0	54.5
Ni	223.0	138.1	101.5	98.5	76.1	116.9	84.3	195.1
Cu	70.1	15.3	444.4	390.4	236.6	30.0	69.2	104.4
Zn	133.7	123.9	92.4	91.7	137.6	123.5	116.0	134.1
Ga	17.0	20.1	16.0	16.4	17.1	20.6	21.7	15.4
Rb	11.4	20.8	17.3	34.3	23.4	20.8	32.4	14.0
Sr	193.8	117.7	225.0	185.4	347.1	117.4	244.0	188.7
Pb	5.8	12.6	6.60	3.20	9.40	10.40	7.20	6.10
U	0.0	3.2	3.10	0.00	1.50	2.60	0.00	1.60
Cs	0.0	0.0	0.00	3.70	0.00	0.00	0.00	0.00
Y	31.7	26.3	23.572	22.799	30.893	26.230	27.130	27.759
Zr	108.3	89.5	76.882	74.936	113.422	124.361	221.208	115.226
Nb	5.1	9.8	5.590	5.805	4.490	7.984	20.507	2.989
Ba	110.1	124.5	106.575	152.557	228.770	169.024	306.285	229.073
La			4.119	3.662	7.308	9.098	16.533	3.758
Ce			10.223	9.624	18.567	17.770	39.427	10.801
Pr			1.585	1.544	3.087	3.004	5.409	1.694
Nd			8.841	8.297	15.542	14.611	26.471	9.276
Sm			2.961	2.809	4.782	4.704	6.024	2.983
Eu			1.059	0.984	1.261	1.521	2.255	1.272
Gd			3.903	3.618	5.751	4.619	6.278	4.062
Tb			0.693	0.696	0.968	0.874	1.032	0.781
Dy			4.778	4.556	6.329	5.529	6.123	5.043
Ho			0.937	0.901	1.216	1.038	1.147	1.086
Er			2.774	2.590	3.449	2.636	2.922	3.421
Tm			0.417	0.367	0.489	0.428	0.390	0.446
Yb			2.616	2.248	3.068	1.945	2.302	3.226
Lu			0.380	0.381	0.443	0.356	0.413	0.438
Hf			1.867	1.944	2.703	2.899	5.225	2.887
Ta			0.140	0.148	0.073	0.333	0.715	0.142
Th			0.357	0.273	1.051	0.833	2.417	0.629
Eu/Eu*[e]			0.952	0.943	0.735	0.998	1.121	1.117
$(La/Yb)_N$[f]			1.129	1.169	1.708	3.356	5.152	0.835
$(La/Sm)_N$[g]			0.898	0.842	0.986	1.249	1.772	0.813
$(Gd/Yb)_N$[h]			1.234	1.332	1.550	1.965	2.256	1.041

[a] Total Fe content, FeOt = Fe_2O_3 / (2 × 159.68 × 71.84)
[b] Loss on ignition
[c] Magesiun number, Mg# = (100 × MgO) / (MgO + FeO_t)
[d] Chemical index of alteration, CIA=Al_2O_3/(Al_2O_3+ CaO*+ Na_2O + K_2O), CaO* represents silicate fraction of sample, after Nesbitt y Young (1982).
[e] Europium anomaly, as proposed by Taylor y McLennan (1985): Eu/Eu* = Eu_N / $\sqrt{(Sm_N \times Gd_N)}$, N—normalized to Chondrite (Sun y McDonough, 1989)
[f] Measure for REE fractionation: (La/Yb) ÷ $(La/Yb)_N$, N—normalized to Chondrite (Sun y McDonough, 1989)
[g] Measure for LREE fractionation: (La/Sm) ÷ $(La/Sm)_N$, N—normalized to Chondrite (Sun y McDonough, 1989)
[h] Measure for HREE fractionation: (Gd/Yb) ÷ $(Gd/Yb)_N$, N—normalized to Chondrite (Sun y McDonough, 1989)

Tabla 22.: *Whole-rock geochemistry of metasedimentary rocks from the Chazumba Lithodeme*

Sample	AYU-456-1	AYU-456-2	AYU-460-1	AYU-M4-1	AYU-M4-2	MH-2	MH-4	MH-7
Major element abundances (wt %)								
SiO_2	66.27	70.21	66.28	69.78	71.11	64.88	64.76	52.44
TiO_2	0.73	0.69	0.70	0.74	0.73	0.82	0.83	0.90
Al_2O_3	15.37	13.16	16.46	14.04	13.40	15.57	16.94	19.91
Fe_2O_3	5.78	4.81	6.18	5.01	4.58	7.14	6.36	8.05
FeO_t[a]	5.20	4.33	5.56	4.51	4.12	6.42	5.72	7.24
MnO	0.08	0.30	0.11	0.07	0.06	0.11	0.10	0.08
MgO	2.14	1.94	2.15	1.81	1.68	2.42	1.59	3.50
CaO	2.76	2.59	3.98	2.00	1.60	2.33	0.44	1.44
Na_2O	2.45	1.74	3.01	2.75	2.21	2.58	0.99	1.57
K_2O	2.43	1.80	2.31	2.49	3.16	2.81	3.34	5.05
P_2O_5	0.15	0.21	0.18	0.20	0.18	0.19	0.17	0.23
LOI[b]	1.97	2.02	0.70	1.03	1.18	1.98	3.39	5.18
Total	100.14	99.47	102.06	99.91	99.89	100.82	98.91	98.34
Mg#[c]	29.15	30.95	27.88	28.65	28.96	27.36	21.74	32.58
CIA[d]	66.80	68.22	63.90	65.98	65.78	66.85	78.03	71.18
Trace element abundances (ppm)								
V	115.6	127.2	127.7	95.9	96.0	159.8	170.3	151.7
Cr	82.7	79.3	33.1	64.1	63.5	68.3	117.2	107.3
Co	15.3	7.8	11.9	10.9	9.7	12.8	14.9	18.6
Ni	25.3	34.6	12.3	22.1	21.7	23.3	37.0	49.0
Cu	21.3	20.2	28.0	13.8	4.2	38.1	50.9	60.9
Zn	82.1	106.0	74.0	78.2	70.3	92.3	85.7	127.6
Ga	20.1	18.6	20.2	17.4	16.7	20.8	24.6	27.3
Rb	120.1	80.6	105.2	94.0	114.2	129.5	167.2	191.1
Sr	198.5	168.0	209.2	245.5	227.1	202.5	98.8	196.4
Pb	14.1	15.8	14.7	15.4	15.6	18.1	31.3	21.8
U	2.5	2.4	4.4	7.4	1.1	4.8	4.0	4.1
Cs	9.8	3.2	9.9	3.0	3.3	6.6	8.4	6.7
Y	26.3	29.7	28.725	28.018	26.819	20.870	24.952	42.441
Zr	224.9	263.9	268.412	316.879	281.840	230.454	194.610	240.144
Nb	16.3	18.0	15.768	11.183	11.443	12.178	15.229	17.002
Ba	536.4	1070.1	539.717	617.549	1105.386	950.221	793.380	1569.857
La			36.762	30.877	29.571	26.075	30.025	41.475
Ce			73.430	62.574	57.953	57.554	76.274	82.328
Pr			8.787	7.738	7.476	6.640	7.622	10.444
Nd			34.733	30.690	29.133	26.420	29.652	43.843
Sm			6.452	6.041	5.784	5.279	5.399	8.560
Eu			1.248	1.411	1.344	1.207	1.127	2.002
Gd			4.938	4.809	4.660	3.938	3.938	7.507
Tb			0.875	0.804	0.776	0.703	0.746	1.262
Dy			5.605	5.410	4.949	4.144	5.020	7.711
Ho			1.128	1.125	1.046	0.872	0.964	1.573
Er			3.573	3.461	3.014	2.468	3.127	4.928
Tm			0.470	0.483	0.461	0.359	0.497	0.677
Yb			3.377	3.420	3.045	2.511	3.339	4.522
Lu			0.455	0.453	0.426	0.356	0.493	0.671
Hf			5.402	6.848	6.461	4.981	4.236	5.680
Ta			0.807	0.495	0.492	0.594	0.832	0.921
Th			10.495	8.047	7.820	8.940	15.162	13.491
Eu/Eu*[e]			0.676	0.800	0.791	0.809	0.747	0.764
$(La/Yb)_N$[f]			7.808	6.475	6.966	7.448	6.451	6.579
$(La/Sm)_N$[g]			3.679	3.300	3.301	3.189	3.590	3.128
$(Gd/Yb)_N$[h]			1.210	1.163	1.266	1.297	0.976	1.373

Table 22 (continued)

Sample	MH-37	MH-41	MH-42	MH-46	MH-50	MH-53	MH-56	MH-68
Major element abundances (wt %)								
SiO_2	70.44	74.65	68.92	67.73	76.79	82.62	66.29	68.40
TiO_2	0.53	0.43	0.51	0.51	0.64	0.47	0.94	0.71
Al_2O_3	13.70	12.32	14.42	15.51	9.16	6.85	14.23	14.06
Fe_2O_3	3.90	3.39	4.19	4.25	2.99	3.26	5.64	4.70
FeO_t[a]	3.51	3.05	3.77	3.82	2.69	2.93	5.07	4.23
MnO	0.09	0.09	0.10	0.13	0.02	0.03	0.09	0.07
MgO	1.55	1.19	1.43	1.32	3.92	2.49	1.90	2.00
CaO	2.40	1.95	3.07	3.04	0.43	0.49	2.77	1.39
Na_2O	3.66	2.65	2.54	3.22	1.19	0.60	2.54	1.82
K_2O	1.17	1.69	1.73	1.68	0.96	1.04	2.39	3.06
P_2O_5	0.21	0.05	0.13	0.13	0.14	0.10	0.24	0.19
LOI[b]	0.99	1.00	1.60	1.40	3.19	1.99	1.19	2.48
Total	98.64	99.41	98.64	98.91	99.43	99.93	98.22	98.87
Mg#[c]	30.64	28.06	27.50	25.66	59.30	45.91	27.24	32.11
CIA[d]	65.46	66.20	66.27	66.14	78.02	76.28	64.89	69.16
Trace element abundances (ppm)								
V	78.7	56.6	84.2	72.7	155.2	138.2	103.0	111.0
Cr	62.3	28.7	41.2	35.1	128.7	58.6	75.7	87.7
Co	13.2	9.7	10.8	9.6	11.0	8.7	9.4	10.4
Ni	39.7	11.0	11.8	11.1	54.2	28.5	15.0	26.9
Cu	17.2	9.2	18.2	18.9	11.0	23.0	48.0	20.4
Zn	60.4	53.5	85.4	50.8	12.7	40.5	76.3	82.1
Ga	15.7	13.0	17.3	17.0	12.9	10.9	18.0	18.4
Rb	48.9	58.4	71.6	60.3	23.4	34.1	79.2	113.1
Sr	250.6	197.3	177.2	219.0	36.4	59.4	272.0	162.3
Pb	13.2	14.3	15.3	21.5	6.7	7.3	14.7	21.1
U	0.6	0.4	1.2	6.6	1.8	0.9	1.6	1.8
Cs	4.4	2.4	5.8	4.1	0.0	0.0	0.0	6.8
Y	22.678	27.564	24.902	26.802	14.239	18.588	23.969	24.639
Zr	250.380	232.622	302.033	300.189	115.098	124.355	489.749	256.309
Nb	7.874	8.382	15.650	13.248	10.275	10.194	14.898	12.436
Ba	369.490	647.985	556.525	564.892	517.743	1088.485	740.128	803.817
La	24.903	21.087	29.581	40.737	17.709	15.651	29.359	31.902
Ce	54.561	42.582	64.827	84.819	36.223	29.735	53.591	32.959
Pr	6.557	5.302	8.008	10.212	4.422	3.816	8.487	7.874
Nd	26.123	22.349	29.221	41.869	16.883	16.217	30.721	30.137
Sm	5.145	3.814	6.321	7.537	3.650	3.219	6.670	5.940
Eu	1.383	1.310	1.226	1.717	0.590	0.625	1.602	1.318
Gd	3.642	3.786	4.402	5.548	2.724	3.092	4.923	4.848
Tb	0.708	0.608	0.748	0.887	0.520	0.576	0.766	0.804
Dy	4.388	4.506	4.808	5.266	2.807	3.672	4.879	4.526
Ho	0.959	1.016	1.004	1.077	0.608	0.726	1.034	0.933
Er	2.301	3.275	3.166	3.538	1.820	2.355	2.760	2.923
Tm	0.380	0.547	0.453	0.508	0.245	0.302	0.447	0.500
Yb	2.631	3.685	2.802	4.302	1.679	2.105	2.986	3.201
Lu	0.447	0.677	0.455	0.626	0.256	0.305	0.430	0.416
Hf	4.979	5.414	7.087	6.337	2.619	2.679	10.168	5.659
Ta	0.398	0.338	0.643	0.661	0.584	0.477	0.571	0.618
Th	5.143	5.886	11.073	12.270	6.418	2.877	10.128	8.963
Eu/Eu*[e]	0.976	1.054	0.711	0.812	0.572	0.605	0.855	0.751
$(La/Yb)_N$[f]	6.790	4.105	7.572	6.792	7.566	5.334	7.053	7.150
$(La/Sm)_N$[g]	3.125	3.569	3.021	3.489	3.132	3.139	2.841	3.467
$(Gd/Yb)_N$[h]	1.145	0.850	1.300	1.067	1.342	1.215	1.364	1.253

Table 22 (continued)

Sample	MH-69	MH-71	MH-73	MH-74	MH-75	MH-78	MH-79	MH-80
Major element abundances (wt %)								
SiO_2	57.94	72.00	70.89	70.53	48.56	68.57	91.95	71.28
TiO_2	0.92	0.66	1.13	0.77	1.35	0.74	0.11	0.72
Al_2O_3	19.24	12.86	12.14	13.07	17.09	13.85	2.26	14.02
Fe_2O_3	5.89	4.16	5.31	4.86	10.94	4.50	1.62	3.86
FeO_t[a]	5.30	3.74	4.78	4.37	9.84	4.05	1.46	3.47
MnO	0.06	0.07	0.08	0.14	0.18	0.05	0.01	0.06
MgO	2.81	1.37	1.57	1.75	5.06	1.57	0.43	0.44
CaO	0.77	1.24	1.98	2.02	9.48	1.77	0.04	1.22
Na_2O	1.00	2.72	2.91	2.79	3.44	2.53	0.00	2.94
K_2O	5.36	2.25	1.65	1.68	0.57	2.58	0.62	1.84
P_2O_5	0.20	0.16	0.26	0.23	0.17	0.19	0.02	0.18
LOI[b]	4.40	0.99	0.90	1.00	2.10	1.49	0.59	2.27
Total	98.59	98.48	98.81	98.83	98.94	97.84	97.65	98.83
Mg#[c]	34.65	26.79	24.73	28.58	33.95	27.94	22.78	11.24
CIA[d]	72.96	67.44	64.99	66.82	55.89	66.81	77.40	70.03
Trace element abundances (ppm)								
V	167.3	72.8	107.8	88.3	253.1	90.7	92.8	93.1
Cr	123.4	58.9	79.7	84.2	555.4	70.4	50.8	78.9
Co	16.6	13.2	11.8	14.7	54.5	12.0	4.9	12.1
Ni	25.5	16.0	20.4	24.6	195.1	22.7	12.3	23.7
Cu	38.3	139.0	16.3	168.1	104.4	105.6	168.1	120.4
Zn	220.6	63.2	67.3	75.7	134.1	66.4	22.6	51.2
Ga	27.2	14.1	15.9	13.5	15.4	18.0	3.8	17.0
Rb	191.4	74.4	62.4	74.7	14.0	96.5	28.3	77.0
Sr	128.6	201.0	324.2	202.4	188.7	251.5	10.1	214.8
Pb	29.7	11.8	10.5	20.0	6.1	15.8	8.2	17.9
U	5.0	3.1	5.0	3.1	1.6	0.5	1.8	4.5
Cs	7.8	4.6	5.9	3.7	0.0	4.1	0.0	2.7
Y	41.0	28.7	42.468	30.034	27.759	38.4	4.3	31.0
Zr	221.0	225.8	775.577	389.499	115.226	297.6	11.1	256.3
Nb	16.3	9.8	18.268	19.233	2.989	13.7	4.1	12.8
Ba	1459.6	541.7	473.627	334.818	229.073	862.2	2057.0	483.0
La			49.253	30.041	3.758			
Ce			88.174	61.850	10.801			
Pr			12.819	7.484	1.694			
Nd			49.090	30.022	9.276			
Sm			9.450	6.183	2.983			
Eu			1.940	1.236	1.272			
Gd			8.114	5.487	4.062			
Tb			1.245	0.895	0.781			
Dy			7.307	5.671	5.043			
Ho			1.489	1.108	1.086			
Er			4.456	3.161	3.421			
Tm			0.652	0.492	0.446			
Yb			4.717	3.307	3.226			
Lu			0.714	0.497	0.438			
Hf			14.369	9.325	2.887			
Ta			0.774	0.661	0.142			
Th			12.750	9.401	0.629			
Eu/Eu*[e]			0.677	0.649	1.117			
$(La/Yb)_N$[f]			7.489	6.516	0.835			
$(La/Sm)_N$[g]			3.365	3.137	0.813			
$(Gd/Yb)_N$[h]			1.423	1.373	1.041			

Table 22 (continued)

Sample	MH-83	MH-84	MH-85	MH-87	MH-95	PET-484-1	TEP-474-1	TEP-474-2
Major element abundances (wt %)								
SiO_2	51.39	63.73	90.31	70.75	92.65	89.54	65.26	65.50
TiO_2	0.93	0.75	0.19	0.71	0.15	0.22	0.82	0.83
Al_2O_3	21.45	15.44	3.78	13.21	2.71	4.23	15.85	16.34
Fe_2O_3	6.83	5.23	1.70	4.32	1.20	1.47	5.27	5.41
FeO_t[a]	6.15	4.71	1.53	3.89	1.08	1.32	4.74	4.87
MnO	0.05	0.04	0.04	0.08	0.01	0.00	0.02	0.02
MgO	4.75	2.66	0.75	1.34	0.55	0.53	4.35	4.44
CaO	1.15	1.94	0.19	2.30	0.08	0.02	0.40	0.43
Na_2O	5.75	3.29	0.12	3.02	-0.04	0.00	2.80	2.90
K_2O	1.93	2.08	1.01	2.03	0.72	1.04	2.18	2.22
P_2O_5	0.49	0.24	0.08	0.20	0.12	0.07	0.19	0.20
LOI[b]	3.59	2.27	1.20	0.69	0.60	0.99	3.25	1.78
Total	98.31	97.67	99.37	98.65	98.74	98.12	100.39	100.08
Mg#[c]	43.60	36.11	32.90	25.64	33.75	28.61	47.84	47.70
CIA[d]	70.84	67.87	74.12	64.25	78.10	79.96	74.66	74.65
Trace element abundances (ppm)								
V	156.2	92.7	79.4	77.8	72.4	116.7	140.3	131.5
Cr	104.0	66.0	44.3	68.8	41.7	38.1	90.4	77.3
Co	11.9	12.2	4.9	13.1	3.6	1.6	13.4	12.3
Ni	22.8	18.5	20.5	18.8	12.0	13.4	33.2	97.3
Cu	288.5	182.3	29.7	301.1	46.1	46.9	6.4	7.1
Zn	41.7	50.9	42.0	69.4	33.2	22.7	53.4	47.5
Ga	26.8	17.8	6.3	13.9	5.4	6.5	21.5	17.5
Rb	69.5	50.1	68.5	74.9	22.4	25.0	73.4	31.8
Sr	177.2	261.3	20.0	282.9	31.8	38.0	72.8	220.7
Pb	6.2	15.4	6.1	20.6	5.8	0.0	8.5	10.3
U	5.8	3.4	3.3	2.9	5.5	4.9	1.1	4.3
Cs	0.0	1.2	0.0	5.2	0.0	0.0	0.0	1.6
Y	37.6	31.4	7.039	23.771	6.849	12.275	30.6	28.3
Zr	430.1	247.5	54.579	276.372	43.371	49.546	235.8	295.5
Nb	13.1	10.6	3.541	13.371	2.562	3.543	15.3	11.6
Ba	184.4	741.1	3509.413	504.367	2909.724	6333.038	630.1	276.0
La			8.135	28.611	7.187	13.115		
Ce			13.933	57.552	10.869	16.732		
Pr			1.953	7.216	1.742	3.521		
Nd			7.063	30.227	8.215	14.256		
Sm			1.468	5.852	1.437	2.529		
Eu			0.441	1.428	0.383	0.585		
Gd			1.263	4.704	0.970	2.044		
Tb			0.221	0.760	0.154	0.329		
Dy			1.457	4.770	1.273	2.377		
Ho			0.279	0.909	0.237	0.456		
Er			0.997	2.624	0.828	1.377		
Tm			0.119	0.391	0.141	0.211		
Yb			1.333	2.596	0.682	1.265		
Lu			0.170	0.391	0.136	0.204		
Hf			1.131	6.287	0.930	1.157		
Ta			0.211	0.495	0.106	0.227		
Th			4.343	6.296	2.188	3.316		
Eu/Eu*[e]			0.990	0.832	0.991	0.786		
$(La/Yb)_N$[f]			4.377	7.904	7.564	7.436		
$(La/Sm)_N$[g]			3.577	3.156	3.229	3.348		
$(Gd/Yb)_N$[h]			0.784	1.499	1.177	1.337		

Table 22 (continued)

Sample	TEP-474-3	TEP-474-4	TEP-478-1	TEP-478-2	TUT-477-1	TUT-477-2
Major element abundances (wt %)						
SiO_2	70.77	64.59	74.19	69.27	71.37	68.86
TiO_2	0.81	0.83	0.61	0.80	0.69	0.75
Al_2O_3	12.76	16.35	12.93	14.73	13.59	14.52
Fe_2O_3	4.55	3.87	3.85	4.84	4.62	5.47
FeO_t[a]	4.09	3.48	3.46	4.36	4.16	4.92
MnO	0.05	0.01	0.06	0.06	0.05	0.05
MgO	1.55	5.62	1.37	1.71	1.67	1.57
CaO	2.19	0.31	1.98	2.00	1.94	1.14
Na_2O	2.85	2.18	2.43	2.71	2.35	1.66
K_2O	1.78	2.52	2.13	2.72	2.49	3.16
P_2O_5	0.20	0.19	0.17	0.22	0.19	0.20
LOI[b]	0.99	3.75	0.89	1.18	1.19	2.49
Total	98.50	100.22	100.60	100.25	100.15	99.87
Mg#[c]	27.46	61.74	28.34	28.19	28.66	24.18
CIA[d]	65.17	76.54	66.41	66.47	66.72	70.90
Trace element abundances (ppm)						
V	107.5	133.0	88.6	133.7	97.3	128.8
Cr	74.1	82.8	57.4	89.8	74.6	89.3
Co	8.8	8.2	11.1	10.0	10.5	11.9
Ni	38.3	34.5	19.1	21.5	29.0	28.3
Cu	19.2	4.8	6.8	14.9	15.3	34.3
Zn	69.7	16.2	75.8	89.7	76.7	121.7
Ga	16.1	21.6	14.5	19.6	16.5	20.9
Rb	71.2	93.5	90.1	119.3	88.7	115.5
Sr	261.2	30.4	206.5	287.8	238.6	156.3
Pb	15.2	8.5	20.6	15.4	18.9	19.2
U	0.2	8.4	4.5	3.9	2.2	0.1
Cs	0.0	0.0	5.6	4.7	0.0	5.8
Y	25.192	31.547	24.7	30.9	27.4	31.9
Zr	405.903	335.912	252.5	289.8	257.1	262.1
Nb	12.173	13.070	11.0	13.4	12.2	15.7
Ba	660.056	393.362	571.5	857.5	843.8	956.7
La	28.982	39.315				
Ce	61.724	78.360				
Pr	7.539	9.707				
Nd	30.004	38.812				
Sm	5.569	6.519				
Eu	1.366	1.371				
Gd	4.345	5.911				
Tb	0.736	1.039				
Dy	4.907	6.133				
Ho	1.026	1.201				
Er	2.981	3.577				
Tm	0.452	0.527				
Yb	2.983	3.367				
Lu	0.442	0.434				
Hf	7.997	6.681				
Ta	0.526	0.557				
Th	7.879	10.140				
Eu/Eu*[e]	0.849	0.675				
$(La/Yb)_N$[f]	6.969	8.376				
$(La/Sm)_N$[g]	3.360	3.893				
$(Gd/Yb)_N$[h]	1.205	1.452				

[a] Total Fe content, FeOt = Fe_2O_3 / (2 × 159.68 × 71.84)
[b] Loss on ignition
[c] Magesiun number, Mg# = (100 × MgO) / (MgO + FeO_t)
[d] Chemical index of alteration, CIA=Al_2O_3/(Al_2O_3+ CaO*+ Na_2O + K_2O), CaO* represents silicate fraction of sample, after Nesbitt y Young (1982).
[e] Europium anomaly, as proposed by Taylor y McLennan (1985): Eu/Eu* = Eu_N / $\sqrt{(Sm_N \times Gd_N)}$, N—normalized to Chondrite (Sun y McDonough, 1989)
[f] Measure for REE fractionation: (La/Yb) ÷ $(La/Yb)_N$, N—normalized to Chondrite (Sun y McDonough, 1989)
[g] Measure for LREE fractionation: (La/Sm) ÷ $(La/Sm)_N$, N—normalized to Chondrite (Sun y McDonough, 1989)
[h] Measure for HREE fractionation: (Gd/Yb) ÷ $(Gd/Yb)_N$, N—normalized to Chondrite (Sun y McDonough, 1989)

Tabla 23.: *Sm-Nd isotopic data of amphibolites and metasedimentary rocks of the Chazumba Lithodeme*

Sample	Nd (ppm)	Sm (ppm)	Sm/Nd	$\frac{^{147}Sm}{^{144}Nd}$	$\frac{^{143}Nd}{^{144}Nd}$	2σ	T(i) (Ma)	$\epsilon_{Nd}(0)$[a]	Nd(i)	T_{DM}[b] (Ga)
Amphibolites										
AYU-462-1	71.68	10.34	0.14	0.0872	0.512 391	6	190	−4.82	−2.16	0.79
AYU-462-2	58.61	10.52	0.18	0.1085	0.512 441	7	190	−3.84	−1.70	0.88
AYU-458-2	24.56	6.14	0.25	0.1512	0.512 744	5	190	2.07	3.17	0.74
AYU-460-2	22.71	5.16	0.23	0.1373	0.512 777	6	190	2.71	4.15	0.55
MH-48	24.26	6.04	0.25	0.1506	0.512 765	7	190	2.48	3.60	0.69
AYU-466-1	*12.22*	*3.74*	*0.31*	*0.1851*	*0.512 958*	*7*	*190*	*6.24*	*6.53*	–
MH-30	11.58	3.55	0.31	0.1850	0.512 887	6	190	4.86	5.14	–
MH-32	17.58	4.70	0.27	0.1617	0.512 713	6	190	1.46	2.31	0.97
AYU-469-2	*7.21*	*2.39*	*0.33*	*0.2005*	*0.512 934*	*7*	*190*	*5.77*	*5.68*	–
MH-75	*8.69*	*2.92*	*0.34*	*0.2032*	*0.513 108*	*7*	*190*	*9.17*	*9.01*	–
Metasedimentary rocks										
MH-53	16.34	3.41	0.21	0.1260	0.512 602	6	195	−0.70	1.06	0.78
MH-41	18.72	3.76	0.20	0.1213	0.512 469	6	195	−3.30	−1.42	0.95
MH-42	23.77	4.70	0.20	0.1195	0.512 157	6	195	−9.38	−7.46	1.42
MH-73	49.16	9.36	0.19	0.1150	0.512 142	7	195	−9.68	−7.65	1.38
MH-74	31.51	6.45	0.20	0.1237	0.512 185	6	195	−8.84	−7.02	1.44
MH-85	7.82	1.58	0.20	0.1224	0.512 260	7	195	−7.37	−5.53	1.30
TEP-474-3	30.07	5.83	0.19	0.1172	0.512 211	7	195	−8.33	−6.35	1.31

[a] ϵ_{Nd} values are relative to $^{143}Nd/^{144}Nd$ = 0.512638 and $^{147}Sm/^{144}Nd$ = 0.196593 for present-day chondrite uniform reservoir (CHUR; Jacobsen y Wasserburg, 1980) and $\lambda^{147}Sm = 6.54 \cdot 10–12/yr$ (Steiger y Jäger, 1977)

[b] Depleted mantle model ages (T_{DM}) were calculated using the depleted mantle model of DePaolo (1981a). Values in italic type face denote samples with model ages that are considered unreliable due to high $^{147}Sm/^{144}Nd$ (>0.165; Stern, 2002)